

# Improving the Imaging of Small High-Density Structures in Computed Tomography

Printed by: Febodruk b.v., The Netherlands  
<http://www.febodruk.nl>

Cover theme: Artifacts in an imaging system: A reflection of the true object  
Cover design: Empar Rollano Hijarrubia

Copyright © 2007 by Empar Rollano Hijarrubia

Several chapters of this thesis are based on published papers. Copyrights of these papers remain with the journals.

The printing of this thesis has been supported by the Erasmus University Rotterdam.

*A la Yaya, Lourdes, la Mare, i Pablo*



**Improving the Imaging of Small High-Density Structures in  
Computed Tomography**

Verbeterend het beeld van kleine hoogte-dichtheid structuren in  
computed tomografie

**PROEFSCHRIFT**

ter verkrijging van de graad van doctor aan de  
Erasmus Universiteit Rotterdam  
op gezag van de  
rector magnificus  
Prof. dr. S.W.J. Lamberts  
en volgens besluit van het College voor Promoties.

De openbare verdediging zal plaatsvinden op  
**woensdag 24 oktober 2007 at 11.45 hrs**

door

**Maria Empar Rollano Hijarrubia**

geboren te Valencia, Spanje



## **PROMOTIECOMMISSIE**

Promotor(en):               **Prof. dr. W.J. Niessen.**

Overige leden:       **Prof. dr. P.M.T. Pattynama**

**Prof. dr.ir. H.H. Weinans**

**Prof. dr. ir. C.W.E. van Eijk**

Copromotor(en): **Dr. R. Stokking**

# Preface

This thesis represents the work of four years of research in the Biomedical Imaging Group Rotterdam (BIGR) at the Erasmus MC. Without the support of the members of BIGR and many other people from the departments of Medical Informatics and Radiology this thesis would not have been possible. To all of these people I acknowledge their help and support, not only in the academic but also in the personal area, that have contributed to the completion of this thesis.

I owe an especial acknowledgment to my thesis director Wiro Niessen. It was in the last months of my thesis when he started as leader of BIGR. The fact that he accepted to become my advisor was decisive for my thesis. His good judge, scientific rigor, and capacity to take decisions were the motor of my research. Our multiple and very long discussions helped me to focus on the subject, go deeper in my studies, and become more confident in my work. Thanks for your trust and support!

I also owe an especial mention to my codirector Rik Stokking for all his support and friendly understanding during these four years. I always appreciated very much your unconditional confidence in my research and in the crucial decisions I had to take in some moments. Your communication skills and ability to understand people were an example for me, and made my life at meetings much easier. Thanks for your time and patience!

I want to express all my gratitude to Prof. Krestin, who always supported me and trusted my research. His good judge and critical mentality to lead the department were also crucial to the completion of this thesis.

I cannot forget that Henri Vrooman decided to support me as a PhD student in his group. Jan Grashuis was always friendly and close to me. Frits van der Meer and Filippo Cademartiri were both relevant the first years of my thesis; the ideas that followed the discussions with each of them were fundamental for the definition of the research lines of my thesis. Sennay Ghebreab always was ready to listen. I really thank the frank and direct talk of Erik Meijering. I also acknowledge the support of Jifke Veenland. With my office mate, Danijele Vukadinovic, I spent many funny moments. Although for a very short time, I had the pleasure to collaborate with Rashindra Manniesing. I would also like to thank to all the other members of BIGR, among them: Theo van Walsum, Albert Vossepoel, Lejla Alic, Michiel Schaap, Fedde van der Lijn, and Ihor Smal. Most of them joined the group the last year of my PhD, and made the group “BIGgeR” in all the aspects and the working atmosphere more stimulating.

I spent most of my time at Erasmus in the Radiology department. There I met wonderful people from the professional and human point of view. Peter Pattynama, I thank your support and your enthusiasm for research and new ideas. Thomas de Weert,

working with you was always easy and rewarding. The Italian “family” Manuel, Patrizia, Francesca, and Peppe, with which I shared office during more than a year, gave colour to my working days at Erasmus and made them much more cheerful. Rufina and Carmen, from the Radiology department, I welcomed so much your visits and meeting you in the corridors for a short chat!

I also want to acknowledge Harry Weinans, from the Orthopaedic department, for allowing me to use his equipment and sharing his knowledge with me.

When I started having lunch in a “Spanish way” with my Spanish friends at Erasmus MC, my lunch time was so much more joyful that I could even forget the cantina menus and the mostly grey Dutch days. The lunch group just started with three of us: Cristina (with whom I spent so many nice moments), Javi (always made us laugh! ...Never stopped talking!) and me. And it ended in a large international community: Maria (with whom I share so many hobbies), Begoña, Oscar, Laura... Also thanks to them I could get to know the lovely Elena and Javi Junior, David, Lourdes and Jose Antonio. Most of you have been part of my daily life and have made it much more plentiful.

In my five years living in Delft I had the chance to meet many very nice people. I spent a very good time with my friends Marta and Stefan (I hope to join you in Barcelona!), Paloma and Luke, Silvia and Josep, Helen and Bruno, and Ruth and Paul: It will be very nice to meet all you again in Delft! I had also the luck to meet my most chaotic friend, Patricia from Peru, with whom I spent so many unconventionally great evenings.

My friends from Spain, Lupe and Asen, Sergi (my teacher of C!), Chus, Marta and the people from the “BEN” (I’ll see you all in our “sopars del BEN”!). All of you, although in the distance, have also contributed to this thesis with your friendship and the good moments spent together.

To My family. El Tío Juanpe, who has always encouraged me to finish my thesis and everything I started. La tía Carmen, Nacho y Alejandro for their support and their presence in my thesis defense. Pedro, who has already become part of our family. Carlos, Mari, Nacho, Edu, and Dani e Inma; I have become part of their family. And I also would like to thank Constan, Andres, Begona, Mercedes, Ramon y Lisa, to be as good as a family for us, and especially for my mother.

My last words go to the persons I love most. My grandmother (la Yaya), who was and is an angel to me, my sister Lourdes, a la que vull tant, and my mother (la mare), que estime i trobe tant a faltar. They, as me, have endured for such a long time the distance and the continuous missing to each other, but despite this distance we have always been very close in our hearts. Pablo, the only person who is able to make me laugh in the good as well as in the “not so good” moments. You have brought sunlight to my life since I met you. Gracies per tot el que m’heu donat.

Empar Rollano Hijarrubia  
Rotterdam, July 2007



# Contents

<b>1. Introduction .....</b>	<b>1</b>
1.1 General introduction .....	1
1.2 Thesis overview .....	3
References.....	6
 <b>2. Imaging of Small High-density Structures in CT: a Phantom Study</b>	<b>9</b>
2.1 Introduction.....	10
2.2 Materials and Methods.....	12
2.2.1 Phantoms .....	12
2.2.2 64-slice Multi-Detector Row CT .....	13
2.2.3 Scanning protocols .....	13
2.2.4 Evaluation criteria and quantification methods .....	15
2.2.5 Simulations and experiments .....	15
2.3 Results.....	16
2.3.1 PSF measurement.....	16
2.3.2 Phantom experiments and simulations.....	16
2.4. Discussion .....	30
References.....	34
 <b>3. Accuracy Comparison of a 16 and 64 MDCT Scanner to Image Small High-density Structures.....</b>	<b>37</b>
3.1 Introduction.....	38
3.2 Materials and Methods.....	39
3.2.1 Phantom description.....	39
3.2.2 Scanning systems and imaging protocols .....	41
3.2.3 Evaluation criteria and quantification methods .....	42
3.3 Results.....	44

3.3.1	Results for the “High Resolution” protocol .....	44
3.3.2	Results for the “Heart View” protocol.....	54
3.4.	Discussion .....	55
	References.....	59
<b>4.</b>	<b>Histogram-based Selective Deblurring to Improve Computed Tomography Imaging of Calcifications .....</b>	<b>63</b>
4.1	Introduction.....	64
4.2	Materials and Methods.....	65
4.2.1	Phantom description.....	65
4.2.2	In vitro samples .....	66
4.2.3	Multidetector row Spiral CT system (MSCT) .....	66
4.2.4	Microfocus X-ray CT system.....	67
4.2.5	Histogram-Based Selective Deblurring (HiSD).....	67
4.2.6	Evaluation of the image quality .....	70
4.3	Results .....	72
4.3.1	Input parameters for Wiener filter .....	72
4.3.2	Qualitative evaluation .....	73
4.3.3	Quantitative evaluation .....	77
4.3.4	Restoration of patient images.....	82
4.4.	Discussion .....	84
	References.....	87
<b>5.</b>	<b>Histogram-based Selective Deblurring and Automated Vessel Segmentation for Improved In Vivo Calcification Visualization and Quantification in CTA .....</b>	<b>91</b>
5.1	Introduction.....	92
5.2	Materials and Methods.....	92
5.2.1	Imaging data.....	92
5.2.2	Image Acquisition and Reconstruction .....	93
5.2.3	Vessel Segmentation .....	93

5.2.4 Histogram-based Selective Deblurring (HiSD) .....	93
5.2.5 Evaluation of the image quality .....	97
5.3 Results .....	97
5.3.1 Lumen segmentation .....	97
5.3.2 Qualitative evaluation .....	98
5.3.3 Quantitative analysis .....	100
5.4. Discussion .....	105
References.....	107
<b>6. Summary and Discussion.....</b>	<b>111</b>
References.....	116
<b>Appendix. Image Quality (IQ) Obtained with HiSD Restoration versus     IQ Obtained with Clinical CT Convolution Kernels.....</b>	<b>119</b>
A.1 Introduction.....	120
A.2 Materials and Methods.....	120
A.2.1 Phantom description.....	120
A.2.2 Imaging acquisition and reconstruction .....	121
A.2.3 Evaluation of the image quality .....	121
A.3 Results.....	122
A.4. Discussion .....	127
References.....	128
<b>Samenvatting en discussie.....</b>	<b>129</b>
<b>Curriculum Vitae.....</b>	<b>135</b>
<b>List of Publications .....</b>	<b>137</b>



# **Chapter 1**

## **Introduction**

### **1.1 General introduction**

#### **CT in cardiovascular disease**

Computed Tomography (CT) is a non-invasive X-ray based imaging method, which generates cross-sectional (tomographic) images of the human body.<sup>1-2</sup> Since the introduction of CT, enormous technological progress has been made in reducing scan time and improving spatial resolution. With the introduction of spiral CT, a nearly isotropic spatial resolution in all three dimensions has been achieved, allowing a detailed three-dimensional representation of anatomical structures. The helical movement of the X-ray tube focal spot relative to the patient table, in combination with the multi-row detector array, allows rapid volumetric data acquisition over large areas of the body. By covering larger volumes in short scan times, multi-row detector spiral CT enables improved imaging of internal organs that are susceptible to respiratory and cardiac motion.

Owing to these advances, CT has become one of the established techniques for imaging the cardiovascular system. CT angiography (CTA) enables visualization of the vessel lumen throughout the body. In addition, CT(A) imaging enables the visualization of small high-density structures such as calcifications and stents. Coronary artery calcification quantification, as assessed by CT, is an important risk factor, since it can be correlated with the progression, stabilization and/or regression of atherosclerosis. Calcification pattern distribution has been recently suggested as an important predictive factor for plaque vulnerability

However, small high-density structures such as calcifications and stents also pose a problem for CT(A) imaging, as these structures are blurred owing to the limited spatial resolution of the system. This leads to difficulties in their quantification and the assessment of their surrounding. The aim of this thesis is to study the limitations of current CT systems in imaging small high density structures and the development and validation of methods to improve their visualization and quantification. In particular we are interested in visualization and quantification of calcifications in CT Angiography images to support the diagnosis of atherosclerotic disease.

## Imaging of high density objects with CT

CT is a sensitive technique to detect high-density objects because of their high X-ray attenuation properties. Consequently, small calcifications and stents can be detected in CT images, while other objects of the same size but lower density cannot be discriminated from noise and artifacts due to insufficient signal-to-noise ratio (SNR). In addition to their role as a potential marker for cardiovascular disease, calcifications also pose a problem for CT angiography (CTA) diagnosis, because calcifications appear overrepresented in the images and with much higher Hounsfield Units (HUs) than their surrounding soft-tissues (*i.e.* calcification peak intensities can reach up to  $\sim 2500$  HU, while soft-tissue plaque range between  $-100$  to  $100$  HU), which, therefore, hamper vessel analyses (see Fig. 1.1). Calcification overrepresentation limits the visualization of adjacent structures, such as the soft-tissue plaque, and often yields underestimation in the measurement of the vessel lumen diameter. Generally, the problem of calcification overrepresentation is referred to as blooming artifact, and it is frequently associated with beam hardening and partial volume artifacts.<sup>1,3</sup> Indeed, these two artifacts influence the imaging of calcifications, but they only affect the attenuation values measured along the projections that intersect high-density objects (Figs. 1.2 and 1.3 show these two artifacts). Therefore, they do not influence the spatial representation of calcifications. The main limitation for the imaging of calcifications is the limited spatial resolution of state-of-the-art CT systems. The consequence of the limited spatial resolution is image blur, which is due to the linear Partial Volume Effect (PVE). The linear PVE is caused by the averaging of the X-ray attenuations of two or more different density materials within the beam width. The beam width is determined by the effective areas of the X-ray source focal spot and the detector element. Therefore, the image blur (or PVE) depends, firstly, on the physical and geometrical characteristics of the acquisition system, and secondly, on the parameters selected for the acquisition and reconstruction of the image (*i.e.*, the imaging protocol).<sup>1,2,4,5</sup> The imaging protocol is selected based on the clinical application, and is a compromise between spatial resolution, image noise, and patient dose.<sup>1,4,5</sup>

The image blur of a given system and imaging protocol can be estimated by measuring the three-dimensional (3D) point-spread function (PSF) of a bead image. For spiral CT systems, the PSF can be approximated by a 3D Gaussian function, and the imaging process can be simulated by convolving the true object with the PSF, and superimposing the noise.<sup>1,6</sup>

## Calcifications in atherosclerotic plaque

Atherosclerotic plaques often contain calcifications, *i.e.* nodules of crystalline calcium (mainly hydroxyapatite), distributed among lipid cores and fibrous tissue.<sup>7-9</sup> Microfocus-CT ( $\mu$ CT) volume images have shown that calcifications generally have heterogeneous densities and amorphous shapes. The maximum diameters and lengths of calcification nodules typically range from only a few hundred micrometers to more than half a centimeter. They are frequently found very close to each other, forming what we refer to as a “cluster of calcifications” (see Fig. 1.1). As a consequence of image blur, calcifications (and other small high-density objects, such as stents) are spread in the

image over their actual size, which hampers their accurate quantification and visualization. Thus, accuracy of calcification quantification with standardized methods (*i.e.*, Agatston score, Calcification Volume, and Hydroxyapatite Mass)<sup>10-12</sup> is hampered by blur; and the visualization of high-density structures is very dependent on the display contrast settings (*i.e.*, the window level and window width).

## 1.2 Thesis overview

In this thesis the imaging of small high-density structures in Computed Tomography is investigated, and a method to improve visualization and quantification is developed and evaluated. First, in Chapters 2 and 3 the capacity of state-of-the art CT systems in imaging small high density structures is investigated. Second, in Chapters 4 and 5 a postprocessing technique to reduce blur of small high-density structures of the image is developed and evaluated on phantom images, and on in vitro and in vivo atherosclerotic plaque images. A more detailed overview of the thesis is given below.

In Chapter 2, the accuracy in estimating object HU and size as a function of the true object size and imaging parameters is studied for one of the latest generation Multi-Detector Row CT (MDCT) scanners. For this purpose, a dedicated phantom has been designed and manufactured. Imaging experiments have been performed and quantitative results have been compared with simulation studies. The results are presented as a function of the number of Full-Width-at-Half-Maximum (FWHM) of the PSF, thus enabling the generalization of our findings to other imaging systems. The results of the study provide a thorough characterization of the capacities of state-of-the-art CT systems in imaging small high density structures.

In Chapter 3 the phantom and measurement protocols developed in Chapter 2 are used to compare two latest generation MDCT scanners. The rapid progress in CT technology has led to the situation that a large variety of MDCT scanners coexist in clinical practice. Differences in system geometries and scanning parameters lead to inter-scanner and inter-protocol measurement variability, which hamper generalization and comparison of patient studies carried out under different experimental conditions. Especially, calcification measurements obtained with standard fixed-threshold based quantification methods are protocol and system dependent, which limit research and clinical diagnosis to very constrained experimental conditions. In this chapter a 16- and 64-slice CT systems are compared with respect to their accuracy in quantifying high density structures. Additionally, the influence of the quantification method on the inter-scanner measurement variability is evaluated. The results of this study are relevant not only to understand and interpret differences in clinical data acquired with different generations of MDCT scanners, but also to optimize protocols in view of these differences, and develop quantification methods that improve measurement accuracy and reduce inter-scanner and inter-protocol measurement dependency.

Chapter 4 and 5 are focused on a post processing technique to improve the imaging of small high-density structures. Digital deconvolution is a technique that allows reduction of image blur by amplifying high-frequency components of the image. Unfortunately, deconvolution also amplifies image noise and introduces edge-related ringing artifacts.<sup>13-15</sup> To avoid these negative side effects we have developed a novel method, referred to as Histogram-based Selective Deblurring (HiSD), which generates a restored image by using the deconvolved image data in regions containing high-density structures and the original CT data in the remaining parts of the image. Chapter 4 introduces and validates the HiSD method both on phantom and in vitro CT images of carotid atherosclerotic plaques. Qualitative and quantitative analyses are carried out on the original and restored CT images in order to evaluate the performance of HiSD. Micro-CT ( $\mu$ CT) images of the in vitro plaques are used as a high-resolution reference.

In vitro studies have inherent limitations due to the difficulty to mimic a realistic environment. Therefore, Chapter 5 focuses on the implementation and validation of HiSD on in vivo CTA data. For this, a number of in vivo contrast-enhanced CT images of atherosclerotic carotid arteries from patients undergoing carotid endarterectomy were used. After endarterectomy, the in vitro atherosclerotic plaques were stored in formaldehyde and scanned in a  $\mu$ CT scanner. Correspondence between CT and  $\mu$ CT plaque volumetric images was found, and high-resolution  $\mu$ CT data were used as reference for the qualitative and quantitative evaluation of the method. Owing to image blur and a partial similarity in the HUs, discrimination between calcifications and contrast-material was non trivial. This required an additional step which consisted on the automated segmentation of the contrast enhanced vessels prior to applying HiSD.

Finally, Chapter 6 provides a summary and a general discussion on the results presented in each chapter, and the clinical relevance and implications of our findings.



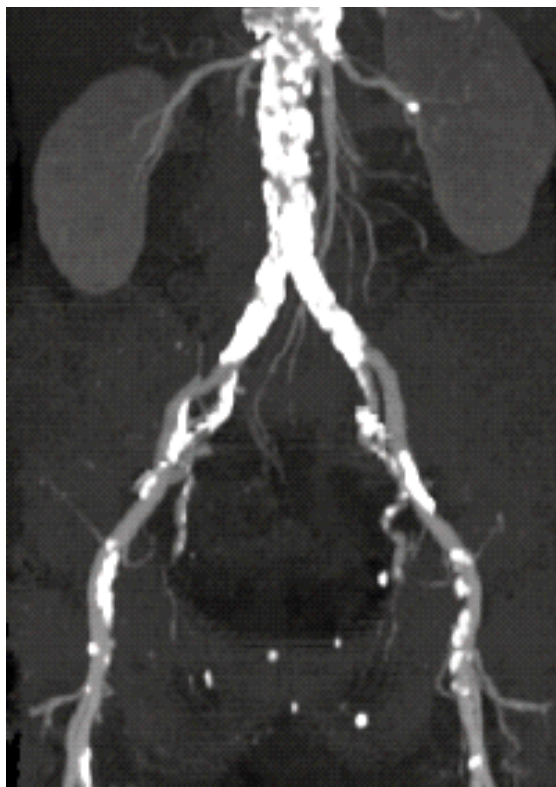


**Figure 1.1.** Maximum Intensity Projection (MIP) image of severe aorta-iliac calcification. Calcified plaque overestimation hampers vessel analysis, and calcification visualization and quantification depends on the contrast display settings and the quantification threshold value, respectively. Hence, with a soft-tissue contrast window, required to visualize small vessels and soft-tissue plaque, calcification overrepresentation increases.

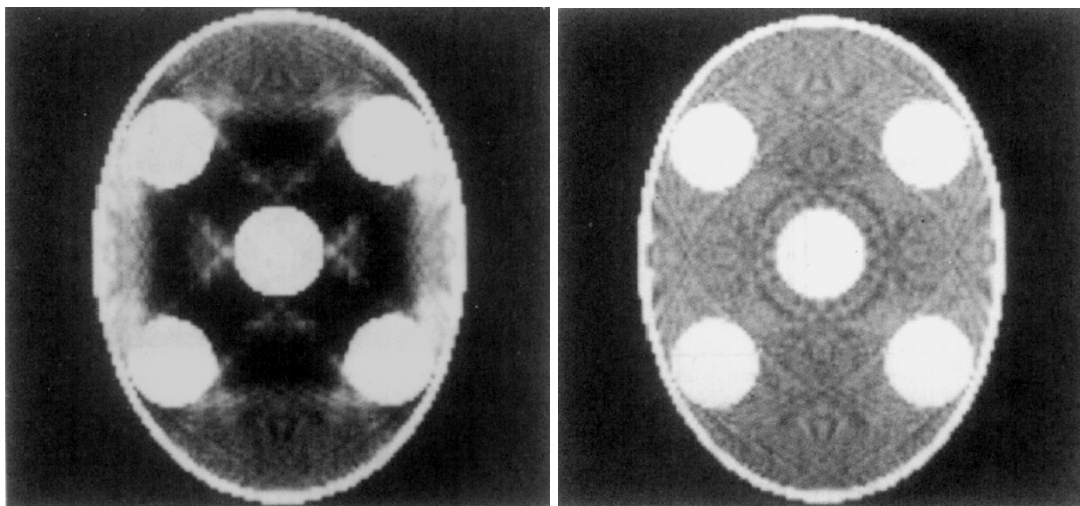


**Figure 1.2.** Left: Example of the Beam Hardening artifact. The wide dark streaks are caused by polychromaticity of the X-ray beam. The spectral distribution of polychromatic radiation changes when passing through matter because photons with lower energy are absorbed with higher probability. Consequently, the effective energy of the beam increases, leading to an underestimation of the attenuation coefficients (*i.e.*, the HUs) along paths intersecting high-density objects. Right: the reconstruction of the same phantom is shown, but now using projections generated with monochromatic radiation.

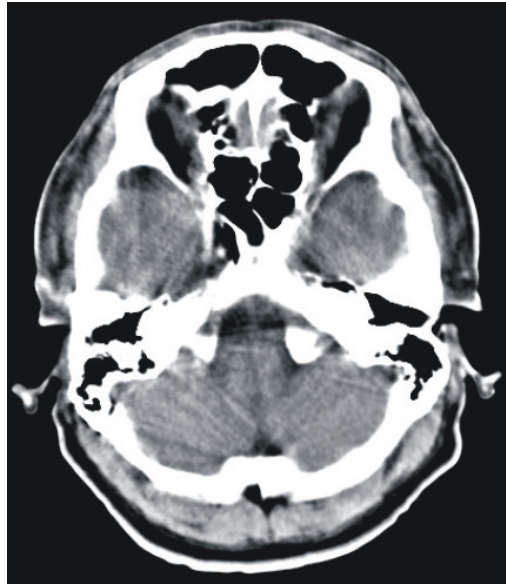


**Figure 1.3.** Example of the non-linear Partial Volume (PV) artifact, shown for a CT image of a posterior cranial fossa.<sup>1</sup> This artifact is caused by severe inhomogeneities of the materials that intersect the projection beam. The reason is that the average of the incident intensity within the detector element is not equivalent to the average of the attenuation coefficient itself. This leads to underestimation of the attenuation values when high-density structures partially intersect the slice image. Non-linear PV artifacts especially occur along the CT longitudinal direction, and increase with increasing collimation and slice thickness. This image shows a critical case of non-linear PV artifacts because bony structures are partly placed within the CT slice.

## References

1. Kalender WA. Computed Tomography: fundamentals, system technology, image quality, applications. In: *Publicis MCD Verlag*, Munich, 2000; Chapter 4 (82-118).
2. Hu H. Multi-slice helical CT: scan and reconstruction. *Med Phys.* 1999; 26:5-18.
3. Flohr, T., Schaller, S., Ohnesorge, B., Klingenberg-Regn, K., Kopp, A. F.: Evaluation of Image Artifacts in Multislice CT. *Radiology.* 1999; 213:317.
4. Meinel JF, Jr., Wang G, Jiang M, *et al.* Spatial variation of resolution and noise in multi-detector row spiral CT. *Acad Radiol.* 2003; 10:607-613.
5. McCollough CH, and Zink FE. Performance evaluation of a multi-slice CT system. *Med Phys.* Nov. 1999; 26(11):2223-2230.

6. Rossmann K. Point spread-function, line spread-function, and modulation transfer function. Tools for the study of imaging systems. *Radiology*. 1969; 93:257-272.
7. Wexler L, Brundage B, Crouse J, *et al*. Coronary artery calcification: pathophysiology, epidemiology, imaging methods, and clinical implications. A statement for health professionals from the American Heart Association. Writing Group. *Circulation*. 1996; 94:1175-1192.
8. Stary HC, Chandler AB, Glagov S, *et al*. A definition of initial, fatty streak, and intermediate lesions of atherosclerosis. A report from the Committee on Vascular Lesions of the Council on Arteriosclerosis, American Heart Association. *Circulation*. 1994; 89:2462-2478.
9. Stary HC, Chandler AB, Dinsmore RE, *et al*. A definition of advanced types of atherosclerotic lesions and a histological classification of atherosclerosis - a report from the Committee on Vascular Lesions of the Council on Arteriosclerosis, American Heart Association. *Circulation*. 1995; 92:1355-1374.
10. Yoon HC, Greaser LE, Mather R, *et al*. Coronary artery calcium: Alternate methods for accurate and reproducible quantitation. *Acad Radiol*. 1997; 4:666-673.
11. Agatston AS, Janowitz WR, Hildner FJ, *et al*. Quantification of Coronary Artery Calcium Using Ultrafast Computed Tomography. *J Am Coll Cardiol*. 1990; 15:827-832.
12. Ulzheimer S, Kalender WA. Assessment of calcium scoring performance in cardiac computed tomography. *Eur Radiol*. 2003; 13:484-97.
13. Gonzalez R, Woods R. Digital Imaging Processing. In: Prentice-Hall P, New Jersey, 2003.
14. Sakai O, Shen Y, Takata Y, *et al*. The use of deblurring technique for improving the longitudinal resolution in helical CT of the head and neck region. *Comput Med Imag Grap* 1997; 21:153-164.
15. Schlueter FJ, Wang G, Hsieh PS, *et al*. Longitudinal image deblurring in spiral CT. *Radiology* 1994; 193:413-418.



## **Chapter 2**

### **Imaging of Small High-density Structures in CT: A Phantom Study**

Rollano-Hijarrubia E, Stokking R, van der Meer F, Niessen WJ

#### **Rationale and Objectives**

The aim of this work is to study how the limited spatial resolution of a computed tomography (CT) system affects the imaging of small high-density structures. This knowledge is relevant not only to understand and interpret clinical data, but also to apply and develop quantification methods for calcifications and stented vessels.

#### **Materials and Methods**

A dedicated phantom containing small differently sized Aluminum cylinders was imaged on a 64-slice Multi-Detector Row CT (MDCT) while varying acquisition and reconstruction parameters from a high-resolution protocol. In addition, a bead phantom was imaged to estimate the point spread function (PSF) for the different parameter settings. The accuracy in determining the object density and size was established for various imaging protocols and compared with simulations based on the estimated PSF.

#### **Results**

Attenuation values and size measurements were accurate for objects larger than two times the size of the system PSF at the Full-Width-at-Half-Maximum. For smaller objects, attenuation values were increasingly underestimated and size was increasingly overestimated. The convolution kernel had most influence on object signal and size. The use of edge-enhancing kernels yielded more accurate size measurements and higher signal for small objects. However, their application was constrained by noise amplification and edge-ringing artifacts, which led to lower signal-to-noise ratio, degrading the visualization of low densities and small high-density objects.

#### **Conclusion**

The results as presented in this paper provide insight into the limitations in the quantification of small high-density structures, and their effect on the visualization of surrounding tissues, with recently developed MDCT systems.

*This Chapter has been published in Academic Radiology 2006, 13:893-908.*

## 2.1 Introduction

Computed tomography (CT) imaging of small high-density structures such as calcifications and stents is of high importance in diagnosis, treatment planning and follow-up of patients with cardiovascular disease. Calcification detection and quantification, and stent restenosis assessment are clinically relevant. Calcifications are markers for arterial pathology and the total amount of calcium in coronary arteries and carotids is being used as risk indicator because it is associated with thrombotic syndromes and/or stroke.<sup>1,2</sup> Postsurgical angiography follow-up is used to detect stent restenosis.<sup>3</sup> However, due to patient risks and treatment costs, CT angiography is being investigated as a noninvasive alternative to conventional coronary angiography.<sup>4</sup>

CT is a sensitive technique to detect calcifications in atherosclerotic arteries and to image stents.<sup>1</sup> However, limitations in both spatial resolution and signal-to-noise ratio (SNR) hamper image quality and especially affect the visualization and quantification of the smallest objects. The main consequence of the limited spatial resolution of the system is the blur of the image, which can be characterized by measuring the point spread function, PSF.<sup>5</sup>

Atherosclerotic plaques consist of calcifications, i.e. nodules of crystalline calcium (mainly hydroxyapatite), distributed among lipid cores and fibrous tissue.<sup>1,6-8</sup> In previous work<sup>9</sup> we compared CT volume images of in vitro carotid atherosclerotic plaques with the corresponding microfocus-CT ( $\mu$ CT) volume images, and we observed that calcifications generally have heterogeneous densities and amorphous shapes. The maximum diameters and lengths of these nodules typically range from only a few hundred micrometers to more than half a centimeter, and they are frequently found very close to each other, forming what we refer to as a “cluster of calcifications” (see Fig. 2.1). As a result of the convolution of small high-density objects with the system PSF, imaged object edges are blurred, leading to several problems in their quantification and visualization: *i*) the sizes of small calcifications and stent struts are overestimated; *ii*) objects in close proximity (such as clusters of calcifications and stent struts) are convolved together; *iii*) quantification and visualization of calcifications and stents strongly depend on both the selected HU threshold and the display settings (window level and window width); and *iv*) small calcifications may not be detected (especially when they do not extend along the entire slice thickness) as they are not sufficiently dense to generate the minimal SNR required for detection.<sup>9</sup>

The blur of small high-density objects not only leads to inaccuracies in their quantification and visualization, but also limits the interpretation of their surrounding low-density structures. This would, for example, hamper the measurement of lumen stenosis both in places with calcified plaques and in stented vessels. These measurements have clinical repercussions, since lumen stenosis larger than 70%<sup>10</sup> and in-stent restenosis larger than 50%<sup>11</sup> are considered eligible for surgical intervention. In view of these aspects, limiting the blur of small high-density objects may improve CTA diagnosis. However, there is a trade-off, since limitation of blur can compromise the image quality due to the increasing noise and artifacts.<sup>12,13</sup> Therefore, a detailed evaluation of a scanning system in terms of noise, artifacts and accuracy in imaging of small high-density structures is relevant for clinical applications such as atherosclerotic plaque

characterization and vessel stenosis assessment in the presence of calcifications and stents.

A number of studies related to CT imaging of small high-density structures have already been performed, e.g. fixed-threshold based quantification of true and artificial calcifications,<sup>14-17</sup> investigation of CT accuracy limits in cortical bone thickness and density determination for osteoporosis diagnosis,<sup>18-20</sup> and evaluation of the image spatial resolution and SNR as a function of CT acquisition and reconstruction parameters.<sup>21-23</sup> Compared with these studies, the current paper aims to perform a detailed quantitative evaluation of the different factors that limit the imaging of (individual) high-density objects with diameters and lengths near and under the full width at half maximum (FWHM) of the system PSF for state-of-the-art CT systems. Hereto, a dedicated phantom, consisting of high-density cylinders with sizes distributed along the range of calcification sizes typically found in in vitro atherosclerotic plaques, is scanned while varying the image scanning and reconstruction parameters. The accuracy in estimating object HU and size depending on the true object size and scanning parameters is studied in detail for a 64-slice Multi-Detector Row CT (64 MDCT). Results are given as a function of the number of FWHM of the PSF, thereby generalizing our findings to other imaging systems.

The large amount of experimental data presented in this work, and the accurate and detailed quantitative analyses that are performed, provide a thorough characterization of the recently introduced 64 MDCT, and therefore, provide a valuable and completely new data reference source for clinical applications that involve quantification and visualization of small high-density structures.

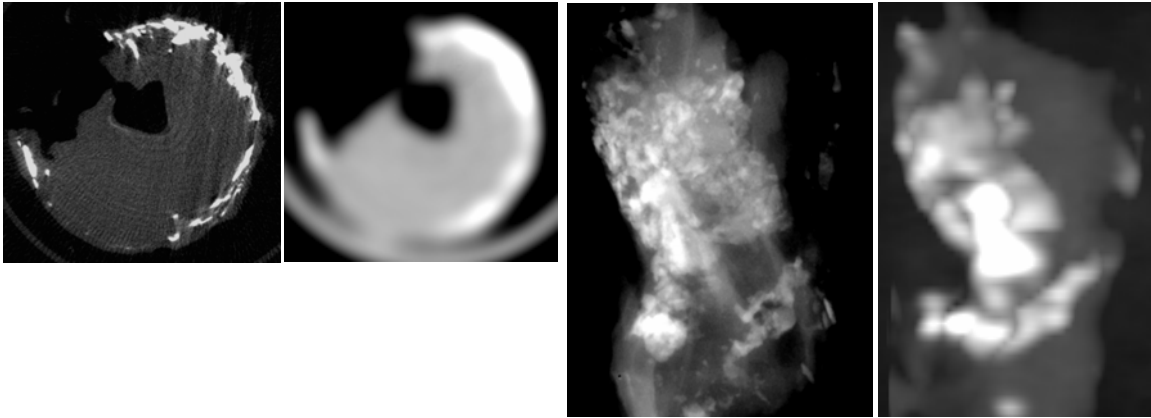


**Figure 2.1.** From left to right: cross-sectional  $\mu$ CT image of an in vitro calcified plaque (image size= $12.6 \times 11.9$  mm, pixel size= $18.2 \mu\text{m}$  both in the  $x$ - and  $y$ - directions); closest corresponding slice acquired with a MDCT (pixel size= $0.098$  mm both in the  $x$ - and  $y$ - directions); longitudinal maximum intensity projection of the  $\mu$ CT image of the whole plaque (image size= $12.6 \times 19.3$  mm, pixel size= $18.2 \mu\text{m}$  both in the  $x$ - and  $z$ - directions), closest corresponding projection acquired with a MDCT (pixel size= $0.098 \times 0.10$  mm in the  $x$ - and  $y$ - directions, respectively).

## 2.2 Materials and Methods

### 2.2.1 Phantoms

#### “Small high-density structures phantom”

A dedicated phantom was manufactured (Experimental Medical Instrumentation Department, Erasmus MC, Rotterdam, The Netherlands) to evaluate the accuracy of a MDCT scanner to image small high-density structures. The phantom consists of small Aluminum cylinders, representing high-density calcifications, which are inserted in the center, parallel to the main axis, of a cylindrical Polymethylmethacrylate (PMMA) module. The lengths of the Aluminum cylinders are approximately equal to their respective diameters, ranging from 0.3 to 5.0 mm, and the distance between them is ~9 mm (see Fig. 2.2). The PMMA module is 10 mm in diameter and mimics the appearance of a mildly enhanced vessel (mean HU of PMMA =  $124 \pm 12$  HU). This PMMA module is introduced into a water-filled cylinder, 16 cm in diameter, to achieve a realistic attenuation environment.

The choice of Aluminum was a tradeoff between several factors. Aluminum has been used extensively as a calibration material for measuring the bone mineral density in Dual-Energy X-ray Absorptiometry.<sup>24,25</sup> Aluminum has an X-ray mass attenuation coefficient similar to that of hydroxyapatite ( $0.202 \text{ cm}^2/\text{g}$  vs.  $0.259 \text{ cm}^2/\text{g}$  at approximately 80 keV), the main compound of human bone and calcifications. However, Aluminum has a higher density ( $\rho = 2.699 \text{ g/cm}^3$ ) than cortical bone ( $\rho = 1.855 \text{ g/cm}^3$ ), leading to a slightly higher attenuation coefficient ( $0.545 \text{ cm}^{-1}$  vs.  $0.412 \text{ cm}^{-1}$  at 80 keV; <http://physics.nist.gov/>). Our general aim is to investigate the imaging of small high-density structures. For this general aim, Aluminum has the advantage of providing a high SNR, which allows quantification of very small objects, and revealing problems with artifacts associated to small metallic structures, which would serve as reference when imaging, for example, stents (typically having a higher density than Aluminum). From a technical point of view, the advantages of using Aluminum over other materials are its strength and malleability, which enables accurate construction of small cylinders, avoiding geometrical deformations during the polishing process and chemical interactions with the embedding material.

To guarantee accurate knowledge on the sizes of the small cylinders, a Microfocus X-ray Computer Tomography ( $\mu$ CT) scanner (*SkyScan-1172*, [www.skyscan.be](http://www.skyscan.be)) was used. Four projections,  $45^\circ$  apart, were acquired with 80 kVp and 100  $\mu$ A. Size measurements obtained from  $\mu$ CT images were used as ground truth to estimate the errors in the CT measurements.



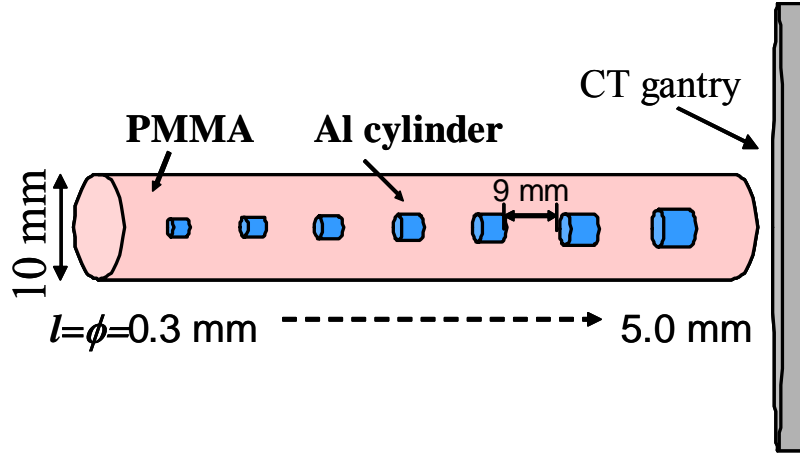


**Figure 2.2.** “Small high-density structures phantom”. Seventeen small Aluminum (Al) cylinders are inserted along the main axis of a PMMA cylindrical module.

### “Bead geometry module”

The second phantom (Catphan CTP591 Bead Geometry Module, [www.phantomlab.com](http://www.phantomlab.com)) consists of a PMMA module containing Tungsten beads of two different diameters, 0.18 and 0.28 mm. The scans of the 0.18 mm beads are used to measure the 3D PSF of our system for a given scanning protocol.<sup>9</sup>

### 2.2.2 64-slice Multi-Detector Row CT

We evaluate the capability to image small high-density structures for one of the latest CT system manufactured by Siemens Medical Systems: *Somatom Sensation 64* MDCT. This scanner consists of 32 detector rows, which acquire 64 overlapping 0.6 mm slices per rotation with a sampling distance of 0.3 mm at iso-center<sup>26</sup> resulting in volume coverage of 19.2 mm in the z-direction per rotation. To double the number of simultaneously acquired slices, the X-ray tube implements a periodic motion of the focal spot in the longitudinal direction (z-flying focal spot) by using an electromagnetic deflection of the electron beam. With this scheme a gantry rotation speed of 0.33 s/rot can be reached.

### 2.2.3 Scanning protocols

In this section the relevant parameters for our study and the values being evaluated for each parameter are presented. Next, we define a “high-resolution protocol”, which is used as the default protocol from which each of the other parameters is varied.

#### Parameters and ranges being evaluated

- **Convolution Kernel:** During image reconstruction a convolution filter is applied. Different filter functions are used to smooth or enhance the image high frequencies.<sup>5,27,28</sup> This study evaluates the performance of nine different kernels; ranging from smoothing, i.e. B20, to most sharpening, i.e. B80 (according to Siemens nomenclature). The shape of these kernels, both in the spatial and frequency domain, can be approximated by an isotropic 2D Gaussian function.<sup>5,29</sup> Lower kernel values refer to narrower filter functions (i.e. smaller filter FWHM) in the frequency domain, which lead to a stronger attenuation of the image high frequencies, thereby smoothing

image edges. Larger kernel values refer to wider filter functions, which allow higher contribution of the image high frequencies, thereby reducing image blur.

- **Reconstruction Field of View (FOV):** Different reconstruction FOV sizes lead to different pixel sizes and, hence, to different SNRs and in-plane partial volume effect, PVE.<sup>5</sup> In this study three different FOV sizes are evaluated, i.e., 50 mm, which is the smallest region that encompasses our phantom, and 160 and 300 mm, which are representative values for clinical practice.
- **Reconstruction Increment (RI):** The RI determines the sampling interval in the CT longitudinal direction.<sup>5,30</sup> In this study the values of RI are selected with respect to the slice collimation ( $c=0.6$  mm) and range from non-overlapped reconstruction (RI=0.6 mm) to highly overlapped reconstruction (RI=0.2 mm).
- **Slice thickness ( $S_{eff}$ ):** The effective  $S_{eff}$  is defined as the FWHM of the PSF along the CT  $z$ -axis.<sup>5,30-33</sup> Three small values of  $S_{eff}$  frequently used in high-resolution clinical examinations, i.e. 0.6, 0.75 and 1.0 mm, are evaluated.
- **Pitch:** In our study the pitch is defined as the table increment divided by the product of the detector collimation with the number of detector rows. In multidetector spiral CT different pitch values lead to different sampling patterns of the projection data.<sup>5,30-35</sup> In general, pitches smaller than 1.0, with fractional values that lead to an interlaced oversampling of the data in the  $z$ -direction, result in better image quality.<sup>35</sup> In this study four pitches smaller than 1.0 are selected.

#### “High-resolution (HR) protocol”

A high-resolution protocol was defined by selecting the parameter settings that theoretically lead to the highest image resolution: minimal collimation width ( $c$ ); minimal  $S_{eff}$ ; minimal pitch available for non-gated reconstructions (i.e., 0.45); a  $RI \leq S_{eff}/2$ ; and a minimum FOV containing the ROI (50 mm). Furthermore, a medium convolution kernel (B41s); minimal rotation time ( $t_r$ ); suitable X-ray source feeding values for the object volume being scanned (i.e., 300 mAs, and 120 kVp); and one scan rotation linear interpolation (360°LI) of the projection data were selected. The parameter values of the “HR protocol” are specified in Table 2.1. All parameters discussed above are varied starting from this protocol, and are also listed in Table 2.1.

Parameter settings	$c$ (mm)	$S_{eff}$ (mm)	Pitch	RI (mm)	Kernel	$t_r$ (s)	FOV (mm)	mAs	kV
HR protocol	0.60	0.60	0.45	0.3	B41s	0.5	50	300	120
Additional values being evaluated	0.75	0.75	0.6	0.2	B20, B30, B35,	---	160	---	---
	1.0	1.0	0.8	0.4	B45, B50, B60,		300		
			0.95	0.6	B70, B80				

**Table 2.1.** Parameter values of the “HR protocol”, and additional parameter values selected to evaluate the influence of a small individual variation of each relevant parameter.

### 2.2.4 Evaluation criteria and quantification methods

In order to evaluate the accuracy of our system in imaging small high-density structures, we consider the following measurements: *i)* the HU values at the center of the cylinders ( $I_{\text{center}}$ ); *ii)* the diameter ( $\phi$ ), area ( $A$ ), length ( $l$ ) and volume ( $V$ ) of the cylinders; and *iii)* the level of noise and artifacts. To perform these measurements we used a number of objective criteria and semi-automated image analysis techniques.

Prior to the quantification, all image data were linearly interpolated along the  $z$ -axis yielding a voxel size of  $0.098 \times 0.098 \times 0.075$  mm (in the  $x$ -,  $y$ -, and  $z$ - directions, respectively), in order to achieve more accurate measurements. For the geometrical measurements we use the 50% relative threshold method,<sup>19</sup> which we refer to as  $t_{HM}$ . This threshold is determined from the  $I_{\text{center}}$  of the cylinders and the mean HU of the PMMA surrounding material ( $\mu_{\text{PMMA}}$ ). The spread of the object borders is also relevant as it has a strong influence on the visualization of the object and its surrounding structures. Parameters, such as the Full-Width-at-one-Tenth-of-Maximum (FWTM), have been proposed to provide additional information of the image blur.<sup>31</sup> We use the difference between the object quantification with  $t_{HM}$  and with the 10% relative threshold ( $t_{TM}$ ) as a measure of the object spread.

Image noise and artifacts are also considered, since these affect the detection and quantification of small objects. The unequivocal detection of a very small object will be possible only when its HU value is higher than the mean high-intensity noise and artifacts of its surrounding tissue. This concept was used to define a quality measure that we referred to as *Signal-minus-Artifact to Noise ratio* (SAN). This measure is used to determine the improvement in the detectability of a small object when varying the protocol:

$$SAN = \frac{\text{Signal}(HU) - \text{Artifact}(HU)}{\sigma_{\text{noise}}(HU)}$$

In order to determine this quantity, the  $\sigma_{\text{noise}}$  of the water surrounding our phantom, the *Signal* (HU at the center of the cylinder), and the *Artifact* have to be measured. We defined the *Artifact* magnitude as the mean intensity of the maximum intensity projection (MIP) image of the PMMA cylinder.

To allow measurement error assessment, each scan protocol was repeated three times using the same  $z$ -axis initial position for the image acquisition and reconstruction. For all quantitative measurements the mean absolute error,  $\Delta\bar{x}$ , of the estimated mean value of the three measurements,  $\bar{x}$ , is shown as an error bar in the diagrams. For a small

number of measurements,  $N$ , the mean absolute error is given by:  $\Delta\bar{x} = t \frac{\sigma}{\sqrt{N}}$ ,<sup>17</sup> where  $\sigma$

is the standard deviation (std. dev.), and  $t$  is the so-called  $t$ -factor. The  $t$ -factor corrects for small  $N$  values, and depends on  $N$  and the probability  $p$  that a measurement falls within the interval  $[\bar{x} - \Delta\bar{x}, \bar{x} + \Delta\bar{x}]$ . For  $N=3$  and  $p=95\%$  (significance), the value of  $t$  is equal to 4.3.

### 2.2.5 Simulations and experiments

The spiral CT imaging process can be approximated as the convolution of the true object with an in-plane isotropic, spatially invariant, 3D separable Gaussian PSF,<sup>5,20</sup> plus a

superposition of noise and artifacts. We use this concept to model our experimental data. To achieve this, the  $x$ - and  $z$ -intensity profiles across the center of the 0.18 mm Tungsten beads were measured and fitted with a 1D Gaussian function for all scan protocols. This process was repeated for three different scans. From this information, a 3D Gaussian PSF was numerically generated and convolved with the synthetic 3D image of the “Small high-density structures phantom” to simulate the CT blurred image. The measurements of the lengths and diameters obtained from the simulated blurred images were compared with the experimental measurements to study how closely our system response can be predicted by means of the PSF.

A number of experiments were carried out to evaluate the performance of the 64 MDCT when imaging small high-density structures with high-resolution parameter settings (see Table 2.1). The influence of the variation of an individual parameter on the imaging of our small Aluminum cylinders was investigated by independently varying one of the CT parameters discussed in section 2.2.3, while fixing the other parameters to their default values given for the “HR protocol”. The evaluation of the resulting images was based on the measurements described in section 2.2.4, which were performed for all the parameter settings.

## 2.3 Results

### 2.3.1 PSF measurement

The  $\text{FWHM}_{xy}$  and  $\text{FWHM}_z$  of the in-plane and longitudinal PSF, respectively, are given in Table 2.2 for the “HR protocol” when applying four representative kernels: B30, B41, B46 and B60. These values are used to numerically generate the 3D Gaussian PSF, in order to simulate the blurred CT images of Aluminum cylinders. As can be seen in Table 2.2, for all convolution kernels the size of the PSF in the longitudinal direction is significantly smaller than in the transaxial direction (i.e.  $\text{FWHM}_z < \text{FWHM}_{xy}$ ). The  $\text{FWHM}_{xy}$  decreases with increasing kernel sharpness, while the  $\text{FWHM}_z$  remains statistically the same for all the kernels.

Kernel	$\text{FWHM}_{xy}$ (mm)	$\text{FWHM}_z$ (mm)
<b>B30</b>	$1.368 \pm 0.010$	$0.677 \pm 0.011$
<b>B41</b>	$1.183 \pm 0.021$	$0.679 \pm 0.010$
<b>B46</b>	$1.044 \pm 0.027$	$0.681 \pm 0.017$
<b>B60</b>	$0.974 \pm 0.021$	$0.68 \pm 0.03$

**Table 2.2.** Values of the  $\text{FWHM}_{xy}$  ( $=2.3548 \sigma_{xy}$ ) and the  $\text{FWHM}_z$  of the PSF obtained with the “HR protocol” for four representative kernels.

### 2.3.2 Phantom experiments and simulations

The results of our phantom measurements are subdivided into three sections: *i*) Signal versus object size. Noise and artifacts; *ii*) Measurement accuracy versus object size; and *iii*) Object spread. In all subsections we first describe the general results and provide tables summarizing the measurements. Subsequently, we describe the influence of acquisition and reconstruction parameters on the measurements.

- **Signal versus object size. Image noise and artifacts:**

The measurements and the simulations of the cylinder signal ( $I_{center}$ ) obtained with the “HR protocol” when using a medium kernel (B41) are shown in Fig. 2.3. The shape of the plot of  $I_{center}$  (in HU) versus cylinder size closely follows the simulation based on the PSF. For small to medium cylinders the whole object is affected by the PVE which makes the  $I_{center}$  decrease very strongly with the volume of the cylinder until becoming undetectable (under the level of noise and artifacts). For larger cylinder sizes the  $I_{center}$  reaches a *plateau*, where the mean HU is determined by the attenuation coefficient of the material. In accordance with the simulations,  $I_{center}$  drops about 2% with respect to the *plateau* for a cylinder with a size twice the FWHM of the PSF ( $FWHM_{PSF}$ ). The decrease of the signal (and consequently, the detectability) of cylinders depends both on the  $xy$ - and  $z$ - CT PSF.

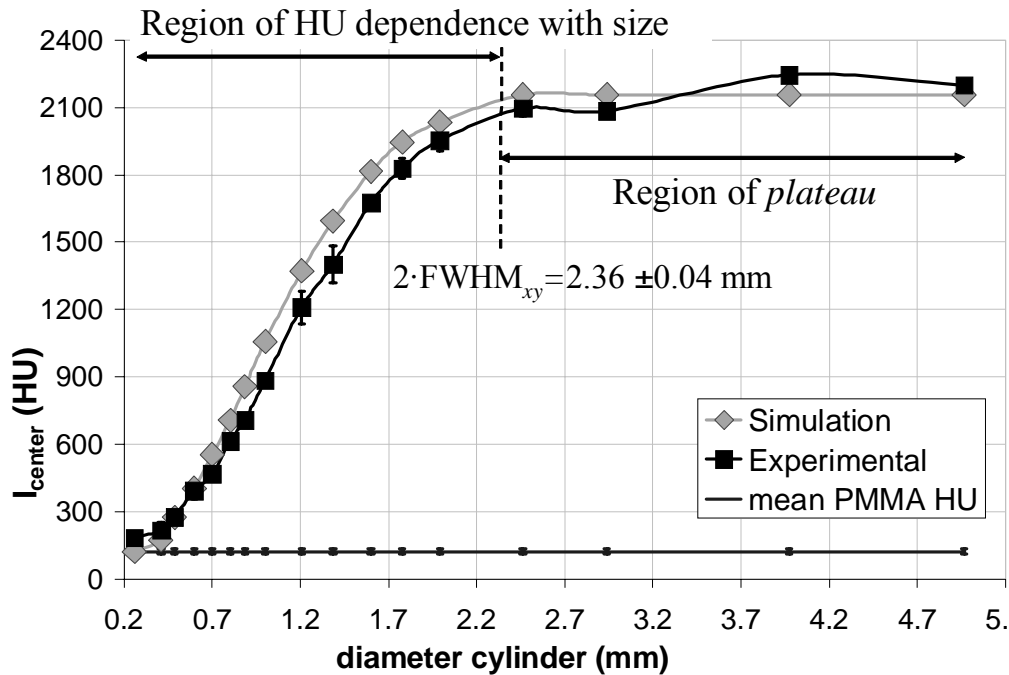


**Figure 2.3.** Measurements of the  $I_{center}$  of the cylinders in the CT images (acquired with the “HR protocol”) and in the simulated images (generated using the PSF of the same protocol).

### Influence of the CT parameter on the signal, noise and artifacts

Measurements of the SAN, noise and artifacts of the three smallest cylinders are summarized in Table 2.3.

#### *Influence of the convolution kernel:*

As can be observed from Table 2.3, the convolution kernel was the parameter with most influence on the signal, noise and artifact magnitude. In Fig. 2.4 we plot the signal as a function of size for different convolution kernels. Although the enhancement of the signal ( $I_{center}$ ) in the region of the smallest cylinders (smaller than two times the  $FWHM_{PSF}$ ) is stronger when using sharper kernels, these kernels also lead to the amplification of the

noise and artifacts, limiting the improvement of the SAN. In the region of smallest sizes (up to  $\sim 0.5$  mm) the SAN was statistically the same for all the kernels. However, when going to larger sizes ( $\sim 1.0$  mm) the SAN improved for smoothing kernels (B20-B35), quickly decreased for medium-sharp kernels (B41-B50), and reached the lowest values for the sharpest kernels (B60-B80).

For the sharpest kernels (B50-B80) we found that the  $I_{center}$  function has a region (approximately centered at two times the  $\text{FWHM}_{\text{PSF}}$ ) in which the signals of the objects are enhanced over the true HU of the material (given by the mean HU in the *plateau*). For some of the Aluminum cylinders, this overenhancement led to a clipping of their HU (which fell outside the CT HU interval  $[-1000 \text{ HU}, +3071 \text{ HU}]$ ), resulting in an erroneous estimation of the  $I_{center}$  and, consequently, in erroneous size measurements. With these sharpening kernels, the maximum intensity ( $I_{max}$ ) is approximately equal to the  $I_{center}$  for cylinder sizes smaller than the size corresponding to the peak of the region of overenhancement (indicated in Fig. 2.4). From there on, the  $I_{center}$  decreases much faster than  $I_{max}$ , which is then found at the edges of the cylinder. The reason is that this overenhancement affects sharp transitions of the image and can be observed as artifactual overshoots and undershoots surrounding the object edges. These artifacts are associated with the convolution process and in some literature are referred to as edge-ringing artifacts.<sup>36</sup> Notice that the mean maximum amplitude of the ringing artifact related to the PMMA cylinder edges is given by the parameter “Artifact” (see definition in section 2.2.4) for each convolution kernel.

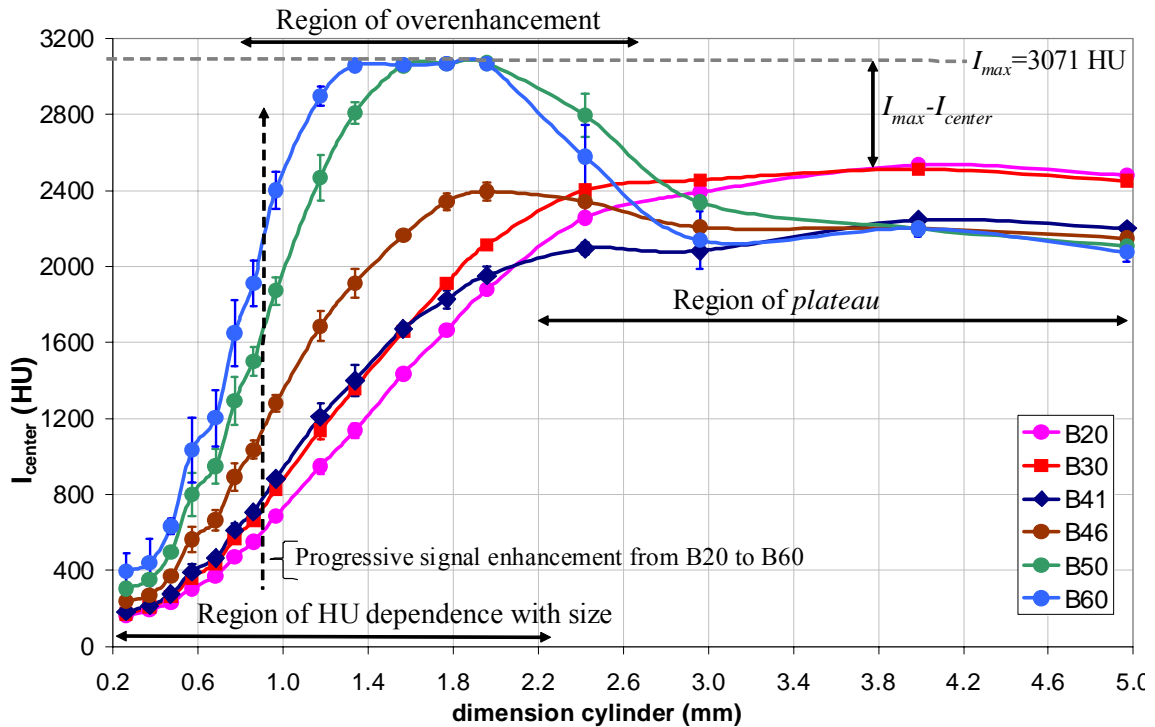


**Figure 2.4.** Measurement of  $I_{center}$  and its standard deviation (in HU) as a function of the ground truth size of the cylinder, for six different kernels (B20 to B60). The size where  $I_{center}$  reaches a *plateau* does not depend strongly on the kernel. However, the

enhancement of the signal at different size ranges depends very much on the kernel. Signal overenhancement (overshoot of the HU) can be observed starting from kernel B46, and strongly increases for B50-B80. Compared with the convolution kernel, the  $S_{eff}$ , RI, and FOV had little influence on the signal and noise, and no influence on the edge-ringing artifacts (see values in Table 2.3).

***Influence of other CT parameters:***

As expected, increasing the  $S_{eff}$ , slightly decreased the image noise due to larger sampling contribution, and slightly lowered the  $I_{center}$  of the cylinders (although values were not different within the std. dev.) due to a larger PVE. Consequently, increasing the  $S_{eff}$  led to a slightly better SAN for medium to large cylinders. No statistical differences in signal and noise were found when varying the RI, the pitch and the FOV. Nevertheless, when using the largest values of these parameters, i.e. RI=0.6 mm, pitch=0.95, and FOV=300 mm, a small decrease in the signal was found, which led to a slightly lower SAN.

CT parameter	SAN (0.26 mm)	SAN (0.57 mm)	SAN (0.97 mm)	$\sigma_{noise(water)}$ (HU)	Artifact (HU)
<b>B20</b>	1.58 ± 0.84	15.9 ± 2.0	53.6 ± 0.9	10.11 ± 0.07	145.4 ± 0.7
<b>B30</b>	1.79 ± 1.30	16.4 ± 2.4	52.6 ± 1.3	12.91 ± 0.14	149.9 ± 0.6
<b>B35</b>	2.22 ± 1.41	16.9 ± 2.6	53.6 ± 1.7	12.39 ± 0.07	141.5 ± 1.0
<b>B41</b>	2.61 ± 1.66	16.8 ± 2.6	50.1 ± 1.7	14.76 ± 0.04	145.4 ± 1.0
<b>B46</b>	2.55 ± 1.49	15.2 ± 2.6	43.0 ± 1.8	25.80 ± 0.16	171.4 ± 1.1
<b>B50</b>	2.14 ± 1.50	14.0 ± 2.7	39.7 ± 1.8	41.70 ± 0.45	217.0 ± 0.4
<b>B60</b>	2.24 ± 1.54	12.7 ± 2.8	35.0 ± 1.6	61.25 ± 0.27	258.0 ± 1.6
<b>B70</b>	2.10 ± 1.76	12.6 ± 2.8	35.4 ± 1.5	67.12 ± 0.68	278.3 ± 1.1
<b>B80</b>	1.66 ± 1.34	13.3 ± 2.9	37.1 ± 0.5	73.8 ± 0.93	323.5 ± 0.4
<b><math>S_{eff}</math> 0.6</b>	2.61 ± 1.66	16.8 ± 2.6	50.1 ± 1.7	14.76 ± 0.04	145.4 ± 1.0
<b><math>S_{eff}</math> 0.75</b>	2.34 ± 1.43	16.9 ± 2.3	53.1 ± 1.3	13.13 ± 0.23	141.3 ± 0.4
<b><math>S_{eff}</math> 1.0</b>	2.26 ± 1.40	18.5 ± 2.2	62.9 ± 1.9	9.75 ± 0.16	136.6 ± 0.8
<b>RI 0.2</b>	2.94 ± 0.79	16.7 ± 2.6	50.1 ± 1.6	14.72 ± 0.06	146.5 ± 0.5
<b>RI 0.3</b>	2.61 ± 1.66	16.8 ± 2.6	50.1 ± 1.7	14.76 ± 0.04	145.4 ± 1.0
<b>RI 0.4</b>	2.41 ± 1.10	16.7 ± 2.7	47.2 ± 1.4	14.72 ± 0.15	146.5 ± 0.4
<b>RI 0.6</b>	2.51 ± 1.95	16.7 ± 2.6	41.2 ± 1.0	14.81 ± 0.11	145.8 ± 1.0
<b>Pitch 0.45</b>	2.61 ± 1.66	16.8 ± 2.6	50.1 ± 1.7	14.76 ± 0.04	145.4 ± 1.0
<b>Pitch 0.6</b>	1.56 ± 1.93	15.5 ± 3.5	48.6 ± 1.8	14.64 ± 0.50	146.8 ± 1.3
<b>Pitch 0.8</b>	1.85 ± 1.20	15.3 ± 2.5	46.8 ± 2.3	14.84 ± 0.30	147.2 ± 1.1
<b>Pitch 0.95</b>	1.52 ± 0.91	13.6 ± 1.7	45.1 ± 3.9	14.59 ± 0.21	145.1 ± 0.3
<b>FOV 50</b>	2.61 ± 1.66	16.8 ± 2.6	50.1 ± 1.7	14.76 ± 0.04	145.4 ± 1.0
<b>FOV 160</b>	2.58 ± 1.59	16.8 ± 2.6	50.9 ± 0.9	14.78 ± 0.03	145.2 ± 1.0
<b>FOV 300</b>	2.37 ± 1.39	16.1 ± 2.3	45.2 ± 4.6	14.70 ± 0.07	145.8 ± 0.9

**Table 2.3.** SAN (given as  $\frac{Signal - artifact}{noise}$ ) for three different cylinder sizes that are affected by the PVE (0.26, 0.57, and 0.97 mm); the  $\sigma_{noise(water)}$ ; and the artifacts (given as the mean HU of the MIP histogram of the PMMA cylinder).

- **Measurement accuracy versus object size:**

***Diameter and length measurements vs. object size***

The accuracy of the diameter and length measurements strongly depends on the object size, as can be seen in Figures 2.5 and 2.6. Three regions can be identified in these plots:

- $R_1$  corresponds to the region of objects smaller than one to one and a half times the  $\text{FWHM}_{\text{PSF}}$ . In this region, measurement accuracy with  $t_{HM}$  is very low and mainly depends on image blur, although noise and artifacts also contribute to the error. For smaller cylinders the measurements progressively deviate from the ground truth leading to very large relative overestimates. With a medium kernel, B41, the relative overestimations in the diameter and length measurements of a cylinder of 1.0 mm were respectively 27% and 18%, and these overestimations increased to 140% and 70% for a cylinder of 0.5 mm. In the range [0.0 mm, 1.0 mm] the measurements can be fitted reasonably well by a straight line, providing a proper description of measurement overestimation and uncertainty in this region.
- $R_2$  corresponds to the region of objects larger than one to two times the  $\text{FWHM}_{\text{PSF}}$ . In this region the measurements with  $t_{HM}$  are accurate, and the uncertainty is mainly limited by the noise and artifacts. For all the evaluated parameter settings, the relative errors in  $R_2$  are small: ~5-8% for the diameter measurements due to underestimation, and ~4-9% for the length measurements due to overestimation. In the range [2.5 mm, 5.0 mm] the measurements can be fitted by a straight line with slope ( $m$ ) and intercept ( $n$ ) approximately equal to the correct values of 1.0 and 0.0 mm, respectively.
- Finally,  $R_{\text{transition}}$  is the region of transition between  $R_1$  and  $R_2$  (corresponding to the range of sizes between one to two times the  $\text{FWHM}_{\text{PSF}}$ ), and accounts for those measurements that cannot be fitted either with the trendline that describes  $R_1$  or with the trendline that describes  $R_2$ .



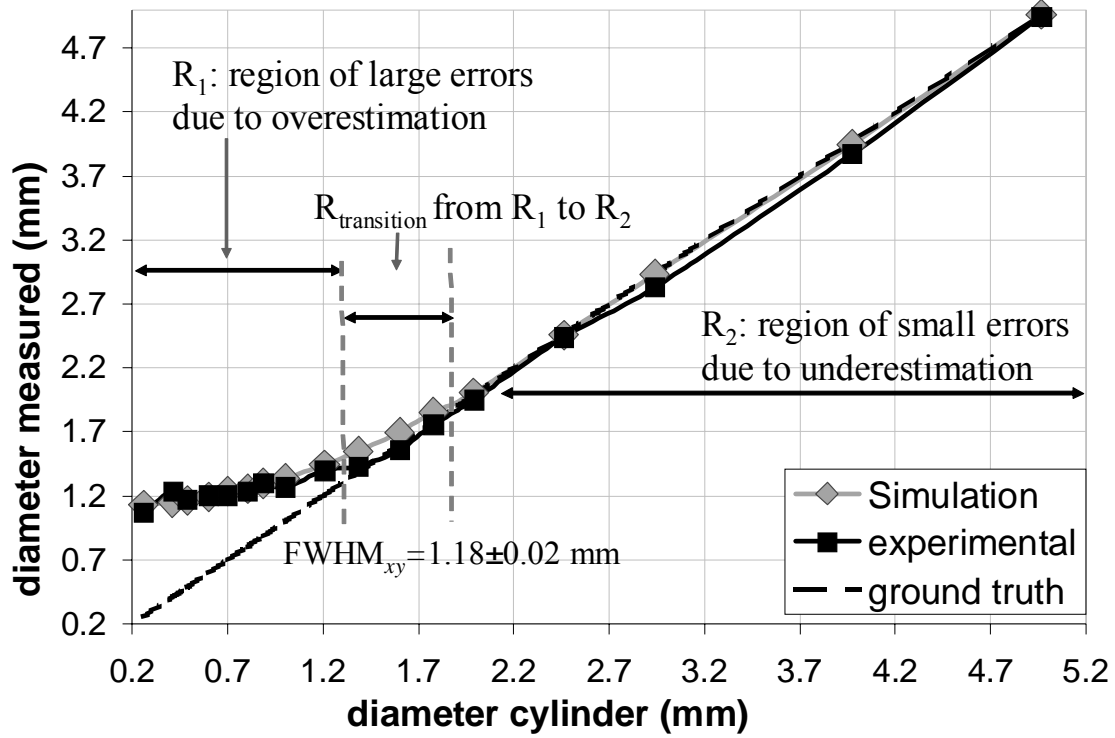


**Figure 2.5.** Experimental vs. ground truth diameter measurements for different cylinder sizes.

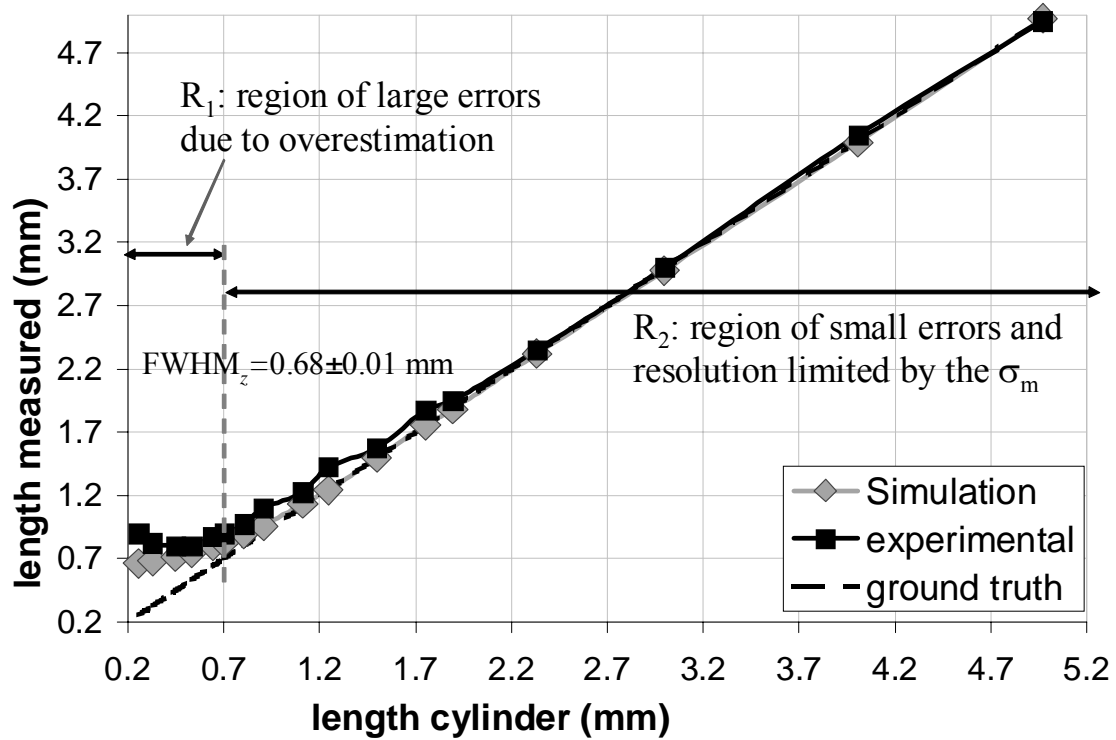


**Figure 2.6.** Experimental vs. ground truth length measurements for different cylinder sizes.

### Area and volume measurements vs. object size

For all cylinders, the area measurements could be predicted from the diameter measurements, and to avoid redundancy the area results are not shown. The volume measurements, however, could not be predicted in a straightforward way from the diameter and length measurements, owing to the combined effect of in-plane and longitudinal blur. For cylinders with a diameter and length larger than the  $\text{FWHM}_{\text{PSF}}$  the estimated volume is approximately linear with the *ground truth volume*, with slope near 1.0 and (negative) intercept near 0.0. For smaller sizes, the linear behavior is lost, and the data goes from a region of underestimation to a region of overestimation (see more details and experimental data in the following “Volume” section).

### Introduction of parameters summarizing the size measurement accuracy

The diameter, length, and volume measurements for different size ranges are described by performing linear fits of  $R_1$  and  $R_2$  (see Fig. 2.7). Additionally, quantification errors in these two regions are provided. A detailed description of the parameters used to summarize our measurements is given in Table 2.4. Through these parameters, Tables 2.5 and 2.6 report the variation of the diameter and volume measurements with the convolution kernel, and Table 2.7 reports the variation of the length measurements with  $S_{\text{eff}}$ , RI, and pitch. Measurements for the two smallest cylinders (0.26 and 0.41 mm) were not included, since these could not be correctly quantified for most of the protocols due to the contribution of surrounding noisy voxels.

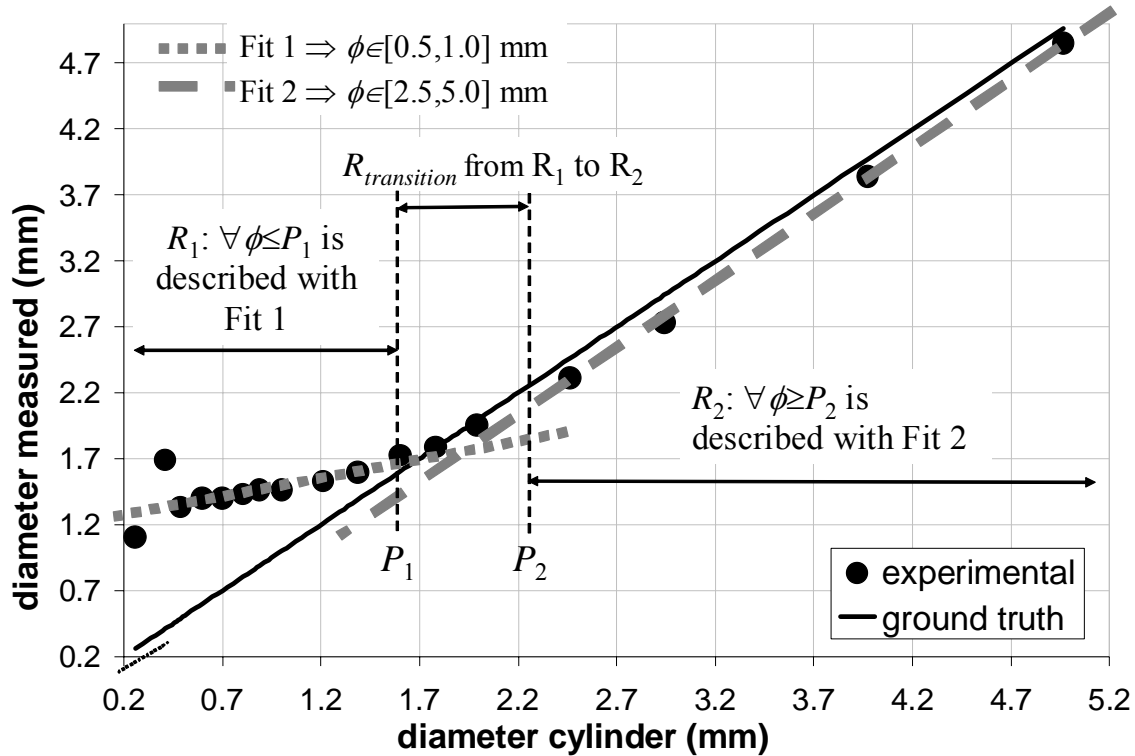


**Figure 2.7.** Description of measurement analyses summarizing our results.

---



---

### Parameters definition

---

**Over:** Relative cylinder diameter/length/volume overestimation (%) in the range [0.49 mm, 0.80 mm]. In this range all the measurements are overestimated independently of the protocol.

**Under:** Relative cylinder diameter/length/volume underestimation (%) in the range [2.46 mm, 4.97 mm]. In this range all the measurements are underestimated independently of the protocol.

**$P_{\text{over/under}}$ :** Cylinder size at which the measurement of the diameter/length/volume goes from underestimation to overestimation.

**$m_{1,2}$  &  $n_{1,2}$ :** Slope and intercept (bias) of the linear fit of the diameter/length/volume measurements for ranges [0.49 mm, 1.00 mm]  $\subseteq R_1$  and [2.46 mm, 4.97 mm]  $\subseteq R_2$ , respectively.

**$P_{\text{fit1}}$  &  $P_{\text{fit2}}$ :** these two values define the regions  $R_{1,2}$  in which the diameter/length/volume measurements can be approximated from  $m_{1,2}$  and  $n_{1,2}$ . The boundaries of these regions are defined by the measurements that statistically deviate from the linear fit more than 1.5 times the std. dev of the fit (calculated in the range [0.49 mm, 1.00 mm] for  $P_{\text{fit1}}$ , and in the range [2.46 mm, 4.97 mm] for  $P_{\text{fit2}}$ ). The region between the two fits is defined as  $R_{\text{transition}}$ .

**Res:** Estimation of the uncertainty ( $\pm \text{Res}/2$ ) in determining the true object size from its image measurement. Within each of the fitted ranges,  $\text{Res}$  is defined as:  $\text{Res} = \frac{2 \cdot \sigma}{m} = \frac{2 \cdot \sqrt{\sigma_m^2 + \sigma_{\text{fit}}^2}}{m}$ , where

$\sigma_m$  is the mean std. dev. of the measurements in the fitted range; and  $\sigma_{\text{fit}}$  is the mean std. dev. between the measurements and the linear fit. The uncertainty of the measurements decreases if the slope  $m$  increases (getting closer to 1.0), the  $\sigma_m$  decreases (implying higher reproducibility of the measurements), and  $\sigma_{\text{fit}}$  decreases (indicating better linearity of the measurements).

**$R^2$ :** This parameter ranges from 0.0 to 1.0, and measures the quality of the linear fit. Since the number of points fitted in each range is small, only those fits leading to a  $R^2 \geq 0.90$  are used to estimate the uncertainty of the measurements in this range.

---

**Table 2.4.** Definition of parameters used to describe and summarize our measurements.

## Influence of the CT parameters on the accuracy of size measurements

### *Influence of convolution kernel:*

**Diameter measurements** (see Fig. 2.8 and Table 2.5): When applying sharpening kernels, the relative error of the measurements along the whole range of sizes is on average reduced (see values of *over* and *under* in Table 2.5). In the region  $R_1$ , i.e. for smaller cylinders, diameters are overestimated and the uncertainties are large. Although this overestimation can be progressively reduced by increasing the sharpness of the kernel, the accuracy achieved with any of the kernels is not enough to perform reliable object size quantification in this interval. Even with a sharp kernel B60, we obtained in the region  $R_1$  (which extends up to 1.2 mm) a slope  $m_1=0.34$  mm and intercept  $n_1=0.69$  ( $R^2=0.999$ ). These two values were translated into a diameter overestimation of 72% for a

cylinder of 0.5 mm, and an uncertainty in determining the true object diameter of  $\pm 0.23$  mm. In region  $R_2$ , i.e. for larger cylinders, the diameter measurements with  $t_{HM}$  are quite accurate for all kernels, although slightly underestimated (see values of  $n_2$  in Table 2.5). This underestimation is probably due to the shape of the kernel, which reduces the overestimation in the region of sizes under or near the  $\text{FWHM}_{\text{PSF}}$  (see in the simulations of Fig. 2.5 that with a Gaussian PSF the measurements in this region would be slightly larger), but at the expense of underestimating the measurements in the region of larger sizes. This effect varies from smoothing kernels to sharpening kernels. For smoothing kernels the underestimation is larger in the range [2.5 mm, 5.0 mm], and this underestimation is progressively reduced down to zero when increasing the sharpness of the kernel (for kernels sharper than B50 the diameter measurements in  $R_2$  were statistically not different from the ground truth). On the other hand, with sharpening kernels (B46-B80) the problem of the measurement underestimation appears in the region of transition (located between one and two times the  $\text{FWHM}_{\text{PSF}}$ ). The maximum underestimation in this region was lower than 15% for all kernels.

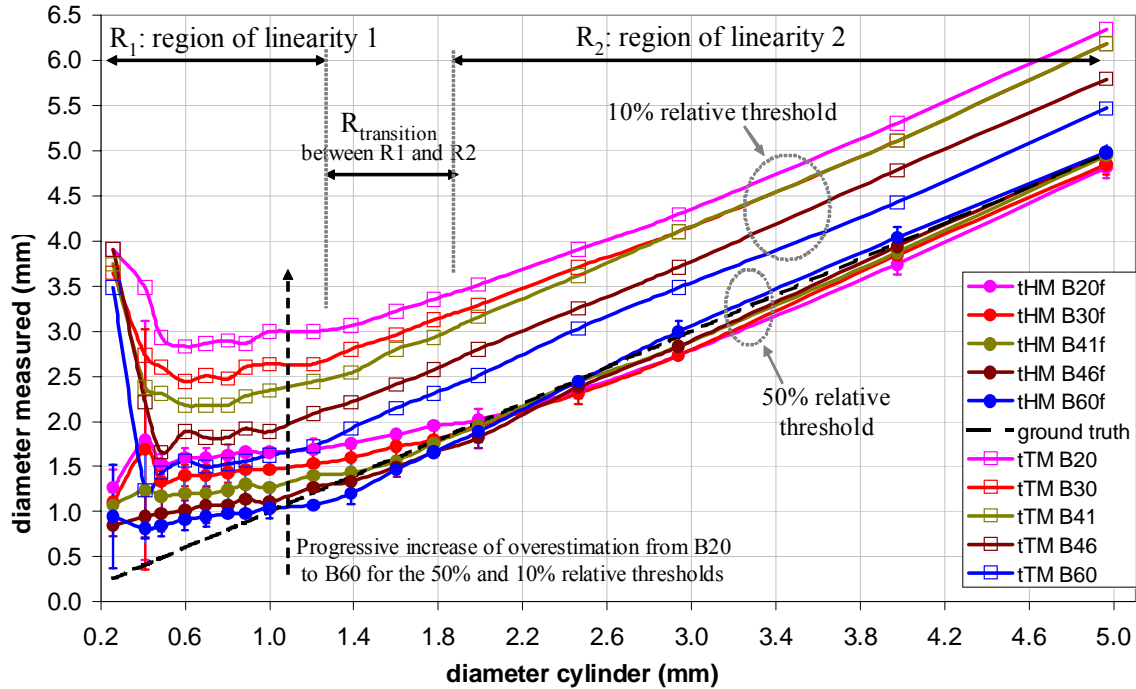


**Figure 2.8.** Diameter measurements with  $t_{HM}$  and  $t_{TM}$  for different representative convolution kernels. Notice that the diameter estimation is not noticeably affected by the signal clipping. This is due to the fact that the edge enhancement produced by sharp kernels reduces threshold dependence of measurements in the  $xy$ -plane.

Kernel	over (%)	under (%)	$P_{\text{over/under}}$	$m_1$	$n_1$ (mm)	$R^2$	$Res_1$ (mm)	$P_{\text{fit } 1}$	$P_{\text{fit } 2}$	$m_2$	$n_2$ (mm)	$R^2$	$Res_2$ (mm)
B20	145	-4.9	2.05	0.25	1.43	0.9063	0.63	1.39	2.46	0.99	-0.15	0.9979	0.15
B30	115	-4.2	1.80	0.25	1.23	0.9063	0.63	1.39	2.46	1.03	-0.24	0.9994	0.18
B35	109	-3.3	1.70	0.28	1.17	0.8812	---	1.21	2.46	1.05	-0.28	0.9998	0.22
B41	86	-1.7	1.50	0.23	1.06	0.8022	---	1.00	1.60	1.01	-0.09	0.9982	0.14
B46	60	-1.5	1.30	0.29	0.85	0.8323	---	1.00	1.78	1.05	-0.22	0.9998	0.11
B50	55	-0.6	1.15	0.22	0.87	0.6977	---	1.39	2.46	1.06	-0.22	0.9983	0.14
B60	42	0.8	1.05	0.34	0.69	0.9551	0.45	1.21	2.46	1.01	0.00	0.9989	0.13
B70	46	1.0	1.05	0.27	0.77	0.9008	0.71	1.21	2.46	1.00	0.03	0.9981	0.10

**Table 2.5.** Parameter values (see their definition in Table 2.4) describing accuracy and uncertainty of diameter measurements within different size ranges for different reconstruction kernels.

**Length measurements** (see Fig. 2.9): The length measurements do not depend on the kernel, although the error and standard deviation of the smallest objects slightly increases for the sharpest kernels (B60, B70 and B80) due to noise. It should be noted that the differences in the length measurements found for the sharpest kernels are due to intensity clipping, which leads to erroneous estimation of the relative threshold  $t_{HM}$ , and therefore to an overestimation of the measurements.

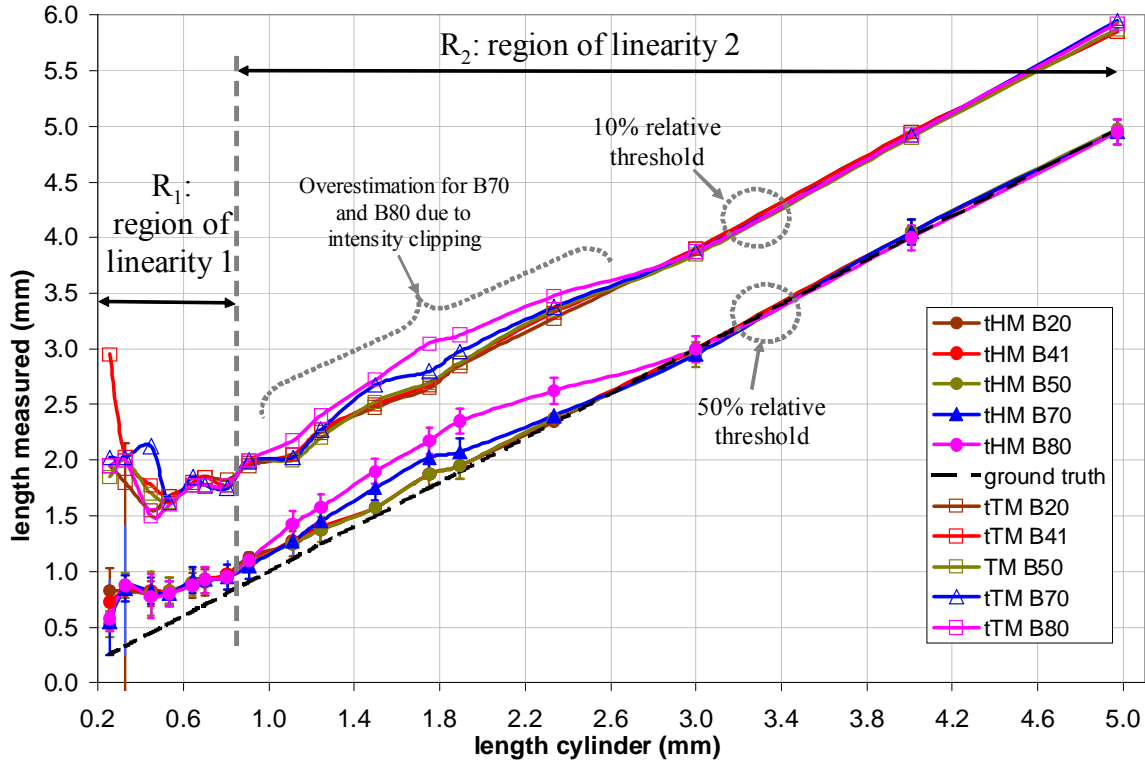


**Figure 2.9.** Length measurements with  $t_{HM}$  and  $t_{TM}$  for different convolution kernels.

**Volume measurements** (see Fig. 2.10 and Table 2.6): The dependence of the volume error on the convolution kernel follows the pattern of the diameter measurements. In region  $R_2$ , i.e. for larger cylinders, the volume measurements with  $t_{HM}$  are quite accurate for all kernels, although slightly underestimated (see values of  $n_2$ ). This underestimation is reduced to zero when using sharper kernels (B60-B80). For kernels sharper than B50, the volume measurements in  $R_2$  were statistically not different from the ground truth. For smaller cylinders, i.e. in the region  $R_1$ , the volume measurements are overestimated, and the relative overestimation increases exponentially with decreasing cylinder size. In the zoomed region of Fig. 2.10, it can be observed that in the region of the small cylinders the measurements are not linear and cannot be approximated by a trendline. However, for sharper kernels, the measurements are approximately linear within the range corresponding to  $\phi \in [0.49 \text{ mm}, 1.60 \text{ mm}]$ , and can be fitted to determine the bias and uncertainty in this region. For three of the kernels (B41, B46, and B60) we found that the uncertainty to estimate the true volumes was equal to  $\pm 0.15 \text{ mm}^3$  in all cases. The volume overestimation (bias) was reduced when applying B60 (with  $n=0.27 \text{ mm}^3$  vs. the  $n=0.35 \text{ mm}^3$  and  $0.53 \text{ mm}^3$  that were obtained for B46 and B41, respectively). With B60, the relative errors on the volume measurement of cylinders 0.5, 0.8, 1.0 and 2.5 mm were respectively +343%, +10%, -20%, and -7%.

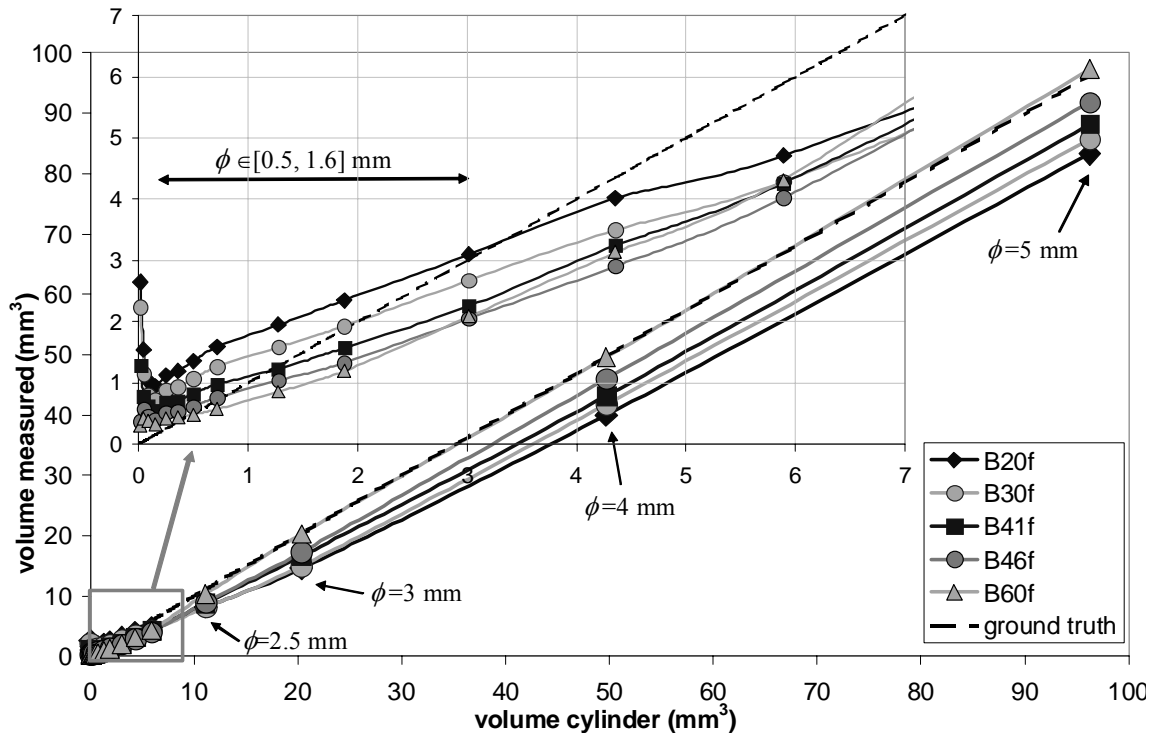


**Figure 2.10.** Volume measurements with  $t_{HM}$  for different representative convolution kernels.

Kernel	<i>over</i> (%)	<i>under</i> (%)	$P_{\text{over/under}}$	$P_{\text{fit 2}}$	$m_2$	$n_2$ (mm <sup>3</sup> )	$R^2$	$Res_2$ (mm <sup>3</sup> )
<b>B20</b>	413	-17.7	1.64	2.46	0.89	-2.88	0.9989	2.30
<b>B30</b>	297	-15.2	1.42	2.46	0.92	-3.08	0.9994	1.66
<b>B35</b>	269	-13.2	1.40	2.46	0.94	-3.00	0.9997	1.30
<b>B41</b>	206	-11.6	1.18	1.99	0.93	-2.24	0.9995	1.57
<b>B46</b>	128	-7.5	1.03	1.99	0.98	-2.26	0.9999	0.68
<b>B50</b>	114	-3.0	0.98	1.99	1.02	-2.22	1.0000	0.96
<b>B60</b>	84	-0.06	0.88	1.20	1.02	-0.80	1.0000	1.64
<b>B70</b>	90	1.5	0.88	0.00	1.02	-0.29	0.9997	1.51

**Table 2.6.** Parameter values (see their definition in Table 2.4) describing accuracy and uncertainty of the volume measurements within different size ranges for different convolution kernels.

#### ***Influence of other CT parameters:***

The variation of  $S_{\text{eff}}$ , RI, pitch and FOV in the ranges being evaluated did not affect the results of the in-plane measurements (diameter and area). The  $S_{\text{eff}}$ , RI, and pitch influenced the results of the length measurements (see Table 2.7), and consequently, to a lesser extent, the results of the volume measurements.

The length measurements in  $R_2$ , i.e. for larger cylinders, are accurate and statistically equal to the ground truth for all the parameters values here evaluated. The accuracy of the length measurements in  $R_1$ , i.e. for cylinders smaller than 1.0 mm, improves when decreasing the  $S_{\text{eff}}$ , RI and pitch. With  $S_{\text{eff}}=0.6$  mm, RI=0.2 mm and pitch=0.45 we obtained the best accuracy. However, this accuracy is still insufficient to perform reliable measurements in  $R_1$ : We obtained an overestimation of 59% for a cylinder length of 0.5 mm and an uncertainty of  $\pm 0.15$  mm for the range up to 1.0 mm.

As expected, an increase in the  $S_{\text{eff}}$  from 0.6 to 1.0 mm noticeably increases the overestimation of the length measurements in  $R_1$  (see Fig. 2.11, and the  $n_1$  in Table 2.7). This overestimation also affects, to a lesser extent, the volume measurements in  $R_1$ . The uncertainties in the length measurements within  $R_1$  are almost the same for  $S_{\text{eff}}=0.6$  and 0.75 mm, but it noticeably increases for  $S_{\text{eff}}=1.0$  mm.

When increasing the RI from 0.2 mm up to 0.4 mm, the errors due to length overestimation in  $R_1$  are statistically the same, but RI=0.4 mm increases the measurement fluctuations leading to a loss of linearity ( $R^2=0.766$ ). With RI=0.6 mm the length measurements in  $R_1$  cannot be considered linear anymore ( $R^2=0.369$ ) and reproducibility of the measurements strongly decreases (the values of the std. dev. in this case were much larger than those of smaller RIs). However, the influence of RI on the volume quantification is negligible even for the largest RI values.

The variation of FOV and pitch did not affect the accuracy of the diameter, length, and volume measurements. The effect of the FOV on the measurements would become more important if the interpolation step prior to the quantification was omitted.

CT parameters	over (%)	$P_{fit1}$	$m_1$ (mm)	$n_1$ (mm)	$R^2$	$Res_1$ (mm)	$P_{fit2}$ (were $m_2 \approx 1, n_2 \approx 0$ )
$S_{eff}$ 0.6	49	0.91	0.55	0.55	0.9496	0.30	1.11
$S_{eff}$ 0.75	67	0.91	0.49	0.69	0.9854	0.29	1.11
$S_{eff}$ 1.0	102	0.91	0.31	1.00	0.9353	0.65	1.50
RI 0.2	46	1.11	0.67	0.46	0.9274	0.19	1.11
RI 0.3	49	0.91	0.55	0.55	0.9496	0.30	1.11
RI 0.4	52	1.89	0.77	0.43	0.7659	----	1.11
RI 0.6	59	3.00	0.82	0.43	0.3683	----	1.24
Pitch 0.45	49	0.91	0.55	0.55	0.9496	0.30	1.11
Pitch 0.6	50	1.11	0.66	0.49	0.9593	0.31	1.11
Pitch 0.8	51	1.11	0.59	0.54	0.9816	0.38	1.11
Pitch 0.95	53	1.11	0.46	0.63	0.9266	0.63	1.11

**Table 2.7.** Parameter values (see their definition in Table 2.4) describing the accuracy and uncertainty of the length measurements within different size ranges for different acquisition and reconstruction CT parameters.

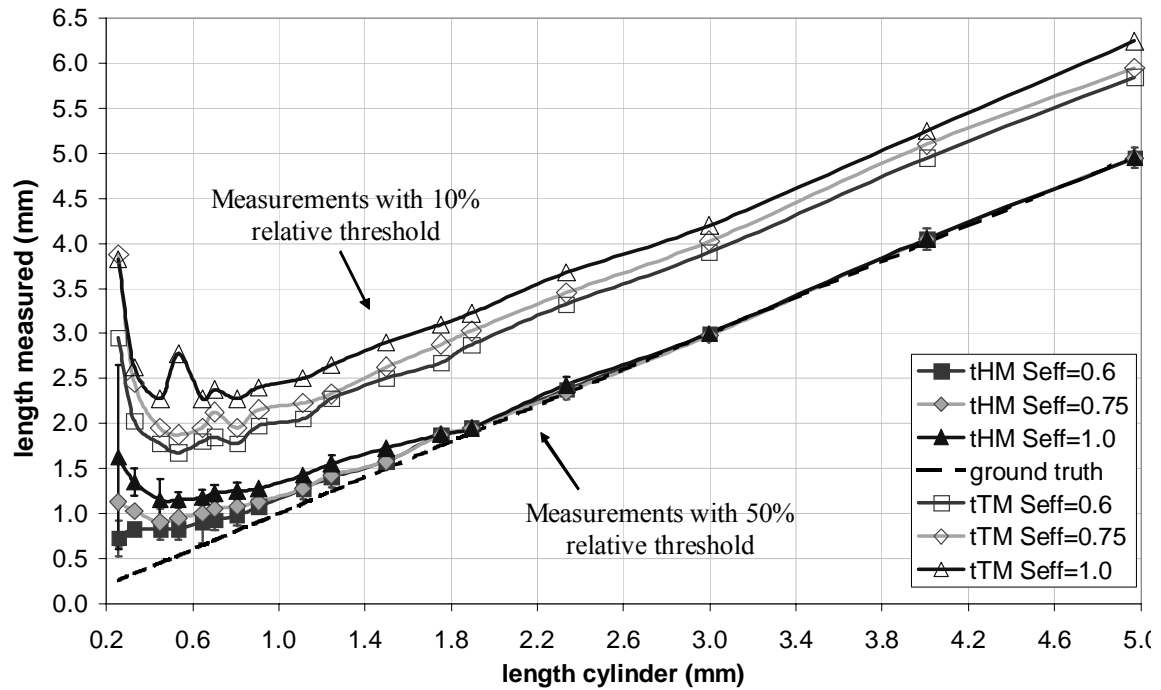


**Figure 2.11.** Diameter measurements with the 50% relative threshold ( $t_{HM}$ ) and the 10% relative threshold ( $t_{TM}$ ), for different reconstruction slice thickness ( $S_{eff}$ ).



### • Object spread measurements

The differences between the measurements with the  $t_{HM}$  and  $t_{TM}$  give an indication of the extent of the object edge spread in the  $xy$ -plane (referred to as  $C_\phi$ ), and the object edge spread along the  $z$ -direction (referred to as  $C_l$ ). Both  $C_\phi$  and  $C_l$  are approximately constant for all the cylinder sizes (see Figures 2.8, 2.9, and 2.11). As expected, the  $C_\phi$  value is influenced by the convolution kernel (Table 2.8), while  $C_l$  is influenced by the  $S_{eff}$ , RI, and pitch (Table 2.9). When increasing the kernel,  $C_\phi$  progressively decreases (from  $1.39 \pm 0.12$  mm with B20, to  $0.59 \pm 0.08$  mm with B60). When reducing the parameters  $S_{eff}$ , RI, and pitch,  $C_l$  progressively decreases. The variation of  $C_l$  is more noticeable for the  $S_{eff}$  (decreasing from 1.20 mm with  $S_{eff}=1.0$  mm, to 0.89 mm with  $S_{eff}=0.6$  mm), and for the RI (decreasing from 1.08 mm with RI=0.6 mm, to 0.87 mm with RI=0.2 mm). For the pitches here evaluated the  $C_l$  values do not statistically vary. The FOV has no influence on the object spread.

Kernel	$C_\phi$ (mm)	$C_l$ (mm)
<b>B20</b>	$1.39 \pm 0.12$	$0.87 \pm 0.06$
<b>B30</b>	$1.22 \pm 0.11$	$0.86 \pm 0.05$
<b>B35</b>	$1.17 \pm 0.12$	$0.86 \pm 0.06$
<b>B41</b>	$1.12 \pm 0.11$	$0.89 \pm 0.05$
<b>B46</b>	$0.84 \pm 0.07$	$0.88 \pm 0.05$
<b>B50</b>	$0.67 \pm 0.09$	$0.87 \pm 0.06$
<b>B60</b>	$0.59 \pm 0.08$	$0.89 \pm 0.08$
<b>B70</b>	$0.55 \pm 0.08$	$0.91 \pm 0.13$
<b>B80</b>	$0.53 \pm 0.09$	$0.85 \pm 0.06$

**Table 2.8.** Mean object spread in the CT plane ( $C_\phi$ ) and along the  $z$ -axis ( $C_l$ ) for different reconstruction kernels.

CT parameters	$C_\phi$ (mm)	$C_l$ (mm)
<b><math>S_{eff}</math> 0.6</b>	$1.12 \pm 0.11$	$0.89 \pm 0.05$
<b><math>S_{eff}</math> 0.75</b>	$1.12 \pm 0.12$	$1.01 \pm 0.07$
<b><math>S_{eff}</math> 1.0</b>	$1.12 \pm 0.13$	$1.20 \pm 0.14$
<b>RI 0.2</b>	$1.10 \pm 0.13$	$0.87 \pm 0.05$
<b>RI 0.3</b>	$1.12 \pm 0.11$	$0.89 \pm 0.05$
<b>RI 0.4</b>	$1.12 \pm 0.12$	$0.94 \pm 0.06$
<b>RI 0.6</b>	$1.11 \pm 0.13$	$1.08 \pm 0.12$
<b>Pitch 0.45</b>	$1.12 \pm 0.11$	$0.89 \pm 0.05$
<b>Pitch 0.6</b>	$1.21 \pm 0.15$	$0.90 \pm 0.07$
<b>Pitch 0.8</b>	$1.15 \pm 0.14$	$0.95 \pm 0.08$
<b>Pitch 0.95</b>	$1.25 \pm 0.16$	$0.98 \pm 0.13$
<b>FOV 50</b>	$1.12 \pm 0.11$	$0.89 \pm 0.05$
<b>FOV 160</b>	$1.12 \pm 0.14$	$0.89 \pm 0.06$
<b>FOV 300</b>	$1.12 \pm 0.13$	$0.88 \pm 0.04$

**Table 2.9.** Mean object spread in the CT plane ( $C_\phi$ ) and along the  $z$ -axis ( $C_l$ ) for different acquisition and reconstruction CT sampling parameters.

## 2.4. Discussion

The present study analyses different factors that affect the visualization and quantification of small high-density structures and their surrounding tissues with currently developed MDCT systems. For this purpose, a custom made phantom consisting of Aluminum cylinders of different diameters and lengths has been used to assess the accuracy and uncertainty in measuring density, diameter, length, area and volume of small high-density objects, while varying scanning and reconstruction parameters of a 64 MDCT system. In addition, a bead phantom is imaged to estimate the PSF for the same scanning and reconstruction parameters, and simulations based on the PSF information are compared with the experimental measurements. We have found that for objects with sufficiently large SNR the simulations are in close agreement with the measurements. This indicates that in these cases the errors in estimating object density and size mainly depend on the true object size and the PSF, and that our findings can be extended to other imaging systems and protocols. However, we also have found that for smaller objects, image noise and artifacts limit measurement reproducibility and increase measurement error. A main contribution of our investigation is that we provide insight into the accuracy with which intensity spatial information of small high-density objects is given by state-of-the-art CT systems. This is highly relevant for clinical applications that involve quantitative analysis of small structures, such as in atherosclerotic plaque characterization.

Influence of CT acquisition and reconstruction parameters is investigated by independently varying the convolution kernel,  $S_{eff}$ , RI, FOV, and pitch, within ranges that are compatible with high-resolution imaging. We have found that object signal and in-plane accuracy are mainly influenced by the convolution kernel. When using sharpening kernels (B46-B80) diameter, area and volume measurements become more accurate at the expense of strongly increasing the image noise and introducing edge-ringing artifacts.<sup>35</sup> Edge-ringing artifacts are stronger for high-contrast structures; for the aluminum cylinders, in the range of sizes between 1.0 and 2.5 mm, these artifacts yield a signal enhancement over the HU of Aluminum. In some cases this results in a clipping of the HU values, thus preventing signal and size measurements. This would be the case for heavily calcified atherosclerotic lesions and metal structures such as stents. Both noise amplification and edge-ringing artifacts introduce difficulties in detecting small calcifications and hamper the imaging of low-contrast tissues. On the other hand, longitudinal accuracy is more influenced by the  $S_{eff}$  than by the RI, and pitch. Despite the slight increase in noise; length measurements become more accurate when decreasing the  $S_{eff}$ , RI, and pitch values.<sup>30-33</sup>

From the simulations and experiments we have found that the object density and size can be accurately determined (i.e. with a relative error smaller than ~5%) in the range of object sizes larger than two times the FWHM of the PSF in each direction of space (i.e. above ~2.0 mm). Under this size, the HU of the inner object voxels decrease with the object size, and size measurements are overestimated due to the PVE both in the axial and transaxial directions. These findings are in agreement with the work presented by Prevrhal *et al.*<sup>19</sup>

When looking at the accuracy and uncertainty of object diameter and length measurements for one of the highest spatial resolution parameter settings (i.e. sharp

kernel B60,  $S_{eff}=0.6$  mm,  $RI=0.2$  mm, and  $pitch=0.45$ ) we find that: In the range of objects larger than 1.95 mm in the  $xy$ -plane, and larger than 1.35 mm in the  $z$ -axis (which correspond to two times the FWHM of the  $xy$ - and  $z$ - PSFs, respectively), the relative errors in diameter and length measurements are smaller than 5%, and the uncertainty of the measurements (about  $\pm 0.06$  mm) is due to image noise. These errors, although progressively increasing (either due to over- or underestimation), are smaller than 13% until reaching an object size of 0.88 mm in the  $xy$ -plane (which is slightly smaller than the FWHM of the  $xy$ -PSF), and 1.02 mm in the  $z$ -axis (which corresponds to one and a half times the FWHM of the  $z$ -PSF). In the range of smaller sizes, measurement uncertainty become very large ( $\pm 0.23$  mm), and relative errors due to measurement overestimation drastically increase with decreasing object size (e.g., for a cylinder 0.5 mm in diameter and length, overestimation of 72%, in the  $xy$ -plane, and 59%, along the  $z$ -axis, have been obtained).

The errors in the area and volume measurements can be approximated by the errors in the diameter and length, although the volume underestimation in the region of large cylinders is higher than expected (especially for smoothing kernels) due to the blur of the cylinder edges.

We have found that for the 64 MDCT measurement accuracy in the longitudinal direction is higher than in the transverse plane. However, when using medium to sharp convolution kernels, the object spread in the transverse plane (computed as the difference between the measurements with the 50% and with the 10% relative thresholds) can be successfully reduced to a lower value than the object spread in the  $z$ -axis.

In our experiments, several choices have been made. First, for the quantitative measurements we have used the 50% relative threshold. Of course, measurement accuracy does not only depend on the imaging system and protocol, but also on the applied quantification method. For small structures, an interesting alternative to relative thresholds is to determine the object size by summing the object intensities (HU) above the surrounding tissue, and dividing the resulting amount by the HU value of the object material. In order to investigate the measurement accuracy of this method compared with the 50% relative threshold, we performed additional analyses of our image data. The results showed that when utilizing the true object HU value (i.e., not affected by PVE), this method indeed improves performance in the quantification of small structures. However, the analyses also indicated that this quantification method performs worse if we have to use the object HU as measured in the CT image, since for small structures HU values are affected by PVE. This especially posed a problem for structures smaller than  $\sim 2.5$  mm in each direction of space, where object signal strongly decreases with the object size. In these cases, the use of the underestimated object HU to divide the integrated intensity yielded a size measurement overestimation that was larger than that obtained with the 50% relative threshold. We therefore believe this method is less appropriate for calcification size quantification, since it is known that calcifications are generally quite small and have heterogeneous densities.

A second potential problem that may have influenced our results is that when repeating each scan three times for statistical assessment, the  $z$ -axis initial positions selected to acquire and reconstruct the images were not varied. This implies that the sampling positions of the projection data and of the reconstructed slices with respect to the scanned objects were the same for the three scans. Consequently, if the selected

reconstruction index (RI) is large compared with the object size (e.g., when using RI=0.3 mm to measure objects smaller than 0.6 mm in the z-axis), differences in the slice position with respect to a scanned object may have influenced the signal and size measurements, since the object can be centered in an image slice or well averaged between two consecutive slices. However, when comparing the results obtained for three different RI values, i.e. 0.2, 0.3 and 0.4 mm (which lead not only to different slice positions with respect to the Aluminum cylinders, but also to different distances between the reconstructed slices) we found that the mean values of the signal and length measurements were almost the same, even for the smallest cylinders, and in none of the cases significantly different. This indicates that this potential problem has only limited impact on our measurements, and has a substantially lower impact than image noise.

### **Optimal parameter settings in clinical applications**

For clinical applications such as atherosclerotic plaque characterization and/or lumen assessment of small arteries, increasing the spatial resolution by applying sharper kernels and thinner slice thickness seems a logical option. However, there is a trade-off owing to the increase in noise and artifacts. These two competing factors make it very complicated and patient dependent to establish the optimal imaging parameter settings. For our experiments a good balance between spatial accuracy and SNR was achieved with a medium-sharp convolution kernel such as B46. For this kernel, ringing artifacts are still negligible, and although small structures cannot be accurately determined (an average bias of 0.85 mm in the region of objects smaller than 1.0 mm, leads to large measurement overestimation in this range), the accuracy rapidly increases with the object size (11% overestimation for 1.0 mm; 5% overestimation for 1.2 mm; and an underestimation smaller than 4% for sizes larger than 2.5 mm). Another advantage of B46 is that it leads to a lower relative underestimation in the region between one and two times the FWHM of the PSF than that obtained with more sharpening kernels (the peak relative underestimation with B41 is -8%, and it becomes -13% with B60). Since for the 64 MDCT the spatial resolution along the z-axis is higher than in the xy-plane, one way to reduce noise is using a slightly larger slice thickness. For example, with  $S_{eff}=0.75$  mm and kernel B46 the object spread in the z-axis and xy-plane is similar, but the noise is slightly decreased. In clinical applications aimed at volume quantification of high contrast objects (such as high-density calcifications), sharper kernels, e.g. B60, are recommended. These kernels increase accuracy (except for metallic structures whose signals may exceed the CT HU interval) and reduce threshold dependency (because object spread is reduced).

### **Validity of our results as reference for patient studies**

The relevance of our work is that it can be used as reference for phantom and in vivo/ex-vivo patient studies. In clinical diagnosis, it can be used not only to select the appropriate scanning parameters in view of the application, but also to interpret clinical data and understand the limitations in quantifying and visualizing small structures. A limitation of our analyses is that these are based on phantom experiments. The choice of Aluminum to investigate the imaging of small high-density structures implies that generalization of our results to calcifications is somewhat affected by the differences in the SNR. The lower SNR of small calcifications would lead to lower detectability, larger size overestimation for objects smaller than  $\sim 2.0$  mm,<sup>19</sup> and lower measurement reproducibility.

In our experiments, the X-ray attenuation generated by the water filled Polymethylmethacrylat (PMMA) cylindrical module allowed us to perform our measurements in presence of a realistic amount of noise. However, the symmetry of the surrounding material and the lack of highly attenuating objects (such as bone) may make our results less representative for clinical applications. In clinical practice there is a number of factors that may influence image quality depending on the specific application, such as: *i*) the beam hardening effect (BHE) and the non-linear PVE due to bone attenuation; and *ii*) the fact that structures of interest can be placed out of the center of the CT gantry, where the in-plane and longitudinal spatial resolutions are slightly lower. In order to investigate the impact of these factors on the measurement accuracy, we repeated a number of experiments in more realistic conditions, i.e., placing the Aluminum cylinders at 60 mm from the CT center, and including additional attenuating material with higher attenuation coefficients and with an asymmetric spatial configuration. Whereas the signal of objects smaller than  $\sim 2.5$  mm was significantly decreased due to larger linear and non-linear PVE, the size measurement overestimation in the range of sizes smaller than  $\sim 2.0$  mm was slightly, but not significantly, increased compared with the results presented in this paper. Hence, the reported results on measurement accuracy are also indicative for the performance in more realistic attenuation environments.

A further limitation of the phantom used in this study is that it does not simulate patient motion, e.g. owing to the heart beating. Although coronary CT imaging quality has noticeably improved as a result of the increased gantry rotation speed and the optimized ECG retrospective gated reconstructions, it is clear that heart motion artifacts would hamper accuracy and reproducibility of small objects measurements, especially for patients with high heart rates and/or arrhythmia.

Thus, the reported results give an insight into the limitations of the imaging of small high-density objects, but these limitations should be viewed as lower limits for clinical practice.

## Conclusions

The accuracy in imaging small high-density structures with a 64 MDCT scanner was investigated using dedicated phantoms. From this study four main conclusions can be drawn. First, the spatial accuracy in the  $z$ -axis is higher than in the  $xy$ -plane. Second, when using high-resolution protocols, relative errors in size and density measurements are smaller than 5% for objects larger than  $\sim 2$  mm in each spatial direction. Under this object size, both the signal intensity and the size measurement accuracy strongly decrease. Third, objects smaller than  $\sim 1$  mm cannot be accurately quantified; object size is overestimated and attenuation values are underestimated. Even with one of the highest resolution protocols (i.e. sharp kernel, B60, and minimal values of  $S_{eff}$ , RI, pitch, and FOV) the relative measurement overestimation of an object of 0.5 mm, which is close to the detection limit, was 72% for the diameter, 59% for the length, 210% for the area, and 342% for the volume. Finally, noise and edge-ringing artifacts associated with sharpening convolution kernels limit the application of these kernels to increase spatial accuracy when the imaging of soft-tissues surrounding calcifications and/or stents are also of clinical interest.

The results as presented in this paper provide an insight into the limitations in the quantification and visualization of small high-density structures with state-of-the-art MDCT systems.

## References

1. Wexler L, Brundage B, Crouse J, *et al.* Coronary artery calcification: pathophysiology, epidemiology, imaging methods, and clinical implications. A statement for health professionals from the American Heart Association. Writing Group. *Circulation* 1996; 94:1175-1192.
2. Beadenkopf WG, Daoud AS, Love BM. Calcification in the Coronary Arteries and Its Relationship to Arteriosclerosis and Myocardial Infarction. *Am J Roentgenol Radium Ther Nucl Med* 1964; 92:865-871.
3. Schuhlen H, Kastrati A, Mehilli J, *et al.* Restenosis detected by routine angiographic follow-up and late mortality after coronary stent placement. *Am Heart J* 2004; 147:317-322.
4. Nieman K, Pattynama PM, Rensing BJ, *et al.* Evaluation of patients after coronary artery bypass surgery: CT angiographic assessment of grafts and coronary arteries. *Radiology* 2003; 229:749-756.
5. Kalender WA. Computed Tomography: fundamentals, system technology, image quality, applications. In: Publicis MCD Verlag, Munich, 2000; Chapter 4 (82-118).
6. Sarty HC, Blankenhorn DH, Chandler AB, *et al.* A Definition of the intima of human arteries and of its atherosclerosis-prone regions - a report from the Committee on Vascular Lesions of the Council on Arteriosclerosis, American-Heart Association. *Circulation* 1992; 85:391-405.
7. Sarty HC, Chandler AB, Glagov S, *et al.* A definition of initial, fatty streak, and intermediate lesions of atherosclerosis. A report from the Committee on Vascular Lesions of the Council on Arteriosclerosis, American Heart Association. *Circulation* 1994; 89:2462-2478.
8. Sarty HC, Chandler AB, Dinsmore RE, *et al.* A definition of advanced types of atherosclerotic lesions and a histological classification of atherosclerosis - a report from the Committee on Vascular Lesions of the Council on Arteriosclerosis, American Heart Association. *Circulation*. 1995; 92:1355-1374.
9. Rollano-Hijarrubia E, van der Meer F, van der Lugt A, *et al.* Improving the imaging of calcifications in CT by histogram-based selective deblurring. In *Conference Proceedings, SPIE, Medical Imaging 2005: Physics of Medical Imaging* 2005; 5745:67-78.
10. El-Omar MM, Dangas G, Iakovou I, *et al.* Update on In-stent Restenosis. *Curr Interv Cardiol Rep* 2001; 3:296-305.
11. Mathias K, Jager H, Hennigs S, *et al.* Endoluminal treatment of internal carotid artery stenosis. *World J Surg* 2001; 25:328-334.

12. Gonzalez R, Woods R. Digital Imaging Processing. In: Prentice-Hall P, New Jersey, 2003.
13. Sakai O, Shen Y, Takata Y, *et al.* The use of deblurring technique for improving the longitudinal resolution in helical CT of the head and neck region. *Comput Med Imag Grap* 1997; 21:153-164.
14. Hong C, Becker CR, Schoepf UJ, *et al.* Coronary artery calcium: Absolute quantification in non-enhanced and contrast-enhanced multi-detector row CT studies. *Radiology* 2002; 223:474-480.
15. Carr JJ, Nelson JC, Wong ND, *et al.* Calcified coronary artery plaque measurement with cardiac CT in population-based studies: standardized protocol of Multi-Ethnic Study of Atherosclerosis (MESA) and Coronary Artery Risk Development in Young Adults (CARDIA) study. *Radiology* 2005; 234:35-43.
16. Becker CR, Knez A, Ohnesorge B, *et al.* Visualization and quantification of coronary calcifications with electron beam and spiral computed tomography. *Eur Radiol* 2000; 10:629-635.
17. Ulzheimer S, Kalender WA. Assessment of calcium scoring performance in cardiac computed tomography. *Eur Radiol* 2003; 13:484-497.
18. Newman DL, Dougherty G, al Obaid A, *et al.* Limitations of clinical CT in assessing cortical thickness and density. *Phys Med Biol* 1998; 43:619-626.
19. Prevrhal S, Engelke K, Kalender WA. Accuracy limits for the determination of cortical width and density: the influence of object size and CT imaging parameters. *Phys Med Biol* 1999; 44:751-764.
20. Prevrhal S, Fox JC, Shepherd JA, *et al.* Accuracy of CT-based thickness measurement of thin structures: Modeling of limited spatial resolution in all three dimensions. *Med Phys* 2003; 30:1-8.
21. Rossmann K. Point spread-function, line spread-function, and modulation transfer function. Tools for the study of imaging systems. *Radiology* 1969; 93:257-272.
22. Meinel JF, Jr., Wang G, Jiang M, *et al.* Spatial variation of resolution and noise in multi-detector row spiral CT. *Acad Radiol* 2003; 10:607-613.
23. Barrett HH. Objective assessment of image quality: effects of quantum noise and object variability. *J Opt Soc Am A* 1990; 7:1266-1278.
24. Steel SA, Swann P, Langley G, *et al.* A phantom for evaluating bone mineral density of the hand by dual-energy x-ray absorptiometry. *Physiol Meas* 1997; 18:233-240.
25. Kolbeck S, Bail H, Weiler A, *et al.* Digital radiography - A predictor of regenerate bone stiffness in distraction osteogenesis. *Clin Orthop Relat R* 1999; 366:221-228.

26. Nikolaou K, Flohr T, Knez A, *et al.* Advances in cardiac CT imaging: 64-slice scanner. *Int J Cardiovasc Imaging* 2004; 20:535-540.
27. Wildberger JE, Mahnken AH, Flohr T, *et al.* Spatial domain image filtering in computed tomography: feasibility study in pulmonary embolism. *European Radiology* 2003; 13:717-723.
28. Flohr T, Schaller S, Stadler A, *et al.* Fast image filters as an alternative approach to reconstruction kernel in computed tomography. *Proceedings of SPIE: medical imaging 2001, image processing*. International Society for Optical Engineering 2001; 4322:924-933.
29. Schaller S, Wildberger JE, Raupach R, *et al.* Spatial domain filtering for fast modification of the tradeoff between image sharpness and pixel noise in computed tomography. *IEEE Trans Med Imaging* 2003; 22(7):846-853.
30. Hu H. Multi-slice helical CT: scan and reconstruction. *Med Phys* 1999; 26:5-18.
31. Polacin A, Kalender WA, Brink J, *et al.* Measurement of slice sensitivity profiles in spiral CT. *Med Phys* 1994; 21:133-140.
32. Polacin A, Kalender WA, Marchal G. Evaluation of section sensitivity profiles and image noise in spiral CT. *Radiology* 1992; 185:29-35.
33. McCollough CH, Zink FE. Performance evaluation of a multi-slice CT system. *Med Phys* 1999; 26:2223-2230.
34. Wang G, Vannier MW. The effect of pitch in multislice spiral/helical CT. *Med Phys* 1999; 26:2648-2653.
35. Glover GH, Eisner RL. Theoretical resolution of computed tomography systems. *J Comput Assist Tomogr* 1979; 3:85-91.
36. Schlueter FJ, Wang G, Hsieh PS, *et al.* Longitudinal image deblurring in spiral CT. *Radiology* 1994; 193:413-418.



## Chapter 3

### Accuracy Comparison of a 16 and 64 MDCT Scanner to Image Small High-density Structures

Rollano-Hijarrubia E, Stokking R, Niessen WJ

#### Objectives

The accuracy in imaging small high-density structures is compared for 16 and 64 multidetector-row computed tomography (MDCT) scanners.

#### Materials and Methods

Phantom experiments and different quantification methods are used to establish size measurement accuracy, object signal, and image noise, for both MDCT systems.

#### Results

At similar scanning doses, image noise is larger (~55%) for the 64-MDCT compared with the 16-MDCT, leading to lower signal-to-noise ratios (~28% for objects <2 mm). Object spread in the *xy*-plane is similar for both systems; while it is reduced along the *z*-axis (by ~0.18 mm) for the 64-MDCT. Measurement accuracy of the 64-MDCT is not significantly higher ( $p < 0.05$ ) compared with the 16-MDCT when using a relative-threshold corresponding to 50% of the object maximum attenuation value. However, when using a fixed-threshold, inter-scanner and inter-protocol measurement differences are statistically significant (e.g. volume relative errors are reduced by ~17% on average for the 64 MDCT).

#### Conclusion

Measurement accuracy of the 16 and 64 MDCT scanners is not significantly different when using a 50% relative threshold. However, image noise is significantly larger for the 64-MDCT. Compared with a fixed-threshold based method, the 50% relative-threshold strongly reduces inter-scanner and inter-protocol measurement dependency and improves accuracy.

*This Chapter has been published in Investigative Radiology 2006; 41:781-792.*

### **3.1 Introduction**

Computed tomography (CT) imaging of small high-density structures, such as calcifications and stents, is of high importance in diagnosis, treatment planning and follow-up of patients with cardiovascular disease. Calcifications are used as markers for arterial pathology detection and their quantification is being used as a risk indicator for thrombotic syndromes and/or stroke.<sup>1,2</sup> Currently, postsurgical coronary stent restenosis follow-up is carried out with catheter based angiography.<sup>3</sup> An alternative imaging technique that would allow a non-invasive evaluation of the coronary arteries with comparable accuracy to conventional angiography would have an enormous clinical value, since it would reduce patient risks and treatment costs.<sup>4</sup> State of the art Multi-row detector CT (MDCT) scanners have high temporal resolution, thereby reducing coronary motion artifacts, and are very sensitive to detect small high-density structures, such as calcifications and stents.<sup>1</sup> However, limitations in both spatial resolution and signal-to-noise ratio (SNR) hamper image quality<sup>5</sup> and especially affect the visualization and quantification of the smallest structures. The consequence of the limited spatial resolution of the system is image blur, which not only leads to inaccuracies in the quantification and visualization of small high-density objects, but also limits the imaging of their surrounding low-density structures. This would, for example, hamper measurements of the degree of soft-plaque restenosis of stents, and would affect quantification of lumen stenosis in the presence of a calcified plaque. Both measurements have clinical repercussions, since in-stent restenosis larger than 50%<sup>6</sup> and arterial lumen stenosis larger than 70%<sup>7</sup> are considered eligible for surgical intervention.

Image blur can be characterized by measuring the image three-dimensional (3D) point spread function (PSF),<sup>8</sup> which depends on the system physical characteristics (detector width and sampling interval), and on the image acquisition and reconstruction parameters. It has been shown that the PSF can predict quite well the geometric accuracy and the accuracy with which the object attenuation value can be determined, as a function of the true object size<sup>9-11</sup>. With the recent developments in MDCT scanners, large differences in system physical characteristics and imaging protocols exist, which lead to different PSFs and SNRs, and therefore to different limitations in the measurement accuracy. The rapid evolution and the variety of MDCT scanners that currently coexist in clinical practice hamper the generalization and comparison of patient studies carried out with different CT systems and imaging protocols. Additionally, studies have indicated<sup>12-18</sup> that image measurements obtained with standard fixed-threshold-based quantification methods are protocol and system dependent, which limit research and clinical diagnosis to very constrained experimental conditions.

The recent development of 16 MDCT scanners already constituted an important step towards noninvasive angiography. Although remarkable results to identify high-grade of coronary stenoses were reported from several groups, its image quality is still affected by numerous limitations.<sup>19</sup> The 16 MDCT systems have been rapidly succeeded by new generations of scanners, such as the state-of-the-art 64 MDCT scanners, that have a larger number of detector-rows, thinner slice collimation, and faster rotation speed, thereby reducing motion artifacts and improving spatial resolution along the z-axis.<sup>20,21</sup> However, the thinner slice collimation and faster gantry rotation may compromise the

image quality due to noise,<sup>8,15,22</sup> and therefore, limit the visualization and quantification of small and low-contrasted structures.

To our knowledge no research has been done to compare the accuracy of two consecutive CT generations in performing clinically relevant measurements, such as object signal and object diameter, area, volume, etc., for objects with sizes near and under the spatial resolution of the system (i.e. small with respect to the system PSF).

The aims of the present study are: *i*) to compare the accuracy in imaging small high-density structures, i.e. the accuracy in determining object attenuation and size, for two of the latest CT scanners (i.e. the 16 and 64 MDCT systems); and *ii*) to evaluate the influence of the quantification method on the inter-scanner differences in measurement accuracy. The comparison of scanners and quantification methods is carried out by scanning a custom-made phantom with a high-resolution protocol for different reconstruction kernel, and with a coronary visualization protocol, which uses a retrospective Electrocardiogram (ECG) gated half-scan rotation reconstruction algorithm.<sup>23</sup>

The results of this study are relevant not only to understand and interpret differences in clinical data acquired with different MDCT generations, but also to optimize protocols in view of these differences, and develop quantification methods that improve measurement accuracy and reduce inter-scanner and inter-protocol measurement dependency.

## 3.2 Materials and Methods

### 3.2.1 Phantom description

A dedicated phantom was manufactured (Experimental Medical Instrumentation Department at the Erasmus MC, Rotterdam, The Netherlands) to evaluate the accuracy of CT systems to image small high-density structures. This phantom was already introduced and validated in previous work.<sup>9</sup> The phantom (see Fig. 3.1) consists of small aluminum cylinders, representing high-density calcifications, which are embedded within a Polymethyl Methacrylate (PMMA) 10 mm in diameter. The embedding of the Aluminum cylinders was achieved by pouring the PMMA around the aluminum cylinders. An optimal polymerization was achieved without air bubbles, following the mixing ratio of a powder (Methylmethacrylate – Copolymer) with a liquid (Methylmethacrylate, Dimethacrylate), and the curing conditions recommended by the PMMA manufacturer ([www.heraeus-kulzer.com](http://www.heraeus-kulzer.com)). Longitudinal and transverse views of the CT volume image of the PMMA phantom (Fig. 3.1) show the absence of air bubbles surrounding the aluminum cylinders, and the homogeneity of the PMMA cylinder ( $120.7 \pm 1.3$  HU). The PMMA cylinder mimics the appearance of a mildly enhanced vessel. The cylinders are arranged parallel to the axis of the PMMA cylinder, with their ends separated by at least 9 mm to avoid partial volume effect (PVE) between them. The lengths of the cylinders are approximately equal to their respective diameters, ranging from 0.3 to 5.0 mm.

The PMMA phantom was scanned within a cylindrical module of water, 16 cm in diameter, using a relatively low tube current (i.e. 300 mAs) to achieve a realistic attenuation environment.

Fig. 3.2 compares the attenuation value of Aluminum with the attenuation values of three different densities of Hydroxyapatite (HA), the main component of artery calcifications,<sup>1</sup> for both the 16 and 64 MDCT scanners.

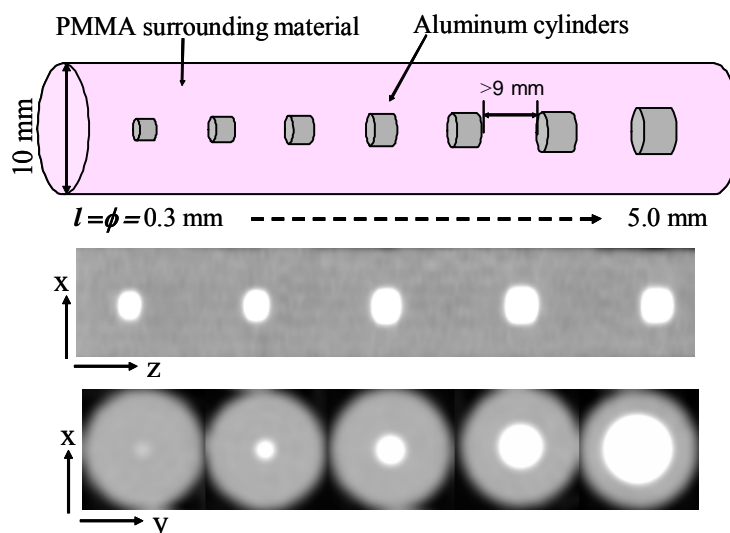


**Figure 3.1.** PMMA module embedding 17 small aluminum cylinders with representative sizes ranging from 0.3 to 5.0 mm. Top frame: illustration of the phantom; Middle and bottom frames: longitudinal and transverse views of the CT volume image of the phantom, which has been scanned in air to minimize image noise, and has been displayed with a low-density contrast window to allow better visualization of the PMMA homogeneity and the absence of air bubbles surrounding the aluminum cylinders.

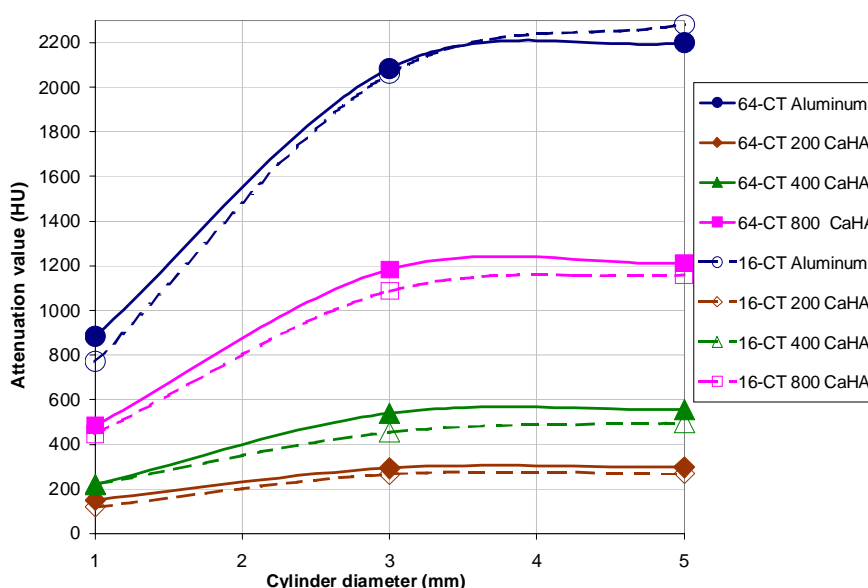


**Figure 3.2.** Attenuation values of Aluminum and three different concentration of HA (200, 400 and 800 mg/cm<sup>3</sup>), for three different cylinder sizes (i.e. 1, 3 and 5 mm). Attenuation values of the HA cylinders have been obtained by scanning the Anthropomorphic Phantom Body<sup>15</sup> with the 16 and 64 MDCT, when using the “HR” protocol and kernel B41.

### 3.2.2 Scanning systems and imaging protocols

#### Description of the MDCT systems

The SOMATOM Sensation 16 consists of 24 detector rows; 16 central rows of 0.75 mm wide, and 4 outer rows located at both sides being 1.5 mm wide. This composition allows the acquisition of non-overlapping slices with two basic collimation modes:  $16 \times 0.75$  mm for high-resolution imaging, and  $16 \times 1.5$  mm for larger longitudinal coverage (i.e. up to 24 mm). The gantry rotation speed is up to 0.37 s/rot.

The SOMATOM Sensation 64 consists of 32 detector rows, which generate a maximum of 64-slice projections with a sampling distance of 0.3 mm. Therefore, 64 overlapping slices of 0.6 mm width are acquired per rotation, and the z-coverage is  $32 \times 0.6$  mm = 19.2 mm. The maximum gantry rotation speed is 0.33 s/rot.

#### Description of the acquisition and reconstruction protocol

An imaging protocol, referred to as “High-resolution (HR)” protocol, was designed and evaluated in previous work<sup>9</sup> and is used in this study to compare the performance of 16 and 64 MDCT systems in clinical applications that require high spatial resolution. The selection of the imaging parameters was based on the following criteria: minimum available values for the scanner collimation width ( $c$ ), reconstruction slice thickness ( $S_{eff}$ ), and pitch; reconstruction increment ( $RI \leq S_{eff}/2$ ); minimal rotation time ( $t_r$ ); suitable X-ray source feeding values for the size of the object being scanned; minimum reconstruction field of view (FOV) containing the region of interest (ROI) (a FOV < 180 mm guarantees an  $xy$ -oversampling of about twice the  $xy$ -plane detector width,  $\sim 0.75$  mm); and a linear interpolation (LI) of one scan-rotation projection data (note that partial scan reconstruction,  $180^\circ LI$ , is only available in coronary applications). The specific values of these parameters (note that the detector collimation and  $S_{eff}$  are system dependent) are given in Table 3.1. Another reconstruction parameter that must be taken into account is the convolution kernel, since it has a strong influence on the spatial resolution in the  $xy$ -plane.<sup>8,9,24-27</sup> Six different representative convolution kernels were considered in this study (see Table 3.1). The four lower values (i.e., B20-B41; Siemens Medical Solutions) go from smoothing to medium kernels; and the three higher values (i.e., B46-B60; Siemens Medical Solutions) go from medium-sharp to sharpening (i.e. edge enhancing) kernels<sup>27</sup>.

Protocol	$c$ (mm)	$S_{eff}$ (mm)	Pitch	RI (mm)	Kernels	$t_r$ (s)	FOV (mm)	mAs	kV	Dose (mGy)	Reconst. mode
“64 HR”	0.60	0.60	0.45	0.3	B20, B30, B35, B41, B46, B50, B60	0.5	50	300	120	23.09	Spiral 360°LI
“16 HR”	0.75	0.75	0.45	0.3	B20, B30, B35, B41, B46, B50, B60	0.5	50	300	120	23.40	Spiral 360°LI

**Table 3.1.** Experimental parameter settings for the “high-resolution protocol” when adapted to the specific characteristics of the 16 and 64 MDCT systems. Dose values are given according to the definition of the CT dose index-volume (CTDI<sub>vol</sub>).

Coronary calcium scoring and coronary visualization are two very important clinical applications of modern CT scanners. Dedicated scanning protocols and reconstruction techniques have been developed to reduce motion artifacts during scanning: the pitch value can be reduced as much as 0.2-0.25 (depending on the scanner), and retrospective ECG partial scan reconstruction (180°LI) is usually applied. Both the lower pitch and partial scan reconstruction may lead to higher spatial resolution along the CT z-axis. However, the lower number of projections leads to lower SNR, which generally has to be compensated by using higher tube currents (up to 900 mAs) and slightly larger  $S_{eff}$ . We therefore also evaluated the influence of the coronary acquisition and reconstruction techniques on the measurement accuracy, and compare the measurements obtained with the 16 and 64 MDCT when using the “Heart View” parameter-settings described in Table 3.2.

Protocol	$c$ (mm)	$S_{eff}$ (mm)	Pitch	RI (mm)	Kernels	$t_r$ (s)	FOV (mm)	mAs	kV	Reconst. mode	ECG Reconst.	temporal resolution
“64 Heart View”	0.60	0.75	0.2	0.4	B20	0.33	50	850	120	Retrospective ECG 180°LI	-350 ms from the R-wave	monophase 164 ms
16 “Heart View”	0.75	0.75	0.25	0.4	B20	0.37	50	700	120	Spiral 180°LI	-350 ms from the R-wave	monophase 187 ms

**Table 3.2.** Experimental parameter settings for the “Heart View” protocol, when adapted to the specific characteristics of the 16 and 64 MDCT systems.

Our experiments were performed for an ideal situation in which the scanned object is in rest, with a regular ECG at 71 beats per minute. This was simulated using the “heart view” application supported by “Somaris/5 Syngo CT 2005” (Copyright© Siemens AG).

### 3.2.3 Evaluation criteria and quantification methods

In order to compare the accuracy of the MDCT scanners in imaging small high-density structures, we consider the following measurements: *i*) cylinder signal (measured as the HU values at the center of the cylinders ( $I_{center}$ ); *ii*) diameter, area, length, and volume of the cylinders; *iii*) cylinder spread in the  $xy$ -plane and along the  $z$ -axis; and *iv*) image noise. To perform these measurements we used a number of objective criteria and automated image analysis techniques.

For the geometrical measurements (i.e., the diameter, area, length, and volume) we use two different threshold-based quantification methods: *i*) Fixed-threshold based quantification (which is used in clinical practice), whose threshold value, referred to as  $t_{fixed}$ , is calculated for each image as  $t_{fixed} = \text{mean HU}_{(PMMA)} + 80 \text{ HU}$ . This choice is based on the Agatston scoring method<sup>28</sup>, which uses a minimum attenuation threshold of 130 HU to differentiate non-calcified from calcified arterial lesions, based on the assumption

that most non-calcified areas would be excluded if the attenuation threshold remains three standard deviations above the mean soft-tissue attenuation of the heart at the electron-beam CT<sup>29</sup>. Assuming that the CT attenuation value of the tissue surrounding calcifications in a non-enhanced scan is equal to ~50 HU (i.e. blood, soft-tissue with thrombus, etc.), we find that the three standard deviations are generally assumed to be approximately equal to 80 HU. *ii*) Relative-threshold based quantification, where the threshold value, referred to as  $t_{HM}$ , is determined for each cylinder at the 50% of the HU difference between the cylinder  $I_{center}$  and the mean HU of the PMMA surrounding material. We selected the 50% relative threshold because it has been shown to provide accurate measurements for objects larger than the system PSF.<sup>9,10</sup> Note that the PMMA mean HU is measured within an image volume (of  $\sim 1.5 \times 10^6$  voxels), where voxels near the aluminum cylinders were excluded to avoid the PVE influencing our measurements. Prior to the quantification with  $t_{fixed}$  and  $t_{HM}$ , all image data are interpolated to a voxel size of  $0.1 \times 0.1 \times 0.1$  mm, in order to achieve more accurate measurements.

The spread of the object borders (i.e. the region surrounding the object that is affected by the PSF) is also relevant as it has a strong influence on the visualization of the object and its surrounding structures. In order to measure the object spread in the transverse and longitudinal directions we use the difference between the object diameter/length measurements obtained with  $t_{HM}$  and those obtained with the 10% (of the maximum object signal intensity) relative threshold.

Finally, image noise is measured as the standard deviation of the HU of the water surrounding the PMMA cylinder. The SNR is defined as the cylinder signal ( $I_{center}$ ) divided by the image noise (standard deviation of the water HU).

For statistical assessment all scans are repeated three times using the same  $z$ -axis initial position for the image acquisition and reconstruction. We have experimentally verified that repositioning of the phantom between scans does not significantly affect the results of our measurements<sup>9</sup>. For all quantitative measurements the mean absolute error,  $\Delta\bar{x}$ , of the estimated mean value of the three measurements,  $\bar{x}$ , is calculated from the measurements standard deviation,  $\sigma$ , and shown as an error bar in the diagrams. For a small number of measurements,  $N$ , the mean absolute error is given by:  $\Delta\bar{x} = t \frac{\sigma}{\sqrt{N}}$ ,<sup>15,30</sup>

where  $\sigma$  is the standard deviation, and  $t$  is the so-called  $t$ -factor. The  $t$ -factor corrects for small  $N$  values, and depends on  $N$  and the probability  $p$  that a measurement falls within the interval  $[\bar{x} - \Delta\bar{x}, \bar{x} + \Delta\bar{x}]$ . For  $N=3$  and  $p=95\%$  (significance), the value of  $t$  is equal to 4.3. The estimation of  $\Delta\bar{x}$  allows us to compare the intra-scanner measurement reproducibility for the 16 and 64 MDCT systems; and to determine the  $t$ -value associated with the two-sample unequal variance Student's  $t$  test. A  $p$ -value  $< 0.05$  is considered statistically significant.

### 3.3 Results

In the first part of this section the image noise, and the object size and attenuation value measurement accuracy of the 16 and 64 MDCT systems are compared when using the “HR” protocol and different reconstruction kernels. The results are presented in three subsections: *i)* Inter-scanner variability of the object signal, object spread and image noise; *ii)* Inter-scanner variability of the size measurements for  $t_{fixed}$  and  $t_{HM}$ ; and *iii)* Measurement variability with the convolution kernel.

In the second part, the measurement accuracy obtained for the “Heart View” protocol is evaluated with the  $t_{HM}$  threshold for both the 16 and 64 MDCT.

All the results in this section are given by means of graphs that plot experimental measurements versus the actual cylinder sizes (given in Table 3.3).

Selected (mm)	Actual cylinder diameter ( $\mu$ CT)	Actual cylinder length ( $\mu$ CT)
0.3	$0.259 \pm 0.002$	$0.255 \pm 0.002$
0.4	$0.411 \pm 0.012$	$0.329 \pm 0.003$
0.5	$0.487 \pm 0.003$	$0.449 \pm 0.009$
0.6	$0.599 \pm 0.006$	$0.534 \pm 0.003$
0.7	$0.700 \pm 0.005$	$0.644 \pm 0.005$
0.8	$0.803 \pm 0.005$	$0.702 \pm 0.008$
0.9	$0.886 \pm 0.010$	$0.806 \pm 0.013$
1.0	$1.001 \pm 0.009$	$0.91 \pm 0.03$
1.2	$1.208 \pm 0.010$	$1.112 \pm 0.006$
1.4	$1.39 \pm 0.02$	$1.24 \pm 0.02$
1.6	$1.601 \pm 0.010$	$1.498 \pm 0.010$
1.8	$1.78 \pm 0.02$	$1.752 \pm 0.006$
2.0	$1.99 \pm 0.03$	$1.89 \pm 0.02$
2.5	$2.46 \pm 0.03$	$2.33 \pm 0.02$
3.0	$2.94 \pm 0.03$	$3.00 \pm 0.05$
4.0	$3.97 \pm 0.06$	$4.01 \pm 0.04$
5.0	$4.97 \pm 0.08$	$4.97 \pm 0.07$

**Table 3.3.** Actual diameters and lengths of the aluminum cylinders measured on the  $\mu$ CT images (the mean values and standard deviations are obtained from three different scans).

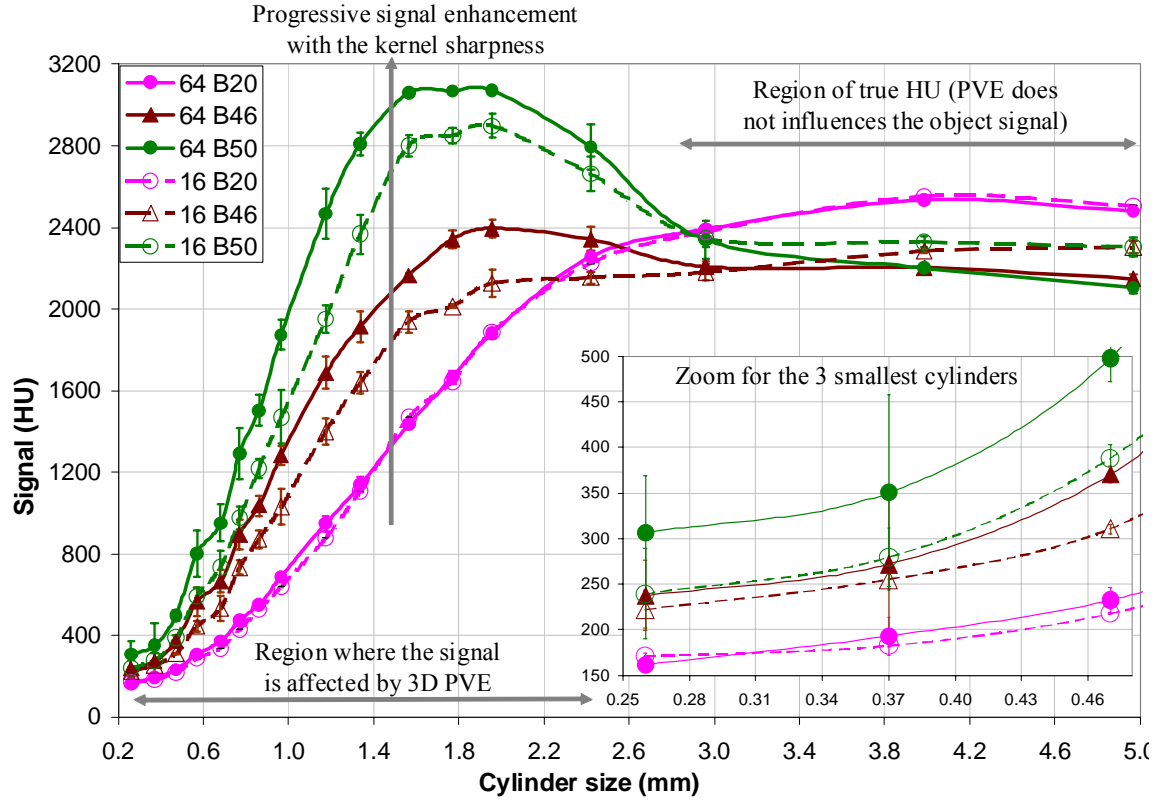
#### 3.3.1 Results for the “High Resolution” protocol

- **Inter-scanner variability of object signal, object spread and image noise**

Fig. 3.3 shows how the object signal decreases with the object size for the 16 and 64 MDCT systems and four representative convolution kernels. Although the kernels that were applied to reconstruct the images with the 16 and 64 MDCT systems are the same, object signal enhancement in the region of small sizes ( $<3$  mm) is stronger for the 64 MDCT, probably due to its lower  $z$ -PSF. Differences in object signal are larger when increasing the sharpness of the kernel. For both systems, we found that in the range of



object sizes larger than 2.5 mm, attenuation values obtained for smooth kernels (B20-B35) were significantly higher than those obtained for medium to sharp kernels (B41-B80). This is probably due to the shape of smooth kernels, which influence the object attenuation values even in the range of sizes larger 2.5 mm.



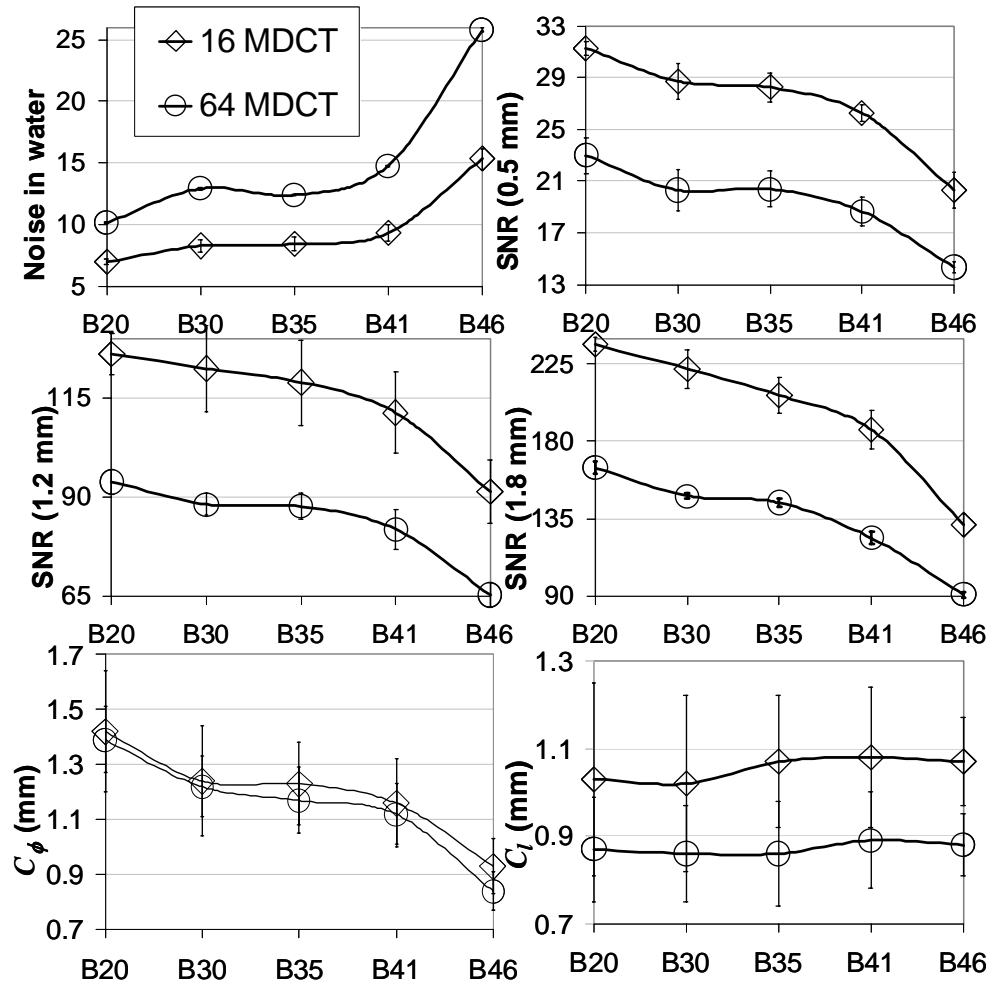
**Figure. 3.3.** Signal measurement with the 16 and 64 MDCT systems for three representative convolution kernels. Two regions are indicated in the graph: *i*) the region where density measurements (i.e., object attenuation values) are affected by the 3D PVE, and therefore depend on the object size; and *ii*) the region where the density can be accurately measured because it does not depend on the object size.

Fig. 3.4 shows for both scanners and four representative convolution kernels the measurements of: *i*) the image noise; *ii*) the SNR for three cylinders whose sizes are distributed in the range where the object signal is affected by PVE; and *iii*) the object spread within the  $xy$ -plane and along the  $z$ -axis (i.e.,  $C_\phi$  and  $C_l$ , respectively).

We found that at similar radiation doses (see values in Table 3.1) image noise is significantly larger for the 64 than for the 16 MDCT, and the differences in image noise increase when using sharper kernels. Consequently, the SNR is significantly larger for the 16 MDCT than for the 64 MDCT (see values in Fig. 3.4 of the SNR for the 0.5, 1.2 and 1.8 mm cylinders), despite the fact that in the range of sizes  $< 2.5$  mm object signal is higher for the 64 than for the 16 MDCT (as is shown in Fig. 3.3). Since image noise also affects the object signal, we found that the intra-scanner signal measurement reproducibility is slightly higher for the 16 than for the 64 MDCT, especially when using

sharpening kernels (e.g., for B46 the measurement mean absolute error in the range of objects  $<2.0$  mm is reduced from 51 HU for the 64 MDCT, to 41 HU for the 16 MDCT).

The object spread in the  $xy$ -plane is very similar for the 16 and 64 MDCT, and it decreases for both systems when increasing the kernel sharpness. The differences between the two systems are larger, although not statistically significant, when comparing the object spread along the  $z$ -axis (it is reduced on average by 0.18 mm for the 64 MDCT compared with the 16 MDCT).



**Figure 3.4.** Measurements of the image noise, object SNR, and object spread, for the 16 and 64 MDCT scanners when using four representative convolution kernels.

- **Inter-scanner variability of size measurement for two quantification methods**

As a general result, we found that the quantification with  $t_{HM}$  rather than with  $t_{fixed}$  allows higher measurement accuracy and reduces measurement dependency with the imaging protocol and with the acquisition system. This is consistent with the literature.<sup>9-11</sup> The performance of these two thresholding methods when quantifying objects in the limit of the spatial resolution of the system can be well understood from Fig. 3.5.

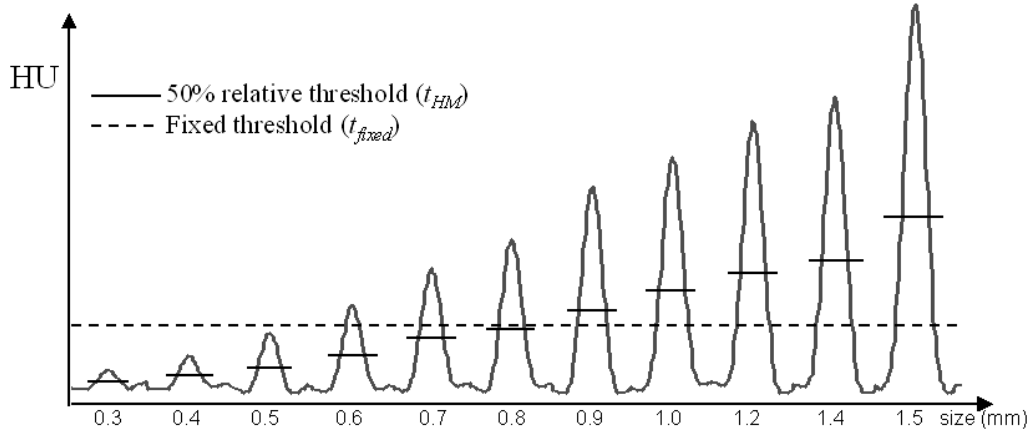


**Figure 3.5.** Positions of  $t_{HM}$  and  $t_{fixed}$  with respect to the cylinder image intensity profile are shown for the range of sizes where the object signal depends on the true object size. This figure illustrates how the relationship between the object signal and the quantification threshold strongly influences size measurements of small objects due to PVE.

For both systems, intra-scanner size measurement reproducibility decreases in the range of sizes smaller than  $\sim 2.0$ - $2.5$  mm (this can be observed later from the error bar of the different geometric measurements). When comparing the two scanners, we found that in this range of sizes the intra-scanner measurement reproducibility in the  $xy$ -plane and along the  $z$ -axis is slightly higher for the 64 than for the 16 MDCT. For example, the averaged mean absolute error of the diameter measurements in this range of small sizes is  $\pm 0.35$  mm for the 16 MDCT, compared with  $\pm 0.13$  mm for the 64 MDCT.

Following these general results, we continue now with the description of the specific results obtained for each of the geometric measurements (i.e., the diameter, length, area, and volume).

### Diameter measurement

Figures 3.6 and 3.7 compare for three representative convolution kernels the mean values of the diameter measurements obtained with the 16 and 64 MDCT systems when using  $t_{HM}$  and  $t_{fixed}$ , respectively. Three main conclusions can be drawn:

i) The mean values of the diameter measurements with  $t_{HM}$  (Fig. 3.6) are not significantly different for the 16 and 64 MDCT systems. However, it can be observed that in the range of sizes smaller than  $\sim 2.0$  mm, the diameter measurement as a function of the actual size shows a more linear behavior for the 64 MDCT than for the 16 MDCT, especially when using sharper kernels (as reference we did a linear fit of the measurements in the range between 0.5 and 1.0 mm for B46, and we found that the correlation coefficient,  $R^2$ , is 0.83 for the 64 MDCT, and 0.15 for the 16 MDCT). For both systems, diameter measurement overestimation in the region of sizes smaller than 2.0-2.5 mm increases with decreasing object size due to the PVE. This overestimation is significantly reduced when increasing sharpness of the kernel, which reduces the object spread in the  $xy$ -plane. For objects larger than 2.0 mm, very similar diameter mean values are obtained for 16 and 64 MDCT systems. In this range measurements are quite accurate ( $< 5\%$  relative

error) for both systems. However, when using kernel B20 the measurements relative error increases slightly due to diameter underestimation (relative underestimations are -7% and -6% for the cylinders of 3 and 4 mm, respectively).

ii) The mean values of the diameter measurements with  $t_{fixed}$  (Fig. 3.7) are also statistically the same for the 16 and 64 MDCT systems when using smoothing to medium kernels. However, when applying a sharp kernel (i.e. B46) the measurement overestimation in the range of objects larger than  $\sim 3.0$  mm is in some cases significantly lower for the 64 MDCT. Despite the fact that the system spatial resolution is high enough to provide accurate measurements in the range of objects larger than 2.0 mm (see measurements with  $t_{HM}$  in Fig. 3.6), measurement accuracy with  $t_{fixed}$  is still poor in this range and strongly depends on the kernel. See in Fig. 3.7 that the overestimation in this range is significantly reduced for the 64 MDCT when increasing the kernel from B20 to B41, and from B41 to B46. For the 16 MDCT the overestimation obtained in this range with B20 and B41 is statistically the same, but this overestimation significantly decreases when applying B46.

iii) When using  $t_{HM}$  the errors and standard deviations of the size measurements of the two smallest cylinders (0.3 and 0.4 mm) are very large for both scanners due to their very low and, for most kernels, insufficient SNRs (since in most cases, the value of  $t_{HM}$  for these two cylinders was lower than two times the standard deviation of the image noise). When using  $t_{fixed}$  these two cylinders could not be quantified because their signals are lower than the fixed-threshold value.

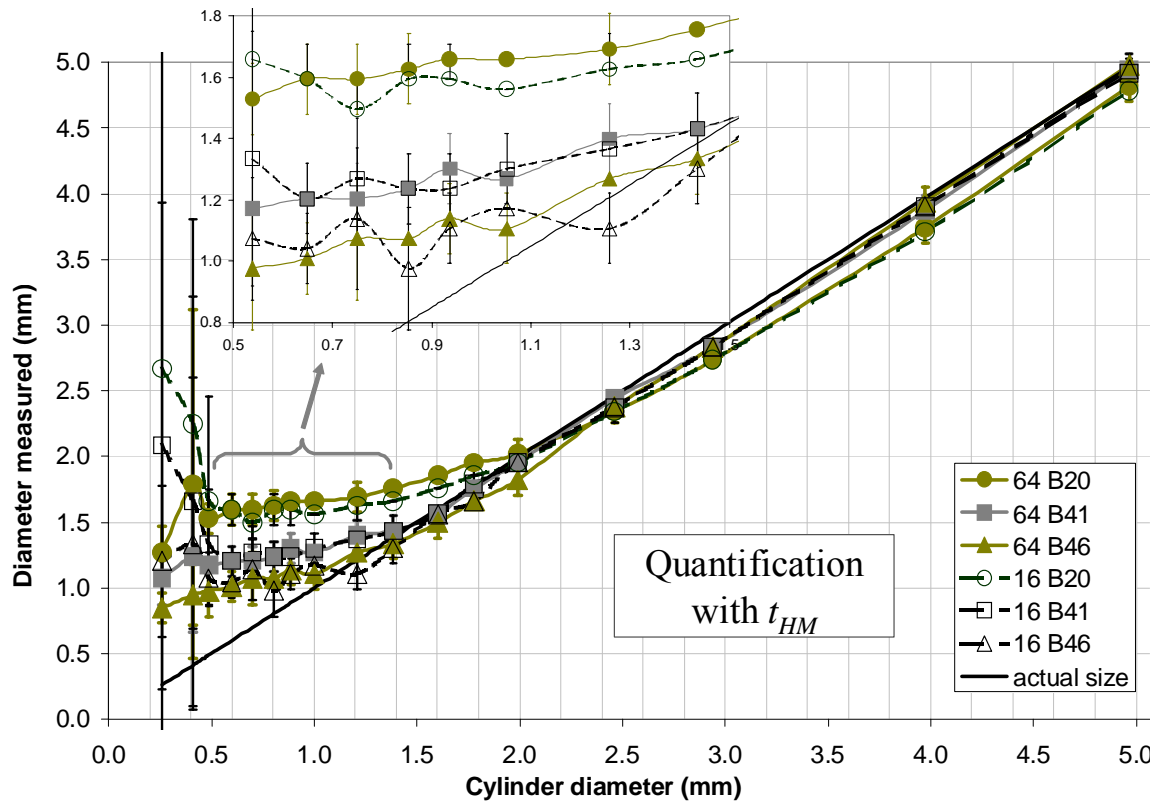


**Figure 3.6.** Diameter measurement with  $t_{HM}$  for the 16 and 64 MDCT systems, when using the “HR” protocol and three representative convolution kernels.

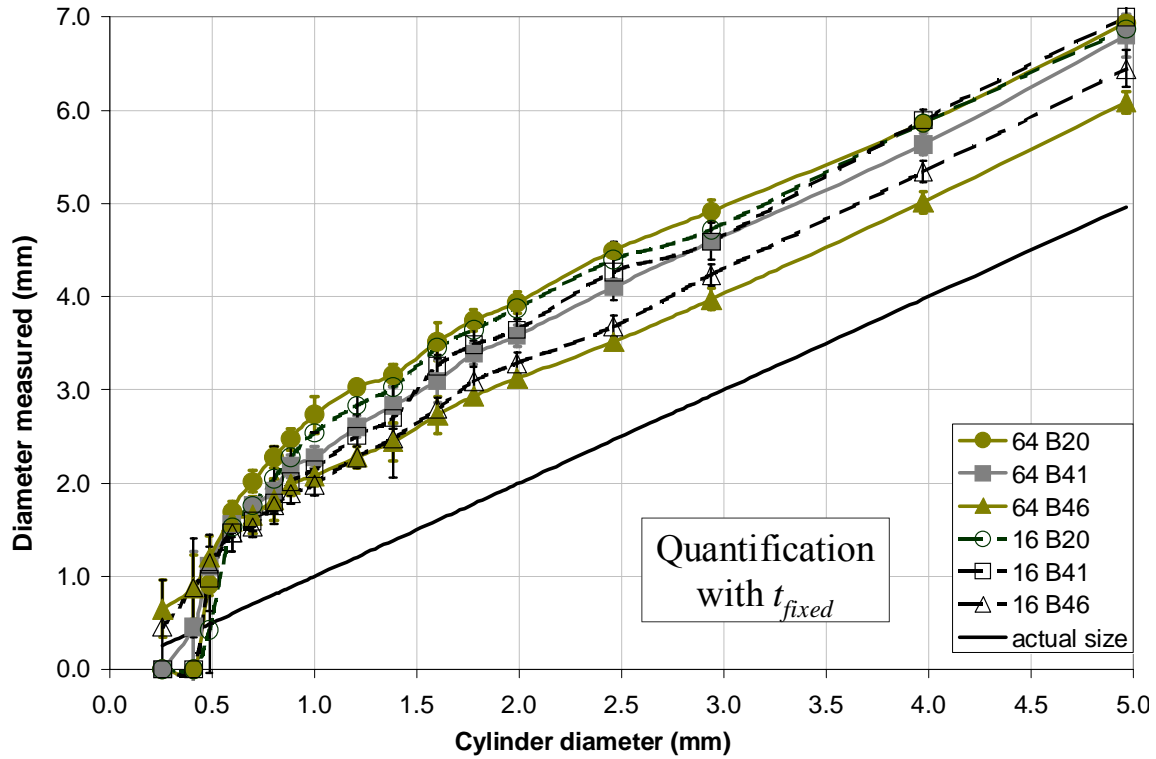


**Figure 3.7.** Diameter measurement with  $t_{fixed}$  for the 16 and 64 MDCT systems, when using the “HR” protocol and three representative convolution kernels.

### Length measurement

Figures 3.8 and 3.9 compare the mean values and standard deviations of the length measurements obtained with the 16 and 64 MDCT systems when using  $t_{HM}$  and  $t_{fixed}$ , respectively. Results are given only for one kernel (B20), because this parameter does not influence the PSF along the z-axis<sup>9</sup>. We found that the length measurements are not statistically different for the 16 and the 64 MDCT systems, regardless of the quantification method.

When using  $t_{HM}$  (Fig. 3.8), the length measurements of objects larger than  $\sim 1.5$  mm are very accurate for both systems. In the range of objects smaller than  $\sim 1.5$  mm, the length measurements mean values of the 64 MDCT are closer to the actual lengths. As reference we did a linear fit of the measurements in the range between 0.5 and 0.8 mm, and we found that the bias (i.e. the ordinate of the line) is reduced from 0.93 mm for the 16 MDCT, to 0.72 mm for the 64 MDCT. However, also in this range, the differences between the two systems are not statistically significant (see the overlap between their error bars).

When using  $t_{fixed}$  (Fig. 3.9), the length measurements of objects larger than  $\sim 0.8$  mm are strongly overestimated due to the z-PSF. This overestimation is slightly, but not significantly, lower for the 64 MDCT. In the range of sizes smaller than  $\sim 0.8$  mm, length measurements abruptly decrease, losing linearity with the actual object lengths.

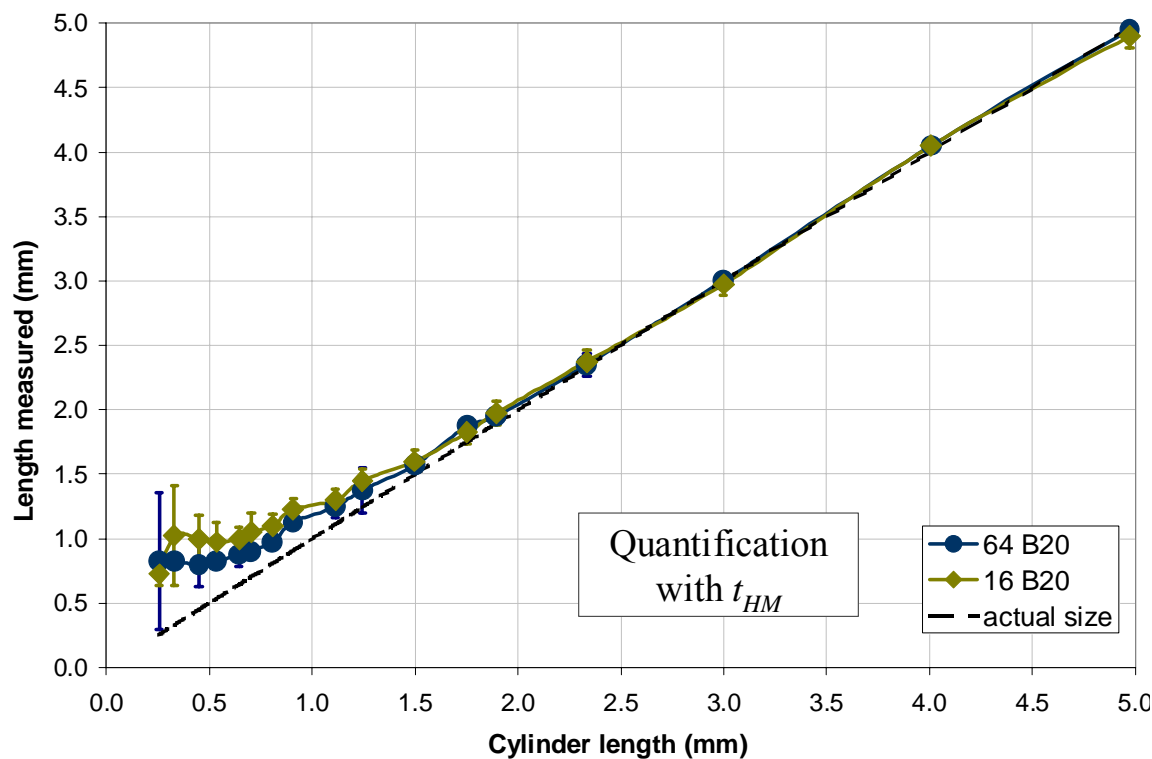


**Figure 3.8.** Length measurement with  $t_{HM}$  for the 16 and 64 MDCT systems, when using the “HR” protocol and kernel B20.

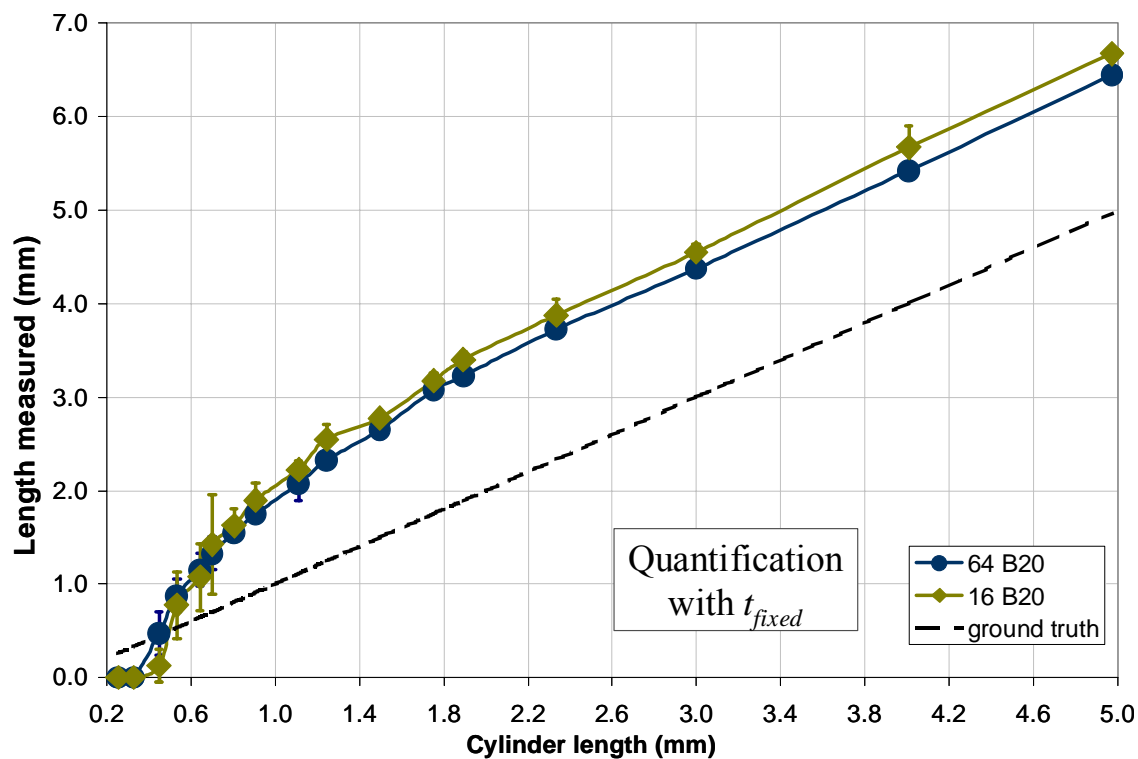


**Figure 3.9.** Length measurement with  $t_{fixed}$  for 16 and 64 MDCT systems, when using the “HR” protocol and kernel B20.

### Area and volume measurement

Relative errors in the area and volume measurement as a function of the object size are given in Figures 3.10 and 3.11, respectively. The differences between the two systems when using  $t_{HM}$  and  $t_{fixed}$  are shown for the sharp kernel B46 (since for this kernel the differences in signal, noise, and diameter measurements are more pronounced). The measurements for the two smallest cylinders are removed from these graphs because their large relative errors would not enable the proper visualization of the measurements for the other cylinders.

When using  $t_{HM}$  the area measurement relative errors are statistically the same for the 16 and 64 MDCT systems for the whole range of sizes. For both scanners, the area measurement relative error in the region of overestimation decreases drastically with increasing object size (e.g., for the 64 MDCT and kernel B46, overestimation decreased from  $\sim 320\%$  for the 0.5 mm cylinder, down to less than 5% for the 1.2 mm cylinder). However, in the region of underestimation (between approximately 1.4 and 2.5 mm) the relative area measurement errors are up to  $-17\%$  for both systems. When using  $t_{fixed}$  area measurement relative errors are much larger than those obtained with  $t_{HM}$ , and the measurements are overestimated for the whole range of sizes. Moreover, the differences between the two scanners are statistically significant (i.e., relative errors are significantly smaller for the 64 MDCT) in the range of sizes larger than  $\sim 1.2$  mm.

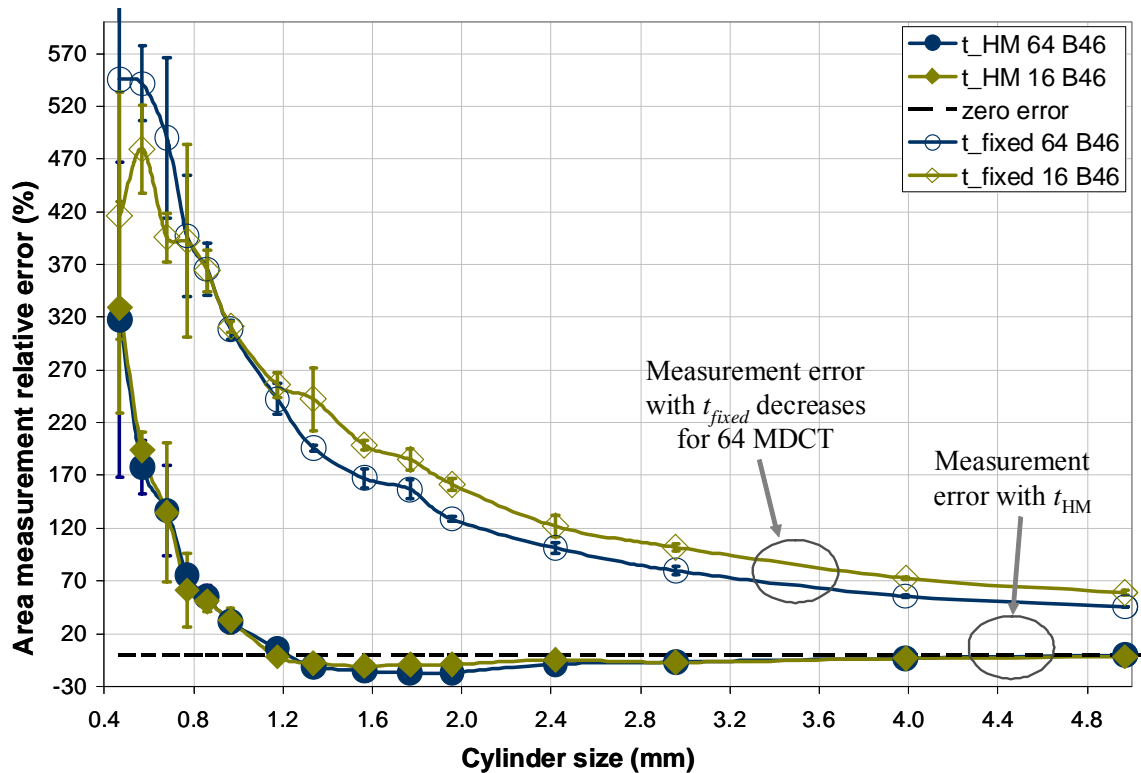


**Figure 3.10.** Area measurement relative error with  $t_{HM}$  and  $t_{fixed}$  for the 16 and 64 MDCT systems, when using the “HR” protocol and kernel B46. Error bars are predominantly smaller than the symbol size for objects larger than  $\sim 1.0$  mm.

Volume measurement relative errors with  $t_{HM}$  are statistically the same for the 16 and 64 MDCT systems. When using  $t_{fixed}$ , relative errors strongly increase along the whole range of sizes, and differences between the two systems become statistically significant in the range of sizes larger than  $\sim 1.2$  mm (see in Fig. 3.11 that volume measurement relative error is significantly larger for the 16 MDCT). It must be noted that with  $t_{HM}$  the mean of the volume measurement relative error for objects  $< 1.0$  mm is lower for the 64 MDCT compared with the 16 MDCT (e.g., the relative overestimation of the 0.5, 0.6, and 0.7 mm cylinders are reduced by 53%, 95% and 60%, respectively). However, due to the large standard deviations of the measurements in this range, the differences between the two systems are not statistically significant.

For both systems, volume measurement relative errors with  $t_{HM}$  in the region of overestimation drastically decrease with increasing object size (e.g., for the 64 MDCT, it is reduced from  $\sim 320\%$  to less than 5% when increasing the cylinder size from 0.5 mm to more than 1.0 mm). However, the volume relative errors increase again in the range between  $\sim 1.0$  mm and 4.0 mm due to measurement underestimation (it is up to  $-30\%$  for both scanners when using the kernel B46).

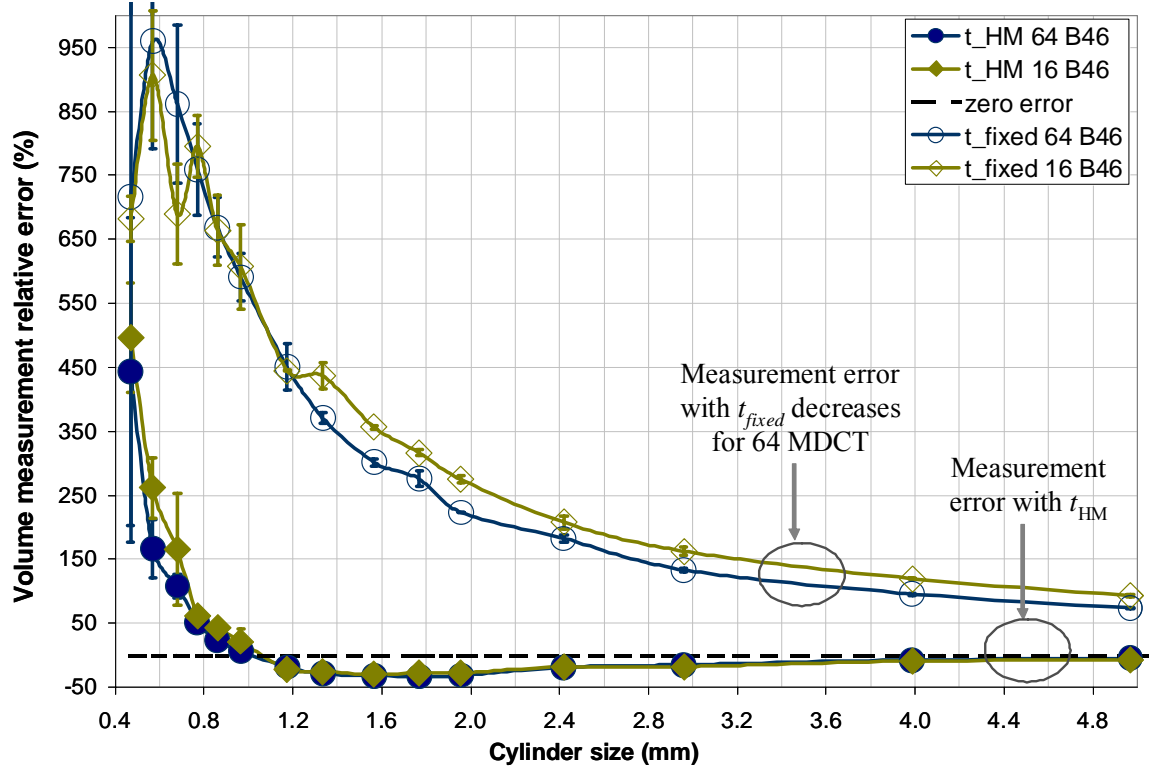


**Figure 3.11.** Volume measurement relative error with  $t_{HM}$  and  $t_{fixed}$  for the 16 and 64 MDCT systems, when using the “HR” protocol and kernel B46.

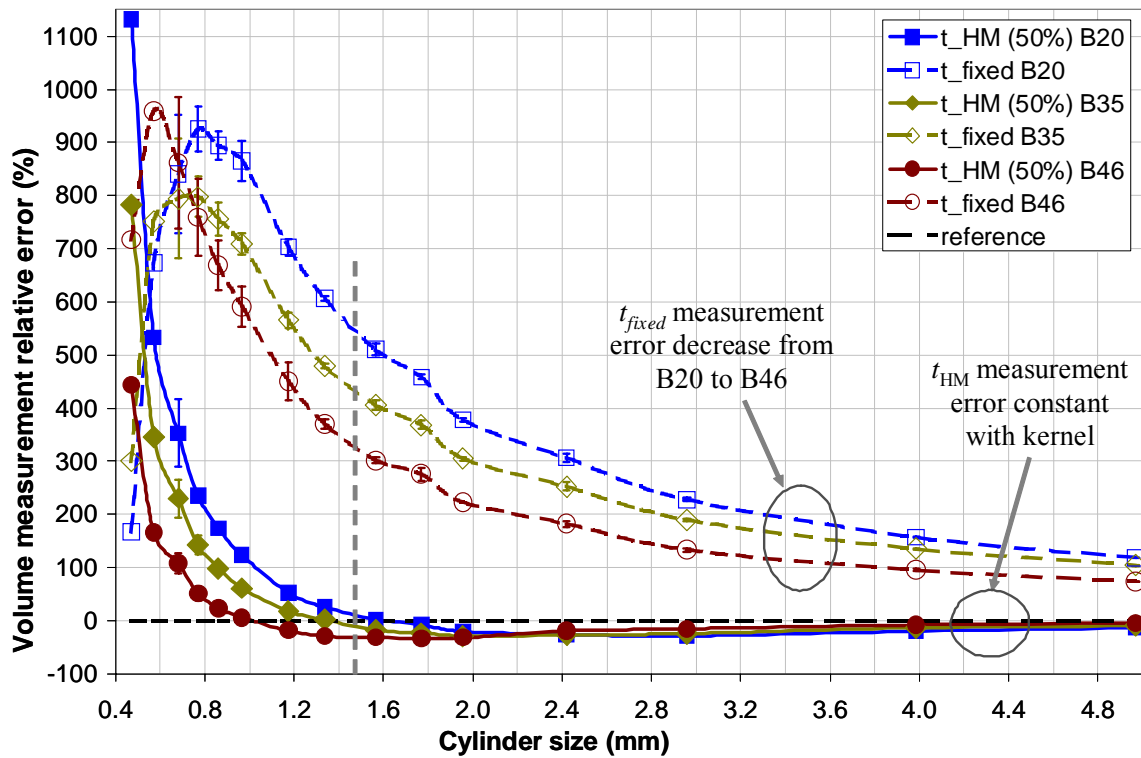
### • Measurement variability with the convolution kernel

Fig. 3.12 shows the variability of the volume measurement with the convolution kernel for  $t_{HM}$  and  $t_{fixed}$ . The results are given for the 64 MDCT and three representative convolution kernels. When comparing Fig. 3.11 with Fig. 3.12 it can be observed that the



inter-scanner measurement differences between the 16 and 64 MDCT is noticeably smaller than the inter-protocol measurement differences of the systems themselves.

When comparing the influence of using sharper kernels on the measurement accuracy for  $t_{HM}$  and  $t_{fixed}$  it can be observed (see Fig. 3.12) that: *i)* In the range of sizes larger than  $\sim 1.5$  mm, size measurements with  $t_{HM}$  are accurate and statistically the same for all the kernels. However, with  $t_{fixed}$  measurement overestimation in this range is still large, and strongly depends on the kernel; *ii)* In the range of sizes smaller than  $\sim 1.5$  mm, measurement relative overestimation with both  $t_{HM}$  and  $t_{fixed}$  increases strongly with decreasing object size, and varies significantly with the sharpness of the kernel. When using  $t_{HM}$  the effect of increasing the kernel sharpness results in a consistent reduction of the measurement overestimation. However, when using  $t_{fixed}$  this effect is inverted for the range of sizes smaller than  $\sim 0.8$  mm, where, after reaching a maximum in the volume measurement relative error, the values of the measurements drop more strongly for a smoothing than for a sharpening kernel. Moreover, the maximum volume measurement relative error (met around a size of 0.8 mm) is higher for sharpening than for smoothing kernels. Therefore, measurement accuracy of very small objects with  $t_{fixed}$  is very irregular and does not consistently improve when increasing the sharpness of the kernel.



**Figure 3.12.** Volume measurement relative error with  $t_{HM}$  and  $t_{fixed}$  for the 64 MDCT, when using the “HR” protocol and three representative kernels (B20, B35, and B46). This graph shows the influence of the convolution kernel on the volume measurement when two different quantification methods are applied.

### 3.3.2 Results for the “Heart View” protocol

We found that the image noise obtained for the “Heart View” protocol was significantly larger compared with the “HR” protocol ( $11.7 \pm 0.7$  HU versus  $7.0 \pm 0.2$  HU for the 16 MDCT when using the kernel B20), despite the fact that the data was acquired with a much higher X-ray intensity (700 versus 300 mAs). This is due to both the lower sampling of the projection data that is obtained when using the ECG-gated reconstruction, and the lower number of projections used to reconstruct the image.

When comparing the “HR” and “Heart View” protocols for one of the MDCT systems (i.e., either the 16 or the 64 MDCT), we found that the measurements of the object attenuation values and object sizes are statistically the same. Fig. 3.13 compares the measurement accuracy along the CT z-axis (length measurements) obtained for the 16 MDCT scanner when applying the “HR” and the “Heart View” protocols. For the two smallest cylinder sizes, measurement error is noticeably larger for the “Heart View” than for the “HR” protocol, probably due to its larger image noise.

When comparing the 16 and 64 MDCT scanners when applying the “Heart View” protocols, we found that object attenuation value and object size measurements are statistically the same. However, for all the measurements, standard deviations obtained for the 16 MDCT are larger than those obtained for the 64 MDCT. Fig. 3.14 shows the length measurements obtained for these two systems when using the “Heart View” protocol. It can be observed that the differences in measurement accuracy between the two scanners are negligible when applying the same reconstruction  $S_{eff}$ .

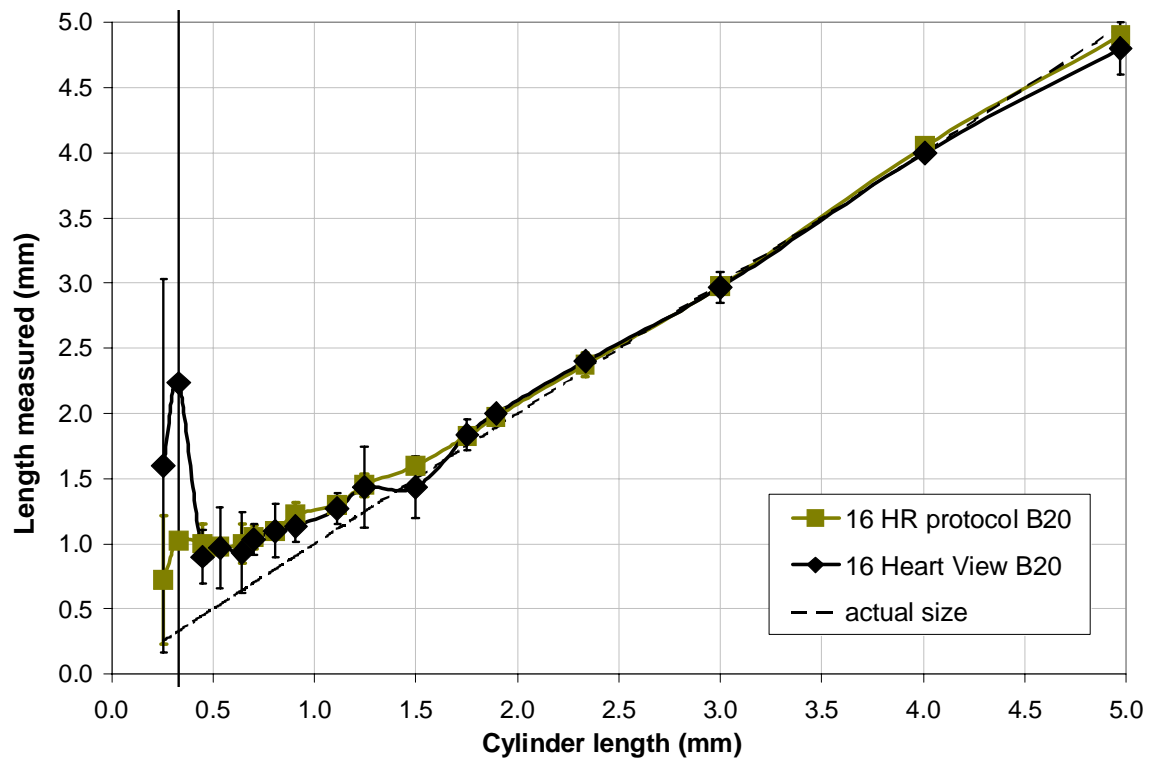


**Figure 3.13.** Length measurement with  $t_{HM}$  for the 16 MDCT system when using the “HR” and the “Heart View” protocol.

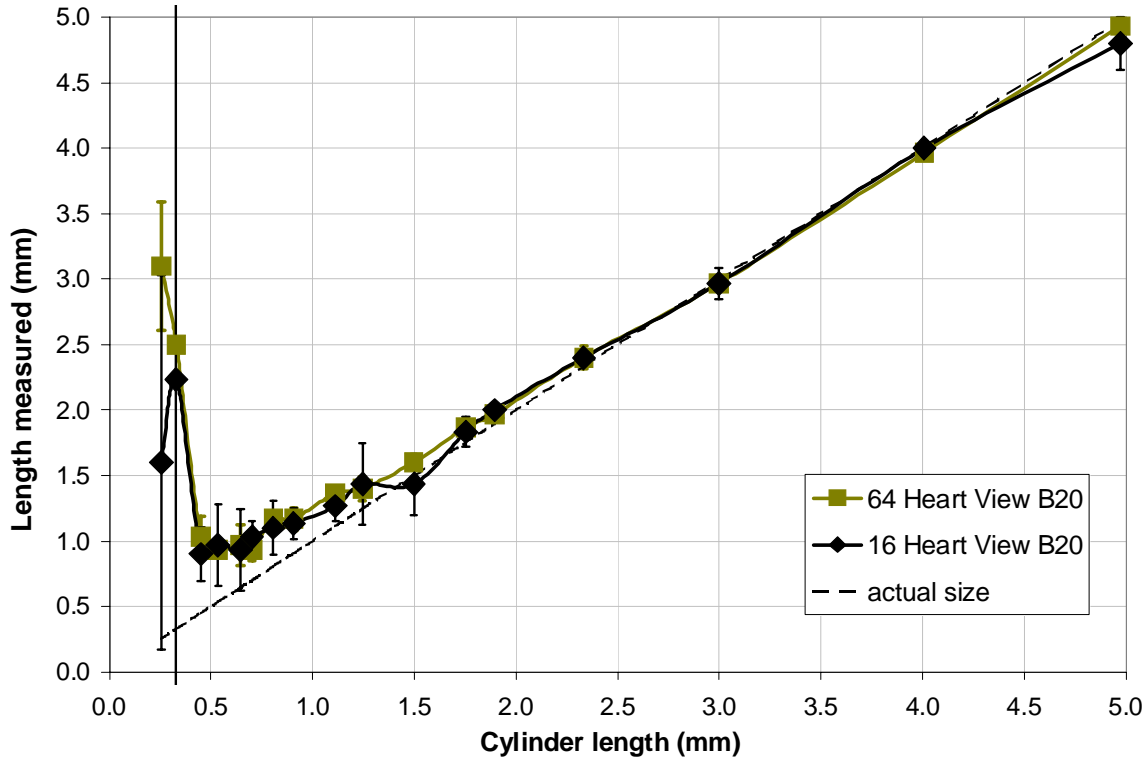


**Figure 3.14.** Length measurement with  $t_{HM}$  for the 16 and 64 MDCT systems, when using the “Heart View” protocol.

### 3.4. Discussion

The present study compares the accuracy that can be achieved with two consecutive generations of CT scanners, i.e. the 16 and 64 MDCT systems, when measuring the object attenuation value and size, for high-density objects whose sizes are near and under the spatial resolution of the system. For this purpose, a custom made phantom with aluminum cylinders of diameters and lengths ranging from 0.3 to 5.0 mm was imaged. The scans were carried out using high-resolution parameter-settings specific for each of the CT systems, while varying the convolution kernel. Automated 3D image quantitative analyses based on two different thresholding methods, i.e. a fixed threshold and the 50% relative threshold, were used to measure the diameter, length, area, and volume of the cylinders.

The results indicate that at similar radiation doses (i.e., 23.40 mGy for the 16 MDCT, and 23.09 mGy for the 64 MDCT) image noise is significantly larger for the 64 than for the 16 MDCT, which is in agreement with the results of Seifarth *et al.*<sup>31</sup> The difference in image noise between the two systems increases when using sharper convolution kernels. The larger image noise of the 64 MDCT yields a lower intra-scanner object signal measurement reproducibility compared with the 16 MDCT. When sharpening kernels are applied, the object signal in the range of sizes <2.0-2.5 mm is

significantly higher for the 64 MDCT due to its smaller  $z$ -PSF. However, for all the reconstruction kernels, the object SNR is significantly higher for the 16 MDCT due to its lower image noise. For objects larger than 2.0-2.5 mm, the object signal becomes approximately constant with the object size and reaches similar values for the 16 and 64 MDCT systems.

Differences between the diameter/length measurements with the 10% and the 50% relative thresholds were computed to estimate the object spread along the transverse and longitudinal directions. We found that the object spread is reduced, although not significantly, for the 64 MDCT compared with the 16 MDCT. The differences between the two systems in object spread are on average: 0.05 mm in the  $xy$ -plane; and 0.18 mm in the  $z$ -axis. This decrease in the  $z$ -object spread of the 64 MDCT positively influences the visualization of low-density structures surrounding high-density objects and allows better resolution of near objects.<sup>31-34</sup>

The intra-scanner reproducibility of geometric measurements, both in the  $xy$ -plane and along the  $z$ -axis, was slightly higher for the 64 than for the 16 MDCT, probably due to the smaller slice collimation and the overlapping acquisition of projection data of the 64 MDCT.

From the quantitative analyses with the 50% relative threshold, we found that in the range of sizes smaller than 2.0-2.5 mm, the mean values of the length and volume measurements are closer to the actual values for the 64 than for the 16 MDCT. However, the differences between the two scanners are not statistically significant because the measurement standard deviations of objects <2.0-2.5 mm are very large for both systems. Measurements in the transverse plane (i.e. diameter and area) are very similar for the two scanners. However, the functions of the diameter and area measurements versus the actual cylinder diameters and areas are more linear for the 64 than for the 16 MDCT, especially when applying sharpening kernels. For objects larger than 2.0-2.5 mm, the mean values and the standard deviations of all the measurements (i.e., diameter, length, area, and volume) are almost the same for the two systems. In this range, geometric measurements are accurate for both systems; with relative errors smaller than 5% for the diameter, 1% for the length, 10% for the area, and 30% for the volume. These results are consistent with previous studies,<sup>9,10</sup> in which experimental and simulated data showed that the object attenuation and size can be accurately measured (relative errors <5%) for objects larger than twice the full-width-at-half-maximum (FWHM) of the system PSF. Therefore, when using the 50% relative threshold, differences between object measurements for different MDCT scanner generations can only be expected in the range of objects smaller than twice the FWHM of the PSF of the lowest spatial resolution scanner, where signal intensity begins to be increasingly underestimated and size increasingly overestimated with decreasing object size.<sup>9,10</sup>

From the quantitative analyses with a fixed-threshold we found that differences between the two systems are not statistically significant for the diameter and length measurements. However, these differences become statistically significant for the area and volume measurements of objects larger than ~1.5 mm. This indicates that the different spatial resolution of these two systems could significantly affect size measurements depending on the method selected for quantification.

When using the 50% relative threshold the measurement error decreases when increasing the kernel sharpness, and the variation of the measurement accuracy with the

object size can be predicted quite well from the image PSF.<sup>9-11</sup> For the MDCT systems here evaluated, measurement accuracy with the 50% relative threshold is very high in the region of objects larger than ~2.0-2.5 mm in the three directions of space, and this accuracy does not depend on the scanning system and imaging protocol (when selecting parameter settings that are compatible with high-resolution applications). On the other hand, when using a fixed threshold, measurement accuracy depends not only on the object size and the image PSF, but also on the relationship between the object HU and the HU of the material surrounding the object being measured.<sup>17</sup> In addition, objects with signals lower than the fixed-threshold are missed in the quantification even if their SNRs are high enough so as to be discriminated from their surrounding tissue. Consequently, the determination of the optimal value for the fixed-threshold is restricted to very specific experimental conditions and a relatively small interval of density variability of the objects being measured.

It must be noted that the orientation of the object with respect to the longitudinal axis of the scanner would influence the diameter and length measurements, and consequently the area and volume measurements, when the PSF is not isotropic in the three directions of space (which is the case for the 64 MDCT, whose PSF is smaller in the z-axis than in the xy-plane<sup>9</sup>). Most small objects in the human body are not aligned with the z-axis of the scanner. For example, the orientation of coronary vessels changes continuously with respect to the CT plane, and multi-planar reformation is used to perform analysis of the lumen stenosis. To investigate the influence of the object orientation on the geometric measurements, we performed simulations based on the convolution of the PSF of the 64 MDCT when using the kernel B20 (for which the difference between the longitudinal and transverse resolutions is larger). The results show that the errors in diameter and length measurements for a cylinder not aligned within the CT z-axis are bound between the errors in the diameter (maximum error) and length (minimum error) measurements found when the cylinder is parallel to the z-axis.

The comparison of the size measurements obtained for these two quantification methods clearly indicate that the 50% relative threshold is more accurate and consistent than the fixed-threshold. However, it must be noted that the HU gradients between human high-density structures, such as small bones and calcifications, and their surrounding tissues (blood, muscle, fat, etc.) are typically lower than the HU gradients between the aluminum cylinders and the PMMA material. This implies that for objects larger than 2.0-2.5 mm (whose signals are not affected by PVE), the fixed threshold used in this study (which represents the standard 130 HU for a non enhanced vessel) would generally be closer to the 50% relative threshold than it is for the aluminum cylinders, and consequently size measurements for objects larger than ~1.0 mm would be slightly less overestimated than they are in this study.

The measurement accuracy found for the 16 and 64 MDCT when applying a high-resolution coronary protocol (in which ECG-gated 180°LI reconstruction is used) are not significantly different from the results found for a high-resolution non-coronary protocol (where a 360°LI interpolation of continuously acquired data is used). Consequently, the differences in measurement accuracy between these two systems were also not statistically significant when using high-resolution coronary protocols and the 50% relative-threshold quantification. Despite increasing the tube current and reducing the

pitch value (from 0.45 to 0.25-0.2), the image noise obtained for the coronary protocol was larger compared with the high-resolution non-coronary protocol, probably due to the lower number of projection data used to reconstruct the image slice.

All the results presented in this study are obtained from in-rest CT images of small high-density structures. The influence of motion on the accuracy and reproducibility of the measurements should be subject to future investigation. For example, in clinical applications involving imaging of the heart, motion artifacts affect the visualization and quantification of small structures.<sup>15,32-35</sup> Therefore, for this type of applications (especially for patients with high heart rates and/or arrhythmia), the differences between the 16 and the 64 MDCT systems could be significant due to their different scanning speeds (with rotation times of 370 ms for the 16 MDCT, vs. 330 ms for the 64 MDCT).<sup>19,21,23,32-34</sup>

## **Conclusions**

The accuracy of the 16 and 64 MDCT systems in imaging in-rest small-high density structures was evaluated by means of phantom experiments. The results revealed that image noise is significantly higher for the 64 than for the 16 MDCT, independently of the convolution kernel. Consequently, object SNR is larger for the 16 than for the 64 MDCT.

In comparing the quantification with the 50% relative-threshold versus a fixed-threshold, we found that the 50% relative-threshold strongly reduces inter-scanner and inter-protocol measurement dependency and improves size measurement accuracy, especially for objects larger than ~2.0 mm.

Both with coronary and non-coronary high-resolution protocols, in-rest object size measurement accuracy with the 50% relative threshold is not significantly improved for the 64 MDCT compared with the 16 MDCT. However, the differences between these two systems are statistically significant when fixed-threshold based quantification is applied.

Object spread along the z-axis is decreased by ~0.18 mm on average for the 64 MDCT compared with the 16 MDCT. Consequently, the visualization of small high-density structures and their surrounding tissues may be improved for the 64 MDCT.

## References

1. Wexler L, Brundage B, Crouse J, *et al.* Coronary artery calcification: pathophysiology, epidemiology, imaging methods, and clinical implications. A statement for health professionals from the American Heart Association. Writing Group. *Circulation* 1996; 94:1175-1192.
2. Beadenkopf WG, Daoud AS, Love BM. Calcification in the Coronary Arteries and Its Relationship to Arteriosclerosis and Myocardial Infarction. *Am J Roentgenol Radium Ther Nucl Med* 1964; 92:865-871.
3. Schuhlen H, Kastrati A, Mehilli J, *et al.* Restenosis detected by routine angiographic follow-up and late mortality after coronary stent placement. *Am Heart J* 2004; 147:317-22.
4. Nieman K, Pattynama PM, Rensing BJ, *et al.* Evaluation of patients after coronary artery bypass surgery: CT angiographic assessment of grafts and coronary arteries. *Radiology* 2003; 229:749-756.
5. Gerber TC, Stratmann BP, Kuzo RS, *et al.* Effect of acquisition technique on radiation dose and image quality in multidetector row computed tomography coronary angiography with submillimeter collimation. *Invest Radiol* 2005;40(8):556-563.
6. Mathias K, Jager H, Hennigs S, *et al.* Endoluminal treatment of internal carotid artery stenosis. *World J Surg* 2001; 25:328-34; discussion 334-336.
7. El-Omar MM, Dangas G, Iakovou I, *et al.* Update on In-stent Restenosis. *Curr Interv Cardiol Rep* 2001; 3:296-305.
8. Kalender WA. Computed Tomography: fundamentals, system technology, image quality, applications. In: *Publicis MCD Verlag*, Munich, 2000.
9. Rollano-Hijarrubia E, Stokking R, van der Meer F, *et al.* Imaging of small high-density structures in CT: a phantom study. *Acad Radiol* 2006; 13(7):893-908.
10. Prevrhal S, Engelke K, Kalender WA. Accuracy limits for the determination of cortical width and density: the influence of object size and CT imaging parameters. *Phys Med Biol* 1999; 44:751-764.
11. Prevrhal S, Fox JC, Shepherd JA, *et al.* Accuracy of CT-based thickness measurement of thin structures: Modeling of limited spatial resolution in all three dimensions. *Med Phys* 2003; 30:1-8.

12. de Weert T, Ouhlous M, Zondervan PE, *et al.* In vitro characterization of atherosclerotic carotid plaque with multidetector computed tomography and histopathological correlation. *Eur Radiol* 2005; 15:1906-1914.
13. Yoon HC, Greaser LE, Mather R, *et al.* Coronary artery calcium: Alternate methods for accurate and reproducible quantitation. *Acad Radiol* 1997; 4:666-673.
14. Kaufman L, Mineyev M, Carlson J, *et al.* Coronary calcium scoring: modelling, predicting and correcting for the effect of CT scanner spatial resolution on Agatston and volume scores. *Phys Med Biol* 2003; 48:1423-1436.
15. Ulzheimer S, Kalender WA. Assessment of calcium scoring performance in cardiac computed tomography. *Eur Radiol* 2003; 13:484-497.
16. Carr JJ, Nelson JC, Wong ND, *et al.* Calcified coronary artery plaque measurement with cardiac CT in population-based studies: standardized protocol of Multi-Ethnic Study of Atherosclerosis (MESA) and Coronary Artery Risk Development in Young Adults (CARDIA) study. *Radiology* 2005; 234:35-43.
17. Muhlenbruch G, Wildberger JE, Koos R, *et al.* Coronary calcium scoring using 16-row multislice computed tomography: non-enhanced versus contrast-enhanced studies in vitro and in vivo. *Invest Radiol* 2005;40(3):148-154.
18. Muhlenbruch G, Thomas C, Wildberger JE, *et al.* Effect of varying slice thickness on coronary calcium scoring with multislice computed tomography in vitro and in vivo. *Invest Radiol* 2005; 40:695-699.
19. Leber AW, Knez A, von Ziegler F, *et al.* Quantification of obstructive and nonobstructive coronary lesions by 64-slice computed tomography: a comparative study with quantitative coronary angiography and intravascular ultrasound. *J Am Coll Cardiol* 2005; 46:147-154.
205. Flohr T, Stierstorfer K, Raupach R, *et al.* Performance evaluation of a 64-slice CT system with z-flying focal spot. *Rofo* 2004; 176:1803-1810.
21. Nikolaou K, Flohr T, Knez A, *et al.* Advances in cardiac CT imaging: 64-slice scanner. *Int J Cardiovasc Imaging* 2004; 20:535-540.
22. Polacin A, Kalender WA, Marchal G. Evaluation of section sensitivity profiles and image noise in spiral CT. *Radiology* 1992; 185:29-35.
23. Flohr T, Ohnesorge B. Heart rate adaptive optimization of spatial and temporal resolution for electrocardiogram-gated multislice spiral CT of the heart. *J Comput Assist Tomogr* 2001; 25:907-923.



24. Flohr T, Schaller S, Stadler A, *et al.* Fast image filters as an alternative approach to reconstruction kernel in computed tomography. In: Sonka M, Hanson KM, *Proceedings of SPIE: medical imaging 2001, image processing*. International Society for Optical Engineering 2001; 4322:924-933
25. Gonzalez R, Woods R. Digital Imaging Processing. In: *Prentice-Hall P*, New Jersey, 2003.
26. Schaller S, Wildberger JE, Raupach R, *et al.* Spatial domain filtering for fast modification of the tradeoff between image sharpness and pixel noise in computed tomography. *IEEE Trans Med Imaging* 2003; 22:846-853.
27. Wildberger JE, Mahnken AH, Flohr T, *et al.* Spatial domain image filtering in computed tomography: feasibility study in pulmonary embolism. *Eur Radiol* 2003; 13:717-723.
28. Agatston AS, Janowitz WR, Hildner FJ, *et al.* Quantification of Coronary-Artery Calcium Using Ultrafast Computed-Tomography. *J Am Coll Cardiol* 1990; 15:827-832.
29. Hong C, Bae KT, Pilgram TK. Coronary artery calcium: accuracy and reproducibility of measurements with multi-detector row CT--assessment of effects of different thresholds and quantification methods. *Radiology* 2003; 227:795-801.
30. Hoffmann J. Taschenbuch der Messtechnik, 2nd edn. Fachbuchverlag, Leipzig, 2000.
31. Seifarth H, Ozgun M, Raupach R, *et al.* 64- Versus 16-slice CT angiography for coronary artery stent assessment: in vitro experience. *Invest Radiol* 2006; 41:22-27.
32. Mollet NR, Cademartiri F, van Mieghem CA, *et al.* High-resolution spiral computed tomography coronary angiography in patients referred for diagnostic conventional coronary angiography. *Circulation* 2005; 112:2318-2323.
33. Leschka S, Alkadhi H, Plass A, *et al.* Accuracy of MSCT coronary angiography with 64-slice technology: first experience. *Eur Heart J* 2005; 26:1482-1487.
34. Raff GL, Gallagher MJ, O'Neill WW, *et al.* Diagnostic accuracy of noninvasive coronary angiography using 64-slice spiral computed tomography. *J Am Coll Cardiol* 2005; 46:552-557.
35. Fishman EK. Multidetector-row computed tomography to detect coronary artery disease: the importance of heart rate. *Eur Heart J Suppl* 2005; 7:G4-G12.



## Chapter 4

# Histogram-based Selective Deblurring to Improve Computed Tomography Imaging of Calcifications

Rollano-Hijarrubia E, Niessen WJ, Weinans H., van der Lugt A, Stokking R.

### Objectives

Computed Tomography (CT) imaging of small high-density structures, e.g. calcifications, is hampered by image blur. This study aims to deconvolve calcifications in the transverse and longitudinal directions, while avoiding noise amplification and edge-ringing artifacts in the surrounding low-density structures.

### Materials and Methods

A method referred to as *Histogram-based Selective Deblurring* (HiSD) has been developed to generate a restored image by combining the low-intensity (*i.e.* Hounsfield Units) information of the original image with the high-intensity information of the deconvolved image. HiSD is evaluated on phantom and in vitro atherosclerotic plaque CT images, by comparing both qualitatively and quantitatively the original and restored images with their corresponding reference micro-CT images.

### Results

HiSD reduces calcification blur in the transverse and longitudinal directions, without introducing noise and ringing-artifacts in the surrounding tissues. Calcification area and volume measurements are significantly improved in the restored images (reducing on average overestimation by 32% and 83%, respectively).

### Conclusions

HiSD significantly improves CT visualization and quantification of small high-density structures.

*This Chapter has been published in Investigative Radiology 2007; 42:8-22.*

## 4.1 Introduction

Atherosclerosis is one of the leading causes of death in the Western World.<sup>1</sup> The detection of the disease and the choice of treatment are typically based on imaging of the vessel, followed by visual analysis of the vessel and quantitative assessment of abnormalities such as stenoses and calcifications. The degree of arterial stenosis is a crucial factor for pre-surgical evaluation.<sup>2,3</sup> Coronary artery calcium scoring is increasingly being considered as an additional important factor, since the total amount of calcification may be used as a risk indicator for the progression, stabilization and/or regression of atherosclerosis.<sup>4-8</sup> In addition, assessing the morphological characteristics of atherosclerotic plaques may help to determine their vulnerability.

Over the last few years multislice spiral/helical computed tomography (MSCT) has undergone an enormous increase in its use for cardiovascular imaging, and for many anatomies it is rapidly becoming the established technique for minimally invasive imaging.<sup>8,9</sup> The advantages of MSCT in comparison with other tomographic imaging modalities are its higher temporal resolution, which minimizes motion artifacts, and its higher contrast resolution, which allows minimally invasive contrast-enhancing protocols. State-of-the-art MSCT allows volumetric images of the human body with a high, near isotropic, spatial resolution (in the range of 0.3-0.4 mm in the transverse and longitudinal directions).<sup>10</sup> The spatial and contrast resolution of the image depends on the scanner geometry and on the acquisition and reconstruction parameters.<sup>11-13</sup> The choice of these parameters influences the blur, noise and artifacts of the CT images. The image blur of a given system and imaging protocol can be estimated by measuring the three-dimensional (3D) point-spread function (PSF) of a bead image. For spiral CT systems, the PSF can be approximated by a 3D Gaussian function,<sup>14-21</sup> and the imaging process can be numerically simulated by convolving the true object with the PSF, and superimposing noise and artifacts.<sup>7</sup>

Atherosclerotic plaques consist of nodules of crystalline calcium, mainly hydroxyapatite, distributed among lipid cores and fibrous tissue.<sup>4-7</sup> These nodules ("calcifications") have various shapes: spherical, elliptical, laminar, etc., and their maximum length typically ranges from only a few hundred micrometers to more than half a centimeter. Frequently, several nodules are found very close to each other, forming what we refer to as "clusters" of calcifications. Due to the blur, small high-density structures, such as calcifications, are spread in the image over their actual size, hampering their accurate quantification and visualization.<sup>18-21</sup> Quantification of "clusters" of calcifications is especially affected by image blur, since various calcified nodules can be convolved together appearing as one big calcification. Other problems related to image blur are:<sup>18-21</sup> *i*) Visualization and quantification of small low-density structures surrounding high-density objects due to linear partial volume effect (PVE). For example, blurred calcifications may lead to lumen/soft-plaque underestimation; *ii*) Dependency of measurements with the threshold value (Hounsfield Units, HU) when a fixed-threshold based quantification method is applied; *iii*) Dependency of the visualization of high-density structures with the display contrast settings (window level and window width); and *iv*) A limited detection of small objects (especially when these do not extend along the entire slice collimation) due to insufficient signal-to-noise ratio (SNR).

Image blur can be reduced by applying digital deconvolution. Deconvolution techniques use the information of the image blur and noise to invert the imaging process and obtain the best estimate of the true object from its “degraded” image. As a result of the deconvolution, high-frequency components of the image are amplified, thereby reducing the blur of image edges. This especially improves the imaging of small objects (relative to the system PSF size), enhancing their signal and reducing their spread. Unfortunately, deconvolution also amplifies noise and artifacts in the original image and introduces edge-ringing artifacts,<sup>15-17,22-24</sup> which degrades the imaging of low-density structures. To avoid these negative side effects we have developed a method, referred to as Histogram-based Selective Deblurring (HiSD), which generates a restored image by combining the low-density voxel information of an original CT image with the high-density voxel information of the deconvolved version of the image.

The purpose of this study is to investigate the potential of HiSD to allow a relatively strong 3D deconvolution of the small high-density objects of the image, while avoiding noise amplification and edge-ringing artifacts on the surrounding low-density structures. In this work we focus on selective deblurring of calcifications in atherosclerotic plaques. Hereto, HiSD is applied on several CT phantom images and images of in vitro specimens from carotid artery stenotic lesions. Qualitative and quantitative analyses are carried out on the original and restored CT images in order to evaluate the performance of HiSD. Micro-CT images of the in vitro plaques are used as a high-resolution reference for the plaque morphology. Several factors are considered to assess image quality of the restored data, i.e.: image blur and SNR of different sized calcifications; low-density visualization; and errors in the calcification area and volume measurements for different quantification thresholds.

Finally, the method is applied to a number of patient images to illustrate the potential of HiSD to improve vessel lumen segmentation and quantification in the presence of high-density structures such as calcifications, bones and stents.

## **4.2 Materials and Methods**

### **4.2.1 Phantom description**

The “Small high-density structures” phantom<sup>19,25</sup> (Fig. 4.1) is used to evaluate the performance of our deblurring method on small high-density structures of various sizes. In the phantom, aluminum cylinders, with diameters and lengths ranging from 0.3 to 5.0 mm, are arranged parallel to the axis of a Polymethyl Methacrylate (PMMA) cylinder 10 mm in diameter, which represents a mildly enhanced lumen.

The PMMA phantom was scanned in a cylindrical module of water, 16 cm in diameter, using a relatively low tube current (i.e. 300 mAs) to achieve a realistic attenuation environment. The phantom scan was repeated three times to assess inter-scan variability for the original and restored images. Independent restorations and quantifications were performed for each of the three scans.

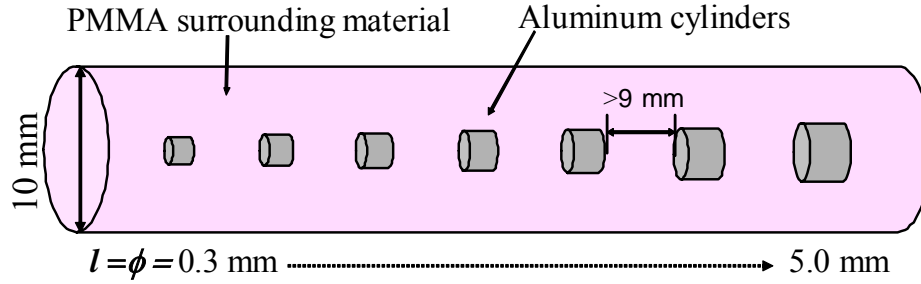


**Figure 4.1.** Schematic drawing of the "Small high-density structures" phantom. The PMMA cylindrical module embeds 17 small Aluminum (Al) cylinders with diameters and lengths ranging from 0.3 to 5.0 mm.

#### 4.2.2 *In vitro* samples

Six *in vitro* atherosclerotic plaques from stenotic carotid arteries are used to evaluate HiSD. The six plaques were scanned both with a MSCT and a  $\mu$ CT scanner. The plaques (Fig. 4.2) were categorized according to their total content of calcification: *Sample 1* to *Sample 6*, ranging from lightest to the heaviest calcified plaque. The samples were fixed using plastic holders to avoid movement between scans and to correlate the CT images with the  $\mu$ CT images. Because the attenuation values of water and soft-tissue are very similar (water is generally used as soft-tissue equivalent),<sup>14</sup> the samples were scanned in air to allow qualitative and quantitative assessment of the imaged soft-tissue plaque before and after HiSD.

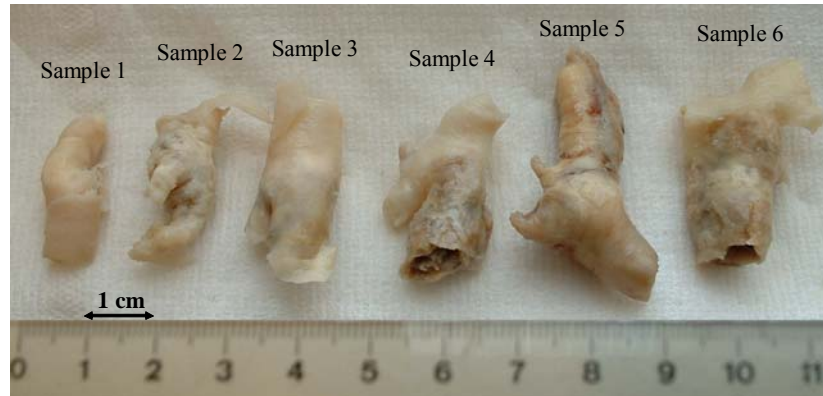


**Figure 4.2.** From left to right, the six atherosclerotic *in vitro* plaques used in this study are arranged in order of increasing calcium content.

#### 4.2.3 Multidetector row Spiral CT system (MSCT)

CT images were acquired with a 16-Slice MSCT system (*Somatom Sensation 16*; Siemens Medical Systems). All scans were performed using high-resolution parameter settings, i.e.; minimal values for the slice collimation ( $c=0.75$  mm), effective slice thickness ( $S_{eff}=0.75$  mm), pitch ( $P=0.45$ ), and field of view (FOV=50 mm); and a *reconstruction increment (RI)* smaller than a half of the slice collimation (i.e.  $RI=0.3$  mm, which provides an image overlap larger than 50% along the  $z$ -axis). An X-ray tube

voltage of 120 kVp and current of 249 mAs were used to acquire the data. A medium-sharp kernel B46f (Siemens Medical Solutions) was selected to reconstruct the phantom images. As the level of noise of the in vitro plaque images is lower than the noise of the phantom images, a medium-sharp kernel B50f (which is sharper than B46f) was selected to reconstruct the in vitro plaque images.

#### 4.2.4 Microfocus X-ray CT system

A Microfocus X-ray CT ( $\mu$ CT) system (*SkyScan-1172*, [www.skyscan.be](http://www.skyscan.be)) was used to acquire high-resolution images of the atherosclerotic plaques. Previous research has shown that  $\mu$ CT analysis of the coronary artery wall is feasible, and that it provides quantitative information about plaque morphology equivalent to that achieved with histomorphometric analysis.<sup>26,27</sup>  $\mu$ CT has several notable advantages compared with histology: first,  $\mu$ CT is a non destructive technique, and therefore does not alter the structural integrity of the plaque (histology preparation typically produces fragmentation, deformation and/or shrinkage of tissue components of the plaque).<sup>28</sup> Second,  $\mu$ CT provides a 3D high-resolution reference for the CT image, since  $\mu$ CT can achieve a resolution of up to  $2\mu$ , which is much higher than current MSCT scanners, and the interpretation of the image intensity information is the same as in CT.

In vitro plaque image data were acquired with 80 kVp and 100  $\mu$ A;  $1.125^\circ$  of rotation step; and a FOV smaller than 18.6 mm (yielding an acquisition voxel size smaller than  $18\mu$  in each direction of space).  $\mu$ CT images were reconstructed using the Feldkamp algorithm (for cone-beam volumetric reconstruction), and standard corrections for ring artifacts and beam hardening effects.

#### 4.2.5 Histogram-Based Selective Deblurring (HiSD)

HiSD is a newly developed method that generates a restored image by combining the low-intensity (HU) voxel information of a CT volume image with the high-intensity voxel information of the deconvolved image of the original CT volume. The 3D deconvolution of the original CT image is achieved using the Wiener Filter. The construction of the Wiener Filter requires the determination of the 3D PSF, which is system and imaging protocol dependent.

- **Determination of the 3D PSF**

Tungsten beads of 0.28 mm in diameter (Catphan CTP591 Bead Geometry Module, from The Phantom Laboratory [www.phantomlab.com](http://www.phantomlab.com)), placed approximately in the center of the FOV, were scanned. The intensity profiles across the center of the beads were measured along the  $x$ -,  $y$ - and  $z$ -axes, and fitted with a 1D Gaussian function. The standard deviations resulting from the Gaussian fit were corrected by the actual size of the Tungsten beads to obtain the standard deviations (i.e.,  $\sigma_x$ ,  $\sigma_y$  and  $\sigma_z$ ) of the PSF.<sup>29</sup> The operation was performed for three different Tungsten beads to estimate the mean values and errors of  $\sigma_x$ ,  $\sigma_y$  and  $\sigma_z$ , used to deconvolve the images. Note that the PSF has to be estimated only once for a specific CT system and imaging protocol.

### • Deconvolution of the original CT image

The original CT volumes of the phantom and the six in vitro atherosclerotic plaques were deconvolved by applying the plug-in *DeconvolutionJ* of *ImageJ* (<http://rsb.info.nih.gov/ij/>). *DeconvolutionJ* implements 3D deconvolution by multiplying in the frequency domain the Fourier transform of the original image by the regularized Wiener Filter,<sup>22</sup>  $W(\vec{\nu})$ , which has the following expression:

$$W(\vec{\nu}) = \left[ \frac{H^*(\vec{\nu})}{|H(\vec{\nu})|^2 + \gamma} \right] \quad (1)$$

Where  $H^*(\vec{\nu})$  is the complex conjugate of the Modulate Transfer Function (i.e., the Fourier transform of the PSF); and  $\gamma$  is a constant that depends on the SNR of the image. The constant  $\gamma$  controls the strength of the deconvolution and may be tuned based on the degree of image smoothing that is desired.<sup>23,30</sup> Note that if  $\gamma=0$ ,  $W(\vec{\nu})$  turns into the unconstrained inverse filter.

Wiener filter deconvolution can only be applied for images with a linear, space-invariant blur and with additive, uncorrelated noise. In spiral CT, these conditions are not fully met:<sup>10,29,31</sup> the spatial resolution is not completely isotropic due to the cone-beam acquisition; and noise and artifacts increase in regions with highly attenuating objects (e.g. bones, stainless steel stents, etc.). However, for a relatively large region of interest (up to ~240 mm diameter) located at the center of the CT gantry, the PSF can be assumed approximately isotropic and space-invariant.<sup>14,15,17,29,31</sup>

The value of the  $\gamma$  parameter should be determined based on the application. In our case this implies a trade-off between image blur and SNR of small calcifications (see Results section).

### • Image restoration

Our image restoration can be divided in six steps, which are illustrated for one of the in vitro samples in Fig. 4.3. First, a 3D deconvolution of the original CT image is performed using the Wiener Filter. As observed in the deconvolved image of Fig. 4.3, a “strong” deconvolution (small values of  $\gamma$ ) improves the image quality of high-density small structures, but amplifies noise and artifacts and introduces edge-ringing artifacts. The underlying idea of the HiSD method is to use the deconvolved image in regions with high intensities, and the original image in the remainder of the image. In the second step, two thresholds, referred to as detection-threshold ( $t_d$ ) and edge-threshold ( $t_e$ ), are determined. Threshold  $t_d$  is used to detect calcified structures, i.e. to discriminate high-density structures from image noise and artifacts in the original and deconvolved images. Note that the value of the detection-threshold for the deconvolved image, which we refer to as  $t_d'$ , will be generally different from  $t_d$  because deconvolution changes the SNR of the image. Threshold  $t_e$  indicates the edges of the calcifications in the original image.

In the third step, calcified objects in the original image are segmented using 3D region growing from voxels with intensity larger than  $t_d$  until voxels with intensity equal



to  $t_e$ . These segmented volumes are used to generate a 3D binary mask (Mask(a) of Fig. 4.3). Within Mask(a) deconvolved calcifications are detected (with threshold  $t_d'$ ) and segmented until threshold  $t_e$ . Again, the segmented volumes are used to generate a 3D binary mask (Mask(b) of Fig. 4.3). In step 4, Mask(c) is generated by subtracting Mask(b) from Mask(a). Therefore, Mask(c) contains the region that was overshadowed with calcification blur, and is not longer classified as calcification owing to deconvolution. The restored image (step 5) is obtained by: filling the image voxels outside the Mask(a) with the HU values of the original CT image (which correspond to low-density structures); filling the image voxels inside Mask(b) with the values of the deconvolved image (which correspond to the high-density structures); and filling the image voxels inside Mask(c) with the mean HU of the neighboring low-density tissues ( $\mu_{st}$ ). The value of  $\mu_{st}$  (which is generally smaller than  $t_e$ , see Fig. 4.3) is automatically determined from the intensity histogram peak of the original image voxels that are reached when dilating the Mask(a). Finally (step 6), a narrow (one pixel width) Gaussian filter is locally applied to smooth the transition between the original soft-tissue HU values and the values estimated within Mask(c).

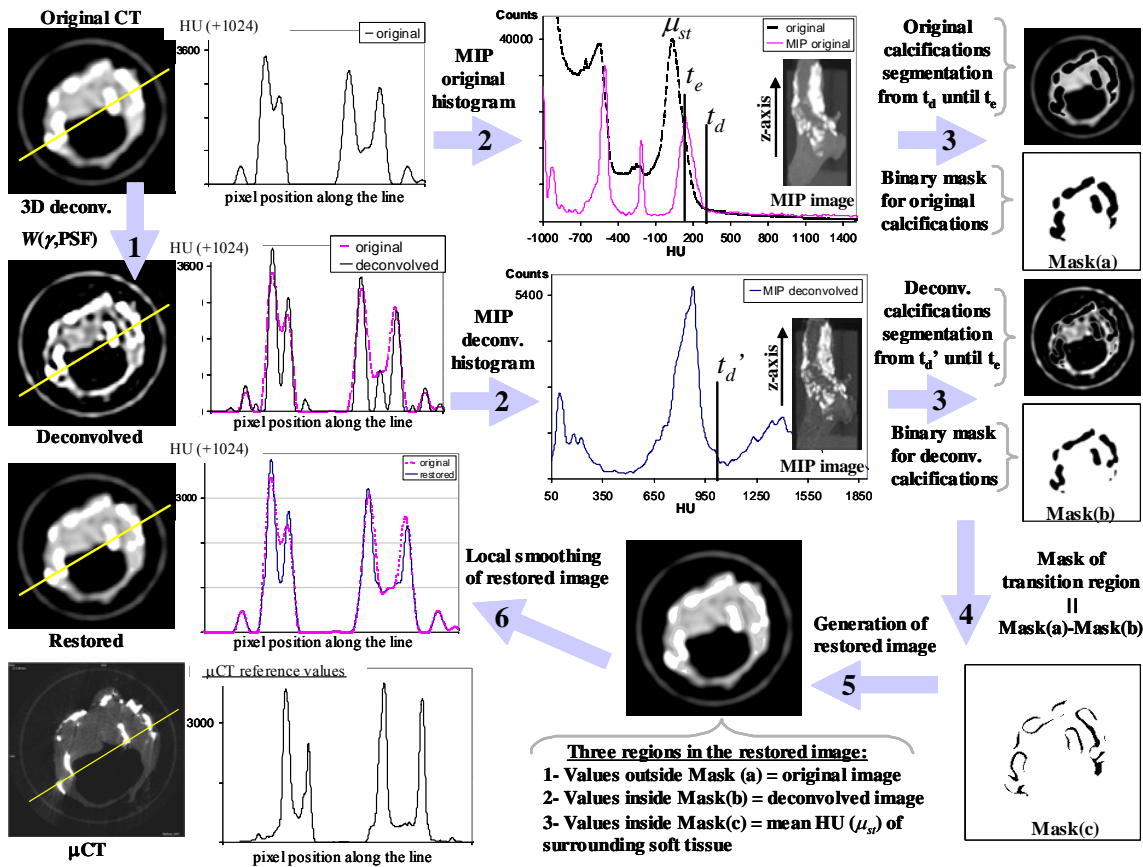


**Figure 4.3.** Flowchart illustrating the intermediate steps followed by HiSD to restore the image: 1) 3D deconvolution of the original image; 2) Determination of the segmentation thresholds ( $t_e$ ,  $t_d$ , and  $t_d'$ ) for the original and deconvolved images; 3) Generation of Mask(a) for original calcification volumes, and Mask(b) for deconvolved calcification volumes; 4) Generation of Mask(c) from the difference between original and deconvolved calcifications; 5) Generation of restored image by combining the original

HU (outside Mask(a)) with the deconvolved HU (inside Mask(b)), and estimating the HU within Mask(c); 6) Smoothing of the region of transition (Mask(c)) between original and deconvolved HU. All the steps are illustrated with images (19×19 mm) of *Sample 5*. The cross-sectional images show calcifications (high-intensity voxels), surrounded by soft-plaque (grey values), within a plastic holder (ring enclosing the plaque). From the comparison of the original CT image and the corresponding  $\mu$ CT image, it can be observed that calcifications in close proximity are convolved together, and small calcifications are overestimated due to image blur. After deconvolution (step 1) image blur is reduced, and calcifications are enhanced and spatially resolved from their adjacent objects. However, this is achieved at the expense of generating edge-ringing artifacts and amplifying noise, which degrades the imaging of low-contrast structures. See in the restored image that deconvolution noise and edge-ringing artifacts are avoided in the low-density tissues, while blur of the calcification peaks is reduced.

- **Determination of the thresholds  $t_d$  and  $t_e$**

The intensity histograms of the axial maximum intensity projection (MIP) of both the original and the “masked” deconvolved images are used to estimate the values of  $t_d$ ,  $t_d'$ , and  $t_e$ . We found that the direction of projection is not critical for the determination of the thresholds, but the number of counts in the soft-tissue histogram peak increases when selecting the direction of projection that displays a larger amount of this tissue. The MIP histogram (see step 2 of Fig. 4.3) contains intensities from calcifications (i.e. all voxels with HU larger than  $\sim 300$  HU), and a number of peaks that contain the highest intensities of the surrounding low-density tissues, i.e., mainly due to the positive component of noise and artifacts in these tissues. Therefore, when selecting for  $t_d$  the HU after the MIP histogram peak of the tissue surrounding calcifications, a good discrimination between the “true” high-density objects and noise and artifacts in the original and restored images is achieved, although very small calcifications may be missed due to insufficient SNR. The edge threshold,  $t_e$ , is estimated as the mean value of the MIP histogram peak of the tissue surrounding calcifications in the original image. This minimizes the propagation of segmented volumes outside the actual edges of calcifications.

#### 4.2.6 Evaluation of the image quality

In order to evaluate HiSD, qualitative and quantitative analyses were performed on the original, restored and  $\mu$ CT volume images for both the phantom and the six in vitro calcified plaques. For the qualitative evaluation we visually compared the restored images with the original and  $\mu$ CT images. We examined several aspects: artifacts introduced by HiSD; blur reduction in the  $xy$ -plane and  $z$ -direction; and missed “true” calcifications and/or introduced “false” calcifications in the restored images.

For the quantitative analysis we performed area and volume measurements using a quantification algorithm based on the calcification volume method.<sup>32</sup> Therefore, area/volume measurements were obtained by quantifying the number of voxels with HU over a certain threshold value, and multiplying this by the image pixel area/voxel volume. Hereto, eight different threshold values distributed between 130 HU (value generally used for calcium quantification)<sup>8,32-35</sup> and 476 HU were used. Since blur of a  $\mu$ CT system is negligible compared with the blur of a MSCT system, calcification quantification in the

$\mu$ CT images was performed for a unique threshold, which was set above the noise and artifact level in the soft-tissue of the  $\mu$ CT images.

For the area and volume quantification of the phantom aluminum cylinders, the mean absolute error,  $\Delta\bar{x}$ , of the estimated mean value of the three measurements obtained from the repeated scans,  $\bar{x}$ , was calculated as  $\Delta\bar{x} = t \frac{\sigma}{\sqrt{N}}$ , where  $\sigma$  is the standard deviation of the measurements ( $N$ ), and  $t$  is the so-called  $t$ -factor. The  $t$ -factor corrects for a small number of measurements, and for  $N=3$  and a probability  $p=95\%$  that a measurement falls within the interval  $[\bar{x} - \Delta\bar{x}, \bar{x} + \Delta\bar{x}]$ , the value of  $t$  is equal to 4.3.<sup>20</sup>

For the calcified plaque area measurements we selected 25 calcifications from the six in vitro plaques whose areas in the  $xy$ -plane were minimally affected by PVE in the  $z$ -direction. This requirement is important when comparing object areas in CT and  $\mu$ CT cross-sections because image slice widths are different. These 25 calcifications were classified into four different groups according to their reference  $\mu$ CT area: *i*) small calcifications ( $<1\text{mm}^2$ ); *ii*) medium calcifications ( $1\text{-}2\text{mm}^2$ ); *iii*) big calcifications ( $>2\text{mm}^2$ ); and *iv*) clusters of calcifications (defined as a group of two or more nearby calcifications that appear convolved in the original CT image). Quantification of the calcification clusters was carried out within a region of interest that enclosed the group of calcifications that appear convolved in the original image. For the in vitro calcified plaque volume analysis, the total volume of calcification was measured for each of the six in vitro samples.

To evaluate the influence of HiSD on soft-tissue quantification, we formulated the following hypothesis: as HiSD is designed to preserve the original low-density tissue HU values in the restored image, the difference in soft-tissue quantification between the original and restored image should correspond then to the decrease in calcification blur owing to deconvolution. To verify this, we first determined for the original and restored images the total volume of soft-tissue plaque with HU values in the range  $[\mu_{\text{st}} - 2\sigma_{\text{st}}, \mu_{\text{st}} + 2\sigma_{\text{st}}]$ , where  $\mu_{\text{st}}$  and  $\sigma_{\text{st}}$  are the mean and the standard deviation of the soft-tissue HU in the original image. Second, we determined the difference in calcification volume between the original and restored image, setting the quantification threshold at  $\mu_{\text{st}} + 2\sigma_{\text{st}}$  (HU). Then, we compared for each in vitro plaque the difference in soft-tissue plaque with the difference in calcification, before and after applying HiSD.

## Statistics

Quantification errors obtained in the original and restored images are compared with two-sample unequal variance Student's  $t$ -Test. A  $p$ -value  $<0.05$  is considered statistically significant.

## 4.3 Results

### 4.3.1 Input parameters for Wiener filter

The mean values of the standard deviations of three different bead images were determined for kernel B46f and B50f (Table 4.1) to construct the 3D Gaussian PSFs that were subsequently used for the Wiener filter deconvolution of the phantom and in vitro plaque CT original images.

Bead	$\sigma_x$ (mm)	$\sigma_y$ (mm)	$\sigma_z$ (mm)
1	0.363±0.001	0.358±0.002	0.367±0.002
2	0.366±0.002	0.365±0.004	0.367±0.001
3	0.364±0.001	0.362±0.001	0.367±0.002
Mean value	0.364±0.001	0.362±0.002	0.367±0.002

**Table 4.1.** Values of the standard deviation of the PSF in the three directions of space for the convolution kernel B50.

The optimum value of the  $\gamma$  parameter in the Wiener Filter was empirically determined based on the trade-off between several factors related with the image quality of the deconvolved image, i.e., the SNR, the blur, and resolution of near objects. To determine the  $\gamma$  value, we performed a number of experiments where the original images were deconvolved using different values of  $\gamma \in [0.5, 0.00005]$  (see Fig. 4.4). We found that for  $\gamma \geq 0.05$  ringing artifacts are small, but calcification blur is not effectively reduced. For  $\gamma < 0.001$  the calcification signal tends to decrease at the expense of increasing ringing artifacts. The best results are obtained for  $\gamma \in [0.01, 0.001]$ , where blur progressively decreases while calcification signal increases. As a trade-off, a  $\gamma = 0.005$  was selected for our study.

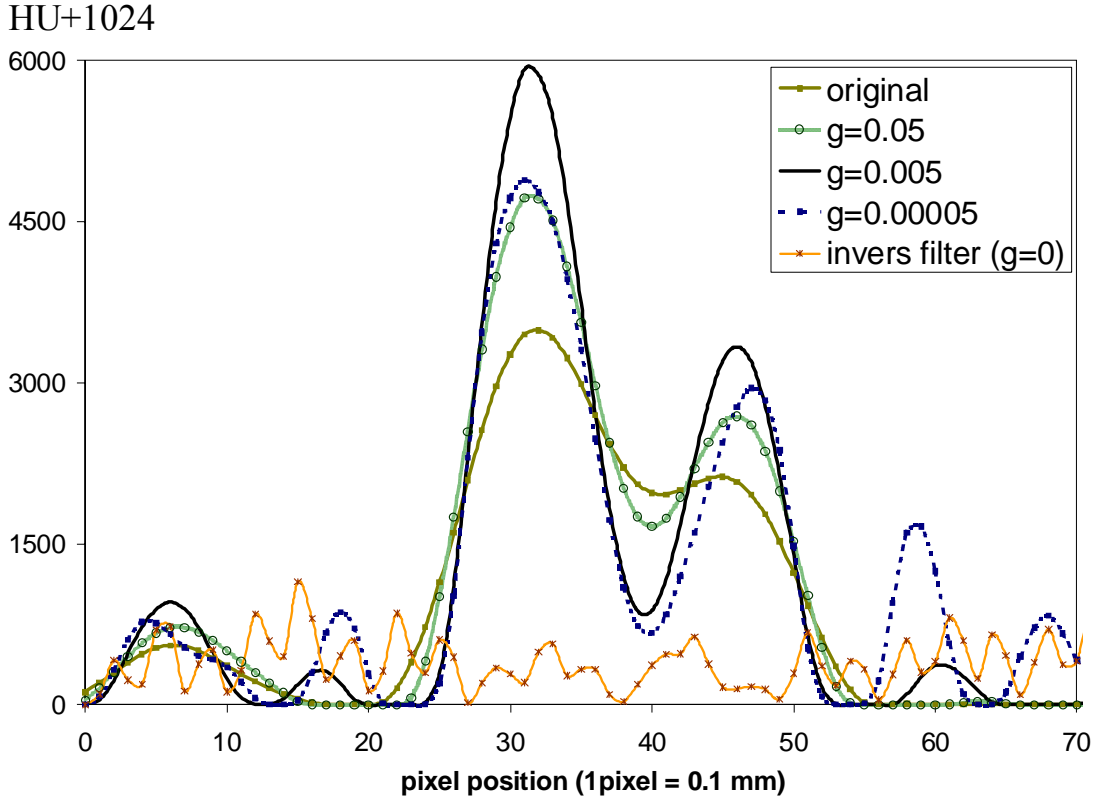


**Figure 4.4.** Intensity profiles along two nearby calcifications of the original CT image and of the images deconvolved with different values of  $\gamma$ . As the value of  $\gamma$  is reduced, the intensity of the peaks increases and the blur decreases. For values of  $\gamma < 0.001$ , the calcification signals progressively decreased at the expense of amplifying noise and edge-ringing artifacts. Finally, with  $\gamma=0$  (for which the Wiener filter turns into the inverse filter) the noise completely overwhelmed the signal.

### 4.3.2 Qualitative evaluation

Figures 4.5-4.7 show the result of HiSD on the phantom and in vitro plaque images. From the cross-sectional and MIP views of the phantom original images (Fig. 4.5) it can be observed that the image noise is not constant all along the whole image; noise and artifacts are larger in the slices intersecting the biggest aluminum cylinders (the noise standard deviation increases from 17 HU up to 47 HU in the regions intersecting the largest cylinders). The qualitative evaluation of the restored images of the phantom and the six in vitro samples reveals that with HiSD: *i*) Blur of high-density structures (calcifications) is reduced in the three directions of space; i.e. size overrepresentation is reduced and SNR is increased, thereby improving the visualization of calcifications; *ii*) The visualization of the low-density structures is not hampered by the noise amplification and edge-ringing artifacts of the deconvolution. Even under heterogeneous noise and metal artifact conditions, HiSD performs well (see phantom images in Fig. 4.5); *iii*) All high-density structures that can be clearly recognized in the original CT images, are segmented and replaced with their corresponding deconvolved structure in the restored images. (The only exceptions being two small calcifications of the in vitro samples –see

discussion later–); *iv*) As a result of the “masking” step and the use of the detection threshold  $t_d'$ , deconvolution artifacts that could potentially have been misclassified as calcifications are avoided in the restored images; *v*) Aluminum cylinders and calcifications in the restored images are surrounded by a small “halo”-like effect (see restored slices in Figures 4.5-4.7). This effect is due to the estimation of the HU in the region of transition between the deconvolved high-density structures and the original HU of the surrounding low-density tissues.

As mentioned above, two small calcifications are lost in the restored images. The reason for this is that in the deconvolved images these calcifications have intensities lower than the detection threshold,  $t_d$ , used to discriminate noise and artifacts. However, these calcifications are small (<1.0 mm in each direction of space) and their contribution to the total amount of calcification in the six in vitro plaques is less than 0.5%, which hardly affects the quantification accuracy. On the contrary, lowering the detection threshold could introduce spurious calcifications owing to deconvolution noise and ringing-artifacts, increasing thus overestimation of calcification measurements.

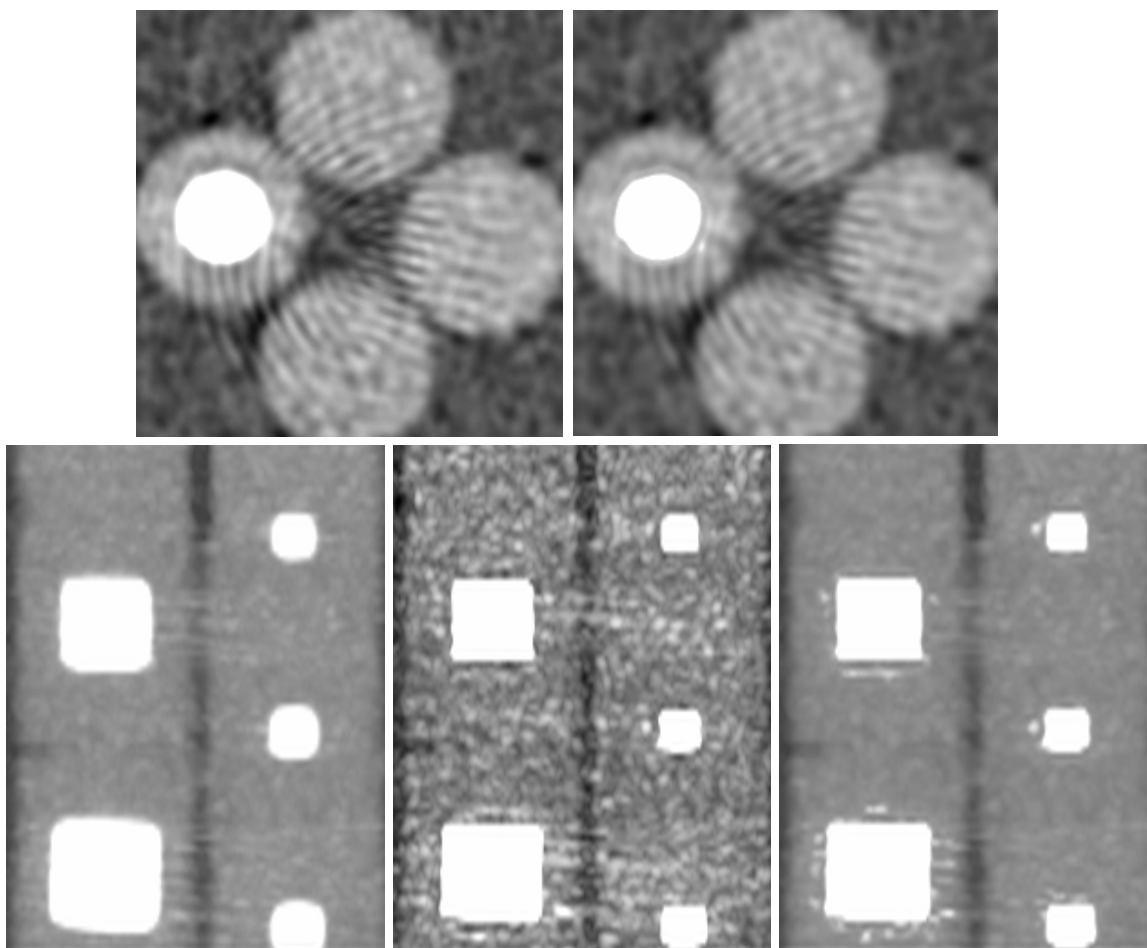


**Figure 4.5.** (Top) cross-sectional views of the original and restored images of the phantom, displayed with a contrast window of 380 HU, centered at 66 HU. (Bottom) axial MIPs of the original, deconvolved, and restored images of the phantom, displayed with a contrast window of 380 HU, centered at 126 HU.

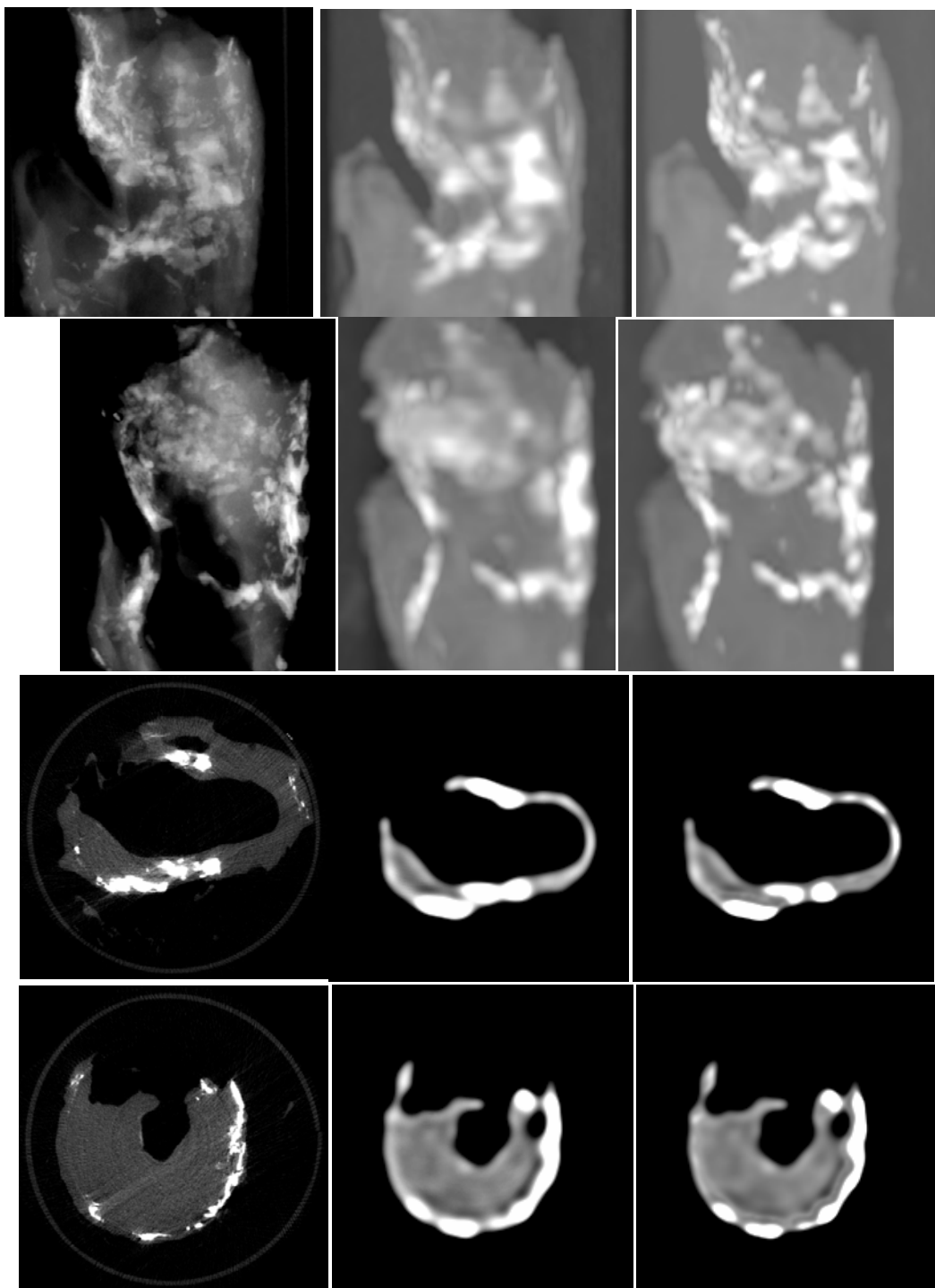


**Figure 4.6.** (From left to right)  $\mu$ CT image, and closest corresponding original and restored CT images of *Sample 4*. The two top frames show the results on axial MIP images taken for two different angles (image dimensions of first row: 18.6 mm  $\times$  18.6 mm; of second row: 14.2 mm  $\times$  18.2 mm, with an isotropic voxel size of 18  $\mu$ m for the  $\mu$ CT image, and 0.1 mm for the CT images). The middle and bottom frames show the results on two different cross-sectional images (17.9 mm  $\times$  17.8 mm), displayed with a contrast window of 1000 HU width, centered at -224 HU.

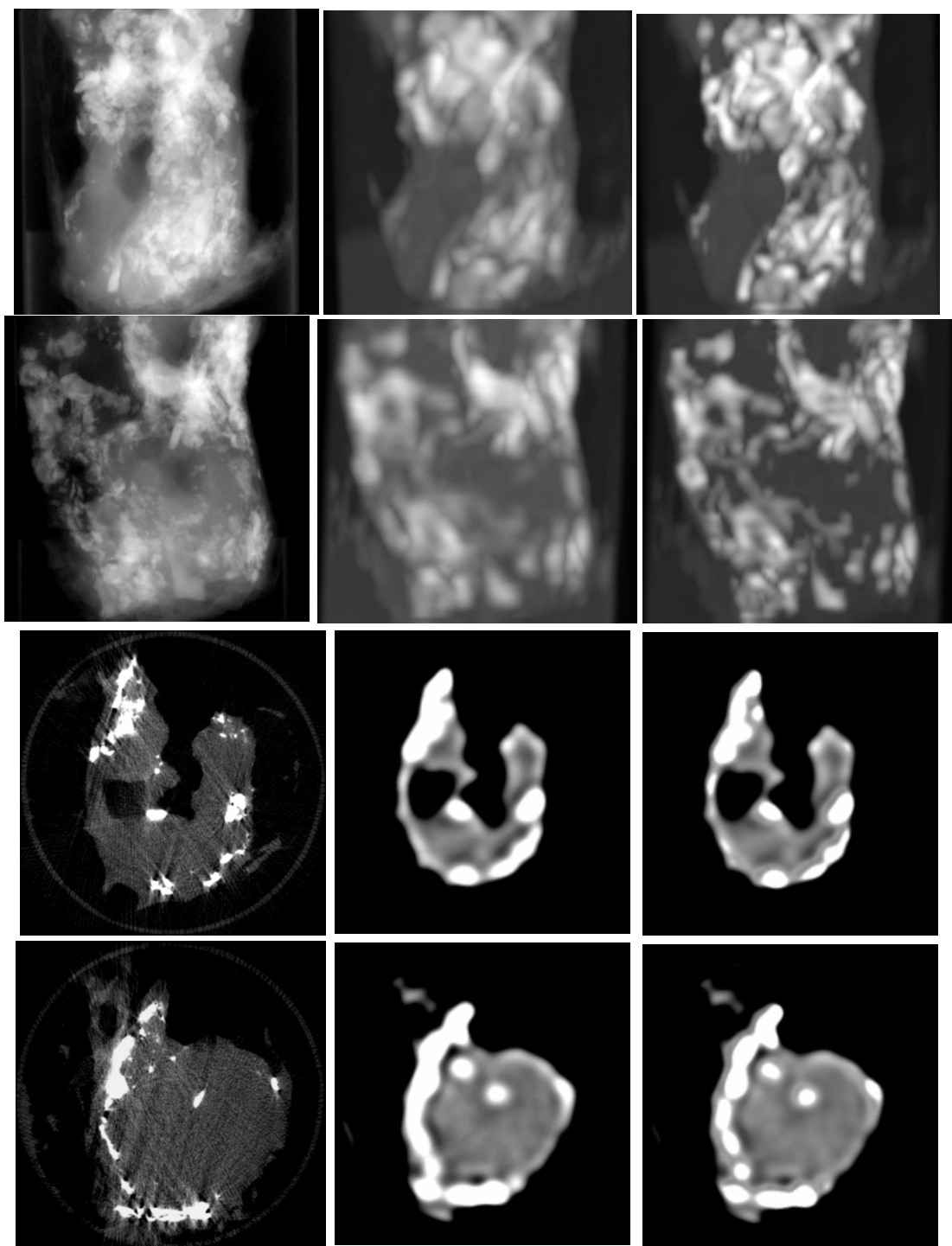


**Figure 4.7.** (From left to right)  $\mu$ CT image, and closest corresponding original and restored CT images of *Sample 6*. The two top frames show the results on axial MIP images taken for two different angles (image dimensions:  $18.6 \text{ mm} \times 18.6 \text{ mm}$ ; for both rows, with an isotropic voxel size of  $18 \text{ }\mu\text{m}$  for the  $\mu$ CT image, and  $0.1 \text{ mm}$  for the CT images). The middle and bottom frames show the results on two different cross-sectional images ( $17.2 \text{ mm} \times 17.1 \text{ mm}$ ), displayed with a contrast window of  $1000 \text{ HU}$  width, centered at  $-224 \text{ HU}$ .



### 4.3.3 Quantitative evaluation

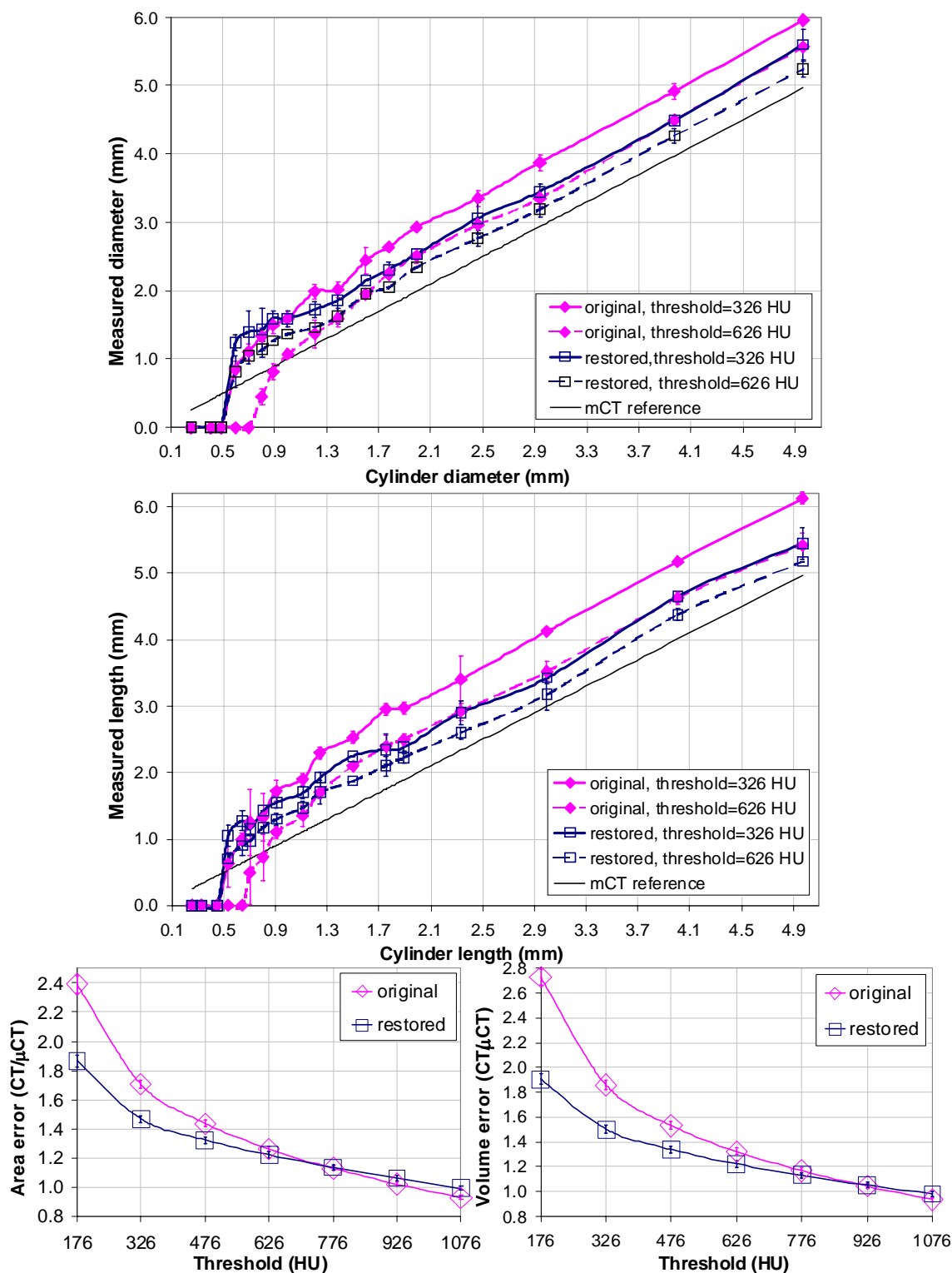
- **Phantom quantification**

Fig. 4.8 shows the measurements of cylinder diameter, length, error on the total cross-sectional area, and error on the total volume, for the original, restored and reference  $\mu$ CT images. It can be observed that size measurements in the restored images are less threshold dependent than in the original images. The diameter and length analyses show that the measurements of the smallest cylinders are more linear with the  $\mu$ CT reference for the restored than for the original image. Moreover, small objects' SNR increases after restoration, which enables to set the quantification threshold above the level of noise and artifacts without missing small objects. Note that measurement reproducibility (given by the error bar) is equal or higher for the restored compared with the original images.

- **In vitro plaque quantification**

#### Calcification area measurement

In Fig. 4.9 the calcification area measurement errors are given for different quantification thresholds. These errors have been averaged for each of the four groups in which the 25 calcifications are classified (see description in section 4.2.6). We found that for all the thresholds, except for the threshold of 130 HU, area measurement error is significantly lower for the restored images than for the original CT images. For the threshold of 130 HU measurement errors are similar for the original and restored images. This is due to the fact that for most of the samples this value is smaller than the threshold  $t_e$ , used to segment calcifications and to indicate the region where the original HU are replaced with the deconvolved values. It can be observed that measurement errors of both original and restored images decrease as the threshold value is increased (from 130 up to 476 HU). This is due to the decrease in the contribution of both calcification blur and noise in the surrounding tissues, which also leads to measurement overestimation. For the larger calcifications we found that above the threshold of 326 HU the restored areas tend to be underestimated. This is probably due to the fact that for big calcifications it is possible to appreciate HU differences due to density heterogeneity, noise and artifacts. These HU differences are enhanced by the deconvolution in the restored images, and consequently influence more strongly the results of the measurements when increasing the value of the quantification threshold. Therefore, to improve quantification it is convenient to select a threshold value higher than the positive fluctuations of noise and artifacts in the tissue surrounding the calcifications, but not too high in order to prevent missing small and/or mild-density calcifications. For our original and restored images, the threshold of 276 HU is larger than noise and artifacts. Therefore, for this threshold value, measurement overestimation is mainly due to calcification blur. This threshold was selected for presenting more detailed results. Fig. 4.10 compares the area measurement of the 25 calcifications obtained for the original and restored images when using the threshold of 276 HU. We found that the errors in the area measurement are significantly lower ( $P=0.001$ ) for the restored than for the original images (overestimation of original area measurements is reduced in the restored images by 31% on average). On the other hand, calcification peak HU values are considerably higher in the restored images than in the original images ( $\sim 1000$  HU on average).



**Figure 4.8.** Two top frames: diameter and length measurements obtained for the original, restored and  $\mu$ CT images. Two bottom frames: error on the area and volume measurements of the original and restored images (note that the error bars are smaller than the data markers).

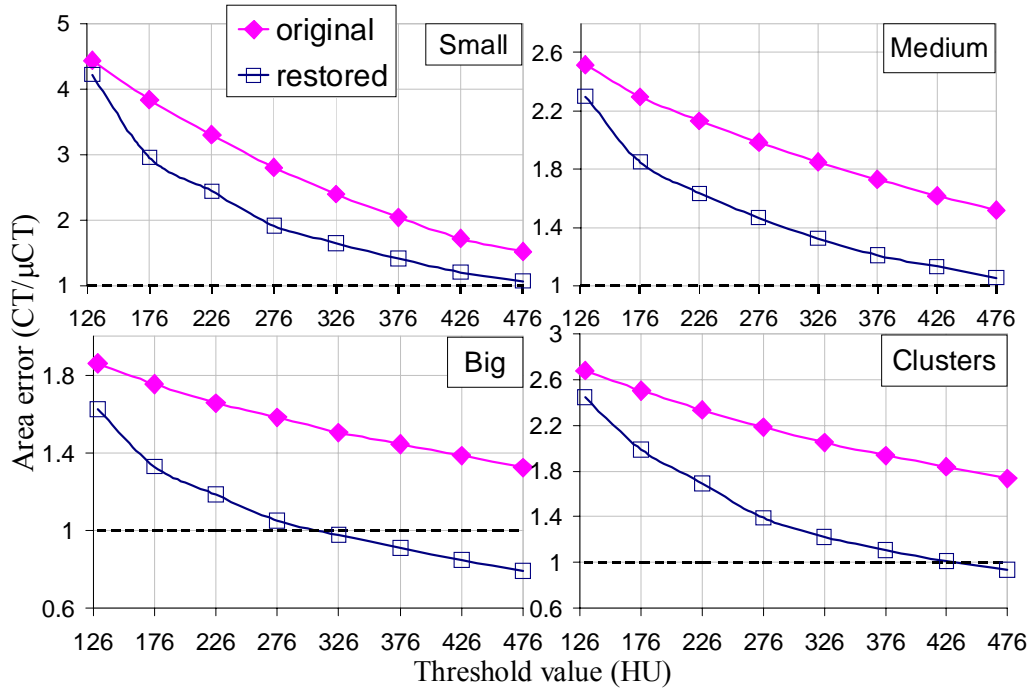


**Figure 4.9.** Error in the calcification area measurement (averaged for each calcification size interval) estimated for the original and restored images using eight different quantification threshold values ranging from 130 HU to 476 HU.

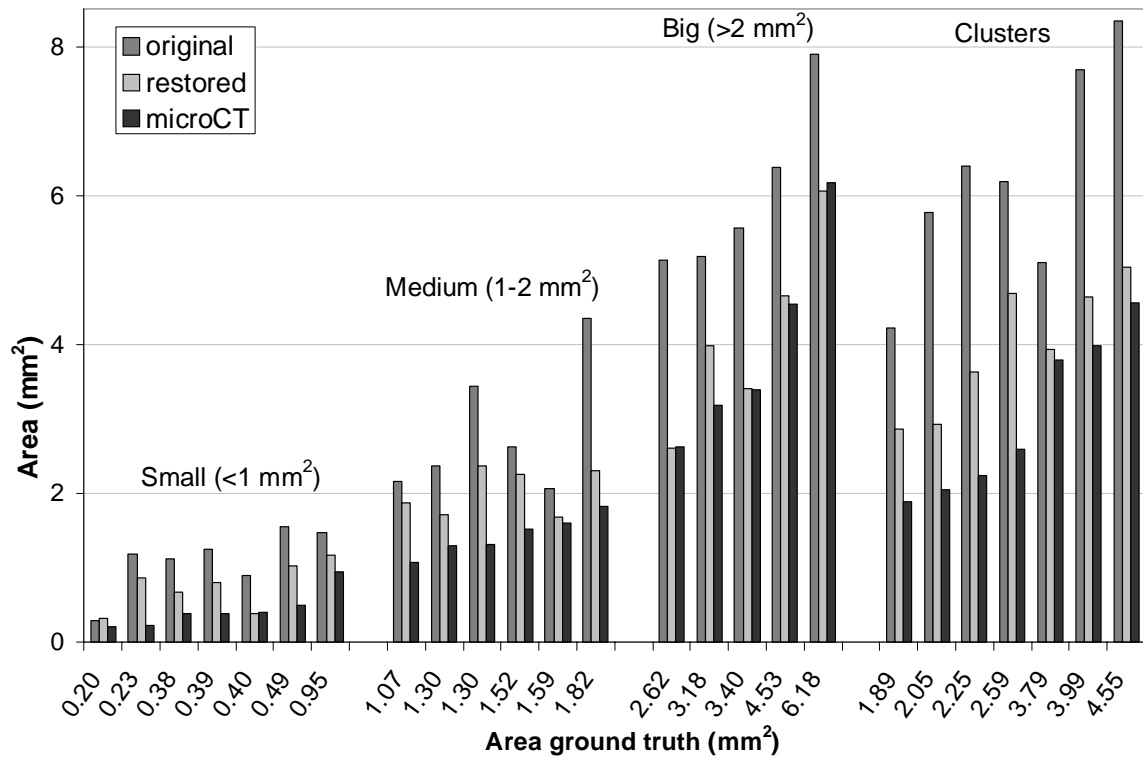


**Figure 4.10.** Area of 25 calcifications measured in the original images and restored images with the threshold of 276 HU, and compared with the reference  $\mu$ CT areas.

### Calcification volume measurement

The total volume of calcification contained in the atherosclerotic plaque was measured for the six in vitro samples. Fig. 4.11 shows the error on the total volume measurement for each of the in vitro samples as a function of the quantification threshold value. Again, measurement errors are noticeably smaller in the restored images independently of the threshold value. For threshold values larger than 176 HU and smaller than 476 HU, in-plaque calcification volume measurement error is significantly reduced for the restored images. It can be observed that volume measurement errors of both original and restored images strongly decrease with increasing threshold value. For the least calcified samples (*Sample 1* to *Sample 3*) the variation of the volume measurements with the threshold is larger than for the heaviest calcified samples (*Sample 4* to *Sample 6*). This is due to the fact that image noise affects more strongly the imaging of small calcifications, i.e. <1-2 mm, because in this range of sizes the SNR decreases.<sup>12</sup> When using a suitable quantification threshold (i.e., slightly larger than noise) image blur is the main cause of calcification size overestimation, and it can be observed (Fig. 4.11) that measurement overestimation is considerably lower for the restored than for the original CT images (i.e., for the threshold of 276 HU, overestimation of original volume measurements is reduced in the restored images by 44% on average). In the heaviest calcified plaque (*Sample 6*) volume measurements are underestimated for quantification thresholds larger than 326 HU. Therefore, for the restored images the lowest measurement errors are obtained with a quantification threshold value between 276 and 326 HU, whereas for the original images these are obtained with a quantification threshold of approximately 476 HU.

### Soft-tissue volume measurement

Fig. 4.12 relates the soft-tissue volume quantification of the original and restored images to the difference in their calcification volume. It can be observed that the increase in the soft-tissue volume of the restored plaques perfectly correlates with the decrease in their calcification volume due to the deblurring process. This indicates that the HU values estimated in the region surrounding calcifications (i.e., where the “halo” effect appears) deviate less than two standard deviations from the mean HU of the original soft-tissue.

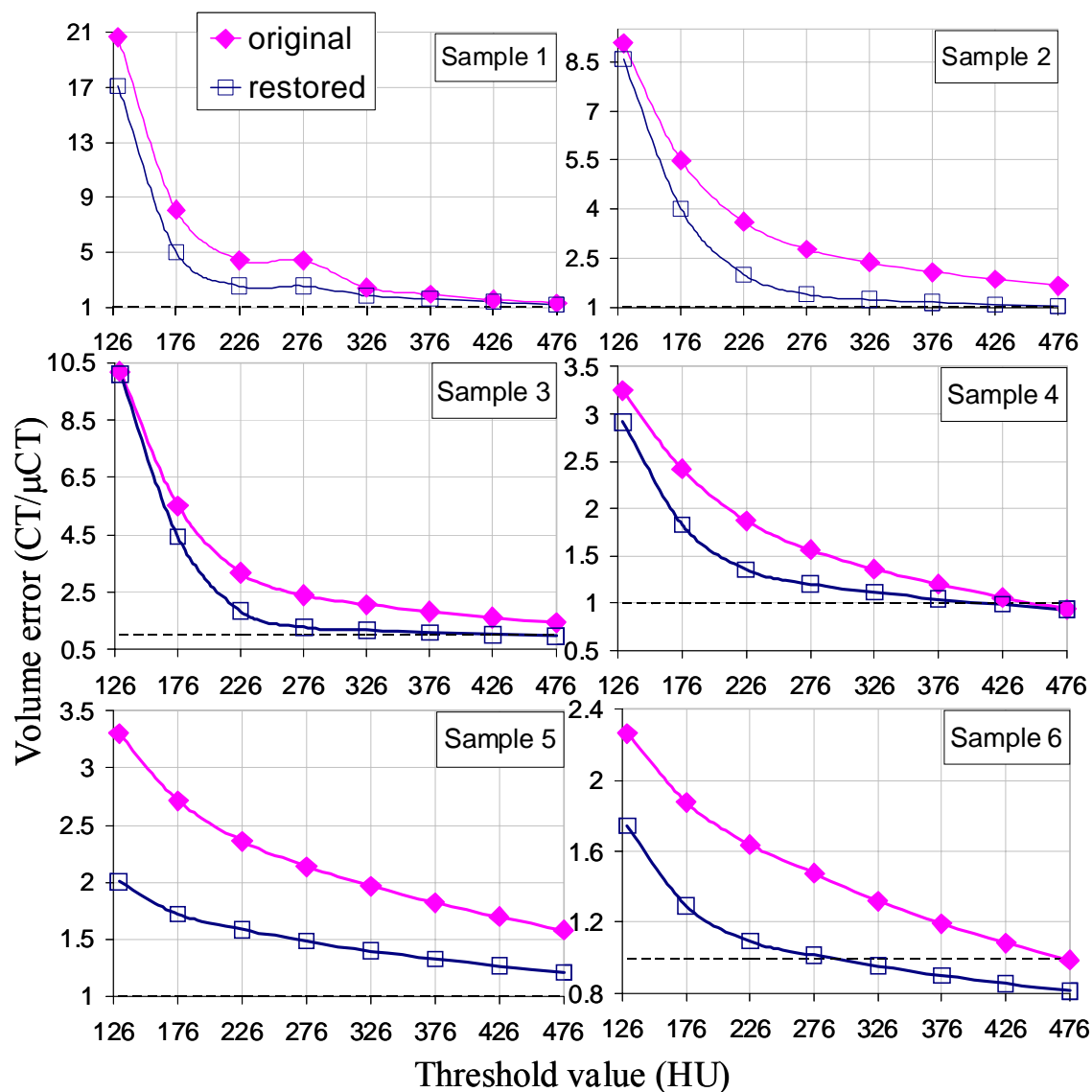


**Figure 4.11.** Error in the calcification volume measurement of each of the six in vitro samples, estimated for the original and restored images using eight different quantification threshold values ranging from 130 HU to 476 HU.

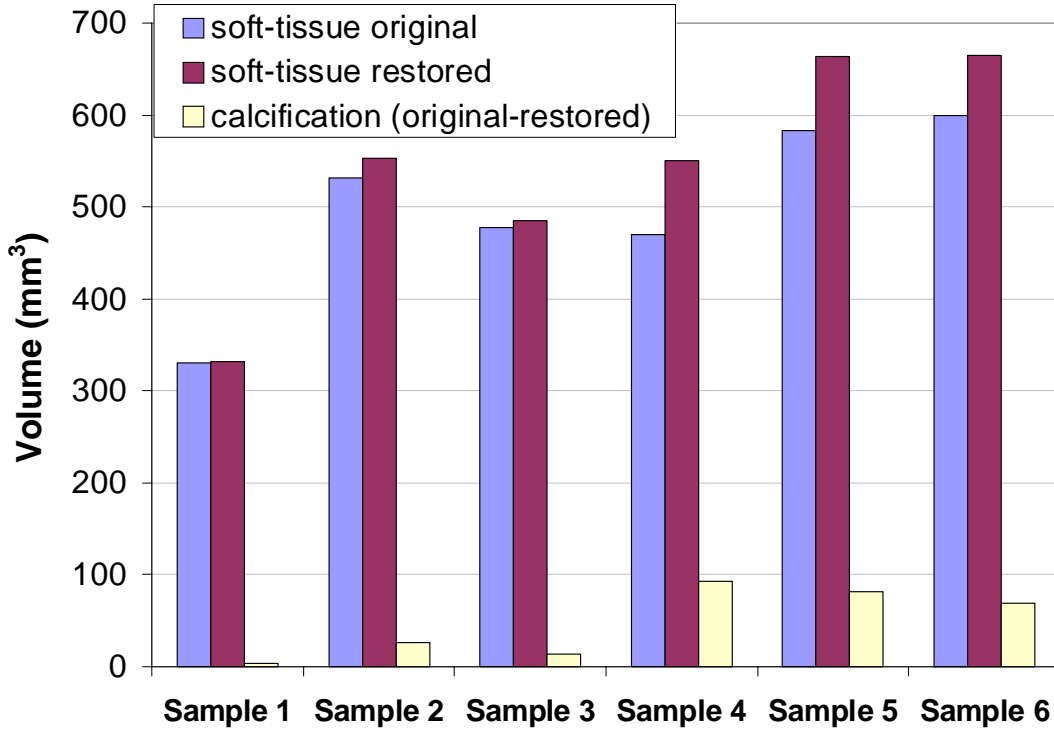


**Figure 4.12.** Volume quantification of the original and restored soft-tissue plaque with HU values between  $[\mu_{st}-2\sigma_{st}, \mu_{st}+2\sigma_{st}]$ , where the mean HU,  $\mu_{st}$ , and the standard deviation,  $\sigma_{st}$ , of the original soft-tissue plaque slightly depend on the in vitro sample. The third light bar of the graph shows the difference between the calcification of the original and restored images, for a threshold value equal to  $\mu_{st}+2\sigma_{st}$ . Note that the difference between the original and restored calcification volumes perfectly correlates with the difference in their soft-tissue volumes for each of the six in vitro samples.

#### 4.3.4 Restoration of patient images

To evaluate the performance of HiSD on in vivo images, we selected a number of patient cases where blur of small high-density structures hampered clinical analyses. The first clinical problem (Fig. 4.13) is the discrimination between bone and calcification for the segmentation and quantification of atherosclerotic intracranial arteries. The second clinical problem (Fig. 4.14) is the estimation of the lumen in stented vessels, where an artificial lumen narrowing due to strut blooming artifacts has been reported.<sup>36,37</sup> Note that in both patient images a high concentration of contrast material (i.e.  $HU > 300$  HU) was used to enhance the lumen. Consequently, to avoid deconvolution artifacts on the enhanced lumen, the segmentation thresholds were determined over the histogram peak of the contrast material.

It can be observed from the intensity profiles of Fig. 4.13 that bone and calcification appear completely convolved in the original image while these can be easily segmented in the restored image. In Fig. 4.14 it can be observed that after restoration the blur of the stent struts is reduced, and the small shift of the peaks due to the convolution of the strut with the contrast material is reduced.

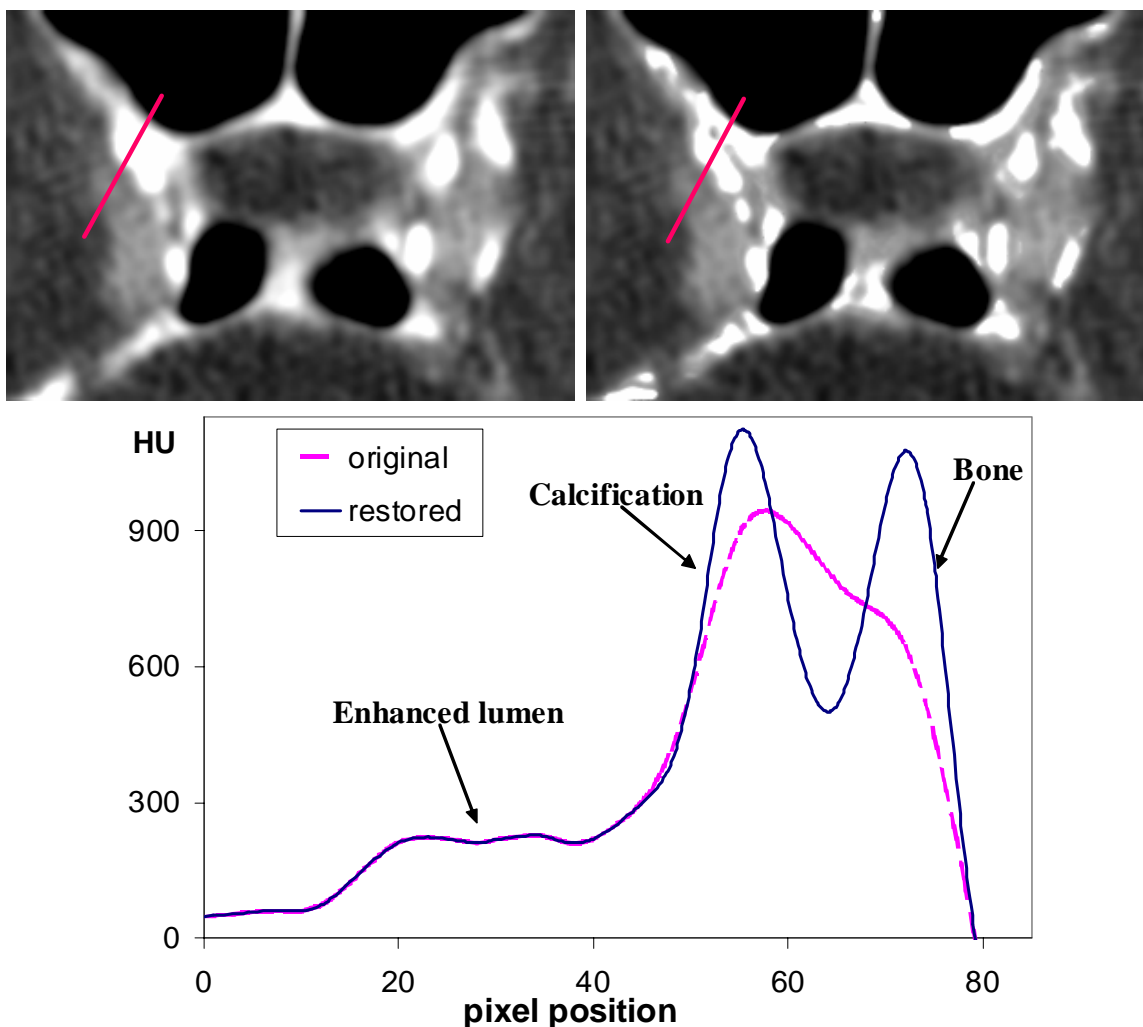


**Figure 4.13.** Cross-sectional views of the original (top left) and restored (top right) images of an intracranial atherosclerotic artery (displayed with a contrast window of 700 HU width, centered at 226 HU). On the bottom frame, line intensity profiles of the original and restored images (pixel size of 0.1 mm). The original CT image was acquired with a 16-slice MSCT (Siemens Somatom Sensation 16): collimation 0.75 mm; pitch 1; tube current of 360 mAs, 120 kVp; slice thickness 1 mm; reconstruction increment 0.6 mm, field of view 120 mm; and convolution kernel B46f.

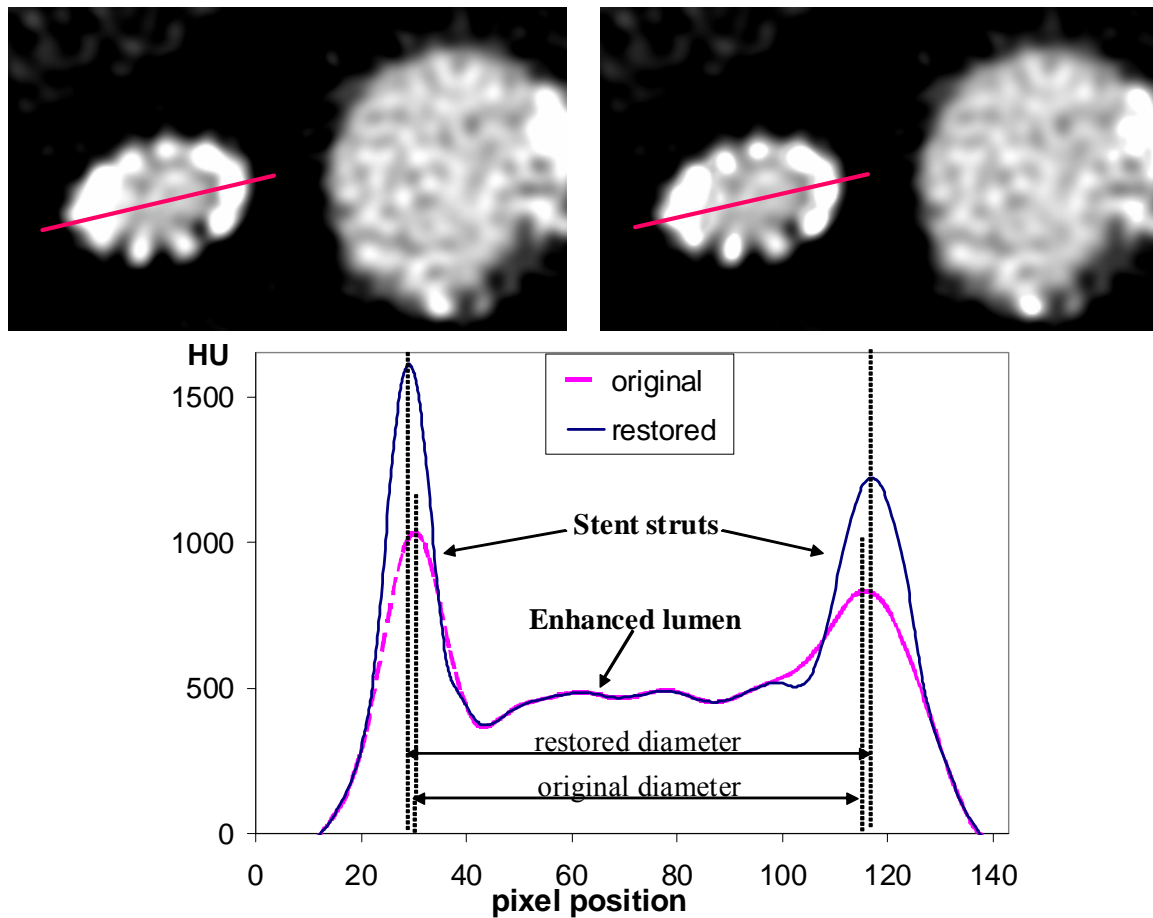


**Figure 4.14.** Cross-sectional views of the original (top left) and restored (top right) images of a stented renal artery (displayed with a contrast window of 576 HU width, centered at 76 HU). On the bottom frame, line intensity profiles of the original and restored images (pixel size of 0.1 mm). The original CT image was acquired with a 64-slice MSCT (Siemens Somatom Sensation 64): collimation 0.6 mm; pitch 1; tube current of 544 mAs, 120 kVp; slice thickness 0.6 mm; reconstruction increment 0.2 mm; field of view 50 mm; and convolution kernel B41f.

## 4.4. Discussion

Digital image deconvolution is frequently used in applications where the system spatial resolution is insufficient to properly resolve the objects of interest from the background. Several authors<sup>15-18,23,24</sup> have recently applied deconvolution to improve clinical diagnosis with CT scanning technique. Most of the work has been addressed to improve visualization of small bony structures in human anatomy, and some studies<sup>23,24</sup> suggested a further application of this technique to enhance visualization of vessels in CTA images. However, the specific application of deconvolution to improve visualization and quantification of calcifications in atherosclerotic plaques has, to the best of our knowledge, not been performed and validated before.

A number of deconvolution algorithms has been developed with the goal of reducing image blur while increasing the SNR. Most of them are based on an iterative



minimization of the divergence between the original image and the estimate of the “true” object obtained in each iteration.<sup>22,38</sup> These methods are powerful in improving the SNR, but unfortunately at the expense of very long computational processing times,<sup>15,17,23,24</sup> since iterative deconvolution requires a large number of iterations to effectively reduce image blur. This limits the application of these techniques for large volume images, especially when deconvolution has to be performed along the three directions of space. Indeed, to the best of our knowledge, the computational times and results reported by other researchers on CT patient data are based on iterative deconvolution of the image either along the CT longitudinal axis,<sup>15,23</sup> or along a given 2D cross-section.<sup>16,17,24</sup> On the other hand, the computational requirements and processing times needed to perform 3D image deconvolution with a regularized Wiener filter are relatively small compared with iterative deconvolution methods,<sup>15-17</sup> especially when the number of pixels in each dimension is equal to a power of 2, since the Fast Fourier algorithm can be used.<sup>39</sup> This makes the Wiener Filter more advantageous for clinical practice. This study investigates for CT volume images whether the Wiener Filter can be used to achieve a fast and strong 3D deconvolution of the high-density objects (which have a larger SNR and generally correspond to small/thin human body structures such as calcifications and cortical bone), while avoiding noise amplification and edge-ringing artifacts on the remaining low-density structures (which have a lower SNR and consequently are more negatively influenced by noise and artifacts). For this purpose, we developed a method, referred to as HiSD, which consists of two main parts: first a strong Wiener Filter 3D deconvolution of the CT volume image is performed, and subsequently the low-intensity voxel information of the original CT image is combined with the high-intensity voxel information of the deconvolved image to generate a restored image.

The method has been evaluated on CT images of the “Small high-density structures” phantom and of in vitro atherosclerotic plaques. Hereto, the phantom and six in vitro atherosclerotic carotid plaques were scanned both with a 16-slice spiral CT system and with a microfocus CT scanner, and qualitative and quantitative image analyses of the resulting original and restored images were carried out, taking the  $\mu$ CT images as reference for the calcification morphology. Qualitative analyses show that blur of high-density structures is noticeably reduced in the restored images along the three directions of space. Consequently, calcification overrepresentation is decreased and calcification SNR is increased, resulting in improved visualization. Artifacts and SNR of the remaining low-density structures of the restored image are the same as in the original CT image. Quantitative analyses show that calcification size measurement errors are noticeably (and in most cases significantly) reduced by HiSD independently of the threshold value used for the quantification. When using a quantification threshold slightly larger than the positive component of noise and artifacts in the tissues surrounding the calcifications, errors on the area and volume measurements obtained for the original CT images are on average reduced for the restored images by 31% and 44%, respectively. Therefore, both qualitative and quantitative analyses show that HiSD improves CT imaging of high-density structures (calcifications).

The quantification algorithm used in this study is based on the calcification volume method. It has been reported that the calcification volume and the calcification mass methods improve measurement accuracy and reproducibility compared with the Agatston score, which strongly depends on the acquisition system and imaging protocol.<sup>24,32</sup> We

chose the calcification volume method to validate our results because  $\mu$ CT images provide reference data for the calcification geometry.

The estimation of the HU in the region of transition between the deconvolved and the original CT values introduces a visual “halo”-like effect surrounding calcifications. Problems related to this “halo” effect are limited in the sense that the HU in this region of transition are smaller than two times the standard deviation of noise and artifacts in the neighboring low-density tissues, which avoids the “halo” effect affecting the quantification of these low-density tissues and the visualization of the MIP images. Nevertheless, we are currently investigating a slightly different approach in which an intensity-weighting interpolation function between the original and deconvolved HU is being designed to estimate the HU surrounding deconvolved calcifications. This approach would probably reduce the “halo” effect and improve the problem of missing small calcifications in the restored image.

In this study, HiSD is used on CT images reconstructed with medium sharp convolution kernels B46 and B50, but it can also be applied to images reconstructed with other convolution kernels, whose corresponding PSFs have been measured a priori. The final image quality depends on the visibility of both low-density and high-density structures. While SNR of high-density structures is maximized when using a suitable  $\gamma$  value for the Wiener Filter, SNR of low-density structures is improved when selecting an optimal convolution kernel to reconstruct the original image. Basically, the outcome of the HiSD procedure can be interpreted as the combination of two types of clinically available convolution kernels (which effectively deconvolve in the transverse direction); i.e. a very sharp kernel for the high-densities, and a medium kernel for the low-densities; plus a deconvolution of the image along the longitudinal direction.

When applying deconvolution it is important that the original image is acquired and reconstructed with a relatively high sampling frequency. Therefore, a relatively small slice thickness (i.e.  $S_{eff} \approx c=0.75$  mm), a FOV<160 mm, and a RI<0.3 mm (which yields a sampling distance smaller than half of the detector size) are used for this study. These parameter values guarantee that high frequencies of the projection data are not lost during image reconstruction, and therefore can be enhanced by digital deconvolution.

One limitation of this study is that HiSD is evaluated on phantom and in vitro samples. In clinical practice several factors; such as image noise, a wide variety of tissue densities, the use of an enhancing substance,<sup>40</sup> motion artifacts, etc., may influence the results of the application of this method. The influence of more realistic image noise has been investigated through phantom experiments, showing that despite the larger and heterogeneous image noise and metal artifacts our method performs well. Additionally, the method has been applied on in vivo patient CT enhanced images. The restored images are qualitatively improved, but additional work aimed to the lumen quantification and validation of the measurements with an appropriate reference is needed.

With current MSCT scanners, motion artifacts are a further limitation for the image quality of small high-density structures in clinical applications that involve imaging of the heart. For low heart frequencies, motions artifacts are less severe, and therefore the application of HiSD would probably improve the imaging of small high-density objects, thereby reducing blur in their edges. However, for high heart frequencies and/or arrhythmia, motion artifacts yield severe problems in the depiction of small objects,<sup>34</sup>

whose restoration would require sophisticated processing techniques to correct heart motion in the projection data before image reconstruction.

Future work will be aimed to the application and quantitative validation of HiSD on clinical image data. Furthermore, different alternatives to achieve an automated estimation of the thresholds used to detect and segment the high-density structures in original and deconvolved images will be investigated.

## Conclusion

A novel method for selective deblurring of small high-density structures, HiSD, has been introduced. This method considerably improves qualitative and quantitative analyses of in vitro atherosclerotic plaques by reducing calcification image blur in the transverse and longitudinal directions while avoiding noise amplification and edge-ringing artifacts in the surrounding low-density tissues.

## References

1. Martin GM. Atherosclerosis is the leading cause of death in the developed societies. *Am J Pathol.* 1998; 153(4):1319-1320.
2. Mathias K, Jager H, Hennigs S, *et al.* Endoluminal treatment of internal carotid artery stenosis. *World J Surg* 2001; 25:328-34; discussion 334-336.
3. El-Omar MM, Dangas G, Iakovou I, *et al.* Update on In-stent Restenosis. *Curr Interv Cardiol Rep* 2001; 3:296-305.
4. Wexler L, Brundage B, Crouse J, *et al.* Coronary artery calcification: pathophysiology, epidemiology, imaging methods, and clinical implications. A statement for health professionals from the American Heart Association. Writing Group. *Circulation* 1996; 94:1175-1192.
5. Sary HC, Blankenhorn DH, Chandler AB, *et al.* A Definition of the Intima of Human Arteries and of Its Atherosclerosis Prone Regions. A Report from the Committee on Vascular Lesions of the Council on Arteriosclerosis, American Heart Association. *Circulation* 1992; 85:391-405.
6. Sary HC, Chandler AB, Glagov S, *et al.* A definition of initial, fatty streak, and intermediate lesions of atherosclerosis. A report from the Committee on Vascular Lesions of the Council on Arteriosclerosis, American Heart Association. *Circulation* 1994; 89:2462-2478.

7. Stary HC, Chandler AB, Dinsmore RE, *et al.* A Definition of Advanced Types of Atherosclerotic Lesions and a Histological Classification of Atherosclerosis - a Report from the Committee on Vascular-Lesions of the Council on Arteriosclerosis, American-Heart-Association. *Circulation* 1995; 92:1355-1374.
8. Agatston AS, Janowitz WR. Ultrafast computed tomography in coronary screening. *Circulation* 1994; 89:1908-1909.
9. Becker CR, Ohnesorge BM, Schoepf UJ, *et al.* Current development of cardiac imaging with multidetector-row CT. *Eur J Radiol* 2000; 36:97-103.
10. Flohr T, Stierstorfer K, Bruder H, *et al.* Image reconstruction and image quality evaluation for a 16-slice CT scanner. *Med Phys* 2003; 30:832-845.
11. Chau A, Gopal A, Mao S, *et al.* Comparison of three generations of electron beam tomography on image noise and reproducibility, a phantom study. *Invest Radiol.* Jun 2006;41(6):522-526.
12. Gerber TC, Stratmann BP, Kuzo RS, *et al.* Effect of acquisition technique on radiation dose and image quality in multidetector row computed tomography coronary angiography with submillimeter collimation. *Invest Radiol.* Aug 2005;40(8):556-563.
13. Muhlenbruch G, Thomas C, Wildberger JE, *et al.* Effect of varying slice thickness on coronary calcium scoring with multislice computed tomography in vitro and in vivo. *Invest Radiol.* Nov 2005; 40(11):695-699.
14. Kalender WA. Computed Tomography: fundamentals, system technology, image quality, applications. In: Publicis MCD Verlag, Munich, 2000.
15. Schlueter FJ, Wang G, Hsieh PS, *et al.* Longitudinal image deblurring in spiral CT. *Radiology* 1994; 193:413-418.
16. Wang G, Skinner MW, Vannier MW. Temporal bone volumetric image deblurring in spiral computed tomography scanning. *Acad Radiol* 1995; 2:888-895.
17. Wang G, Vannier MW, Skinner MW, *et al.* Spiral CT image deblurring for cochlear implantation. *IEEE Trans Med Imaging* 1998; 17:251-262.
18. Prevrhal S, Fox JC, Shepherd JA, *et al.* Accuracy of CT-based thickness measurement of thin structures: Modeling of limited spatial resolution in all three dimensions. *Med Phys* 2003; 30:1-8.
19. Rollano-Hijarrubia E, Stokking R, van der Meer F., *et al.* Imaging of small high-density structures in CT: a phantom study. *Acad Radiol.* 2006, 13(7):893-908.
20. Prevrhal S, Engelke K, Kalender WA. Accuracy limits for the determination of cortical width and density: the influence of object size and CT imaging parameters. *Phys Med Biol* 1999; 44:751-764.

21. Kaufman L, Mineyev M, Carlson J, *et al.* Coronary calcium scoring: modelling, predicting and correcting for the effect of CT scanner spatial resolution on Agatston and volume scores. *Phys Med Biol* 2003; 48:1423-1436.
22. Gonzalez R, Woods R. Digital Imaging Processing. In: *Prentice-Hall P*, New Jersey, 2003.
23. Sakai O, Shen Y, Takata Y, *et al.* The use of deblurring technique for improving the longitudinal resolution in helical CT of the head and neck region. *Comput Med Imag Graph* 1997; 21:153-164.
24. Jiang M, Wang G, Skinner MW, *et al.* Blind deblurring of spiral CT images-comparative studies on edge-to-noise ratios. *Med Phys* 2002; 29:821-829.
25. Rollano-Hijarrubia E, Stokking R, Niessen WJ. Accuracy Comparison of a 16 and 64 MDCT Scanner to Image Small High-density Structures. *Invest Radiol* 2006; 41:781-792.
26. Langheinrich AC, Bohle RM, Greschus S, *et al.* Atherosclerotic lesions at micro CT: Feasibility for analysis of coronary artery wall in autopsy specimens. *Radiology* 2004; 231:675-681.
27. Marxen M, Thornton MM, Chiarot CB, *et al.* MicroCT scanner performance and considerations for vascular specimen imaging. *Med Phys* 2004; 31:305-313.
28. Rakebrandt F, Crawford DC, Havard D, *et al.* Relationship between ultrasound texture classification images and histology of atherosclerotic plaque. *Ultrasound Med Biol* 2000; 26:1393-1402.
29. Meinel JF, Wang G, Jiang M, *et al.* Spatial variation of resolution and noise in multi-detector row spiral CT. *Acad Radiol* 2003; 10:607-613.
30. Yanch JC, Flower MA, Webb S. A Comparison of Deconvolution and Windowed Subtraction Techniques for Scatter Compensation in Spect. *IEEE T Med Imaging* 1988; 7:13-20.
31. Sylvie D, Yves G. Experimental determination of CT point spread function anisotropy and shift-variance. In *19th International Conference - IEEE, EMBS*. Chicago, IL. USA, 1997:788-791.
32. Yoon HC, Greaser LE, Mather R, *et al.* Coronary artery calcium: Alternate methods for accurate and reproducible quantitation. *Academic Radiology* 1997; 4:666-673.
33. Agatston AS, Janowitz WR, Hildner FJ, *et al.* Quantification of Coronary Artery Calcium Using Ultrafast Computed Tomography. *Journal of the American College of Cardiology* 1990; 15:827-832.
34. Ulzheimer S, Kalender WA. Assessment of calcium scoring performance in cardiac computed tomography. *Eur Radiol* 2003; 13:484-497.

35. de Weert T, Ouhlous M, Zondervan PE, *et al.* In vitro characterization of atherosclerotic carotid plaque with multidetector computed tomography and histopathological correlation. *Eur Radiol* 2005; 15:1906-1914.
36. Maintz D, Seifarth H, Flohr T, *et al.* Improved coronary artery stent visualization and in-stent stenosis detection using 16-slice computed-tomography and dedicated image reconstruction technique. *Invest Radiol*. 2003; 38:790–795.
37. Seifarth H, Ozgun M, Raupach R, *et al.* 64- Versus 16-slice CT angiography for coronary artery stent assessment: in vitro experience. *Invest Radiol* 2006; 41:22-27.
38. Katsaggelos AK. Iterative Image-Restoration Algorithms. *Opt Eng* 1989; 28:735-748.
39. Danielson GC, Lanczos C. Some improvements in practical Fourier analysis and their application to X-ray scattering from liquids. *J. Franklin Inst.* 1942; 233, no. 4 and 5:365-380; 435-452.
40. Muhlenbruch G, Wildberger JE, Koos R, *et al.* Coronary calcium scoring using 16-row multislice computed tomography: non-enhanced versus contrast-enhanced studies in vitro and in vivo. *Invest Radiol*. 2005; 40(3):148-154.

# Chapter 5

## Histogram-based Selective Deblurring and Automated Vessel Segmentation for Improved In Vivo Calcification Visualization and Quantification in CTA

Rollano-Hijarrubia E, Manniesing R, Niessen WJ

### Objectives

Visualization and quantification of small structures with Computed Tomography (CT) is hampered by the limited spatial resolution of the system. *Histogram-based Selective Deblurring* (HiSD) is a deconvolution method that restores small high-density structures, *i.e.* calcifications, of a CT image, using the high-intensity voxel information of the deconvolved image, while preserving the original Hounsfield Units (HUs) in the remaining tissues. This study aims to implement and evaluate HiSD on in vivo contrast-enhanced CT images of atherosclerotic plaques.

### Materials and Methods

HiSD is applied and validated on fifteen calcification samples of carotid atherosclerotic plaque contrast-enhanced CT images. The current version of HiSD allows an automated segmentation of calcifications, and implements a weighted interpolation between the original and deconvolved CT images. Automated segmentation of contrast-enhanced vessels is performed prior to image restoration to support segmentation of calcifications with HUs similar to the contrast material. The method is evaluated qualitatively and quantitatively on in vivo CT images, using micro-CT images as high-resolution reference for the calcification volume.

### Results

The combination of vessel lumen segmentation and HiSD reduced calcification blur in the three directions of space, while avoiding noise amplification and edge-ringing artifacts in the surrounding tissues. Restoration with HiSD significantly ( $P < 0.005$ ) improved in vivo calcification quantification: measurement errors due to volume overestimation (obtained for quantification thresholds  $< 430$  HU) and volume underestimation (for thresholds  $\geq 430$  HU) were reduced by 23.5% on average.

### Conclusion

HiSD in combination with vessel segmentation significantly improves calcification visualization and quantification on in vivo contrast-enhanced CT images.

*This Chapter is in preparation to be submitted.*

## 5.1 Introduction

Cardiovascular disease remains the leading cause of morbidity and death in the Western World.<sup>1</sup> Computed Tomography (CT) is increasingly used in the diagnostic evaluation of patients with risk factors for coronary artery disease.<sup>2-5</sup> Coronary artery calcification quantification, as assessed by CT, is an important risk factor, as it can be correlated with the progression, stabilization and/or regression of atherosclerosis.<sup>6-11</sup> Calcification pattern distribution has been recently suggested as an important predictive factor for plaque vulnerability.<sup>12-14</sup>

State-of-the-art Multislice Spiral CT (MSCT) allows volumetric images of the human body with near isotropic spatial resolution in the order of 0.3-0.4 mm.<sup>15</sup> The spatial and contrast resolution of CT is limited by the finite size of both the X-ray source focal spot and the detector element in the CT array, and by several factors that contribute to noise (*e.g.* the detector efficiency and system geometry).<sup>16,17-20</sup> The limited spatial resolution of the system results in partial volume effects (PVEs) which are visible as image blur. Image blur influences most strongly the visualization and quantification of small/thin structures such as calcifications and cortical bone, yielding overestimation in their sizes and underestimation in their signal (*i.e.*, Hounsfield Units, HUs).<sup>17,18</sup> Some of the problems related to the image blur are: *i*) the dependency of the calcification volume quantification with the threshold value (HU); and *ii*) the dependency of the visualization of high-contrast structures with the display contrast window.<sup>19-21</sup>

A number of image deconvolution techniques have been proposed to reduce image blur. These techniques attempt to solve the inverse problem of obtaining the best estimate of the true object from the acquired image, using a model of the image blur and image noise.<sup>22-27</sup> Deconvolution amplifies high-frequency components of the image, which enhances image edges and especially improves the imaging of small high-density objects by increasing their signal while reducing their spread. Unfortunately, deconvolution also amplifies original image noise and artifacts and introduces edge-ringing artifacts on the surrounding structures.<sup>22-27</sup> Histogram-based Selective Deblurring (HiSD) has recently<sup>28,29</sup> been developed to selectively deconvolve small high-density structures while preserving the remaining information of the CT image. Previous work<sup>28,29</sup> showed that HiSD improves the visualization and quantification of small-high density structures both for phantom and in vitro atherosclerotic plaque CT images. However, in vitro studies have inherent limitations owing to the difficulty of reproducing a realistic experimental environment. The present work focuses on the implementation and validation of HiSD on in vivo CTA image data. In CTA data, the additional challenge of estimating the boundary between calcification and lumen needs to be addressed, and therefore HiSD is combined with an automated vessel lumen segmentation algorithm.

## 5.2 Materials and Methods

### 5.2.1 Imaging data

Ten in vivo CTA images of atherosclerotic carotid arteries from patients undergoing carotid endarterectomy were used to evaluate HiSD in combination with vessel segmentation. After endarterectomy, the atherosclerotic plaques were stored in 4%



formaldehyde. MSCT and micro-focus CT ( $\mu$ CT) images of the ten in vitro plaques were used as reference in our evaluation. In these 10 atherosclerotic plaques, we found a total of 15 clearly separable clusters of calcifications (*i.e.*, nearby calcifications that are convolved together in the CT image). The 15 calcification clusters were categorized according to their total calcification volume measured in the  $\mu$ CT images (from least to heaviest): *Sample 1* to *Sample 15*; and were used to quantitatively evaluate our method.

### 5.2.2 Image Acquisition and Reconstruction

In vivo CTA and in vitro CT images of the atherosclerotic plaques were acquired on a 16-Slice MSCT system (*Somatom Sensation 16*; Siemens Medical Systems), with a standardized optimized contrast-enhanced protocol<sup>30</sup> (120 kVp, 180 mAs, collimation  $16 \times 0.75$  mm, effective slice thickness 1.0 mm, pitch 1, field of view 120 mm, convolution kernel B46, and reconstruction increment 0.6 mm). For the in vitro images, the plaques were surrounded by a 160 mm cylinder of water (whose HUs are similar to soft-tissue)<sup>16</sup> in order to achieve a realistic attenuation environment of non-contrast-enhanced CT scans.

High resolution reference data were acquired with a Microfocus X-ray CT ( $\mu$ CT) (*SkyScan-1172*, [www.skyscan.be](http://www.skyscan.be)), using a standardized protocol (*i.e.*, 80 kVp, 100  $\mu$ A; rotation step  $1.125^\circ$ , and voxel size  $<18 \mu\text{m}$  in each direction of space).  $\mu$ CT volumetric images were reconstructed using a modified Feldkamp algorithm with automatic adaptation to scan geometry (<http://www.skyscan.be/products/nrecon.htm>). Standard corrections for ringing artifacts and beam hardening effects were applied.

### 5.2.3 Vessel Segmentation

Owing to image blur and a partial similarity in the HUs, discrimination between calcification and contrast-enhanced vessel lumen is nontrivial in CTA data. Therefore, prior to applying HiSD, automated 3D vessel segmentation, using the method by Manniesing *et al.*,<sup>31</sup> was performed. First, voxels that are very likely to represent calcifications were masked by selecting a threshold above the noise in the contrast material (*i.e.*, equal to  $t_d$ , whose value is automatically determined –see the following section for the details on its determination-). Then, the vessel lumen is segmented with a so-called level set evolution,<sup>32</sup> which is a 3D surface that evolves in an image to capture the boundaries of interest. The level set is initialized by manually placing seed points in the vessel to be segmented, and evolves with a speed function which depends on the image intensity,<sup>31</sup> and on the image gradient.<sup>33</sup> Parameters were equal to those used in the study of Manniesing *et al.*,<sup>31</sup> which showed accurate diameter measurements in phantom and patient data.

### 5.2.4 Histogram-based Selective Deblurring (HiSD)

HiSD was recently introduced and validated on in vitro plaque CT images.<sup>28,29</sup> In this paper we extend the HiSD approach, and combine it with vessel lumen segmentation. Next, we start with a short description of the original HiSD approach, and then we discuss a number of extensions we have made for the current study.

HiSD consists of the following steps (see Fig. 5.1): 1) 3D deconvolution of the original image using the Wiener Filter ( $W(\gamma, \text{PSF})$ ),<sup>22,26,29</sup> 2) Determination of intensity thresholds  $t_d$  and  $t_d'$  for detecting calcifications in the original and deconvolved image respectively, and intensity threshold  $t_e$  for detecting calcification edges; 3) Region growing based calcification segmentation of the original and deconvolved images using the detection threshold for finding seed points and the edge threshold for stopping the region growing; 4) Generation of 3D binary masks: Mask(orig), Mask(deconv), and Mask(diff), which contain, respectively, the calcification volume in the original image, the calcification volume in the deconvolved image, and the difference between these two latter volumes; 5) Construction of a restored image by combining the original HU information (all voxels outside Mask(orig)) with the deconvolved HU information (all voxels within Mask(deconv)), and estimating the HU values of voxels belonging to Mask(diff); 6) Filling the transition region between original and deconvolved Masks (*i.e.*, a volume enclosing Mask(diff)). A detailed description of these steps can be found in our previous study.<sup>29</sup>

In this paper, HiSD is extended by enabling *i*) fully automated estimation of the detection and segmentation thresholds, and local optimization of the segmentation threshold; *ii*) improved estimation of HU within the Mask(diff) region (step 6 above).

Detection thresholds  $t_d$  and  $t_d'$  were defined from the intensity histograms of the axial Maximum Intensity Projection (MIP) of the original and deconvolved images. First, the contrast-enhanced lumen histogram peak is automatically detected in the original and deconvolved images, as the peak with the highest HU in the histogram. The detection threshold is set right after the contrast material peak (see definition of criterion in the legend of Fig. 5.1) to avoid the largest values of contrast material voxels to be selected as calcifications.

For each calcification, a locally optimized edge threshold is determined, since calcifications can neighbor different tissue densities (e.g., from arteries, veins, soft-tissue). A local intensity image histogram is built from a volume enclosing the calcification (referred to as background). The background intensities represent the first peak in this histogram, and the threshold  $t_e$  is determined as the mean HU of the peak plus 3 times the SD of the background image noise (which is  $\sim 15$  HU for our imaging protocol). This way, the  $t_e$  value is taken significantly above the background noise.

In order to improve robustness in determining the thresholds, a number of constraints are applied based on a priori knowledge of contrast material and tissue HU ranges: *i*) Contrast material in the enhanced artery is typically larger than  $\sim 300$  HU, but certainly lower than 500 HU, therefore  $t_d \in [300, 500]$  HU; *ii*) Soft-tissue plaque and blood HU are typically  $\sim 50$ -60 HU, therefore the minimum value allowed for  $t_e$  is set at 95 HU, which corresponds to 50 HU plus 3 SD of the image noise. This lower limit avoids segmentation evolving through noise and artifacts beyond the calcification boundaries. *iii*) Finally, we impose that  $t_d'$  be equal or larger than  $t_d$ , because deconvolution increases the original image noise.

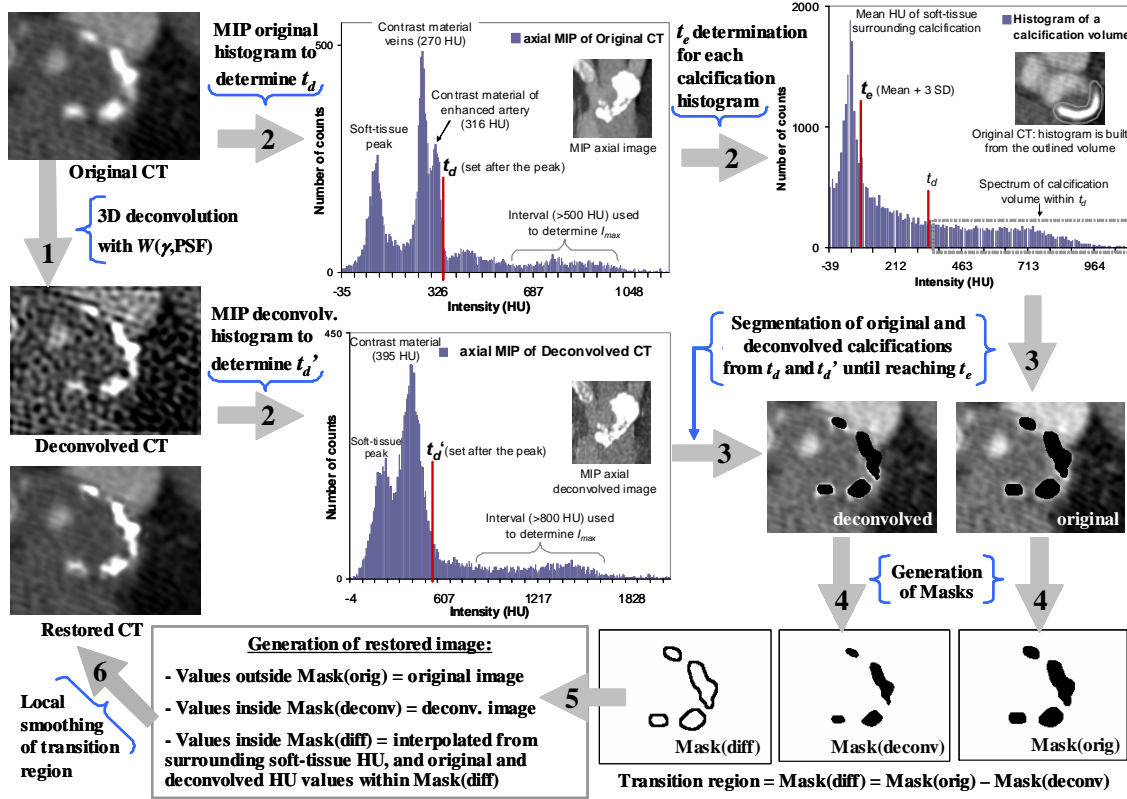


**Figure 5.1.** Flow chart illustrating the steps of the HiSD procedure: The cross-sectional images show arterial lumen stenosis caused by atherosclerotic plaque composed by soft tissue and calcifications (highest intensity voxels). MIP histograms are used to determine the detection thresholds ( $t_d$  and  $t_d'$ ). We first calculate the maximum number of counts,  $I_{max}$ , along the calcification histogram. The intensity interval used to calculate  $I_{max}$  is selected significantly above the range of typical contrast material HU found in clinical images, and lower than typical HU of cortical bone; i.e.:  $I_{max} \in [500 \text{ HU}, 800 \text{ HU}]$ . Note that for the deconvolved image this interval is set at higher HU to compensate for the increase in noise and ringing artifacts. Therefore, when the calcification histogram peak is detected, the threshold is set above the HU value corresponding to the channel whose number of counts is equal to two times the value of  $I_{max}$  (this number of counts is taken as indicative for the beginning of the peak). Note that for a larger calcification, the value of  $I_{max}$  would be higher. To prevent the detection threshold value from depending on the calcification size, we grow the volume used to compute the MIP histogram until the maximum number of counts in the contrast material peak is about ten times the number of counts averaged over the interval where  $I_{max}$  is determined.

In HiSD, Mask(diff) refers to the transition region that was overshadowed with calcification blur in the original image, and is not longer classified as calcification owing to deconvolution. To estimate the HU in Mask(diff), HiSD uses the information of three different image data sources: *i*) The original HUs of soft tissues surrounding calcifications (which are not influenced by calcification blur); *ii*) The original HU of voxels within Mask(diff); and *iii*) The deconvolved HU of voxels within Mask(diff). This

algorithm follows two steps: First, to estimate the reference values in Mask(diff), an iterative interpolation with a 2D Gaussian function is performed, starting from the outer boundary until reaching the deconvolved calcification boundary. Second, the restored values in the transition region are estimated using a weighting function that interpolates, for each voxel, the original and the deconvolved HUs. The weights used by this interpolation function vary from voxel to voxel because they depend on the reference values previously estimated. For each voxel, the differences between the reference HU and the original and deconvolved HUs are seen as errors that would be equal to zero in the absence of blur (in the case of the original image), and in the absence of ringing artifacts (*i.e.*, the case of the deconvolved image). Consequently, the value of the original and deconvolved image that is closer to the reference HU is more strongly weighted by the interpolation function (see Eq. 5.1 and Fig. 5.2).

$$\begin{aligned} \varepsilon_{oi} &= |I_{oi} - I_{ei}|, \quad \varepsilon_{di} = |I_{di} - I_{ei}|, \quad \Delta_i = |\varepsilon_{oi} - \varepsilon_{di}|, \quad \Delta_{\max} = \max\{|\varepsilon_{oi} - \varepsilon_{di}|\}, \quad \forall i \in R_t, \\ \omega_i &= -\frac{0.5}{\Delta_{\max}} \cdot \Delta_i + 0.5, \quad \text{If } \varepsilon_{oi} \geq \varepsilon_{di} \Rightarrow I_{ri} = \omega_i \cdot I_{oi} + (1 - \omega_i) \cdot I_{di}, \quad \text{If} \\ \varepsilon_{oi} &< \varepsilon_{di} \Rightarrow I_{ri} = (1 - \omega_i) \cdot I_{oi} + \omega_i \cdot I_{di} \end{aligned} \quad (\text{Eq. 5.1})$$

Where  $\varepsilon_{oi}$  and  $\varepsilon_{di}$  are the errors associated to the original and deconvolved image, respectively, for the voxel “ $i$ ” of the transition region,  $R_t$ ;  $I_{oi}$  and  $I_{di}$  are the HU values in the voxel “ $i$ ” of the original and deconvolved images, respectively;  $I_{ei}$  is the reference HU estimated for the voxel “ $i$ ”; and  $\omega_i$  is the weight of the interpolation function used to estimate the restored value,  $I_{ri}$ , in the voxel “ $i$ ”. Note that if  $\varepsilon_{oi} = \varepsilon_{di}$  both the original and deconvolved values are equally weighted; but if  $\varepsilon_{di} \gg \varepsilon_{oi}$  or  $\varepsilon_{oi} \gg \varepsilon_{di}$  only the HU corresponding to the smallest error determines the interpolated value.

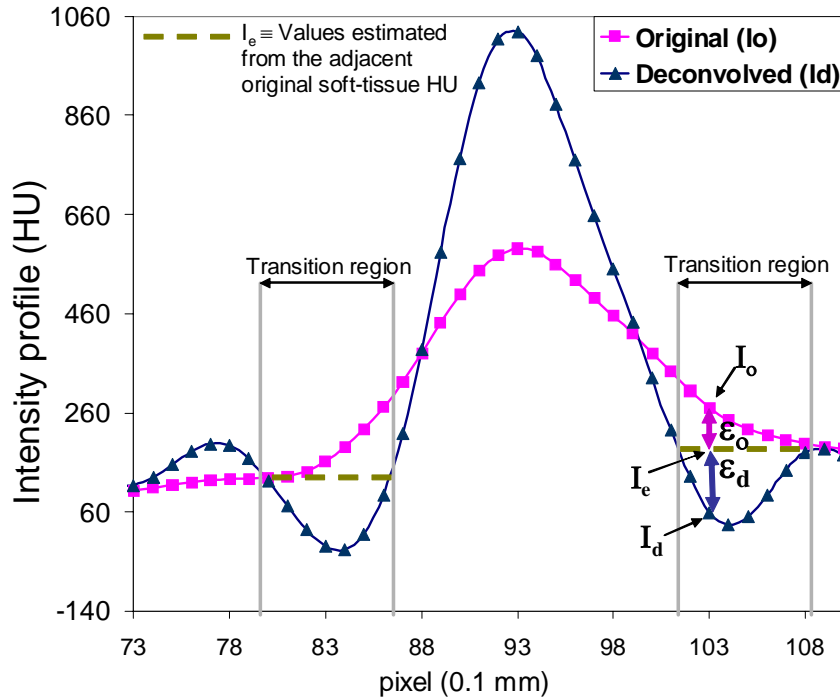


**Figure 5.2.** Intensity profile along a calcification for the original and deconvolved image. Parameters used in the weighting interpolation function (Eq. 5.1) are indicated here.

### 5.2.5 Evaluation of the image quality

Both qualitative and quantitative analyses were performed on the original, restored and  $\mu$ CT volume images of the 15 calcification clusters (described in section 5.2.1). For the qualitative analyses, the regions were visually compared, using the  $\mu$ CT as reference.<sup>29,34,35</sup> Qualitative inspection included visual enhancement of calcifications, resolution of nearby calcifications, loss of small calcifications, and noise/artifacts eventually introduced in the surrounding structures. For the quantitative analyses, measurements of the soft-tissue noise, calcification signal, calcification SNR, and calcification volume were carried out. The volume measurements were performed using the calcification volume method<sup>36</sup> for a total of 15 different quantification threshold values: 13 out of the 15 threshold values were distributed along an interval centered at the mean HU of the contrast material (*i.e.*,  $\sim 350$  HU), ranging from 130 HU (standard value used for the calcium quantification<sup>8,36-38</sup>) until 730 HU in intervals of 50 HU; and two additional values, lower than 130 HU and higher than soft tissue (*i.e.* 103 and 76, respectively), were considered in order to investigate whether the calcification blur is indeed effectively reduced in the transition region.

Since image blur in  $\mu$ CT is negligible compared to MSCT, calcification volume quantification in the  $\mu$ CT images was performed for a unique threshold value, which was set just above the  $\mu$ CT image noise and artifacts in the soft-tissue plaque.

Quantification errors obtained in the original and restored images were compared with the two-sample unequal variance Student's t-Test. A p-value  $< 0.05$  was considered statistically significant.

## 5.3 Results

### 5.3.1 Lumen segmentation

Examples of the lumen segmentation are given in Fig. 5.3. Fully automated lumen segmentation was successful in 13 out of 15 calcification samples. For two of the most heavily calcified samples, which contained large clusters of small calcifications partially attached to the lumen, the vessel segmentation encountered problems to discriminate calcifications from contrast material (as an example see Fig. 5.4). In both cases, the lumen was oversegmented towards adjacent calcifications with HU values similar to the contrast material. If these segmentations would not be corrected, part of the calcifications would not be fully deconvolved, but no noise/ringing artifacts would be introduced in the surrounding tissues. A manual correction of the lumen segmentation in these two regions was performed in order to allow calcification volume quantification of these two samples for thresholds lower than the contrast material HU.

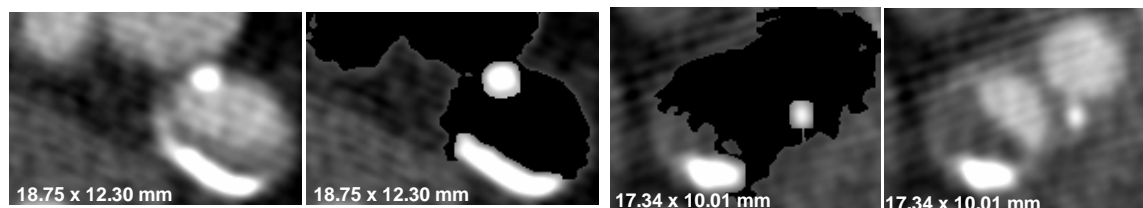
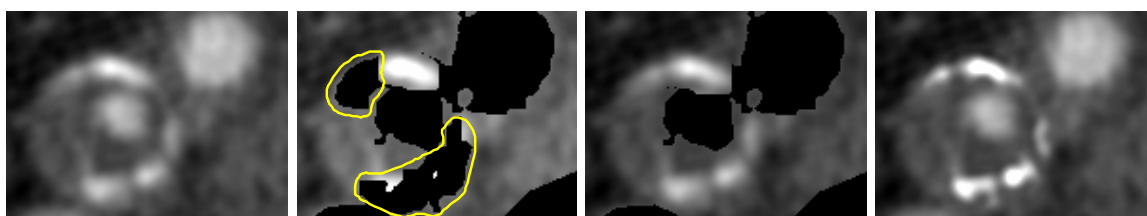


**Figure 5.3.** Examples of lumen segmentation for Samples 1 and 5. Image dimensions are given on the images. All the images are displayed with the same contrast window: *i.e.*,  $C_w(\text{center}, \text{width}) = C_w(1200, 600)$  in HU. Voxel sizes of  $\mu\text{CT}$  and CT images are isotropic: of 18  $\mu\text{m}$  and 0.1 mm, respectively.



Dimensions and contrast window of the images above: 17.34 x 13.01 mm,  $C_w(1200,600)$

**Figure 5.4.** (Left to right) cross-sectional image of Sample 2 showing one of the two cases where lumen was oversegmented towards adjacent calcifications (see 2<sup>nd</sup> frame). The lumen oversegmentation was manually corrected (see 3<sup>rd</sup> frame), thereby allowing a complete quantification of the calcification in the original and restored image (see 4<sup>th</sup> frame).

### 5.3.2 Qualitative evaluation

In general, HiSD performed well in all in vivo CT images, allowing a fully automatic restoration of the whole atherosclerotic plaque. The correspondence between the atherosclerotic plaque in the in vivo CT images and in the in vitro  $\mu\text{CT}$  images was good for all the plaques that are subject of this study. Figures 5.5 and 5.6 show MIP and cross-sectional images of two of the most heavily calcified plaques. It can be observed that deconvolved high-density structures correspond to calcifications in the  $\mu\text{CT}$  images. These calcifications appear enhanced and with less blur in the restored images, without introducing noise and ringing artifacts in the surrounding tissues.

Fig. 5.7 illustrates the effect of the interpolation method we employ in the transition region. After restoration, calcifications in close proximity are better resolved.

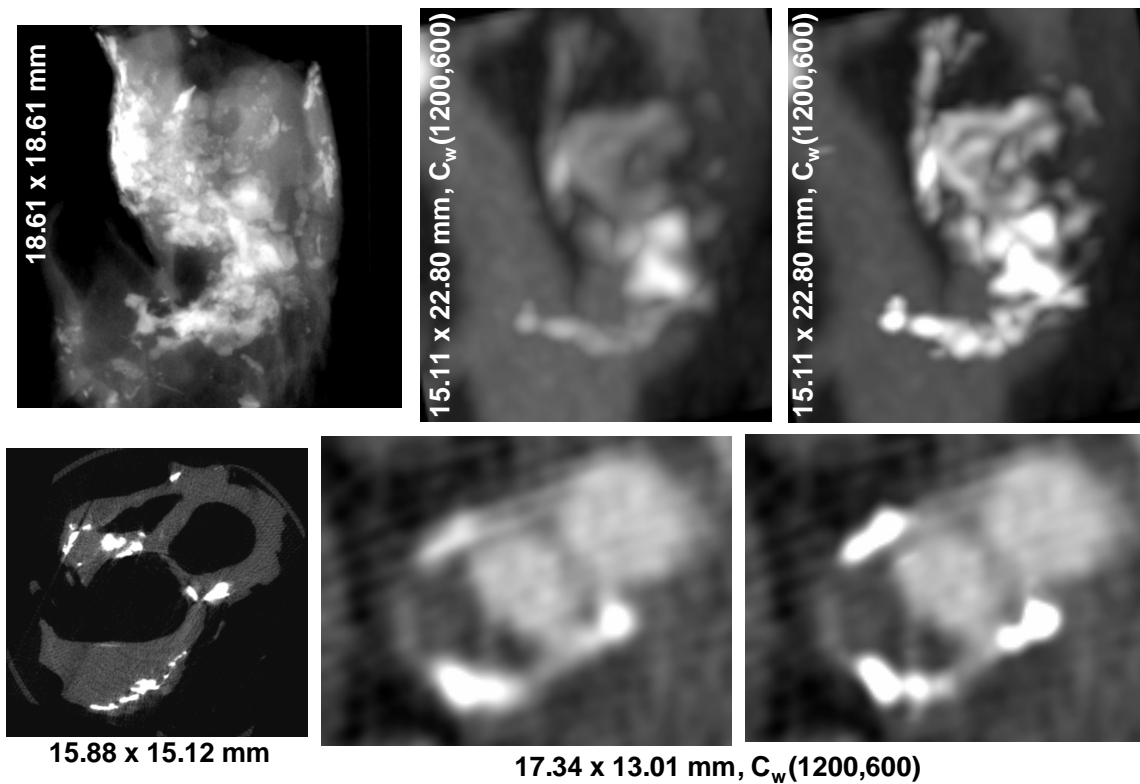


Figure 5.5

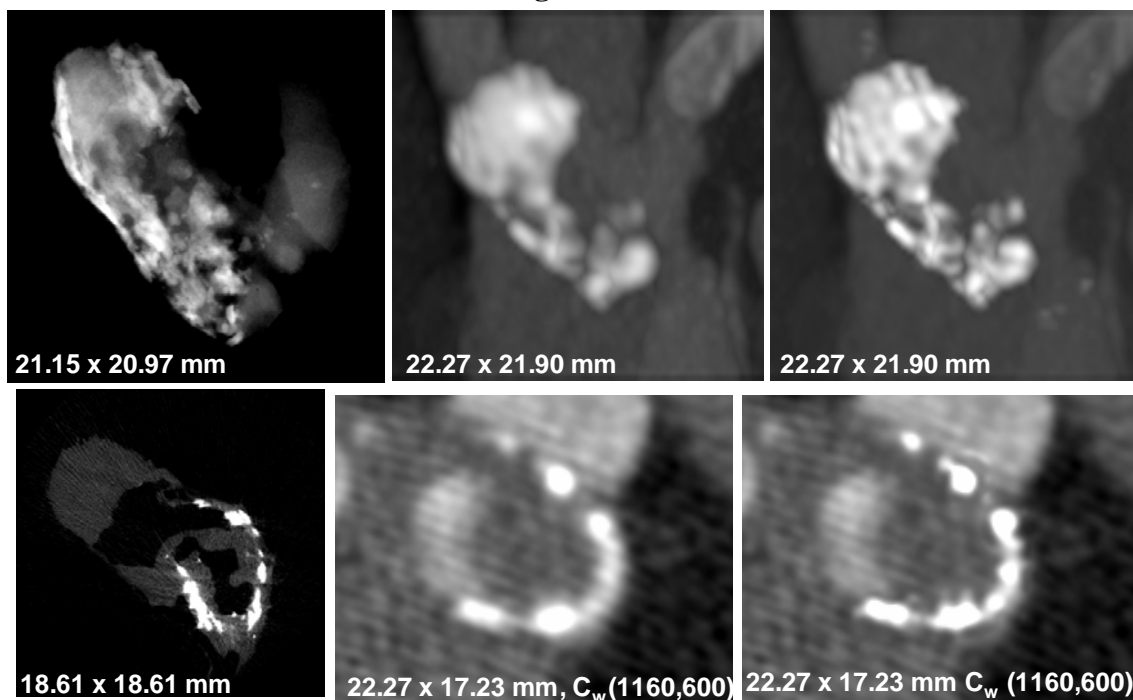
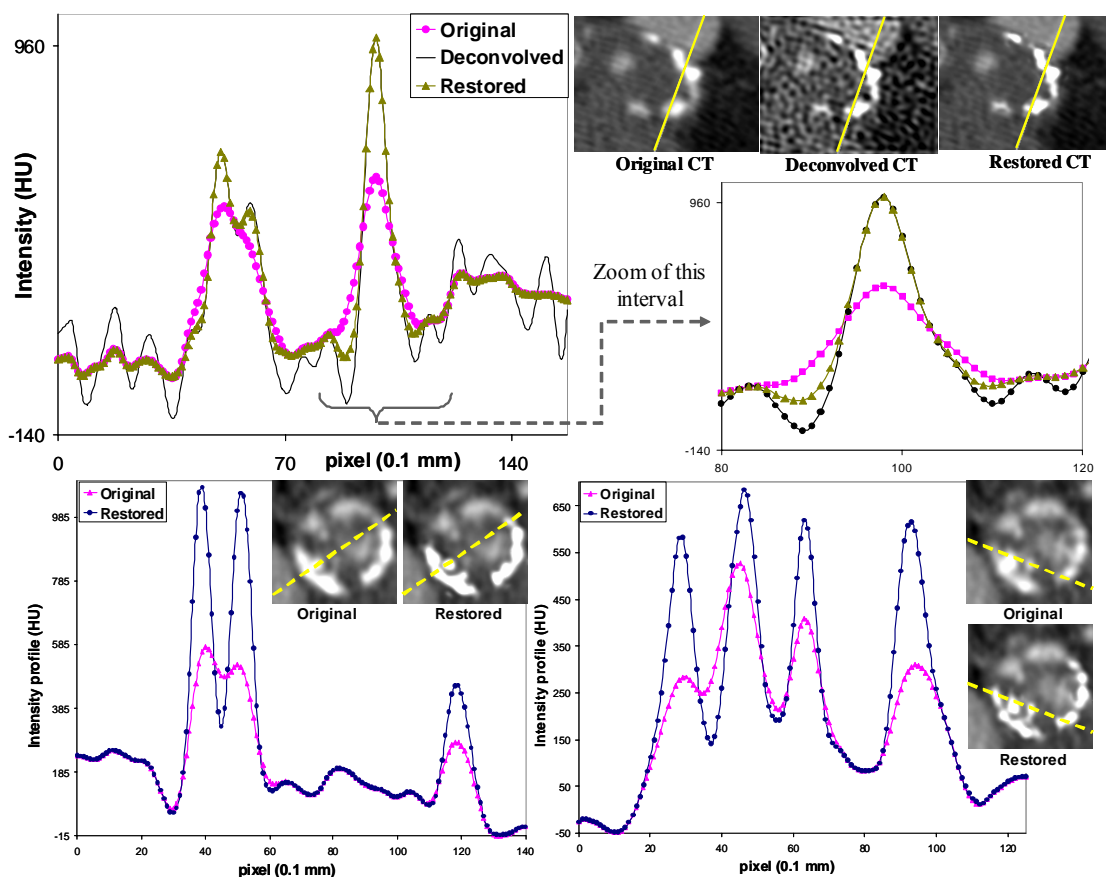


Figure 5.6

**Figure 5.5 and 5.6.** Axial MIPs (top frames of Figs. 5.5 and 5.6) and cross-sectional views (bottom frames of Figs. 5.5 and 5.6) of (from left to right) the reference  $\mu$ CT, the original CT, and restored image, for two of the most heavily calcified samples.





**Figure 5.7.** Intensity profiles along the lines indicated in the original and restored cross-sectional images of Sample 6 (top frames) and Sample 3 (bottom frames).

### 5.3.3 Quantitative analysis

Fig. 5.8 shows the intensity histogram of the original and restored images for one of the plaques. It can be observed that the histogram peaks corresponding to soft-tissue and contrast material are the same for the original and restored images, while the histogram corresponding to calcification is enhanced, *i.e.*, HU extend towards higher values. Table 5.1 lists the Full Width at Half Maximum of the soft-tissue peak ( $\text{FWHM}_{\text{st}}$ ), the maximum calcification signal, and the SNR for all plaques, both for the original and post-processed images. For the restored images, noise in the surrounding soft tissue is not amplified (note that the  $\text{FWHM}_{\text{st}}$  is the same for the original and restored images), and calcification signal is increased (by 850 HU on average), leading to an increase in calcification SNR.



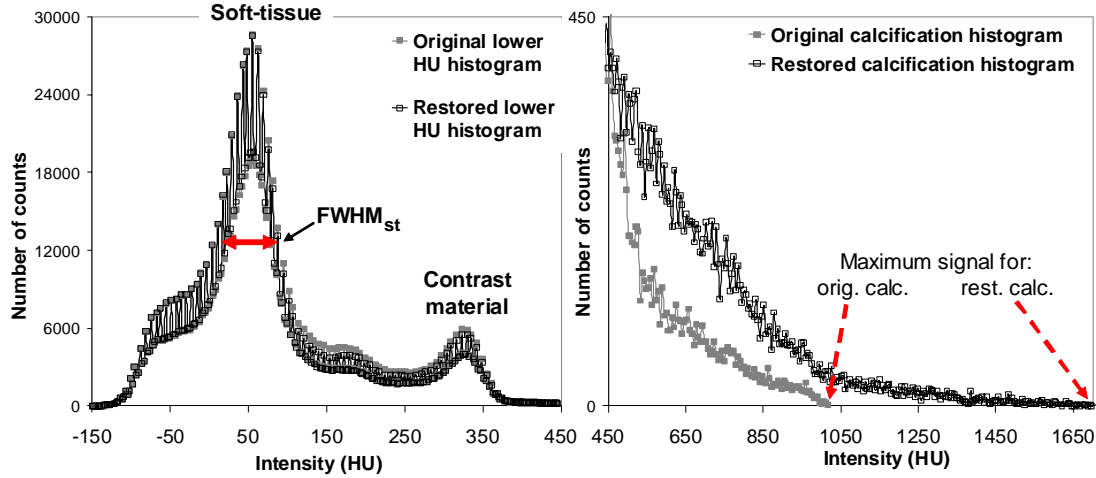


**Figure 5.8.** Intensity histogram of voxels surrounding calcifications (left) and intensity histogram of calcification volume (right), for one of the in vivo plaques before and after HiSD restoration.

Plaque	FWHM <sub>st</sub> original	SD	FWHM <sub>st</sub> restored	SD	Max. signal calc. original	Max. signal calc. restored	diff. signal	SNR original	SD	SNR restored	SD
1	82.5	10.0	82.4	9.8	1186	2105	919	14.4	1.7	25.6	3.0
2	51.7	1.5	51.7	1.4	925	1699	774	17.9	0.5	32.9	0.9
3	61.2	4.3	59.3	3.6	1048	2244	1196	17.1	1.2	37.8	2.3
4	52.3	2.7	52.3	2.5	1540	2436	896	29.4	1.5	46.6	2.2
5	64.3	3.2	64.5	2.9	1982	2587	605	30.8	1.5	40.1	1.8
6	112.6	4.9	112.2	4.8	1050	2025	975	9.3	0.4	18.1	0.8
7	52.4	3.5	52.5	3.2	1028	1733	705	19.6	1.3	33.0	2.0
8	51.8	4.3	52.3	4.1	1192	2070	879	23.0	1.9	39.6	3.1
9	45.8	1.3	45.9	1.3	2143	2881	738	46.8	1.4	62.8	1.8
10	52.8	3.6	53.3	2.8	1432	2242	810	27.1	1.9	42.0	2.2
Mean	63	6	63	6	1353	2202	850	24	3	38	4

**Table 5.1.** Measurements of the Full Width at Half Maximum of the soft-tissue peak (FWHM<sub>st</sub>); Maximum signal of calcification (max. signal calc.); Difference in signal between the original and deconvolved calcification (diff. signal); and SNR (*i.e.*, the maximum signal divided by the FWHM<sub>st</sub>), for the original and restored images of each of the ten in vivo plaques. The average values are provided in the last row.

Fig. 5.9 shows the error in calcification volume for the original and restored in vivo CTA images, for fifteen different thresholds, averaged over 15 in vivo samples. The volume error reaches its minimum value at ~430 HU for the original images, and at ~480 HU for the restored images. For these threshold values, the minimum error is not significantly lower for the restored than for the original image. However, both overestimation for lower thresholds (<280 HU), and underestimation for higher

thresholds ( $>480$  HU), are significantly ( $P < 0.05$ ) reduced in the restored images (i.e. by 23.5% on average), which indicates that HiSD significantly reduces calcification image blur.

Fig. 5.10 shows the errors in calcification volume of the original and restored images for the in vitro non contrast-enhanced CT scans. In this case, the minimum error for the volume measurement is reached at  $\sim 350$  HU for the original images, and at  $\sim 480$  HU for the restored images. Over and under these threshold values, volume error increases due to underestimation and overestimation, respectively, for both original and restored images. However, the volume error is reduced by 19.1% on average for the restored images. It can be observed that the minimum volume errors of the in vitro and in vivo quantifications are obtained for the same threshold value (i.e.,  $\sim 480$  HU) for the restored images, while it changes for the original images (it is  $\sim 350$  for the in vitro, and  $\sim 430$  for the in vivo).

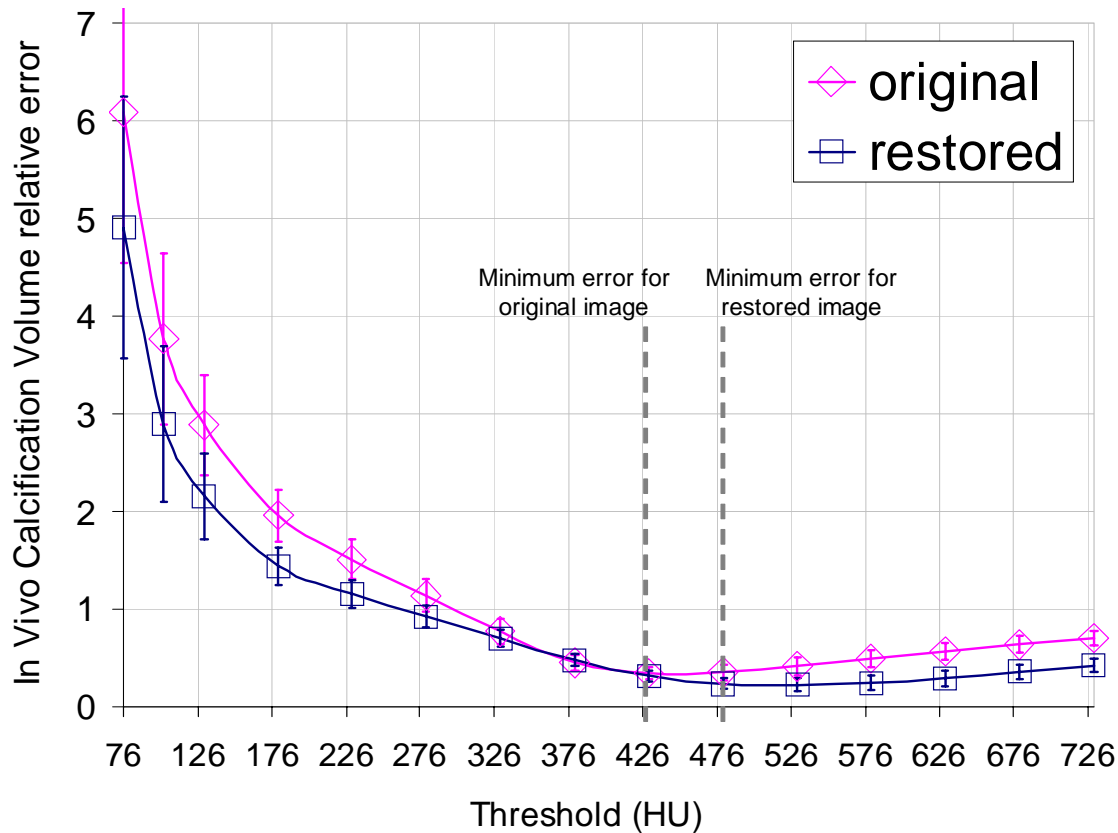


**Figure 5.9.** Relative error in the in vivo calcification volume measurement (mean and standard deviation of the volume relative errors obtained for the 15 in vivo samples). Relative errors are computed as the differences between CT and  $\mu$ CT calcification volumes, divided by  $\mu$ CT calcification volumes. Volume measurements are repeated for 15 different threshold values, ranging from 76 to 730 HU.

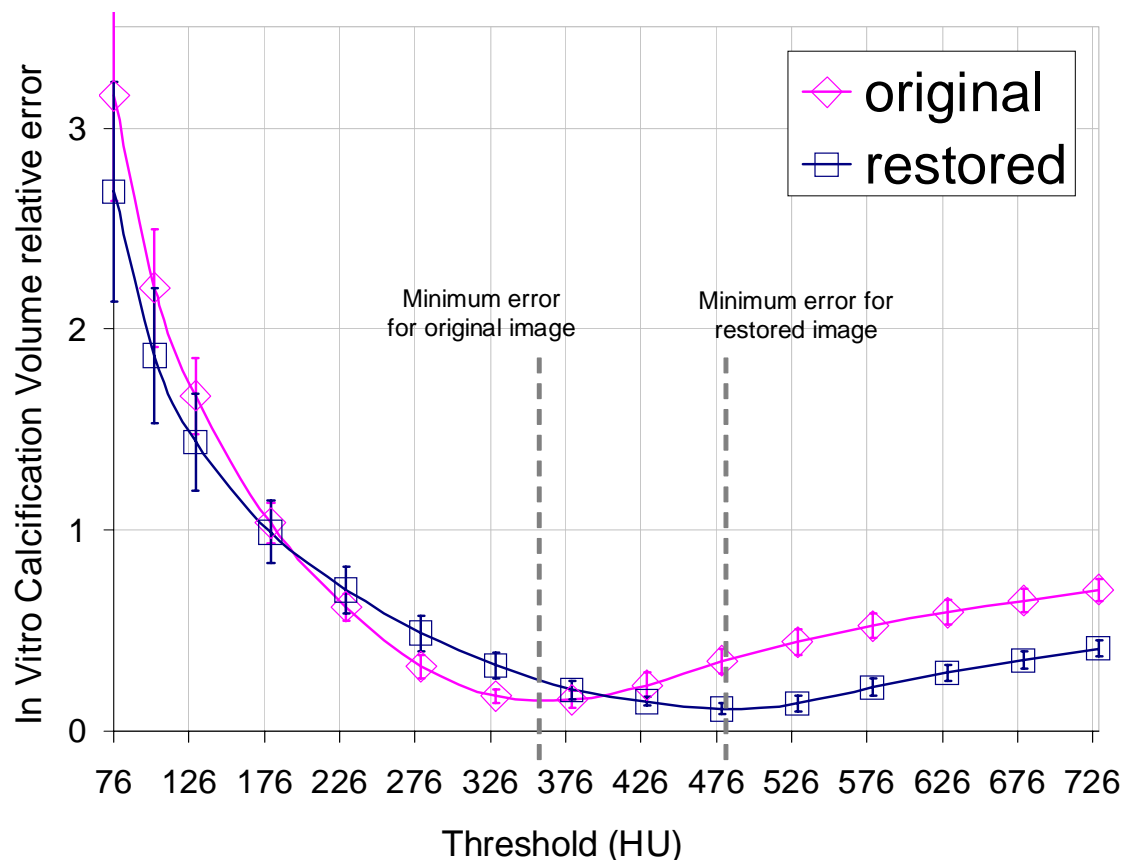


**Figure 5.10.** Relative error in the in vitro calcification volume measurement (mean and standard deviation of the volume relative errors obtained for the 15 in vitro samples) for 15 different threshold values.

The top graph of Fig. 5.11 shows the difference in calcification volume (see values represented with triangles) for the in vivo original image before and after segmenting the vessel. It can be observed that at the threshold value of  $\sim 480$  HU this difference approaches zero, indicating that for thresholds  $\geq 480$  HU volume quantification can be performed without requiring the removal of contrast-enhanced vessels from the image. In the same graph (represented with circles), we show the differences in calcification volume between the in vivo contrast-enhanced and the in vitro non-enhanced CT original data. It can be observed that these differences significantly decrease for thresholds  $\geq 430$  HU, and are near zero for thresholds  $\geq 480$  HU.

The bottom graph of Fig. 5.11 shows the relative error in the calcification volume measured for the in vivo original and restored images whose contrast-enhanced vessels have not been previously segmented. It can be observed that in the range of thresholds  $\geq 480$  HU, the relative error is significantly lower for the restored image. Moreover, we have found that for this range of threshold values the difference between the in vivo and in vitro calcification quantification is significantly reduced for the images postprocessed with HiSD.

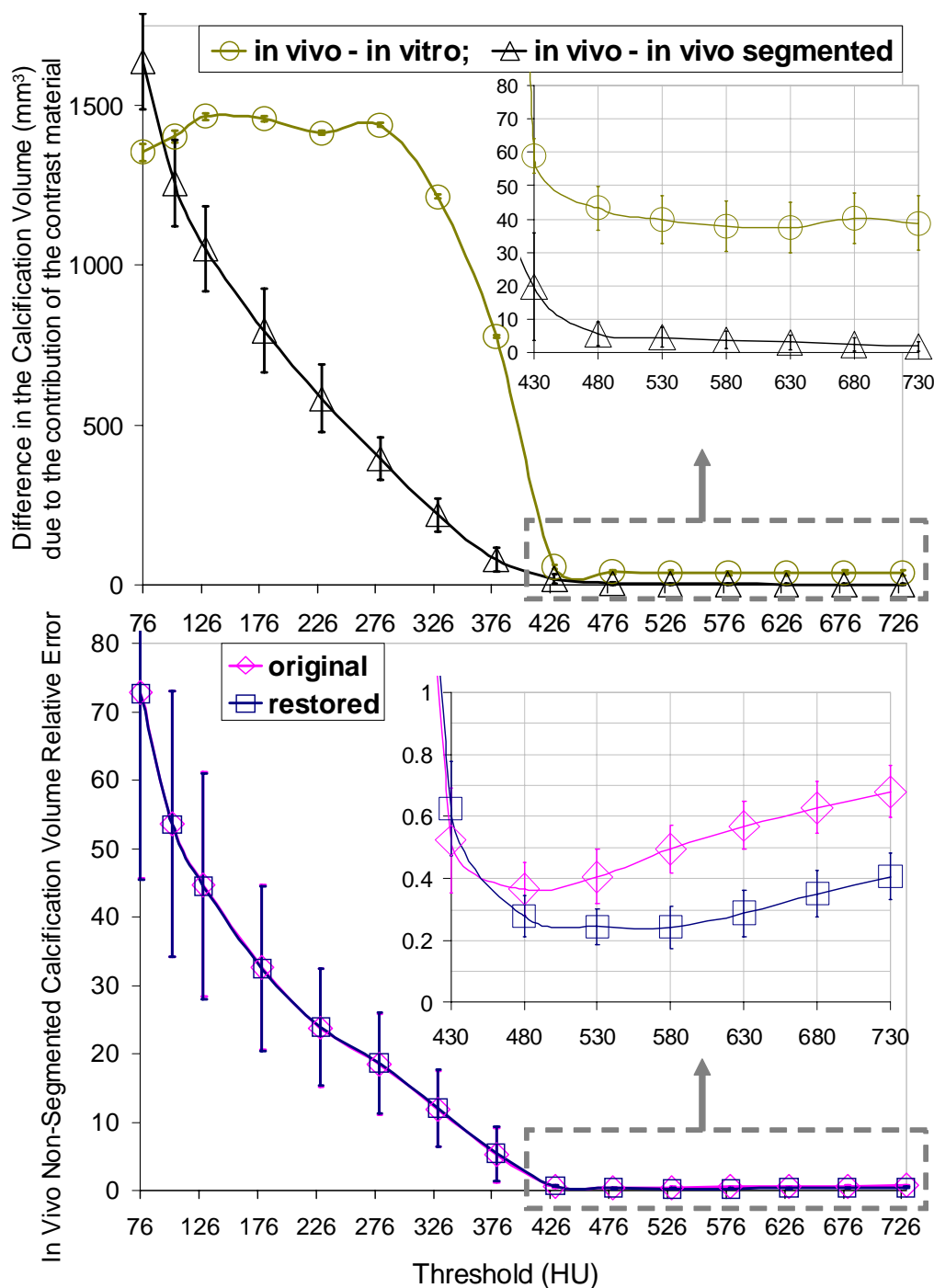


**Figure 5.11.** Top graph (values represented with triangles): difference in calcification volume for the in vivo original image before and after segmenting the vessel. Top graph (values represented with circles): difference in calcification volume for the in vivo enhanced original CTA and the in vitro non-enhanced original CT. Bottom graph: relative error in the calcification volume measurement for the original and restored images, before performing the lumen segmentation.

## 5.4. Discussion

Selective deconvolution of high-density small structures with HiSD was recently proved to be an effective method to improve in vitro calcification visualization and quantification.<sup>28,29</sup> In this study, an improved version of HiSD has been combined with vessel segmentation for the purpose of improved calcification visualization and quantification in CTA. To the best of our knowledge, the application and validation of deconvolution to improve in vivo CT imaging of calcifications has not been published before.

In comparison to our previous work, two extensions to HiSD have been introduced in this paper. First, automated methods for estimating both threshold values for detecting calcifications, and locally optimal edge thresholds for segmenting calcifications, are introduced. These methods are based on analysis of the MIP of the intensity histogram. In all studied data sets, appropriate thresholds were automatically found enabling the segmentation and subsequent deconvolution of the calcifications. Second, a new approach to estimate the HU in the region of transition between the deconvolved and original image has been introduced. In the previous version of HiSD, the estimated HU values were constant all along the transition region, which resulted in a “halo”-like effect around calcifications, and in missing very small calcification without enough SNR to be detected in the deconvolved image.<sup>28,29</sup> These two problems have now been remedied by incorporating information from voxels adjacent to the transition region, and interpolating original and deconvolved voxel values within the transition region.

To estimate the HU in the transition region different approaches were investigated. The first approach was based on the iterative Gaussian interpolation of the original HU adjacent to calcification (*i.e.*, the first step used in the current approach). This approach reduced the “halo-like” effect, but did not remedy the problem of missing small calcifications. This suggested the need of introducing the information of the original and deconvolved images in the transition region. Initially, we applied a linear interpolation of the values, but this introduced certain amount of blur and ringing artifacts because both original and deconvolved images were weighted equally, independently how far their values were from the true HU. This indicated the need of using a weighting interpolation function based on the numerical proximity of the original and deconvolved HUs to the values most likely to be the actual HU in this region. We assumed these values to be the intensities interpolated from the adjacent tissues. The results of this last approach were very good: Blur and ringing artifacts were avoided in the restored image, and the problem of missing calcifications was solved, since small calcifications with insufficient SNR were also restored in the final image because both original and deconvolved calcification peaks contributed positively to the interpolated value.

A third methodological contribution of this paper is the combination of HiSD with automated vessel segmentation, to enable the discrimination between the contrast-enhanced lumen and calcification voxels with similar HU. Our automated vessel segmentation method only requires two user-defined points for initialization, and successfully segmented the vasculature in 13 out of 15 cases. In two cases, a small post-processing step was required, as an oversegmentation into calcifications occurred. Further

advances in automated vessel segmentation of in the presence of calcification will result in a direct improvement of the HiSD performance

A qualitative evaluation has been performed using in vitro micro-CT data as reference standard. HiSD effectively reduces calcification blur in the three directions of space, while avoiding noise amplification and ringing artifacts associated with deconvolution. After restoration, calcification SNR is improved, and calcification visualization over the contrast material is enhanced. Quantitative analyses have been performed using micro-CT high-resolution data as reference for calcification volume. The results show that errors in the calcification volume measurement are significantly ( $P < 0.005$ ) reduced after applying HiSD for most quantification threshold values. Both volume overestimation obtained with low thresholds (*i.e.*,  $< 430$  HU), and volume underestimation obtained with high thresholds (*i.e.*,  $\geq 430$  HU) are significantly reduced (*i.e.*, by 23.5% on average) for the restored images. This also indicates that HiSD decreases the dependency of the calcification visualization with the display contrast window, and the calcification quantification with the threshold value. For both original and restored in vivo plaque CTA images, errors in the calcification volume measurement are smallest for thresholds between 430 and 480 HU. In this HU interval, volume errors are lower, but not significantly, for the restored images. However, in the restored images the optimal quantification threshold value does not depend on the HUs of the tissues surrounding calcifications; For the original images the optimal quantification threshold is lower for the in vitro than for the in vivo images (*i.e.*, it is 350 HU and 430 HU respectively), while for the restored images this threshold has the same value for both in vivo and in vitro images (*i.e.*, it is 480 HU). This is due to the fact that calcification enhancement obtained by deconvolution makes measurement less threshold dependent, and reduces the influence of surrounding tissues on the calcification quantification. In practice, this implies that the quantification threshold can be fixed at 480 HU, independently of the tissue surrounding the calcification. An additional advantage of the threshold of 480 HU is that it allows calcification quantification without removal of the contrast-enhanced lumen.

## Conclusions

A recently introduced method for selective deblurring of small high-density structures, HiSD, has been extended and applied to in vivo contrast-enhanced CT images of atherosclerotic plaques. This method reduces in vivo calcification blur in the transverse and longitudinal directions, while avoiding noise amplification and edge-ringing artifacts in the surrounding tissues. In vivo calcification volume measurements are significantly improved and less threshold dependent after applying HiSD. Restored images allow the use of a unique optimal threshold value (*i.e.*, 480 HU) to quantify calcifications independently of their surrounding tissue HU, and without the need of removing the contrast-enhanced lumen.

## References

1. Martin GM. Atherosclerosis is the leading cause of death in the developed societies. *Am J Pathol.* 1998; 153(4):1319-20.
2. Mathias K, Jager H, Hennigs S, *et al.* Endoluminal treatment of internal carotid artery stenosis. *World J Surg.* 2001; 25:328-34.
3. El-Omar MM, Dangas G, Iakovou I, *et al.* Update on In-stent Restenosis. *Curr Interv Cardiol Rep.* 2001; 3:296-305.
4. Agatston AS, Janowitz WR. Ultrafast computed tomography in coronary screening. *Circulation.* 1994; 89:1908-9.
5. Becker CR, Ohnesorge BM, Schoepf UJ, *et al.* Current development of cardiac imaging with multidetector-row CT. *Eur J Radiol.* 2000; 36:97-103.
6. Pletcher MJ, Tice JA, Pignone M, *et al.* Using the coronary artery calcium score to predict coronary heart disease events - A systematic review and meta-analysis. *Arch Intern Med.* 2004; 164:1285-1292.
7. Wilson PWF, D'Agostino RB, Levy D, *et al.* Prediction of coronary heart disease using risk factor categories. *Circulation.* 1998; 97:1837-1847.
8. Pham PH, Rao DS, Vasunilashorn F, *et al.* Computed tomography calcium quantification as a measure of atherosclerotic plaque morphology and stability. *Invest Radiol.* 2006; 41:674-680.
9. Rumberger JA, Simons DB, Fitzpatrick LA, *et al.* Coronary-Artery Calcium Area by Electron-Beam Computed-Tomography and Coronary Atherosclerotic Plaque Area - a Histopathologic Correlative Study. *Circulation.* 1995; 92:2157-2162.
10. Sangiorgi G, Rumberger JA, Severson A, *et al.* Arterial calcification and not lumen stenosis is highly correlated with atherosclerotic plaque burden in humans: a histologic study of 723 coronary artery segments using nondecalcifying methodology. *J Am Coll Cardiol.* 1998; 31:126-33.
11. Shaw LJ, Raggi P, Schisterman E, *et al.* Prognostic Value of Cardiac Risk Factors and Coronary Artery Calcium Screening for All-Cause Mortality. *Radiology.* 2003;228:826-833
12. Burke AP, Kolodgie FD, Farb A, *et al.* Morphological predictors of arterial remodeling in coronary atherosclerosis. *Circulation.* 2002; 105:297-303.
13. Taylor AJ, Burke AP, O'Malley PG, *et al.* A comparison of the Framingham risk index, coronary artery calcification, and culprit plaque morphology in sudden cardiac death. *Circulation.* 2000; 101:1243-8.

14. Ehara S, Kobayashi Y, Yoshiyama M, *et al.* Spotty calcification typifies the culprit plaque in patients with acute myocardial infarction: an intravascular ultrasound study. *Circulation*. 2004; 110:3424-9.
15. Flohr T, Stierstorfer K, Bruder H, *et al.* Image reconstruction and image quality evaluation for a 16-slice CT scanner. *Med Phys*. 2003; 30:832-45.
16. Kalender WA. Computed Tomography: fundamentals, system technology, image quality, applications. In: *Publicis MCD Verlag*, Munich, 2000.
17. Rollano-Hijarrubia E, Stokking R, van der Meer F., *et al.* Imaging of small high-density structures in CT: a phantom study. *Acad Radiol*. 2006, 13(7):893-908.
18. Prevrhal S, Engelke K, Kalender WA. Accuracy limits for the determination of cortical width and density: the influence of object size and CT imaging parameters. *Phys Med Biol*. 1999; 44:751-64.
19. Rollano-Hijarrubia E, Stokking R, Niessen WJ. Accuracy Comparison of a 16 and 64 MDCT Scanner to Image Small High-density Structures. *Invest Radiol*. 2006; 41:781-792.
20. Kaufman L, Mineyev M, Carlson J, *et al.* Coronary calcium scoring: modelling, predicting and correcting for the effect of CT scanner spatial resolution on Agatston and volume scores. *Phys Med Biol*. 2003; 48:1423-36
21. Muhlenbruch G, Thomas C, Wildberger JE, *et al.* Effect of varying slice thickness on coronary calcium scoring with multislice computed tomography in vitro and in vivo. *Invest Radiol*. Nov 2005; 40(11):695-699.
22. Gonzalez R, Woods R. Digital Imaging Processing. In: *Prentice-Hall P*, New Jersey, 2003.
23. Schlueter FJ, Wang G, Hsieh PS, *et al.* Longitudinal image deblurring in spiral CT. *Radiology*. 1994; 193:413-8.
24. Wang G, Skinner MW, Vannier MW. Temporal bone volumetric image deblurring in spiral computed tomography scanning. *Acad Radiol*. 1995; 2:888-95.
25. Wang G, Vannier MW, Skinner MW, *et al.* Spiral CT image deblurring for cochlear implantation. *IEEE Trans Med Imaging*. 1998; 17:251-62.
26. Sakai O, Shen Y, Takata Y, *et al.* The use of deblurring technique for improving the longitudinal resolution in helical CT of the head and neck region. *Comput Med Imag Graph*. 1997; 21:153-164.
27. Jiang M, Wang G, Skinner MW, *et al.* Blind deblurring of spiral CT images-comparative studies on edge-to-noise ratios. *Med Phys*. 2002; 29:821-9.



28. Rollano-Hijarrubia E, van der Meer F, van der Lugt A, *et al.* Improving the imaging of calcifications in CT by histogram-based selective deblurring. In *Conference Proceedings, SPIE, Medical Imaging 2005: Physics of Medical Imaging 2005*; 5745:67-78.
29. Rollano-Hijarrubia E, Niessen W, Weinans H, *et al.* Histogram-based selective deblurring to improve computed tomography imaging of calcifications. *Invest Radiol.* 2007; 42:8-22.
30. De Weert T, Ouhlous M, Zondervan PE, *et al.* In vitro characterization of atherosclerotic carotid plaque with multidetector computed tomography and histopathological correlation. *Eur Radiol.* 2005; 15:1906-14.
31. Manniesing R, Velthuis BK, van Leeuwen MS, *et al.* Level set based cerebral vasculature segmentation and diameter quantification in CT angiography. *Med Image Anal.* 2006; 10:200-214.
32. Sethian JA. Level Set Methods and Fast Marching Methods. *Cambridge University Press*, 1999.
33. Manniesing R, Viergever MA, Niessen WJ. Vessel axis tracking using topology constrained surface evolution. *IEEE Trans Med Imaging.* 2007; 26(3):309-16.
34. Langheinrich AC, Bohle RM, Greschus S, *et al.* Atherosclerotic lesions at micro CT: Feasibility for analysis of coronary artery wall in autopsy specimens. *Radiology* 2004; 231:675-681.
35. Marxen M, Thornton MM, Chiarot CB, *et al.* MicroCT scanner performance and considerations for vascular specimen imaging. *Med Phys* 2004; 31:305-13.
36. Yoon HC, Greaser LE, Mather R, *et al.* Coronary artery calcium: Alternate methods for accurate and reproducible quantitation. *Acad Radiol.* 1997; 4:666-673.
37. Agatston AS, Janowitz WR, Hildner FJ, *et al.* Quantification of Coronary Artery Calcium Using Ultrafast Computed Tomography. *J Am Coll Cardiol.* 1990; 15:827-832.
38. Ulzheimer S, Kalender WA. Assessment of calcium scoring performance in cardiac computed tomography. *Eur Radiol.* 2003; 13:484-97.



# Chapter 6

## Summary and Discussion

Computed Tomography (CT) imaging of small high-density structures such as calcifications and stents is highly relevant in diagnosis, treatment planning, and follow-up of patients with cardiovascular disease. Calcification quantification is increasingly used as a potential marker for cardiovascular disease. However, owing to image blur, accurate calcification quantification is compromised. In addition, blur of high intensity structures hampers the visualization of surrounding soft tissue structures. This for example affects the assessment of the degree of vessel stenoses at locations close to calcified atherosclerotic plaques and/or stent struts. The research described in this thesis focuses on the improved of visualization and quantification of small high density structures, in particular calcifications.

The contribution of this thesis is twofold. First, we study the capacity of modern Multi-row Detector CT (MDCT) scanners in visualizing and quantifying small high density structures, as a function of the imaging parameter settings. This study not only provides insight into the capacities and limitations of current scanners, but also provides information on how to optimize measurement accuracy of small objects and how to interpret image measurements. Second, we develop and evaluate a method to improve the visualization and quantification of atherosclerotic plaque containing calcifications. This method is based on the selective deconvolution of small high-density structures in CT Angiography (CTA) image data. Below, we summarize in more detail the results obtained in the different chapters.

In **Chapter 2** different factors that affect the visualization and quantification of small high-density structures and their surrounding tissues are analyzed for a 64 MDCT scanner (Siemens AG, Medical Solutions, Erlangen, Germany). For this purpose, a custom made phantom consisting of Aluminum cylinders of known different diameters and lengths is scanned using different acquisition and reconstruction parameters. Then, the accuracy and uncertainty in measuring density, diameter, length, area and volume of each cylinder size is assessed. In addition, a bead phantom is imaged to estimate the Point Spread Function (PSF) for each imaging parameter setting, and simulations based on the PSF information are compared with the experimental results. Diameter, length, area and volume measurements are performed automatically using the 50% relative-threshold quantification method.<sup>1</sup>

We show that measurements on the simulated imaging data are in close agreement with those obtained in the experimental data. This indicates that, for objects with good Signal-to-Noise Ratio (SNR), errors in estimating object density and size mainly depend

on the actual object size and the system PSF. Therefore, we hypothesize that the results obtained in this study for the 64 MDCT can be extended to other imaging systems and protocols just by accounting for the differences in the PSF.

From the simulations and experiments we show that object density and size can accurately be determined (i.e. with a relative error smaller than ~5%) for objects larger than two times the Full Width at Half Maximum (FWHM) of the PSF in each direction of space (i.e., for object sizes larger than ~2.0 mm, with current MDCT scanners). Below this size, the Hounsfield Units (HUs) of the inner object voxels decrease, and size measurements are overestimated due to the Partial Volume Effect (PVE) both in the axial and transaxial directions. These findings are in agreement with the work presented by Prevrhal *et al.*<sup>1</sup>

To characterize atherosclerotic plaque and to assess the lumen of small arteries, increasing the spatial resolution by applying sharper kernels and thinner slice thickness seems a logical option. However, there is a trade-off owing to the associated increase in noise and artifacts. These two competing factors, which are partially patient dependent, make it very complicated to establish the optimal imaging parameter settings. In our experiments a good balance between spatial accuracy and SNR is achieved with a medium-sharp convolution kernel: i.e., B46. For this kernel, ringing artifacts are still negligible, and for the range of sizes larger than ~1 mm in each direction of space, the measurement accuracy rapidly increases with the object size (i.e., objects of 1.0 mm are overestimated by 11%, objects of 1.2 mm are overestimated by 5%, and objects larger than 2.5 mm are estimated with an error smaller than 4%). In the range of sizes smaller than ~1 mm, geometric measurements are not accurate: an average bias of 0.85 mm in each direction of space leads to large measurement overestimation in this range.

For clinical applications aimed at volume quantification of high-contrast objects (such as calcifications), sharper kernels, e.g. B60, are recommended. These kernels increase accuracy and reduce threshold dependency because object spread is reduced.

In **Chapter 3** we investigate the differences in image noise and measurement accuracy for two consecutive generations of CT systems that are currently used in clinical practice: i.e., the 16 and 64 MDCT scanners. The accuracy in measuring object attenuation and object size is assessed in the range of sizes near and under the spatial resolution of the system. Quantitative analyses are based on two different thresholding methods: fixed-threshold based quantification,<sup>2,3</sup> and the 50% relative-threshold based quantification.<sup>1</sup>

Quantitative analyses with the 50% relative threshold show that, in the range of object sizes smaller than 2.0-2.5 mm, measurement accuracy in the CT longitudinal direction is slightly, but not significantly, better for the 64 than for the 16 MDCT. Measurements in the transverse plane are very similar for the two scanners. For object sizes larger than 2.0-2.5 mm, both longitudinal and transverse geometric measurements are the same for the 16 and 64 MDCT scanners. However, when applying fixed-threshold quantification, measurement accuracy in the range of objects larger than ~1.5 mm is significantly better for the 64 MDCT.

Measurement accuracy obtained when using the 50% relative threshold mainly depends on the object size and the image PSF. Therefore, for the MDCT scanners being evaluated (whose PSFs' FWHM are  $\leq 1$  mm in each direction of space), measurement accuracy with the 50% relative-threshold is very high in the range of object sizes larger than  $\sim 2.0$ - $2.5$  mm. Above this interval measurements do not depend on the scanner and imaging protocol. However, with fixed thresholds geometric measurements are scanner and protocol dependent even for the range of sizes larger than  $\sim 2.0$ - $2.5$  mm. When using a fixed threshold, measurement accuracy depends not only on the object size and image PSF, but also on the attenuation values of the material surrounding the object. Another limitation of fixed thresholds is the missing of smaller/lower-density objects, even when their SNR is sufficiently high to be discriminated from their surrounding tissues.

The results as presented in Chapter 2 and 3 provide insight into the accuracy limits of state-of-the-art MDCT scanners in imaging small high-density objects. In Chapter 2 it is shown that the measured PSF is an effective means to predict small object measurement accuracy for a given scanning system and imaging protocol. Thus, this enables the interpretation of image measurements for structures in the range of sizes near or under the size of the scanner's PSF. Chapter 3 shows that both geometric measurement errors and inter-scanner/inter-protocol measurement variability can be reduced by applying the 50% relative-threshold quantification, instead of conventional fixed-threshold based quantification methods. Moreover, the data of Chapter 3 can be used to understand and interpret differences in results obtained from clinical studies that have been conducted using different scanners or imaging protocols. The knowledge generated in Chapter 3 can assist to develop quantification algorithms aimed to reduce inter-scanner and inter-protocol measurement variability.

**Chapter 4 and 5** investigate the use of selective digital image deconvolution to improve the imaging of small high-density structures, in particular calcifications. Digital image deconvolution is frequently used in applications where the system spatial resolution is insufficient to properly resolve small objects of interest from the background. Several authors<sup>4-8</sup> have recently applied deconvolution to improve clinical diagnosis in CT. Most of the work has been aimed at improving visualization of small bony structures in human anatomy. Some studies<sup>4,5</sup> suggested the application of this technique to enhance CTA vessel visualization. However, deconvolution to improve the visualization and quantification of atherosclerotic plaque calcifications has, to the best of our knowledge, not been performed and validated before.

A number of deconvolution algorithms have been developed with the goal of reducing image blur while increasing the SNR. Most of them are based on an iterative minimization of a measure reflecting the difference between the original image and the estimate of the "true" object obtained in each iteration.<sup>5-8</sup> Whereas these methods are powerful in improving the SNR, this comes at the expense of very long computational processing times. Computational requirements of 3D image deconvolution with a regularized Wiener filter are relatively small compared with iterative methods.<sup>4,5</sup> This makes the Wiener Filter more advantageous for clinical practice. In Chapter 4 and 5 a

novel method is proposed to locally deconvolve small high-density structures of the image, while avoiding noise amplification and edge-ringing artifacts on the remaining low-density tissues. This method, which we refer to as *Histogram-based Selective Deblurring* (HiSD), performs a strong 3D deconvolution with the Wiener Filter, and subsequently combines the image information of the original CT and its deconvolved data to generate a restored image.

To combine the original and deconvolved image, three regions of interest are defined: a region where the original image intensity is used (background), a region where the deconvolved image is used (small high intensity structures) and a transition region between those two regions. In the original image this transition region corresponded to structures which were affected by the blur of the small high intensity structures. The definition of these regions is achieved by a combination of different thresholds.

In **Chapter 4**, the HiSD method is applied and validated for CT images of phantom and in vitro carotid atherosclerotic plaques. In **Chapter 5**, HiSD is extended, and its performance is assessed on in vivo CTA images of carotid atherosclerotic plaques. The extension of the algorithm is twofold. First, the determination of the threshold values used to define the regions of interest is fully automated. Second, the estimation of the HUs in the *transition region* is improved by applying a weighted interpolation of the original and deconvolved image. This results in a more realistic image pattern around the calcification. Moreover, small calcifications are not missed because both original and deconvolved calcification peaks contribute positively to the interpolated value.

In order to apply HiSD on in vivo CTA data in Chapter 5, the problem of differentiating calcification from contrast-enhanced lumen had to be addressed. This differentiation is required in order to allow a restoration of the whole calcification volume while avoiding deconvolution artifacts in the contrast-enhanced vessels. To achieve this, 3D vessel segmentation is performed prior to applying HiSD, using a method introduced by Manniesing *et al.*<sup>9</sup> In our study, fully automated lumen segmentation was successfully achieved in 13 out of 15 plaque images, and in two cases (minor) manual editing was required.

Qualitative and quantitative analyses presented in Chapters 4 and 5 show that HiSD considerably improves the imaging of small high-density structures in phantom, in vitro, and in vivo enhanced CT images. After applying HiSD, calcification blur is reduced both in the transverse and longitudinal direction, while noise amplification and edge-ringing artifacts are avoided in the surrounding low-density tissues. Consequently, calcification overrepresentation is decreased and calcification SNR is increased, resulting in improved visualization. With HiSD, geometric measurements are significantly improved; reducing overestimation in the calcification volume, and reducing dependency of measurements on the quantification threshold. In Chapter 4, errors on the in vitro calcification area and volume measurements are on average reduced by 31% and 44%, respectively, after applying HiSD. In Chapter 5, both volume overestimation obtained with low quantification thresholds values ( $<430$  HU), and volume underestimation obtained with high threshold values ( $\geq 430$  HU) are significantly reduced (i.e., by 23.5% on average). Moreover, the difference between the in vivo and in vitro calcification

volume quantification with thresholds  $\geq 430$  HU is significantly reduced (to less than 5%) after applying HiSD.

For the quantitative validation of HiSD, high resolution micro-focus CT ( $\mu$ CT) imaging data have been used as reference for phantom, in vitro and in vivo CTA images. Compared with standard histology,  $\mu$ CT provides a more reliable reference for calcification measurements because it provides 3D image data, while not affecting the integrity of the plaque sample.<sup>10-12</sup> Although recent studies have indicated that  $\mu$ CT is a good reference for atherosclerotic plaque characterization, to the best of our knowledge, this is the first time that  $\mu$ CT has been used as reference for visual and quantitative analyses of atherosclerotic plaque CT images.

Compared to the use of sharp kernels, HiSD has a number of advantages. First, HiSD performs deconvolution of small high-density objects both in the  $xy$ -plane and along the  $z$ -axis, while current clinical reconstruction kernels do not implement deconvolution along the  $z$ -axis. Second, image noise is significantly lower for CT images restored with HiSD than for those reconstructed with sharp kernels (e.g., B60), as image noise of restored image remains in most part of the image the same as in the original image. In our study, the original CT images used as input for HiSD are reconstructed with medium to medium-sharp convolution kernels (i.e., B41, B46 and B50). However, HiSD can also be applied to images reconstructed with any other convolution kernels, with the only requirement that the PSF is measured a priori in order to apply the appropriate parameters in the Wiener Filter.

Whereas in this thesis only a limited number of experiments on in vitro and in vivo plaques have been performed, the results indicate that HiSD can improve both the visualization and quantification of calcifications. This is of particular importance in view of current research relating calcium in various vessel beds to cardiovascular disease. The correlation between coronary calcium and the overall incidence of coronary disease has now firmly been established.<sup>13,14</sup> Moreover, some authors<sup>15,16</sup> have reported a strong relationship between coronary calcification and the atherosclerotic arterial plaque burden. Finally, recent studies<sup>17</sup> have suggested that the distribution pattern of calcified deposits within coronary arteries may be of greater predictive value for plaque instability than the overall calcification amount.

In this thesis, HiSD has mainly been applied to CT images of atherosclerotic plaque calcifications. However, the method can also be used to improve diagnosis in other clinical applications where blur of small high-density structures hamper vessel analysis. In Chapter 4 we show two examples of other possible applications of HiSD. First, the method is applied to in vivo CTA images of atherosclerotic intracranial arteries. Second, it is applied to in vivo CTA images of stented renal arteries. In the first case, we show that HiSD improves discrimination between arterial calcifications and intracranial bones. In the second case, HiSD reduces partial volume effects between stent struts and

contrast-enhanced lumen. Therefore, the images are qualitatively improved. Further work is required to quantitatively validate HiSD on these applications.

## General conclusions

Despite the progress of MDCT scanners, the imaging of small structures remains a challenge. Proper imaging parameter settings in combination with suitable quantification methods should be used to optimize the accuracy of geometric measurements. It has been found that measurement accuracy can be well predicted from the image noise and the PSF of a given system and imaging protocol. Selective image deconvolution provides a means to improve image quality of the reconstructed CT image in view of the clinical interest.

## References

1. Prevrhal S, Engelke K, Kalender WA. Accuracy limits for the determination of cortical width and density: the influence of object size and CT imaging parameters. *Phys Med Biol.* 1999; 44:751-764.
2. Yoon HC, Greaser LE, Mather R, *et al.* Coronary artery calcium: Alternate methods for accurate and reproducible quantitation. *Acad Radiol.* 1997; 4:666-673.
3. Ulzheimer S, Kalender WA. Assessment of calcium scoring performance in cardiac computed tomography. *Eur Radiol.* 2003; 13:484-497.
4. Sakai O, Shen Y, Takata Y, *et al.* The use of deblurring technique for improving the longitudinal resolution in helical CT of the head and neck region. *Comput Med Imag Grap* 1997; 21:153-164.
5. Schlueter FJ, Wang G, Hsieh PS, *et al.* Longitudinal image deblurring in spiral CT. *Radiology.* 1994; 193:413-8.
6. Wang G, Skinner MW, Vannier MW. Temporal bone volumetric image deblurring in spiral computed tomography scanning. *Acad Radiol.* 1995; 2:888-95.



7. Wang G, Vannier MW, Skinner MW, *et al.* Spiral CT image deblurring for cochlear implantation. *IEEE Trans Med Imaging*. 1998; 17:251-62.
8. Jiang M, Wang G, Skinner MW, *et al.* Blind deblurring of spiral CT images-comparative studies on edge-to-noise ratios. *Med Phys*. 2002; 29:821-9.
9. Manniesing R, Velthuis BK, van Leeuwen MS, *et al.* Level set based cerebral vasculature segmentation and diameter quantification in CT angiography. *Med Image Anal*. 2006; 10:200-214.
10. Rakebrandt F, Crawford DC, Havard D, *et al.* Relationship between ultrasound texture classification images and histology of atherosclerotic plaque. *Ultrasound Med Biol*. 2000; 26:1393-1402.
11. Langheinrich AC, Bohle RM, Greschus S, *et al.* Atherosclerotic lesions at micro CT: Feasibility for analysis of coronary artery wall in autopsy specimens. *Radiology* 2004; 231:675-681.
12. Marxen M, Thornton MM, Chiarot CB, *et al.* MicroCT scanner performance and considerations for vascular specimen imaging. *Med Phys* 2004; 31:305-13.
13. Shaw LJ, Raggi P, Schisterman E, *et al.* Prognostic Value of Cardiac Risk Factors and Coronary Artery Calcium Screening for All-Cause Mortality. *Radiology*. 2003;228:826-833
14. Pham PH, Rao DS, Vasunilashorn F, *et al.* Computed tomography calcium quantification as a measure of atherosclerotic plaque morphology and stability. *Invest Radiol*. 2006; 41:674-680.
15. Rumberger JA, Simons DB, Fitzpatrick LA, *et al.* Coronary Artery Calcium Area by Electron Beam Computed Tomography and Coronary Atherosclerotic Plaque Area. A Histopathologic Correlative Study. *Circulation*. 1996 Aug 1;94(3):588.
16. Sangiorgi G, Rumberger JA, Severson A, *et al.* Arterial calcification and not lumen stenosis is highly correlated with atherosclerotic plaque burden in humans: a histologic study of 723 coronary artery segments using nondecalcifying methodology. *J Am Coll Cardiol*. 1998; 31:126-33.
17. Ehara S, Kobayashi Y, Yoshiyama M, *et al.* Spotty calcification typifies the culprit plaque in patients with acute myocardial infarction: an intravascular ultrasound study. *Circulation*. 2004;110:3424-3429.



# Appendix

## Image Quality (IQ) Obtained with HiSD Restoration versus IQ Obtained with Clinical CT Convolution Kernels

### Objectives

To compare the accuracy in imaging small high-density structures that is obtained with standard clinical convolution kernels with that obtained after restoring the image with the Histogram-based Selective Deblurring (HiSD) application.

### Materials and Methods

Phantom experiments and different quantification methods are used to establish size measurement accuracy, object spread, object signal, and image noise, for the original CT images (reconstructed with a medium, B41, and a sharp, B60, convolution kernels), and the images restored with HiSD.

### Results

Compared with clinical convolution kernels (that only perform on the CT  $xy$ -plane), restored images deconvolve small high-density objects both in the  $xy$ -plane and along the  $z$ -axis. Therefore, measurement accuracy along the  $z$ -axis is significantly higher in the restored images than in the original CT images, independently of the kernel used in the reconstruction. The amount of deblurring obtained in the  $xy$ -plane with HiSD restoration is lower than that obtained with kernel B60. However, small object volume measurement accuracy achieved in the restored images is as high as that in the original images reconstructed with B60. The advantage of restored images is that their level of noise is significantly lower, and, consequently, their Signal-to-Noise Ratio (SNR) is significantly better.

### Conclusion

HiSD image restoration improves CT volume measurement accuracy to the same extent as that obtained with clinically available high-resolution kernels (ie, B60), while keeping noise and artifacts to the same level as those obtained with non-enhancing convolution kernels (ie, B41).

## A.1 Introduction

In Chapter 5, *Histogram Selective Deblurring* (HiSD) is implemented and validated for in vivo Computed Tomography Angiography (CTA) data. The results show that HiSD, combined with vessel segmentation, improves visualization and quantification of atherosclerotic calcifications. However, it is also necessary to show that HiSD provides a further improvement of the image quality compared with sharp kernels clinically available. The aim of this Appendix is to compare the image quality obtained with HiSD with the image quality obtained with a medium, B41, and a sharp, B60, convolution kernels (Siemens Medical Solutions). In Chapter 2 we evaluated different convolution kernels available in Siemens Medical Solutions Multi-row Detector CT (MDCT) image reconstruction packages. The results showed that the sharper the kernels, the higher the measurement accuracy, but at the expense of increasing noise and ringing artifacts. When comparing the four sharpest kernels, B50, B60, B70, and B80 (from least to most edge-enhancing), we found that B70 and B80 did not significantly improve measurement accuracy compared with B60. However, noise and artifacts were significantly increased for B70 and B80. On the other hand, we found that B41 performs quite neutral, ie, it does not noticeably enhance neither smooth image edges. Therefore, for this study we have chosen kernel B41 to reconstruct the input image for the HiSD application, and kernel B41 and B60 to compare the image quality after restoration. All the measurements are performed for phantom CT images, and image quality is evaluated in terms of measurement accuracy, object borders spread, and Signal-to-Noise Ratio (SNR).

## A.2 Materials and Methods

### A.2.1 Phantom description

The “Small high-density structures” phantom<sup>1-4</sup> (Fig. A.1) was used to show the performance of HiSD compared with the performance of clinically available sharp convolution kernels.

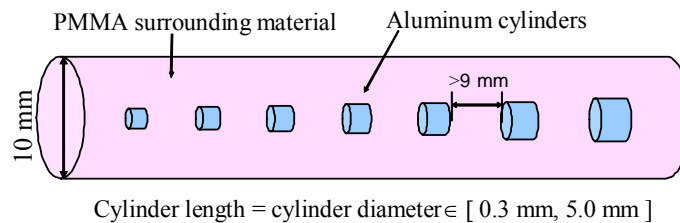


**Figure A.1.** Schematic drawing of the “Small high-density structures” phantom. The 10 mm diameter Polymethyl Methacrylate (PMMA) cylindrical module embeds 17 small Aluminum (Al) cylinders which diameters and lengths range from 0.3 to 5.0 mm. The aluminum cylinders are arranged parallel to the axis of PMMA cylinder, which represents a mildly enhanced lumen.

### A.2.2 Imaging acquisition and reconstruction

Phantom CT images were acquired on a 64-Slice MSCT system (*Somatom Sensation 64*; Siemens Medical Systems), using a standardized high-resolution protocol<sup>1,2</sup> (120 kVp, 249 mAs, collimation 32×0.6 mm, effective slice thickness 0.6 mm, pitch 0.45, field of view 50 mm; and reconstruction increment 0.3 mm). Two different convolution kernels, a medium B41 and a sharp B60 (Siemens Medical Solutions) were selected to reconstruct the images. The phantom was scanned within a cylindrical module of water, 16 cm in diameter, to achieve a realistic attenuation environment. Phantom scans were repeated three times to assess inter-scan variability for the original and restored images. Independent restorations and quantifications were performed for each of the three scans.

### A.2.3 Evaluation of the image quality

Image quality of the CT original images reconstructed with kernels B41 and B60, and the restored image obtained after applying HiSD to the CT original image B41, is compared using a number of quantitative analyses on the phantom data. The analyses include measurements of image noise, SNR, and object size in the *xy*-plane and along the *z*-axis. For the analysis of the geometric accuracy, measurements of diameter, length and volume of the 17 aluminum phantom cylinders are performed. The two relative threshold values used for quantification are calculated, respectively, as the values at the 10% and at the 50% between the mean HU of the background material (PMMA) and the maximum HU of each cylinder.<sup>1,2,5</sup> The difference between the measurements obtained with these two relative thresholds is determined for the cylinder diameter and length, and referred to as  $C_\phi$  and  $C_l$ , respectively. The measures  $C_\phi$  and  $C_l$  provide an estimate of the object spread in the *xy*-plane and along the *z*-axis for each image resolution.<sup>1,2</sup>

To assess inter-scan variability for the phantom quantitative analyses, the phantom was scanned three times, and independent reconstructions and restorations were performed for each of the three scans. The phantom was scanned within a cylindrical module of water, 16 cm in diameter, using a relatively low tube current (i.e. 300 mAs) to achieve a realistic attenuation environment. For the phantom quantification, the mean absolute error,  $\Delta\bar{x}$ , of the estimated mean value of the three measurements obtained from

each of the three scans,  $\bar{x}$ , was calculated as  $\Delta\bar{x} = t \frac{\sigma}{\sqrt{N}}$ , where  $\sigma$  is the standard

deviation of the measurements ( $N$ ), and  $t$  is the so-called *t*-factor. The *t*-factor corrects for a small number of measurements, and for  $N=3$  and a probability  $p=95\%$  that a measurement falls within the interval  $[\bar{x} - \Delta\bar{x}, \bar{x} + \Delta\bar{x}]$ , the value of  $t$  is equal to 4.3.<sup>6</sup>

### Statistics

Quantification errors obtained in the original and restored images are compared with the two-sample unequal variance Student's *t*-Test. A *p*-value <0.05 is considered statistically significant.

### A.3 Results

Figures A.2-A.5 show the quantitative analyses for the phantom images obtained with kernels B60, and B41, and after applying HiSD. In Fig. A.2 it can be observed that after applying HiSD measurement accuracy with the 50% relative threshold is improved in the range of sizes smaller than  $\sim 1.2$  mm. In this of sizes the measurements obtained for the restored images are statistically the same as those obtained with kernel B60. Object spread in the  $xy$ -plane is significantly reduced after restoration (see measurements with the 10% relative threshold and values of  $C_\phi$  for the original B41 and restored B41). However, it is still larger than for the kernel B60. Fig. A.3 shows the length measurements, i.e. the geometric accuracy along the  $z$ -axis. It can be observed that measurement accuracy of kernels B41 and B60 is the same, while after HiSD restoration length measurements improve significantly. Consequently, object spread along the  $z$ -axis ( $C_l$ ) is significantly smaller for the restored B41 than for both the original B41 and B60 images, which have statistically the same value of  $C_l$  (see Fig. A.5). As result of the combination of both the  $xy$ - and  $z$ - spatial resolutions, we obtain (see Fig. A.4) that volume measurement accuracy in the range of objects  $\leq 2$  mm is statistically the same for the restored B41 and the original B60, and significantly higher than that for the original image B41. For both the restored B41 and the original B60, small object signal is significantly higher than that for the original B41. In Fig. A.5 it can be observed that image noise and ringing artifacts are not increased after HiSD restoration (these are same for the original B41 and the restored B41). Consequently, noise and artifacts of restored images are significantly lower than those of original images reconstructed with B60. As result of the signal enhancement achieved with HiSD and the avoidance of ringing artifacts, small object SNR is significantly better for the restored images than for both the original B41 and B60.

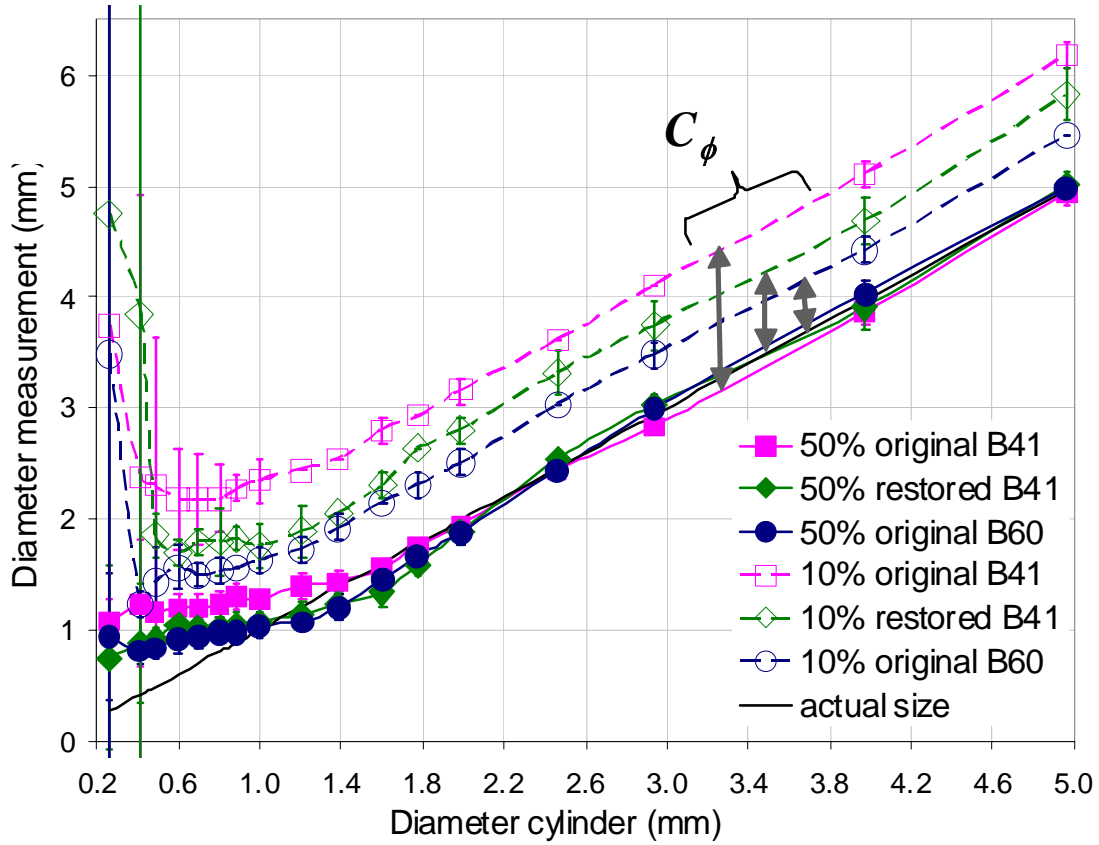


**Figure A.2.** Cylinder diameter obtained with the 10% and the 50% relative thresholds for the original B41, original B60, and restored B41 (which is the output of the HiSD application on the original image B41).

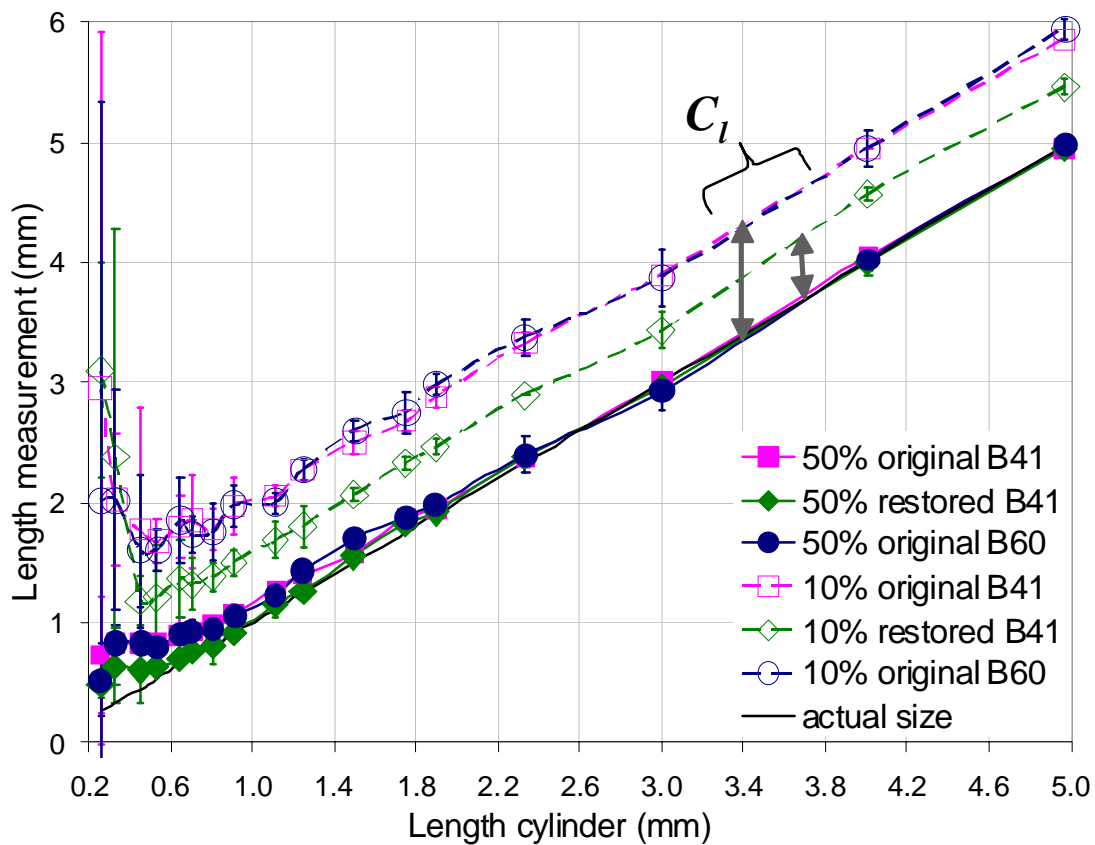


**Figure A.3.** Cylinder length obtained with the 10% and the 50% relative thresholds for the original B41, original B60, and restored B41.



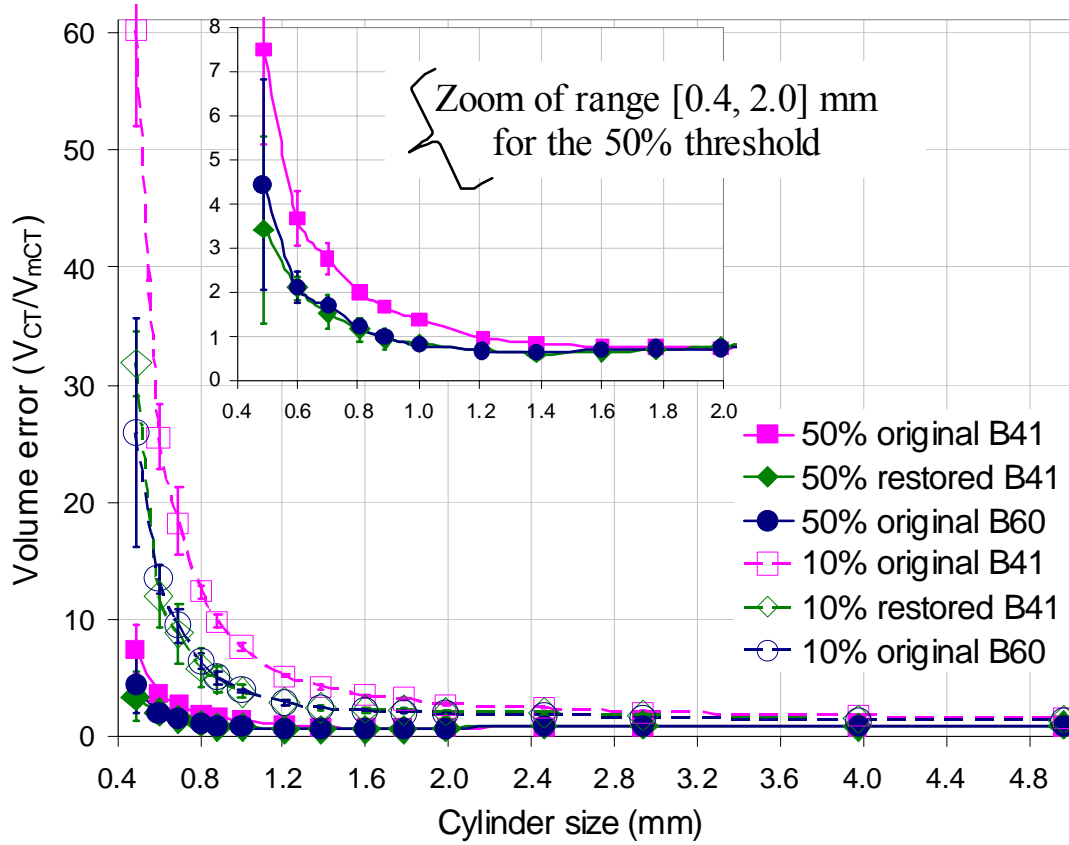


**Figure A.4.** Relative error in the cylinder volume measured with the 50% relative threshold for the original B41, original B60, and restored B41.

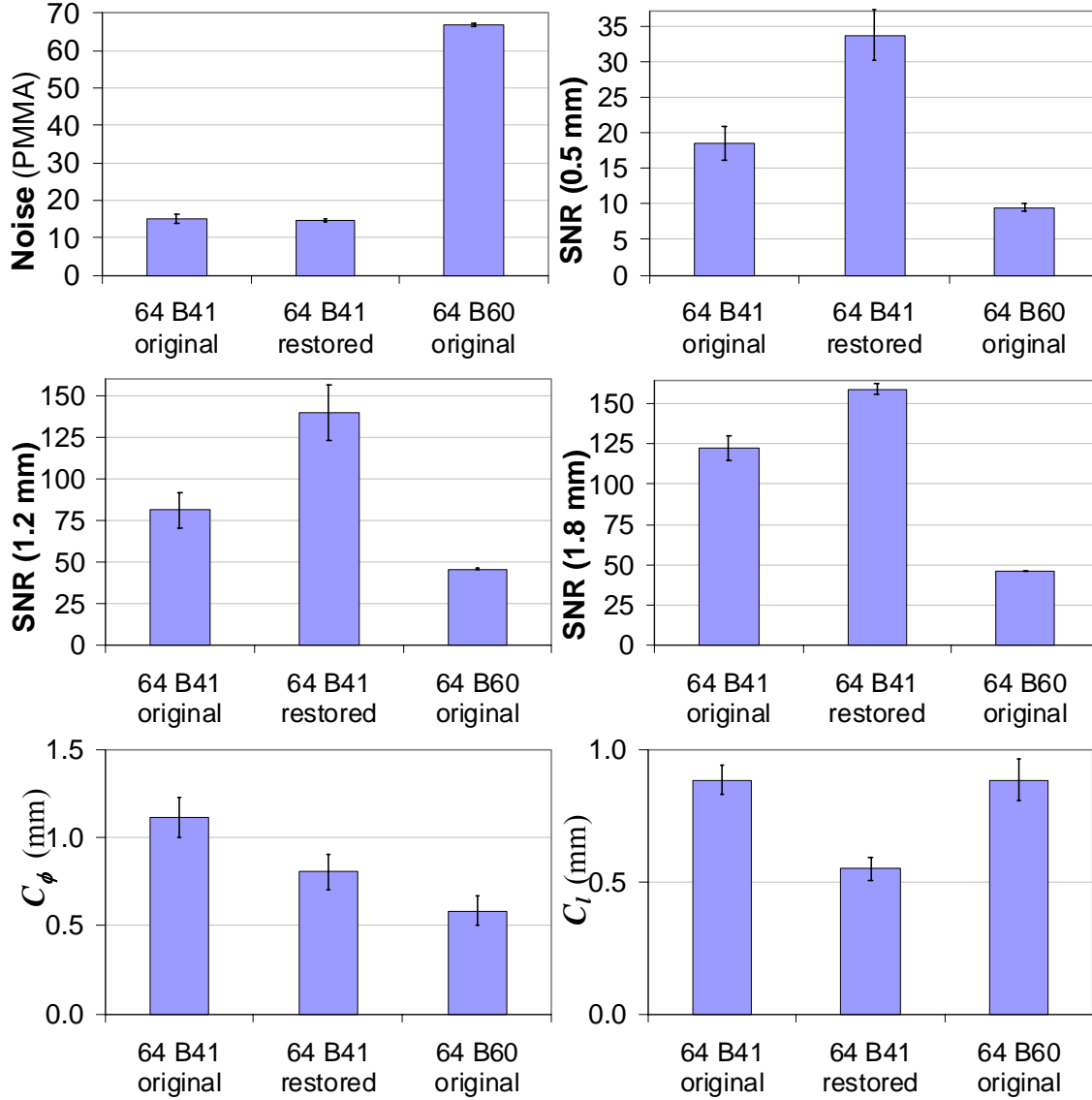


**Figure A.5.** (From left to right, top to bottom) Image noise measured as the standard deviation of the HUs in the PMMA module;<sup>3</sup> SNR in the range of small cylinder sizes, i.e.: for the cylinders with diameters and lengths of 0.5, 1.2 and 1.8 mm; and object spread in the  $xy$ -plane ( $C_\phi$ ) and along the  $z$ -axis ( $C_l$ ), for the original B41, restored B41, and original B60.

## **A.4. Discussion**

The results of our phantom analyses show that HiSD reduces blur of small high-density structures in the three directions of space, without introducing noise and ringing artifacts in the surrounding structures. This improves small object SNR and geometric measurement accuracy.

Image quality analyses show the advantages of HiSD versus clinically available high-resolution convolution kernels (e.g. B60): On one hand, in our restored images small high-density objects are deconvolved both in the  $xy$ -plane and along the  $z$ -axis. Instead, current clinical convolution kernels do not implement deconvolution along the  $z$ -axis. On the other hand, image noise is significantly lower for our restored images than for original images reconstructed with kernel B60. This is due to the fact that image noise of restored images remains the same as in the original input CT image (which should be reconstructed with a medium kernel, e.g. B41, to avoid either enhancement or smoothing of high frequencies in the raw CT image data).

The amount of deblurring obtained in the  $xy$ -plane for the restored images is lower than that obtained for kernel B60. However, the amount of deblurring obtained in the restored image is influenced by the kernel applied to reconstruct the image that is used as input for HiSD. Therefore, the strength of deblurring in the  $xy$ -plane can be increased if the input image of HiSD is reconstructed with a kernel slightly sharper than B41; e.g. B46. Additional analyses and experiments showed that when HiSD is applied to images reconstructed with kernel B41, the amount of deblurring obtained in the  $xy$ -plane is equivalent to that obtained with kernel B46; and when it is applied to images reconstructed with B46, the deblurring comes close to that obtained with kernel B60. Therefore, the paid off of decreasing  $xy$ -blur in the restored image is the introduction of noise and ringing artifacts associated to sharper clinical kernels. Note that image noise and ringing artifacts obtained with the kernel B46 are significantly stronger than those obtained with B41 (see values in Table 2.3 of Chapter 2).

## **Conclusions**

HiSD image restoration improves CT volume measurement accuracy to the same extent as that obtained with clinically available high-resolution kernels (ie, B60), while keeping noise and artifacts to the same level as those obtained with non-enhancing convolution kernels (ie, B41).

## References

1. Rollano-Hijarrubia E, Stokking R, van der Meer F., *et al.* Imaging of small high-density structures in CT: a phantom study. *Acad Radiol.* 2006, 13(7):893-908.
2. Rollano-Hijarrubia E, Stokking R, Niessen WJ. Accuracy Comparison of a 16 and 64 MDCT Scanner to Image Small High-density Structures. *Invest Radiol.* 2006; 41:781-792.
3. Rollano-Hijarrubia E, Niessen W, Weinans H, *et al.* Histogram-based selective deblurring to improve computed tomography imaging of calcifications. *Invest Radiol.* 2007; 42:8-22.
4. Rollano-Hijarrubia E, Manniesing R, Niessen WJ. Histogram-based Selective Deblurring and Automated Vessel Segmentation for Improved In Vivo Calcification Visualization and Quantification in CTA. *In preparation to be submitted.*
5. Prevrhal S, Engelke K, Kalender WA. Accuracy limits for the determination of cortical width and density: the influence of object size and CT imaging parameters. *Phys Med Biol.* 1999; 44:751-64.
6. Ulzheimer S, Kalender WA. Assessment of calcium scoring performance in cardiac computed tomography. *Eur Radiol* 2003; 13:484-497.

## Samenvatting en discussie

Het afbeelden van kleine structuren met hoge dichtheid, zoals calcificaties en stents, met behulp van Computed Tomografie (CT) is van groot belang voor de diagnose, de behandeling en het volgen van patiënten met hart- en vaatziekten. De kwantificatie van calcificaties wordt in toenemende mate gezien als mogelijke indicator van de ernst van hart- of vaatziekte. Nauwkeurige kwantificatie van calcificaties wordt echter gehinderd door de beperkte resolutie van de CT beelden, waardoor deze structuren vervagen. De vervaging van structuren met hoge dichtheid belemmert ook de afbeelding van het zachte weefsel naast deze structuren. Als gevolg hiervan is het bijvoorbeeld moeilijk om de mate van vernauwing van een bloedvat vast te stellen in de nabijheid van calcificaties of stents. Het in dit proefschrift beschreven onderzoek is erop gericht om de afbeelding en kwantificatie van kleine structuren met hoge dichtheid, en dan met name calcificaties, te verbeteren.

De bijdrage van dit proefschrift is tweeledig. Allereerst worden de mogelijkheden van moderne *multi-detector row* CT (MDCT) scanners bestudeerd: er is een studie gedaan naar de afbeelding en kwantificatie van kleine structuren als functie van de beeldingsparameters. Deze studie geeft niet alleen inzicht in de mogelijkheden en beperkingen van moderne scanners, maar geeft ook informatie over hoe de meetnauwkeurigheid geoptimaliseerd kan worden, en hoe metingen geïnterpreteerd dienen te worden. Daarnaast is een methode ontwikkeld en geëvalueerd om gecalcificeerde atherosclerotische plaque af te beelden en te kwantificeren. Deze methode is gebaseerd op selectieve deconvolutie van kleine structuren met hoge dichtheid in CT angiografie (CTA) beelddata. In het navolgende worden de resultaten zoals besproken in de hoofdstukken van dit proefschrift samengevat.

In Hoofdstuk 2 worden verschillende factoren geanalyseerd die de afbeelding en kwantificatie van kleine structuren van hoge dichtheid en het omliggende weefsel beïnvloeden. Het onderzoek is uitgevoerd met beelden verkregen met een 64 MDCT scanner (Siemens AG, Medical Solutions, Erlangen, Germany). Ten behoeve van de studie is een fantoom ontworpen, bestaande uit aluminium cilinders met verschillende (bekende) diameters en lengtes. Dit fantoom is gescand met verschillende instellingen voor de beeldacquisitie en beeldreconstructie. Vervolgens is de nauwkeurigheid en onzekerheid bepaald van dichtheid, diameter, lengte, oppervlak en volume metingen van elke cilinder. Daarnaast is een fantoom met metalen bolletjes gescand om de zogenaamde *point spread function* (PSF) te bepalen voor elk van de acquisitie- en reconstructieinstellingen. Simulaties gebaseerd op de gemeten PSF zijn vergeleken met de resultaten van de experimenten. Diameter, lengte, oppervlak en volume metingen zijn automatisch gedaan, volgens de 50 % relatieve drempel kwantificatie methode.<sup>1</sup>

De metingen in de gesimuleerde data blijken nauw overeen te stemmen met de metingen verkregen uit de experimentele data. Dit toont aan dat, voor structuren met een goede SNR, fouten in schattingen van de dichtheid en afmetingen van de structuur met name afhangen van de grootte van de structuur en de PSF van het systeem. Onze hypothese is dat de resultaten van deze studie voor een 64-slice MDCT scanner ook gelden voor andere beeldvormende systemen en andere beeldacquisities mits er rekening gehouden wordt met de verschillen in de PSF.

De simulaties en experimenten laten ook zien dat de dichtheid en afmeting van een structuur nauwkeurig bepaald kunnen worden (i.e. met een relatieve fout kleiner dan ~5 %) voor structuren die in elke richting groter zijn dan twee maal de FWHM van de PSF (i.e. voor structuren met een afmeting groter dan ~2.0 mm, voor de huidige generatie MDCT scanners). Voor structuren van kleinere afmetingen neemt de Hounsfield waarde (HU) van de voxels in de structuur af en worden de afmetingen van de structuur overschat. Dit wordt veroorzaakt door het *partial volume effect* (PVE) in de axiale en transaxiale richtingen. Deze bevindingen zijn in overeenstemming met het werk van Prevhal *et al.*<sup>1</sup>

Het lijkt logisch om ten behoeve van de karakterisatie van atherosclerotisch plaque en voor het bepalen van de lumen diameter in kleine bloedvaten, de spatiële resolutie te verhogen door scherpere reconstructiekernels en een kleinere plakdikte te hanteren. Een hogere spatiële resolutie leidt echter ook tot meer ruis en artefacten. Deze tegenstrijdige factoren, die ook nog eens voor een deel patiënt-afhankelijk zijn, maken de keuze van optimale instellingen voor het afbeelden gecompliceerd. In onze experimenten werd een goede balans tussen spatiële nauwkeurigheid en SNR verkregen met een gemiddeld scherpe reconstructiekernel: B46. Bij gebruik van dit filter zijn de ring artefacten nog verwaarloosbaar, terwijl voor structuren met afmetingen groter dan ~1 mm in elke richting de meetnauwkeurigheid snel toeneemt met de afmeting van de structuur (i.e. structuren van 1.0 mm worden 11 % overschat, structuren van 1.2 mm worden 5 % overschat, en structuren groter dan 2.5 mm hebben een fout die kleiner is dan 4 %). Geometrische metingen aan structuren met afmetingen kleiner dan ~1 zijn niet nauwkeurig: een gemiddelde bias van 0.85 mm in elke richting zorgt voor grote overschattingen in de afmetingen.

Scherpere reconstructiekernels (bijvoorbeeld B60) worden aanbevolen voor klinische toepassingen die gericht zijn op het kwantificeren van het volume van structuren met hoog contrast (zoals calcificaties). Deze kernels vergroten de nauwkeurigheid en verminderen de afhankelijkheid van de drempels, omdat de structuur minder vervaagd wordt.

In Hoofdstuk 3 onderzoeken we de verschillen in beeldruis en meetnauwkeurigheid tussen twee opeenvolgende generaties van CT scanners die momenteel in de klinische praktijk gebruikt worden: de 16 en 64 MDCT scanners. De nauwkeurigheid in het meten van de verzwakking en afmeting van een structuur is bepaald voor structuren met afmetingen die vergelijkbaar zijn met en kleiner zijn dan de spatiële resolutie van het systeem. De kwantitatieve analyses zijn gebaseerd op twee verschillende drempel

methoden: de vaste drempel gebaseerde kwantificatie<sup>2,3</sup> en de 50 % relatieve drempel gebaseerde kwantificatie (FWHM).<sup>1</sup>

De kwantitatieve analyses met de 50% relatieve drempel laten voor structuren kleiner dan 2.0—2.5 mm zien dat de meetnauwkeurigheid in de longitudinale richting enigszins, maar niet significant, beter is voor de 64 dan voor de 16 MDCT scanner. Metingen in de transversale richting zijn voor beide scanners vergelijkbaar. Voor structuren groter dan 2.0—2.5 mm zijn de geometrische metingen in zowel de longitudinale als de transversale richting voor de beide scanners hetzelfde. Echter, als de vaste drempel gebaseerde kwantificatie gehanteerd wordt, dan is de meetnauwkeurigheid voor structuren groter dan ~1.5 mm significant beter voor de 64 MDCT scanner.

De meetnauwkeurigheid die verkregen wordt wanneer de FWHM drempel methode gehanteerd wordt, hangt met name af van de afmeting van de structuur en de PSF van het beeld. Voor de MDCT scanners die geëvalueerd zijn is de FWHM van de PSF  $\leq 1$  mm in elke richting, daarom is de meetnauwkeurigheid met de 50 % relatieve drempel erg hoog voor structuren die groter zijn dan ~2.0—2.5 mm. Voor structuren boven deze grens hangen de metingen niet af van de scanner en het beeldvormingsprotocol. De geometrische metingen met de vaste drempel methode daarentegen hangen wel af van scanner en beeldvormingsprotocol voor structuren groter dan ~2.0—2.5 mm. Bij een vaste drempel hangt de meetnauwkeurigheid niet alleen af van de afmeting van de structuur en de PSF, maar ook van de verzwakkingswaarden van het weefsel rondom de structuur. Een andere beperking van het gebruik van vaste drempels is dat het kan leiden tot het missen van kleinere structuren of structuren met een lagere dichtheid, zelfs wanneer de signaal-ruis verhouding voldoende hoog is om deze structuren te onderscheiden van het omliggende weefsel.

De resultaten van Hoofdstuk 2 en 3 geven inzicht in de grenzen aan de nauwkeurigheid van het afbeelden van kleine structuren met hoge dichtheid met moderne MDCT scanners. Hoofdstuk 2 laat zien dat de gemeten PSF een effectief middel is om voor een gegeven scanner en beeldvormingsprotocol de meetnauwkeurigheid voor kleine structuren te voorspellen. Dit maakt de interpretatie mogelijk van metingen aan structuren die afmetingen hebben die ongeveer even groot zijn als of kleiner zijn dan de PSF van de scanner. Hoofdstuk 3 laat zien dat zowel de geometrische meetfouten als de variabiliteit in metingen tussen verschillende scanners en beeldvormingsprotocollen verminderd kan worden door gebruik te maken van de 50 % relatieve drempel kwantificatie, in plaats van de gebruikelijke vaste drempel kwantificatie. Daarnaast kunnen de gegevens uit Hoofdstuk 3 gebruikt worden voor de interpretatie van resultaten die verkregen zijn in klinische studies waarbij verschillende scanners en/of beeldvormingsprotocollen zijn gebruikt. De kennis opgedaan in Hoofdstuk 3 kan gebruikt worden bij het ontwikkelen van kwantificatie algoritmen die de variabiliteit in metingen tussen verschillende scanners en/of beeldvormingsprotocollen minimaliseren.

In Hoofdstuk 4 en 5 wordt selectieve digitale beeld deconvolutie voor de verbetering van het afbeelden van kleine structuren met hoge dichtheid onderzocht. Digitale beeld deconvolutie wordt vaak gebruikt in toepassingen waar de spatiële resolutie van het systeem onvoldoende is om kleine structuren goed te onderscheiden van de achtergrond.

Deconvolutie is recentelijk door een aantal auteurs<sup>4-8</sup> toegepast om de klinische diagnose in CT te verbeteren. Het grootste deel hiervan was erop gericht de afbeelding van kleine botstructuren te verbeteren. Een aantal studies<sup>4-5</sup> stelt voor om deze techniek toe te passen om de afbeelding van bloedvaten met CTA te verbeteren. Deconvolutie voor het verbeteren van de afbeelding en kwantificatie van calcificaties in atherosclerotische plaque is echter, voor zover wij weten, niet eerder toegepast en gevalideerd.

Er zijn deconvolutie algoritmes die een vermindering van de vervaging van het beeld beogen en tegelijk de SNR verbeteren. De meeste van deze algoritmes zijn gebaseerd op iteratieve minimalisatie van een maat die in elke iteratie het verschil weergeeft tussen het oorspronkelijke beeld en een schatting van de “werkelijke” structuur.<sup>5-8</sup> Deze methoden zijn erg goed in het verbeteren van de signaal-ruis verhouding, maar bereiken dit slechts ten koste van zeer lange rekentijden. De vereiste rekenkracht voor een 3D beeld deconvolutie met een geregulariseerd Wiener filter is klein vergeleken met deze iteratieve methoden.<sup>4,5</sup> Daarom is het Wiener filter meer geschikt voor de klinische praktijk. In Hoofdstuk 4 en 5 wordt een nieuwe methode geïntroduceerd die lokaal kleine structuren met hoge dichtheid deconvolueert, waarbij versterking van de ruis en ring artefacten in de overige weefsels vermeden worden. Deze methode, die we Histogram-gebaseerde Selectieve Deblurring (HiSD) noemen, bestaat uit een sterke 3D deconvolutie met het Wiener Filter, en een vervolgstap waarin een gerestaureerd beeld wordt verkregen door het oorspronkelijke CT beeld met het gedeconvolueerde beeld te combineren.

Voor de combinatie van het originele en gedeconvolueerde beeld worden drie gebieden onderscheiden: een gebied waar de intensiteit van het originele beeld wordt gebruikt (achtergrond), een gebied waar het gedeconvolueerde beeld wordt gebruikt (kleine structuren met hoge intensiteit) en een overgangsgebied tussen deze twee gebieden. In het oorspronkelijke beeld correspondeert dit overgangsgebied met structuren die aangetast worden door de vervaging van de kleine structuren met hoge intensiteit. De verschillende gebieden worden bepaald door een combinatie van een aantal drempels.

In Hoofdstuk 4 wordt de HiSD methode toegepast en gevalideerd voor CT beelden van een fantoom en in-vitro atherosclerotische plaque van de halsslagaders. In Hoofdstuk 5 wordt HiSD uitgebreid, en wordt de toepassing voor in-vivo CTA beelden van atherosclerotische plaque in de halsslagaders geëvalueerd. De uitbreiding van het algoritme is tweeledig ten opzichte van Hoofdstuk 4. Allereerst worden de drempelwaarden die de verschillende gebieden bepalen volledig automatisch bepaald. Daarnaast wordt de schatting van de HU in het overgangsgebied verbeterd door een gewogen interpolatie van het oorspronkelijke en het gedeconvolueerde beeld. Dit geeft een realistischer beeld rond de calcificaties. Verder worden kleine calcificaties niet gemist omdat de pieken van zowel de originele als de gedeconvolueerde calcificaties positief bijdragen aan de geïnterpoleerde waarde.

Om HiSD op in-vivo CTA beelden te kunnen toepassen, is het van belang calcificaties te kunnen onderscheiden van het lumen van het bloedvat, wat door het contrast middel ook hoge waarden heeft. Dit onderscheid is noodzakelijk voor een restauratie van alle calcificaties, waarbij gelijktijdig deconvolutie artefacten in het met contrast middel



gevulde lumen van de vaten voorkomen worden. Daarom wordt er, voordat HiSD wordt toegepast, een 3D vat segmentatie uitgevoerd volgens een methode beschreven door Manniesing *et al.*<sup>9</sup> In onze studie was volledig automatisch segmentatie van het lumen van het vat succesvol in 13 van de 15 beelden. In twee gevallen was (beperkte) handmatige correctie nodig.

De kwalitatieve en kwantitatieve analyses in Hoofdstuk 4 en 5 laten zien dat HiSD het afbeelden van kleine structuren met hoge intensiteit in fantomen, en in in-vivo en in-vitro CT beelden aanzienlijk verbeterd. De vervaging van de calcificaties is na de toepassing van HiSD minder in zowel de transversale als de longitudinale richting, terwijl de versterking van ruis en ring artefacten in het omliggende weefsel voorkomen worden. Als gevolg hiervan wordt de overrepresentatie van de calcificaties minder en de SNR van de calcificaties beter, wat leidt tot betere afbeelding van de calcificaties. Bij het gebruik van HiSD zijn de geometrische metingen significant beter; zowel de overschatting van het volume van de calcificaties als de afhankelijkheid van de metingen van de gebruikte drempel nemen af. In Hoofdstuk 4 leidt de toepassing van HiSD tot een vermindering van fouten in de in-vitro metingen van oppervlakte en volume van de calcificaties van respectievelijk 31 % en 44 %. In Hoofdstuk 5 worden zowel volume overschatting bij lage kwantificatie drempels ( $< 430$  HU) als volume onderschatting bij hoge kwantificatie drempels ( $\geq 430$  HU) significant kleiner (i.e. gemiddeld 23.5 %). Ook het verschil tussen de kwantificatie van het volume van de calcificaties in-vivo en in-vitro bij drempels  $\geq 430$  HU is significant minder (tot minder dan 5 %) na toepassing van HiSD.

Voor de kwantitatieve validatie van HiSD zijn hoge resolutie micro CT ( $\mu$ CT) beelden gebruikt als referentie voor de fantoom, in-vitro en in-vivo CTA beelden.  $\mu$ CT beelden zijn een betrouwbaardere referentie voor metingen aan calcificaties dan standaard histologie, omdat  $\mu$ CT 3D beelden geeft, en de integriteit van het plaque specimen niet aantast.<sup>10-12</sup> Hoewel recente studies aangeven dat  $\mu$ CT een goede referentie is voor de karakterisatie van atherosclerotische plak, is dit, voor zover wij weten, de eerste keer dat  $\mu$ CT gebruikt is als referentie voor visuele en kwantitatieve analyse van CT beelden van atherosclerotische plaque.

HiSD heeft een aantal voordelen ten opzichte van het gebruik van scherpe reconstructiekernels. Ten eerste deconvolueert HiSD kleine structuren met hoge dichtheid zowel in het  $xy$ -vlak als langs de  $z$ -as, terwijl de huidige klinische reconstructiekernels niet deconvolueren langs de  $z$ -as. Ten tweede is de beeldruis significant minder voor CT beelden die gerestaureerd zijn met HiSD dan voor CT beelden die gereconstrueerd zijn met scherpe reconstructiekernels (bijv. B60), aangezien bij HiSD de beeldruis van het gerestaureerde beeld voor grote delen van het beeld gelijk is aan de beeldruis van het oorspronkelijke beeld. In onze studie zijn de CT beelden waarop HiSD is toegepast gereconstrueerd met gemiddeld tot gemiddeld-scherpe reconstructiekernels (i.e., B41, B46 en B50). HiSD kan echter ook toegepast worden op beelden die gereconstrueerd zijn met andere reconstructiekernels, zolang de PSF maar bekend is zodat de juiste parameters voor het Wiener Filter gekozen kunnen worden.

Hoewel in dit proefschrift slechts een beperkt aantal experimenten op in-vitro en in-vivo plaque specimens is uitgevoerd, geven de resultaten aan dat HiSD zowel de afbeelding als de kwantificatie van calcificaties kan verbeteren. Dit is in het bijzonder van belang voor het huidige onderzoek naar de relatie tussen kalk in de verschillende vaatstructuren enerzijds en hart- en vaatziekten anderzijds. De correlatie tussen kalk in de kransslagaders en de incidentie van kransslagaderlijke ziekte is inmiddels vastgesteld.<sup>13,14</sup> Sommige auteurs hebben ook een duidelijk relatie gevonden tussen calcificatie van de kransslagaders en de totale hoeveelheid atherosclerotische slagaderlijke plak. Tenslotte wordt in recente studies<sup>17</sup> gesuggereerd dat het verdelingspatroon van de afzetting van kalk in de kransslagaders een betere voorspellende waarde heeft voor de instabiliteit van plak dan de totale hoeveelheid calcificaties.

In dit proefschrift wordt HiSD voornamelijk toegepast op CT beelden van atherosclerotische plaque met calcificaties. De methode kan echter ook gebruikt worden om de diagnose te verbeteren in andere klinische applicaties waar de vervaging van kleine structuren met hoge dichtheid de analyse van vaten belemmert. In Hoofdstuk 4 laten we twee voorbeelden zien van andere mogelijke toepassingen van HiSD. Allereerst wordt de methode toegepast op in-vivo CTA beelden van atherosclerotische vaten in het brein. Daarnaast wordt het toepast op in-vivo CTA beelden van nierslagaders met stents. In het eerste geval laten we zien dat HiSD het onderscheid tussen calcificaties in de slagaders en bot verbetert. In het tweede geval vermindert HiSD de uitsmering van de stent over het lumen gevuld met contrast middel. Deze verbetering van de beelden is kwalitatief. In de toekomst is een kwantitatieve validatie van HiSD voor deze toepassingen nodig.

### **Algemene conclusies**

Het afbeelden van kleine structuren blijft een uitdaging, ondanks de vooruitgang van de MDCT scanners. Om de nauwkeurigheid van geometrische metingen te optimaliseren moeten de juiste afbeeldinginstellingen gecombineerd worden met geschikte kwantificatie methoden. Het is gebleken dat de meetnauwkeurigheid prima voorspeld kan worden op basis van de beeldruis en de PSF van een gegeven systeem en beeldvormingsprotocol. Selectieve deconvolutie is een manier om in de klinische praktijk de beeldkwaliteit van de gereconstrueerde CT beelden te verbeteren.

# Curriculum Vitae

Empar Rollano Hijarrubia

31-03-1974	Born in Valencia, Spain
1988-1992	Secondary school at Instituto Lluís Vives in Valencia
1992-1997	Licenciado in Physics, University of Valencia, Spain
1998-2000	Research assistance at Physics department, University of Valencia, Spain
2000-2002	M.Sc. Physics, University of Valencia, Spain
2002-2007	Ph.D research at Erasmus MC – University Medical Center of Rotterdam, The Netherlands Under the supervision of Prof. dr. W.J. Niessen Subject: Improving the imaging of small high-density structures in Computed Tomography.



## List of Publications

1. Ferrero JL, Roldan C, Juanes D, Rollano-Hijarrubia E, and Morera C. Analysis of pigments from Spanish works of art using a portable Energy-Dispersive X-ray Fluorescence (EDXRF) spectrometer. *X-Ray Spectrometry*. 2002; 31:441–447.
2. Rollano-Hijarrubia E, van der Meer F, van der Lugt A, *et al.* in *Proc. SPIE, Medical Imaging 2005: Physics of Medical Imaging* 2005;67-78.
3. Rollano-Hijarrubia E, Stokking R, van der Meer F, *et al.* Imaging of small high-density structures in CT: A phantom study. *Academic Radiology* 2006; 13:893-908.
4. Rollano-Hijarrubia E, Stokking R, Niessen WJ. Accuracy comparison of a 16 and 64 multidetector-row computed tomography scanner to image small high-density structures. *Investigative Radiology* 2006; 41:781-792.
5. Rollano-Hijarrubia E, Niessen W, Weinans H, *et al.* Histogram-based selective deblurring to improve computed tomography imaging of calcifications. *Investigative Radiology* 2007; 42:8-22.
6. Rollano-Hijarrubia E, Manniesing R, Niessen WJ. Histogram-based Selective Deblurring and Automated Vessel Segmentation for Improved In Vivo Calcification Visualization and Quantification in CTA. *In preparation to be submitted.*

